



Effect of composition and morphology on the electrochemical performance of $\text{Na}_3\text{V}_2(\text{PO}_4)_2\text{F}_3/\text{Na}_3\text{V}_2(\text{PO}_4)_2\text{FO}_2$

Runhe Fang

► To cite this version:

Runhe Fang. Effect of composition and morphology on the electrochemical performance of $\text{Na}_3\text{V}_2(\text{PO}_4)_2\text{F}_3/\text{Na}_3\text{V}_2(\text{PO}_4)_2\text{FO}_2$. Material chemistry. Sorbonne Université, 2022. English. NNT : 2022SORUS001 . tel-03723143

HAL Id: tel-03723143

<https://theses.hal.science/tel-03723143>

Submitted on 14 Jul 2022

HAL is a multi-disciplinary open access archive for the deposit and dissemination of scientific research documents, whether they are published or not. The documents may come from teaching and research institutions in France or abroad, or from public or private research centers.

L'archive ouverte pluridisciplinaire **HAL**, est destinée au dépôt et à la diffusion de documents scientifiques de niveau recherche, publiés ou non, émanant des établissements d'enseignement et de recherche français ou étrangers, des laboratoires publics ou privés.

Sorbonne Université

Ecole doctorale 397

Laboratoire de Chimie de la Matière Condensée de Paris

Effect of composition and morphology on the electrochemical performance of $\text{Na}_3\text{V}_2(\text{PO}_4)_2\text{F}_3/\text{Na}_3\text{V}_2(\text{PO}_4)_2\text{FO}_2$

Par **Runhe FANG**

Thèse de doctorat de Physique-Chimie des Matériaux

Dirigée par Sophie Cassaignon

Soutenance prévue le 13 Janvier 2022

Devant le jury composé de :

Mme. Souad AMMAR-MERAH	Professeure de l'Université de Paris,	Rapportrice
M. Dominique LARCHER	Professeur de l'Université de Picardie Jules Vernes,	Rapporteur
Mme. Souhir BOUJDAY	Professeure de Sorbonne Université,	Examinatrice
M. Olivier CROSNIER	Maître de conférences à Polytech'Nantes,	Examineur
M. Jacob OLCHOWKA	Chargé de Recherche à l'Institut de Chimie de la Matière Condensée de Bordeaux,	Encadrant
Mme. CROGUENNEC Laurence	Directrice de Recherche à l'Institut de Chimie de la Matière Condensée de Bordeaux,	Encadrante
Mme. Sophie CASSAIGNON	Professeure de Sorbonne Université,	Directrice de thèse

Acknowledgements

First of all, I would like to express my gratitude to all my director and supervisors, Sophie Cassaignon, Jacob Olchowka and Laurence Croguennec, for guiding me in the science world. It was Sophie who brought me to the kind LCMCP, where I spent almost four years (including the previous six months as an intern) and patiently answered all my questions and helped me to arrange and solve all my problems. Secondly, Laurence, who brought me to know all the friendly people in ICMCB. I really appreciate her expertise and wisdom in our projects. Finally, Jacob, who was always there to answer my questions about electrochemistry and to organize the collaboration between Chloé, Rafaël and me.

I want to thank all the members of my jury: Souad Ammar-Merah, Dominique Larcher, Souhir Boujday, Olivier Crosnier, Jacob Olchowka, Laurence Croguennec and Sophie Cassaignon for their acceptance to my thesis presentation and for their time to review my work. Special thanks to the two reporters, Souad Ammar-Merah and Dominique Larcher, for completing my thesis report in such a short time during the holidays.

I want to also thank the lab directors, Chtristian Bonhomme and François Ribot, for their dedication to the lab running and providing us a safe and comfortable working environment during the pandemic. And great thanks to the administrative stuff in LCMCP: Corinne Pozzo Di Borgo, Hélène Gervais, Simon Dadoun, Diana Lesueur and Nora Abdoul-Aribi for helping me with various administrative and work-related issues.

I would like to thank all my friends at LCMCP and ICMCB for their help and encouragement in my life and work: Mélissa, Caroline, Fernando, Edouard, Lise, Amandine, Anissa, Ryma, Adeline, Jérémy, Corentin, Binghua, Kankan, Yang, Guillaume, Maxime, Chloé, Daniel, Ronan, etc.

Finally, I would like to thank my family and Yujin for the mental and life support they have given me. Thank Yujin for being with me every day.

Thanks to all of you

Runhe

Table of contents

Glossary.....	2
General introduction.....	4
Chapter I State of the art	8
1. Introduction of batteries	10
2. Sodium ion battery	12
2.1 Negative electrodes for sodium-ion batteries.....	14
Sodium metal.....	14
Graphite	14
Hard carbon	15
Other materials	15
2.2 Electrolytes for Sodium-ion batteries.....	15
3. Positive electrode materials.....	17
3.1 Layered transition metal oxides	17
3.2 Polyanion compounds	19
$\text{Na}_2\text{Fe}_2(\text{SO}_4)_3$ and related materials	21
NaFePO_4 and related materials.....	22
$\text{Na}_3\text{V}_2(\text{PO}_4)_3$	22
4. $\text{Na}_3\text{V}_2(\text{PO}_4)_2\text{F}_3$ and $\text{Na}_3\text{V}_2(\text{PO}_4)_2\text{F}_{3-y}\text{O}_y$ family (NVPFO _y)	24
Structure	24
Element substitution.....	28
Synthesis.....	31
Morphology	32
Carbon-coating	32
Characterization techniques	33

5. Conclusion.....	36
References:	37
Chapter II: Effect of the particles morphology on the electrochemical performance of $\text{Na}_3\text{V}_2(\text{PO}_4)_2\text{F}_{3-y}\text{O}_y$	46
1. Introduction	50
2. Results and discussions	51
2.1 Structural and morphological characterization	51
2.2 Electrochemical properties	61
3. Conclusion.....	68
4. Experimental Section	69
4.1 Materials preparation.....	69
4.2 Characterization techniques	70
Acknowledgement.....	71
Reference.....	72
Additional Information.....	75
Chapter III Impact of the F^- for O^{2-} substitution in $\text{Na}_3\text{V}_2(\text{PO}_4)_2\text{F}_{3-y}\text{O}_y$ on their transport properties and electrochemical performance.....	78
1. Introduction	82
2. Experimental Section	83
2.1 Materials preparation	83
2.2 Characterization techniques	85
3. Results and discussions	87
3.1 Structural and morphological characterization	87
3.2 Transport and Electrochemical properties.....	96
4. Conclusion.....	106
Acknowledgements	106

References	107
Chapter IV: Nanosizing and ionic liquid particle's coating: two ways to improve transport properties of $\text{Na}_3\text{V}_2(\text{PO}_4)_2\text{FO}_2$ electrode material.....	111
1. Introduction	114
2.1 Materials preparation	115
2.2 Characterization techniques	116
3 Results and discussions	117
3.1 Structural and morphological characterization	117
3.2 Transport kinetics and energy storage performance.....	126
4. Conclusion.....	138
5. Reference.....	139
Chapter V: Synthesis of polyanionic electrode material $\text{Na}_3\text{V}_2(\text{PO}_4)_2\text{F}_{3-y}\text{O}_y$ in deep eutectic solvent	144
1. Introduction	147
2. Experimental Section	148
2.1 Materials preparation	148
2.2 Characterization techniques	149
3. Results and discussions	150
3.1 Structural and morphological characterization	150
3.2 Transport kinetics and energy storage performance.....	157
4. Conclusion.....	159
Reference.....	160
Conclusion.....	163

Glossary

CV	Cyclic voltammetry
DES	Deep eutectic solvent
DMC	Dimethyl carbonate
EC	Ethylene carbonate
EIS	Electrochemical impedance spectroscopy
FEC	Fluoroethylene carbonate
GCD	Galvanostatic charge/discharge
GITT	Galvanostatic intermittent titration technique
ICP-OES	Inductively coupled plasma-optical emission spectroscopy
IL	Ionic liquid
IR	Infrared spectroscopy
LIB	Lithium ion battery
LMO	layered metal oxide
NASICON	Na Super Ionic CONductor
NMP	N-Methyl-2-pyrrolidone
NMR	Nuclear magnetic resonance
NVPF	$\text{Na}_3\text{V}_2(\text{PO}_4)_2\text{F}_3$
NVPFO ₂	$\text{Na}_3\text{V}_2(\text{PO}_4)_2\text{FO}_2$
NVPFO _y	$\text{Na}_3\text{V}^{3+}_{2-y}\text{V}^{4+}_y(\text{PO}_4)_2\text{F}_{3-y}\text{O}_y$
PC	Propylene carbonate

PVDF	Polyvinylidene fluoride
SEI	Solid electrolyte interphase
SEM	Scanning electron microscopy
SIB	Sodium ion battery
TEM	Transmission electron microscopy
XPS	X-ray photoelectron spectroscopy
XRD	X-ray diffraction

General introduction

As more and more countries begin to shift their focus from fossil fuel to renewable energy sources, the need for energy storage technologies for electricity grids, mobile devices and electrical vehicles is continuously growing. For these application areas, Lithium-Ion Battery (LIB) is currently the most used and suitable technology to fulfill the specifications needed for these purposes. With the development of related industries, the consumption of related resources will definitely increase rapidly and their costs will certainly drop further. However, LIBs are also facing a latent crisis, i.e. the imbalance between supply and demand. Most of the world's lithium resources today come from Australia and South America, yet battery manufacturing plants are primarily located in Asia. The long distances between related industries can easily cause a break in the supply chain at special times: such as the current pandemic period. Among the many alternative technologies available, sodium ion batteries (SIB) are emerging for certain applications, and especially for grid energy storage. The ubiquitous availability of sodium resources greatly alleviates the anxiety of uneven resource distribution. At the same time, it has attracted the attention of many researchers with its predictable cost advantage. Meanwhile, the technology of SIB is similar to LIB which do not need to change too much the production chain in the factories, also allowing its fast commercialization.

In the SIB system, the positive electrode plays an important role. Although weaker than layered oxide materials in some aspects, such as electrical conductivity, polyanionic materials have become one of the two main categories of positive electrode materials with their excellent electrochemical stability and high operating voltage. $\text{Na}_3\text{V}_2(\text{PO}_4)_2\text{F}_{3-y}\text{O}_y$ ($0 \leq y \leq 2$) family is especially the most outstanding in terms of electrochemical performance. However, the electrochemical performance is limited because of the rather poor electronic conductivity induced by the isolated vanadium bi-octahedra units within the structure. There have been many studies to improve the electrochemical properties of $\text{Na}_3\text{V}_2(\text{PO}_4)_2\text{F}_{3-y}\text{O}_y$ by means of carbon coating and special morphology etc. However, unconscious improvements in multiple aspects can lead to neglected further understanding of one specific changed element, due to the ultimately electrochemical performance enhancements.

Therefore, this PhD thesis consists of well controlling all the varieties and comparing the morphology and composition impact of $\text{Na}_3\text{V}_2(\text{PO}_4)_2\text{F}_{3-y}\text{O}_y$ without any carbon coating in order to improve its final electrochemical performance through a more fundamental perspective. Thus, this work is composed of the next parts under the form of deposited articles.

- ❖ In the first chapter, which is a state of the art, the background of the development of batteries and especially the sodium ion batteries will be briefly introduced. The common materials for each different part of the SIB will be further described. Next, attention will be focused on $\text{Na}_3\text{V}_2(\text{PO}_4)_2\text{F}_{3-y}\text{O}_y$ and show the current status of its research in detail in terms of crystal structure and synthesis, etc.
- ❖ Then in the second chapter, a series of slightly tuned synthesis with the same precursors were carried out to obtain the $\text{Na}_3\text{V}_2(\text{PO}_4)_2\text{F}_{3-y}\text{O}_y$ particles with different morphologies and similar composition and then investigate the effect of morphologies on energy storage performance.
- ❖ In the subsequent chapter III, from one most performant morphology found in the second chapter, the effect of the oxygen content on transport properties and electrochemical performance within $\text{Na}_3\text{V}_2(\text{PO}_4)_2\text{F}_{3-y}\text{O}_y$ (different O^{2-} substitution percent) were investigated, while keeping the morphologies unchanged.
- ❖ In the next chapter IV, the $\text{Na}_3\text{V}_2(\text{PO}_4)_2\text{FO}_2$ found in chapter III with those synthesized through different methods with the same particle composition but totally different morphologies and surface functionalization were compared to further understand the morphology and surface coating impact on the energy storage capacity.
- ❖ At last, deep eutectic solvent, one kind of ionic liquid, was used as a new synthesis medium to reach a totally new and special morphology not reported before and a new approach to make a carbon coating.

In order to facilitate reading, the figures and tables in the supporting information of each publication are integrated into the body of the chapters.

Chapter I State of the art

1. Introduction of batteries

After the digital revolution, human society is growing at an exponential rate with the adoption and proliferation of the digital electronics. This also provides a necessary condition for the increasing presence of smart devices in the lives of ordinary people. Another key precondition is a rather expense-saving and mobile energy supply system, thus, battery. Meanwhile, it also plays an important role in the saving of climate warming issue.

As the rapid development of human productivity since the twentieth century, the average global temperature has risen by more than one degree.^[1] This insignificant small average change sometimes obscures the real serious climate change behind it. The 2020 average temperature in Europe rose by 2.2 °C than the average from 1951 to 1980 while France rose 2.1 °C.^[2] These changes are believed to be the cause of nowadays increasingly common extreme weather phenomena. German, Belgium and China suffered from the giant flooding this summer and the local people's property life and property was greatly damaged during the disaster. In the summer of 2021, Lytton of Canada met the record breaking 49.5 °C which not only caused more than 230 deaths in British Columbia, but also lit several forest fires and released again numerous carbon dioxide into the atmosphere, thus, entering a vicious circle. In order to tackle the climate change problem, 196 countries adopted the Paris agreement in 2015 to limit the temperature increase. With the advancement of related policies in various countries, more and more governments have made commitments to reach carbon neutrality. European climate law was adopted by European commission and European council this year to achieve the climate-neutral, net zero greenhouse gas emissions, by 2050 for European union countries.^[3]

In 2020, the total emission with international transport of EU-27 is around 4 million kilo ton CO₂ equivalents.^[4] One of the key methods to decrease the emission is to increase the proportion of renewable energy. The wind energy and solar energy ratio increased from 9.15% and 3.5% to 14.37% and 5.21% for electricity production in EU-27 since the adoption of Paris Agreement.^[5] However, solar energy and wind energy are not stable and often cause heavy burden to local electric grid. Therefore, electrical energy storage systems are necessary, and batteries are one of the most promising technologies. Another major source of CO₂ emission is the transport sector which compose around 16% greenhouse gas release in 2020, with 12% coming from the burning of petrol and diesel.^[6] The booming electric vehicle industry based on lithium ion batteries nowadays is a powerful measure to alleviate this problem.

Because of this essential technology which is vital to the modern human society, the Noble Prize in 2019 was awarded to three founders of lithium batteries system, John Goodenough, Stanley Whittingham and Akira Yoshino. In response to the oil crisis of the 1970s, Whittingham created an efficient type of battery, which used lithium and had a titanium disulfide (TiS_2) positive electrode under the intercalation/deintercalation mechanism and thus presented rechargeable property.^[7,8] The rather low redox potential caused by the TiS_2 was then overcome by changing the electrode material to more efficient lithium cobalt oxide LiCoO_2 with similar layered structure by Goodenough, leading to a more powerful battery.^[9] This results then inspired many other researches and lead to the most popular $\text{Li}_x(\text{Ni,Mn,Co})\text{O}_2$ afterwards. This group then further develop the olivine LiFePO_4 material as positive electrodes in 1997.^[10] Yoshino developed the first commercially viable lithium ion battery in 1985 combing the LiCoO_2 positive electrode with negative electrode of petroleum coke which can also store the lithium ions.^[11] This swap avoids the highly reactive lithium metal and the resulted lithium dendrites upon cycling which can contribute to fire and violent explosion through the inner short circuit.

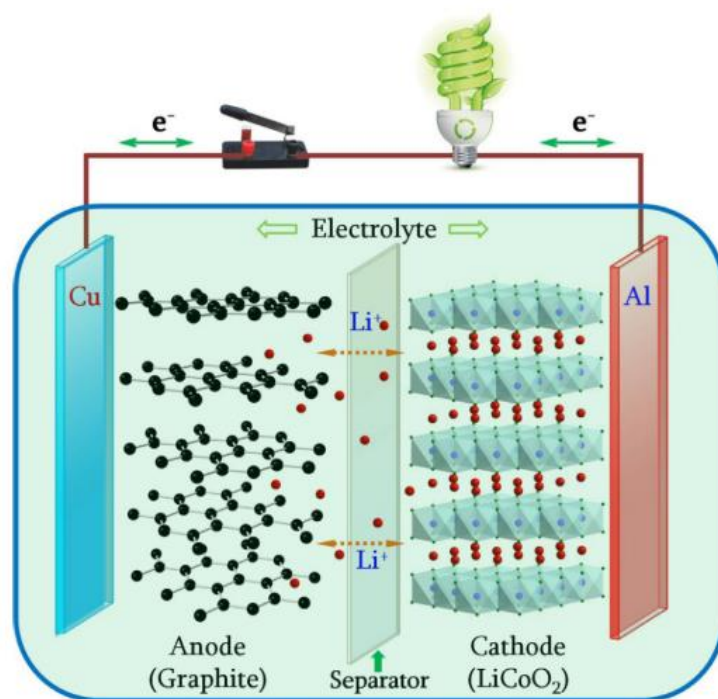


Figure 1: structure of a Lithium-ion battery (adapted from ref^[12])

As indicated in **Figure 1**, the lithium-ion battery is normally composed by positive electrode (also named cathode when battery is discharging, usually LiCoO_2 or its derivative and Al as current collector), organic electrolyte containing Li^+ salt under the form of carbonate solvent,

separator and negative electrode (also named anode, usually graphite with Cu as current collector). During charge, the Li^+ ions are deintercalated from the active materials of positive electrode with the oxidation of Co or other transition metal element. Then the Li ions migrate to negative electrode and is stored in the graphite under the force of electric field generated by outer circuit. The stored Li^+ will be released back to the host structure in positive electrode with the reduction of correspond transition metal when the battery is discharging.

2. Sodium ion battery

As mentioned before, the lithium is increasingly needed. Nevertheless, the lithium reserve distribution is uneven around the world and most of it situated in the south America. Chile, Argentina and Australia now cover 90% of lithium mining. The lack of diversification would make a big problem for the lithium price. Although, the concentration of lithium in the used LIBs is around 5-7 wt% which is far higher than in the natural resources, the efficiency to recycle the lithium from electrode or electrolyte is still not enough and the cost is too high to change the industry from lithium mining to the recycling.^[13,14] The focus is still on the recovery of cobalt and nickel.

Compared to the relatively rare lithium resource with 20 ppm in earth's crust, sodium, primarily from the rock salt and brine salt, is quite abundant and homogeneously distributed with 23,000 ppm and it is also present in relatively high abundance in the sea. Not to mention the 300 million tons yearly production of salt is more than the 80 million tons total resources of lithium.

Table 1: precursors and current collector price comparison of LIBs and SIBs

Precursors	Price
Li_2CO_3	10,000 US\$/ton
Na_2CO_3	<200 US\$/ton
Current collector	Price
Cu (11%)	5,000 US\$/ton
Al (5%)	1,500 US\$/ton

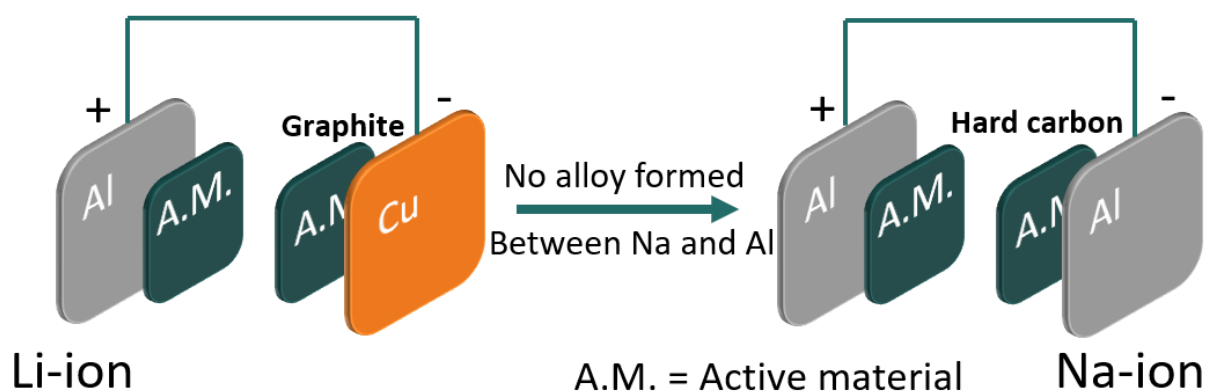


Figure 2: comparison between the structure of a lithium-ion batteries and sodium-ion batteries.

The abundance of sodium lead to rather low-cost precursors used in the syntheses of battery electrode. The sodium carbonate is just hundreds of dollars per ton compared to ten thousand dollars of lithium carbonate (**Table 1**). The advantages of sodium ion battery are not only based on the attractive price of sodium precursor, but also from the use of cheaper current collector (**Figure 2**). Al, 1500 dollars per ton, is used as the current collector for both positive and negative electrodes in SIBs whereas Cu is used as current collectors for negative electrodes in LIBs. As Li can form an alloy with Al at low voltage and thus destroy the current collector. Furthermore, the Al collector is much lighter than Cu collector. Early estimates predict a 30% cost decrease while ensuring sustainability.^[15]

Due to the similarity of sodium and lithium, the research of sodium ion battery electrode materials advanced quickly. But the radius of Na^+ is 1.02 Å, quite larger than the radius 0.76 Å of Li^+ ions, somehow leads to relatively larger interlayer expansion of 1.5 Å for layered type materials when Na^+ is extracted than the expansion of 0.5 Å for Li^+ extraction in LIBs. Larger structural expansions induce deformation between domains with different degrees of intercalation in the crystal structure, which leads to cracks, particle fragmentation, and amorphization after repeated cycling.^[16] Meanwhile, the redox couple for sodium is -2.71V vs SHE as compared to -3.02V vs. SHE for lithium.^[17] Thus, a direct extrapolation from the LIBs system to sodium ion battery system is not possible. Despite these shortcomings, it has shown considerable competitiveness in areas with low demands for gravimetric and volumetric energy such as stationary energy storage systems etc.

In general, sodium batteries exhibit their own characteristics and shortcomings, and likewise show potential for further performance improvements.

2.1 Negative electrodes for sodium-ion batteries

The energy density of a battery depends, on the one hand, on the specific capacity of electrode materials, and on the other hand, on the working voltage. The voltage is determined by the compatibility of the whole system, including the positive electrode, negative electrode and electrolyte etc. In the case of perfect electrolyte and positive electrodes, the negative electrodes should have the lowest possible voltage because the working voltage equals the difference in chemical potential between the positive electrode and the negative electrode. Thus, the aim is to find the materials with highest possible specific capacity and lowest voltage.

For sodium ion batteries, there are some typical negative electrodes:

Sodium metal

Ideally, Na metal should be the best negative material with the lowest possible cell potential and a very high theoretical capacity of 1166 mAh/g. However, full cell SIBs are usually fabricated by other materials because of the high reactive problem of metallic sodium with organic electrolyte solvents, unstable solid electrolyte interphase (SEI) in most organic electrolyte and the resulted growth of dendrite as well as the internal short circuit. With the rising trend of solid-state lithium battery research, considerable attention has been devoted to solid-state electrolytes for SIBs to prevent dendritic growth of the use of Na metal as well as the inherent safety problem due to the swap from flammable organic liquid to nonflammable formulations. However, the Na metal is still important in the fundamental battery testing. The new positive electrode material is usually cycled versus Na metal (half-cell) to test the energy storage performance.

Graphite

Graphite is a common negative electrode material for lithium ion batteries. However, as for the SIBs, Na⁺ insertion into graphite is significantly impeded and degradation of electrolyte and/or electrode materials was observed. Ge et al. found the electrochemical insertion of sodium into graphite results in NaC₆₄, corresponding to very low theoretical capacity of only 35 mAh/g.^[18] Stevens et al. found it is more energetically favorable for the sodium to electroplate on the surface of the carbon.^[19] Nevertheless, graphite can still present good electrochemical ability through some modification. Wen et al. created expanded graphite with wider interlayer space

which exhibit good host capability for Na^+ .^[20] Jache et al. found that graphite can also host the sodium intercalation/deintercalation by using the Na^+ -solvent co-intercalation phenomena.^[21]

Hard carbon

Different from graphite, hard carbon is composed by disordered carbon layers usually obtained through pyrolysis of solid organic precursors, such as celluloses, sugar, and/or resins etc.^[22,23]



Figure 3: morphology schematic of hard carbon.^[24]

This material presents more powerful performance than graphite in SIB with high specific capacity 300 mAh/g, approximates to graphite in LIB.^[23] However, the irreversible capacity loss in the first cycle is a serious issue in this negative electrode. Much of sodium ions are trapped in the hard carbon or reacted with electrolyte to form the SEI.^[25] Nevertheless, hard carbon is still the most widely used carbon source of SIB negative electrodes.

Other materials

Same as in LIB, reduced graphene oxide is used in SIB because of its high electrical conductivity and large interlayer distances and exhibit a specific capacity of 141 mAh/g at 40 mA/g.^[26] TiO_2 appeared as an attractive non-carbonaceous negative electrode material due to its abundance, environmental friendliness and inexpensive price. It demonstrates a specific capacity of 150 mAh/g over 1000 cycles in the nanocrystal forms. This nanosized, however, leads to more SEI formation and thus a large irreversible capacity loss.^[27] Other titanium-based materials such as $\text{Na}_2\text{Ti}_3\text{O}_7$ and $\text{Na}_2\text{Ti}_6\text{O}_{13}$ are also reported but do not show clear advantages.^[28–30]

2.2 Electrolytes for Sodium-ion batteries

Although electrolytes are not as active as the materials of two electrodes, the development of passive electrolytes is still complex and many issues need to be considered. Fortunately, due to the high similarity to lithium batteries, the relevant research experience can also be useful.

In general, electrolytes are composed of solvent, salt and additive, considering the following properties: the chemical, electrochemical and thermal stability; ionic conductivity and electronic insulation, ability to form a stable SEI; environmental friendliness and low production expense.

Although water-based electrolyte is possible in SIB, its use is limit because of the rather narrow potential window (~ 1.23 V).^[31] The researches in water-in-salt electrolyte succeeded in expanding the potential window of aqueous batteries to ~ 3 V. However, the consequent increase in cost and the difference in energy density and cycling stability with organic electrolytes batteries require further work.^[32] In the more widely studied and applied organic liquid electrolytes in most of the SIBs, NaClO_4 or NaPF_6 is usually used as the electrolyte salts.

Propylene carbonate (PC) is one common solvent in electrolyte due to its low cost and large electrochemical stability window in LIB. One problem of PC is its reaction with Li and result in poor cycling stability^[33,34] Hard carbon electrodes in SIBs with PC have a similar observation.^[35] But it is still used in SIB electrolyte due to the low cost and improved stability by mixing with other solvents.

Ethylene carbonate (EC) plays also an important role in SIB electrolyte, which has low viscosity but usually in solid state (melting point of 36.4 degrees) and thus often mixed with PC to stay in liquid form. The 1:1 mixture in SIBs can form a highly protective SEI layer at the petroleum coke negative electrode.^[36] Meanwhile, this protective layer can exploit full potential of hard carbon as solving the metal plating problem.

Dimethyl carbonate (DMC) is another most used solvent in LIBs because of its rather good ionic conductivity coming from the low viscosity. Its mixture with EC has wide electrochemical stability and become a standard in LIBs.^[37] Then this combination is also commonly used in SIBs.

Apart from the salts and solvents, additive is another key factor to improve the electrochemical stability of battery. Fluoroethylene carbonate (FEC) is the most popular additive in SIBs.

Appropriate amount of FEC can help the formation of a stable passive layer on the electrode surface which can decrease the side reaction between electrolyte and Na metal.^[38]

Room temperature ionic liquids are another alternative as the electrolyte solvents because of their good thermal, electrochemical stability, nonflammability and negligible vapor pressure.^[39] They are usually composed by cations like imidazolium (BMI^+ , EMI^+), ammonium (DBDM^+ , DEDE^+ , P224^+) and pyrrolidinium (Pyr_{14}^+ , $\text{C}_1\text{C}_3\text{pyr}^+$, Pyr_{H4}^+) with anions like tetrafluoroborate (BF_4^-), bis(trifluoromethanesulfonyl)imide (TFSI^-) and bis(fluorosulfonyl)imide (FSI^-).^[40] However, the synthesis of high purity ionic liquids remains an industrial challenge, which has led to its high cost and lack of widespread use.

Besides, safer solid-state electrolytes consist mostly of solid polymer or gel electrolytes are also researched due to their nonflammability and prevention of dendritic growth.^[41–43]

In summary, the standard sodium battery electrolyte, $\text{EC/DMC} = 1/1$, was used in all experiments in the next sections to avoid the performance fluctuations carried by the electrolyte.

3. Positive electrode materials

The positive electrode materials are composed of two major kinds: the layered oxides and the polyanionic materials.^[44] In addition to these two mainstream materials, there are materials such as Prussian blue analogues and some organic compounds.^[45]

3.1 Layered transition metal oxides

As one of the major electrode material type, layered metal oxide (LMO) supports the society full of mobile smart equipment with its high specific capacity. Thus, to further understand these materials, the layered oxide classification proposed by Delmas et al. is inevitable.^[46] These layered materials are constructed by MO_2 edge-sharing octahedra sheet with the interspace which can accommodate the alkali ion. P and O indicate the prismatic and octahedral site occupied by alkali ion, 2 and 3 means the total layer numbers in a repeat unit. A, B and C in the **Figure 4** indicate different position type in the layer. Bigger ion size of sodium this time make the sodium ion occupy successfully the prismatic sites and form stable P2 type phases, which do not exist in Li-based LMO.^[47]

At the beginning, different phases (O3, O'3, P3 and P2, primes here indicate the non-periodicity caused by distortion) of Na_xCoO_2 has been investigated. Among them, the P2 phase presents best thermodynamically reversible behavior with a potential range of 2.2V-4.0V and energy density of 440 Wh/kg.^[48] Besides, the superconductivity of hydrate $\text{P2-Na}_{0.35}\text{CoO}_2 \cdot 1.3\text{H}_2\text{O}$ was found by Takada et al.^[49] Thus, the P2-type Na_xCoO_2 attracted attentions of many researchers. Despite of its rather high rate capability and cycling stability, the cost of cobalt is one major problem in extensive application like that in LIBs.^[50]

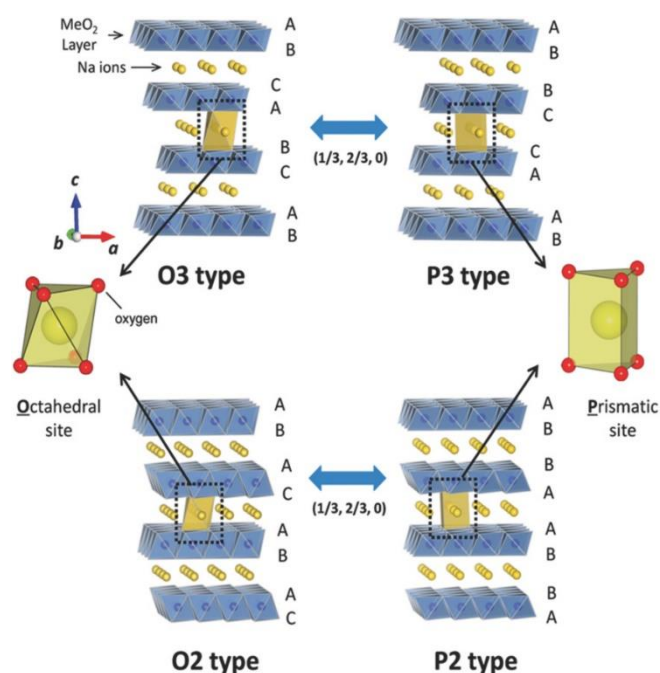


Figure 4: Classification of layered oxide materials. Image adapted from ref^[44].

The switch of Co to Fe (O3-type NaFeO_2) is a reasonable first thought, due to the abundance and low cost of Fe. However, like its Li counterpart, the poorer rate capability and lower energy density (around 280 Wh/kg) hinders further application.^[51] The simple substitution from Co to Mn does not present good results, either. Although $\text{Na}_{0.6}\text{MnO}_2$ presents good thermal stability, this P2 type layered oxide exhibits bad rate capability and electrochemical stability. The host structure collapse gradually after 8 cycles.^[52] However, Zuo et al. expanded P2 type $\text{Na}_{0.67}\text{MnO}_2$ with a water-mediated strategy which significantly increase the electrochemical performance and add the materials an excellent tolerance to humidity.^[53] The Cr replacement NaCrO_2 demonstrates a reversible capacity of 120 mAh/g.^[54] It is found the major cause of the capacity lose is the reaction with electrolyte. The carbon coating proves its protection efficiency to increase the cycling stability.^[55]

Just like LIBs, the research of layered oxide materials evolves to multiple transition metal substitution because of its effectively improve of electrochemical performances. The O3 phase $\text{NaFe}_{0.5}\text{Co}_{0.5}\text{O}_2$, which combines the advantages of Co and Fe, exhibits rather horizontal voltage profile at 3.1V as well as good structural stability and rate capability.^[56] Further replacement of Co with Ni ($\text{NaNi}_{1/3}\text{Co}_{1/3}\text{Fe}_{1/3}\text{O}_2$) reduces more the production cost while retaining the inherent advantages of $\text{NaFe}_{0.5}\text{Co}_{0.5}\text{O}_2$.^[57] In order to further reduce the Co use, different Co-free layered oxide materials were reported. P2-type $\text{Na}_{2/3}[\text{Fe}_{1/2}\text{Mn}_{1/2}]\text{O}_2$, increase significantly the energy density to 520 Wh/kg while maintain the low material cost. However the capacity retained just 75% after 30 cycles.^[58] The substitution with Ni, $\text{NaFe}_{0.4}(\text{Ni}_{1/2}\text{Mn}_{1/2})_{0.6}\text{O}_2$, leads to energy density of 400 Wh/kg and has better capacity retention (85% after 50 cycles).^[59] P2 type $\text{Na}_{0.5}[\text{Ni}_{0.23}\text{Fe}_{0.13}\text{Mn}_{0.63}]\text{O}_2$ synthesized by Hasa et al. demonstrates good reversibility of 180 mAh/g for over 70 cycles and surprising rate capability. It can be charged and discharged stably at the rate of 100 mA/g for over 100 cycles and keep the capacity of 100 mAh/g at 2C and 60 mAh/g at 5C.^[60]

For O3 type material, substitution of larger non-transition metal (such as Sn and Ti) is another effective method. The replacement of Sn for Mn in O3- $\text{NaNi}_{0.5}\text{Mn}_{0.5-y}\text{Sn}_y\text{O}_2$ can stabilize the O3-P3 transformation and increase the redox potential from 2.8V to 3.2V.^[61] Cu/Ti double substitution for Mn and Ni in the positive electrode material increases not only the extraction of sodium ion to 0.9 Na^+ per formula and the resistance to lattice volume change, but also the capacity against moisture.^[62] Ti/Zn substitution can also suppress significantly the phases transition at high voltage. The layered $\text{NaNi}_{0.45}\text{Zn}_{0.05}\text{Mn}_{0.4}\text{Ti}_{0.1}\text{O}_2$ gives rise to stable 170 mAh/g specific capacity with extraction of ~ 0.8 Na. Meanwhile, its 18650 Na-ion cells show comparable electrochemical performance to that of $\text{Na}_3\text{V}_2(\text{PO}_4)_2\text{F}_3/\text{C}$ cells.^[63]

In general, the layered oxide can provide high specific capacity while maintain the high rate cycling, nonetheless, low cyclability and bad stability under moisture exposure. Meanwhile, some of the layered oxides only have less than 2/3 Na:M ratio to form a specific phase. Considering the stability of material, not all the Na^+ can be extracted to participate in the energy conversion process due to the irreversible structural change at high deintercalation ratio.^[61,64,65]

3.2 Polyanion compounds

Although, the electronic conductivity of the polyanionic materials is lower than the layered oxide, these materials account for a significant proportion of the positive electrode materials

for SIBs, due to their high working potential and stable structural framework, which usually lead to the high energy density and long-run cycling stability. For polyanionic materials, there are numerous structure type like NASICON (Na Super Ionic CONductor), Olivine, Tavorite etc. Among the different types of polyanions, the sulfate (SO_4^{2-}), phosphate (PO_4^{3-}), and pyrophosphate ($\text{P}_2\text{O}_7^{4-}$) ions has received a lot of attention and research (**Figure 5**). However, the specific capacity of polyanionic materials are usually lower than layered oxide materials. The reason why polyanionic material can lead the track of SIBs is the inductive effect which makes the redox potential of one structure phase can be tuned easily.^[66]

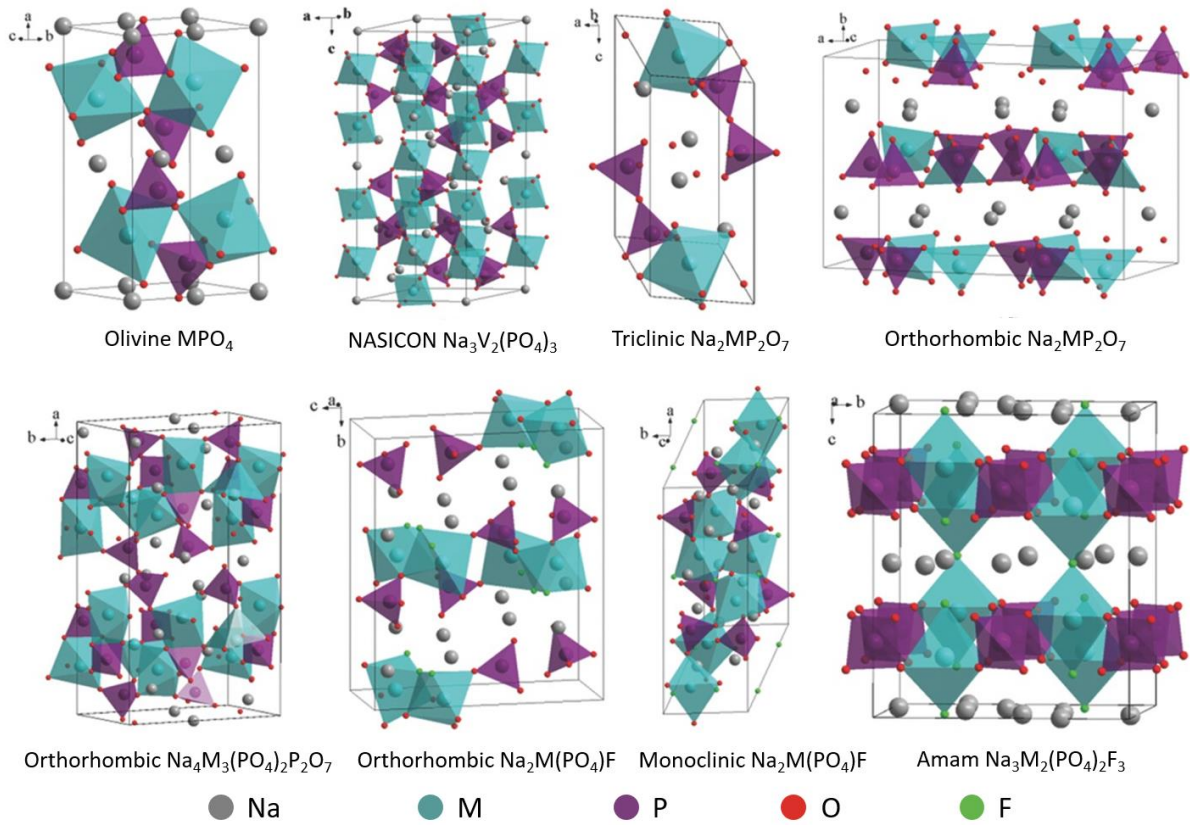


Figure 5: Illustration of crystal structures of main polyanionic (based on phosphorus) compounds adapted from ref^[67].

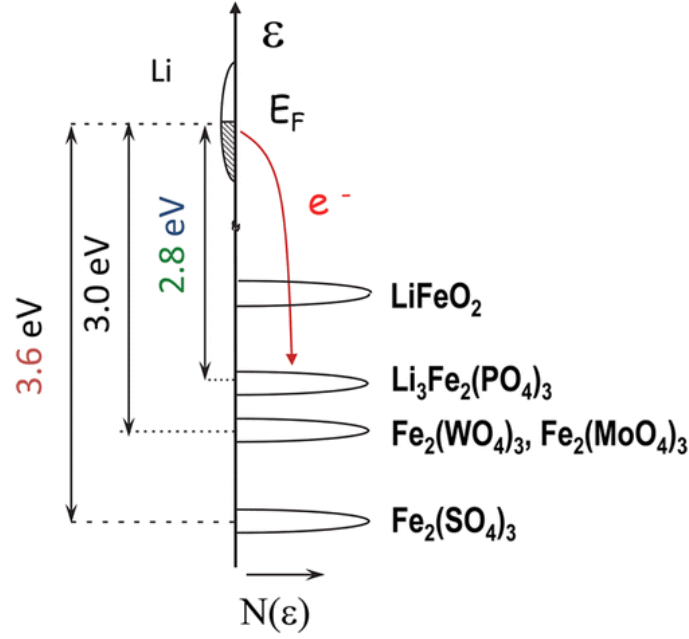


Figure 6: respective positions of the $\text{Fe}^{3+}/\text{Fe}^{2+}$ redox couple vs Li^+/Li adapted from ref^[68].

In the example of $\text{Fe}_2(\text{XO}_4)_3$ polyanionic material (X can be Mo W or S in this example case) (**Figure 6**), the inductive effect of polyanion group XO_4 can decrease or increase the covalency of the Fe-O bonds, depending on the electronegativity of X. Here, the replacement from Mo or W to S makes the Fe-O bond less covalent with the increase of electronegativity of X and thus decreases the antibonding state energy and hence increases the difference between the $\text{Fe}^{3+}/\text{Fe}^{2+}$ and the Li^+/Li couples which means higher operating potential.^[66,68] This theory was further extended to other polyanion materials of positive electrode for Li^+ and Na^+ batteries.

$\text{Na}_2\text{Fe}_2(\text{SO}_4)_3$ and related materials

$\text{Na}_2\text{Fe}_2(\text{SO}_4)_3$, alluaudite-type polyanionic material, is attractive for its abundant elements. Meanwhile, this material can present a redox potential at 3.8V for $\text{Fe}^{3+}/\text{Fe}^{2+}$ vs. Na. The as-prepared $\text{Na}_2\text{Fe}_2(\text{SO}_4)_3$ demonstrates excellent rate capability of up to 20 C and good cyclability with small volume change of 1.6%. And it exhibits excellent coulombic efficiency compared to the Na-lack P2 type layered oxide. Although the final reversible specific capacity is around just 100 mAh/g, the low cost from precursors and energy consumption is still attractive. However, the $\text{Na}_2\text{Fe}_2(\text{SO}_4)_3$ is not stable in aqueous condition and faced degradation after long time exposure to moisture to form $\text{Na}_2\text{Fe}(\text{SO}_4)_2 \cdot 4\text{H}_2\text{O}$.^[69] The further optimization by reaching sodium rich $\text{Na}_{2.5}\text{Fe}_{1.75}(\text{SO}_4)_3$ improves the diffusion efficiency and leads to better electrochemical performance.^[70]

NaFePO₄ and related materials

Because of the success of olivine-type LiFePO₄ (LFP) in LIBs, it's normal to consider the NaFePO₄ (NFP) as positive electrode materials for SIBs with the cost and abundant as well as the environmentally friendly element Fe.^[71–74] Compared to the Li counterpart, NFP exhibits lower potential plateau at 2.86V and bigger polarization. Meanwhile, most of the olivine-type NFP was synthesized by sodiation of delithiated LFP, which causes another disadvantage.^[75] Indeed, the direct synthesis of NFP leads to the Maricite polymorph. As for Maricite NFP, there is no obvious sodium diffusion channels due to the isolation of phosphate groups unlike the olivine type materials.^[44,76] Although olivine-type NFP is not as impressive as expected, the amorphous NFP presents better specific capacity of 152 mAh/g and 95% cycling capacity retention over 300 cycles.^[77] Another olivine type phosphate materials, NaFe_{0.5}Mn_{0.5}(PO₄) synthesized by interesting simple solid-state molten salt reaction at temperature inferior than 100°C. However, its low working potential of 2.7V is not competitive in SIBs.^[78] The pyrophosphates form, Na₂FeP₂O₇, has a low theoretical capacity of 90 mAh/g with one Na⁺ extracted reversibly and excellent thermal stability up to 500 °C.^[79] However, the unimpressive electrochemical properties combined with the weight problems associated with pyrophosphate make this material not attractive.

Na₃V₂(PO₄)₃

Compared to the polyanionic materials mentioned before, vanadium phosphate based materials Na₃V₂(PO₄)₃ (NVP) draw much more attention due to their better electrochemical performance.

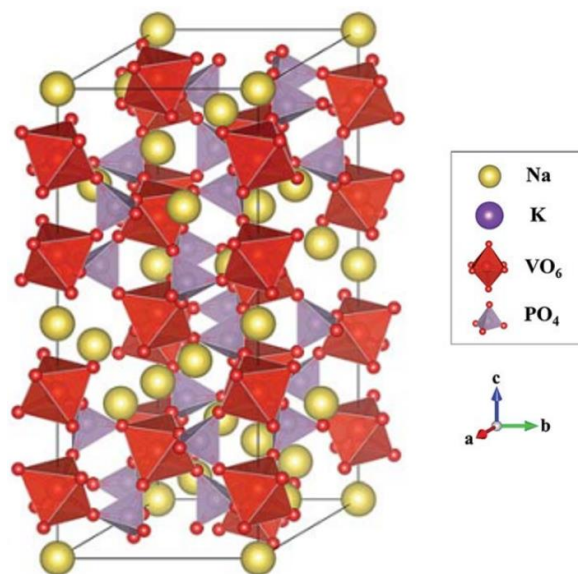


Figure 7: Crystal structure of NVP composed of “lantern”, adapted from ref^[80].

NVP has a 3D “lantern” framework with two VO_6 octahedra and three PO_4 tetrahedra joined to each other by corners sharing. Each lantern connects to each other to form a 3D path for Na^+ ions (**Figure 7**).^[81] Although the phosphate groups constitute a robust structure for high operating voltage, they also isolate the transition metal from each other, leading to rather low electronic conductivity. Thus, carbon coating to improve conductivity is usually applied.

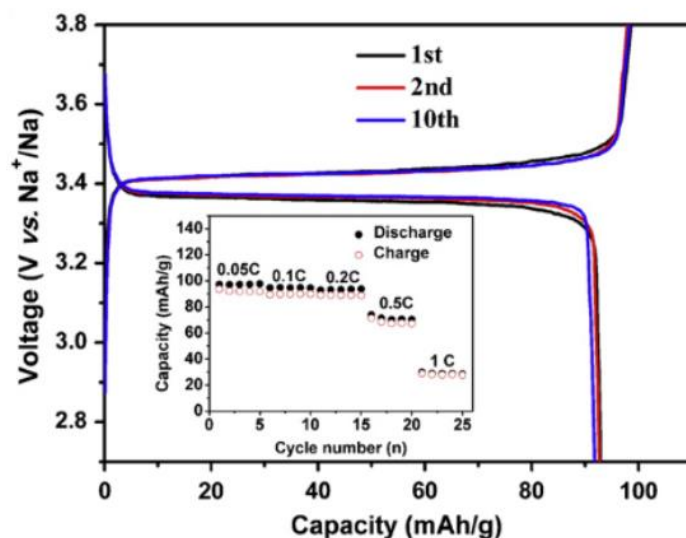


Figure 8: Charge/discharge curves for the $\text{Na}_3\text{V}_2(\text{PO}_4)_3/\text{C}$ sample at a current rate of 0.05 C in a voltage range of 2.7–3.8 V vs. Na^+/Na . Inset is the rate performance. Adapted from ref^[82].

The carbon coated NVP has a 3.4 V horizontal voltage profile, corresponding to the extraction of 2 Na^+ through a bi-phasic reaction (**Figure 8**).^[82] Graphene is another choice to improve

significantly the rate capability other than amorphous carbon. The NVP/Graphene demonstrates ~85 mAh/g capacity at 10C and maintain the structural integrity for over 300 cycles.^[83] Other carbon resources like mesoporous carbon and reduced graphene oxide were also reported to increase the cycling stability to thousands of cycles.^[84,85] Another interesting point of the NASICON type NVP is that the vanadium can be partially replaced by other transition metals, such as Mn^{2+} , Ti^{4+} , Ni^{2+} , Al^{3+} and Fe^{3+} .^[86–90] Among them, the Mn substituted $\text{Na}_4\text{V}^{3+}\text{Mn}^{2+}(\text{PO}_4)_2$ presents a high capacity of 156 mAh/g due to the extraction of three Na^+ with the electrochemical oxidation of V^{4+} to V^{5+} . Yet the irreversibility of this phenomenon and the caused enormous polarization remain a serious problem.^[86]

4. $\text{Na}_3\text{V}_2(\text{PO}_4)_2\text{F}_3$ and $\text{Na}_3\text{V}_2(\text{PO}_4)_2\text{F}_{3-y}\text{O}_y$ family (NVPFO_y)

Structure

The $\text{Na}_3\text{M}_2(\text{PO}_4)_2\text{F}_3$ ($\text{M} = \text{Al}^{3+}$, V^{3+} , Ga^{3+} , Fe^{3+} , Cr^{3+}) materials was first synthesized in 1999 by Le Meins et al.^[91] The vanadium fluoride phosphate $\text{Na}_3\text{V}_2(\text{PO}_4)_2\text{F}_3$ is composed of $\text{V}_2\text{O}_8\text{F}_3$ bi-octahedral units which are linked together by PO_4 tetrahedra via oxygen atoms to generate a three dimensional framework and the highly mobile Na ions are situated in the tunnel along the $[110]$ and $[1\bar{1}0]$ directions (**Figure 9a**).^[92] Though there are many Na^+ diffusion pathways, isolated vanadium bi-octahedra in the structure restricts the intrinsic electronic conductivity and influence heavily the rate capability.

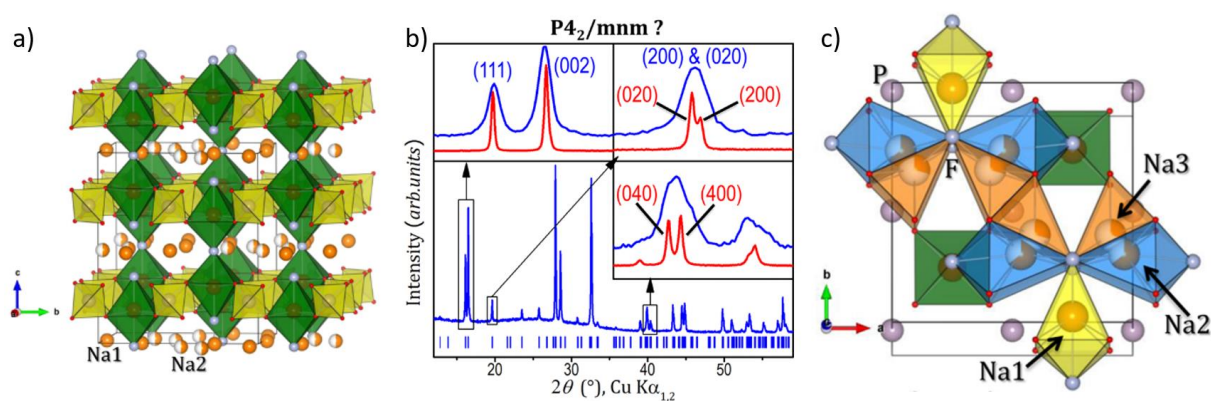


Figure 9: a) crystal structure of $\text{Na}_3\text{V}_2(\text{PO}_4)_2\text{F}_3$ in tetragonal space group $P4_2/mnm$ b) comparison between laboratory (blue) and synchrotron radiation (red) XRD data of $\text{Na}_3\text{V}_2(\text{PO}_4)_2\text{F}_3$ c) distribution of Na ions in the structure of $\text{Na}_3\text{V}_2(\text{PO}_4)_2\text{F}_3$. Adapted from ref^[92].

Its structure was first determined from the single-crystal X-ray diffraction in the tetragonal space group $P4_2/mnm$ at room temperature with cell parameter $a = b = 9.047(2)$ Å and $c = 10.705(2)$ Å in 1999.^[91] Bianchini et al. used high angular resolution synchrotron radiation

diffraction and found a subtle orthorhombic distortion which changes the space group to Amam with cell parameters of $a = 9.02847(3) \text{ \AA}$, $b = 9.04444(3) \text{ \AA}$, $c = 10.74666(6) \text{ \AA}$ (**Figure 9b**). This little modification in structural framework leads to significant impact on the Na ions distribution. There are three crystallographic sites for sodium, one site essentially fully occupied, Na(1), and two sites partially occupied, Na(2) and Na(3). Between these two, Na(2) is more likely to be occupied because of the electrostatic repulsion (**Figure 9c**). After heat up to 400K, the phase of $\text{Na}_3\text{V}_2(\text{PO}_4)_2\text{F}_3$ (NVPF₃) was characterized to I4/mmm space group determined by synchrotron radiation diffraction due to the sodium ions distributed like a circle around the tip Fluorine ion in the bi-octahedra $\text{V}_2\text{O}_8\text{F}_3$, showing the increased ion mobility at high temperature. [92,93]

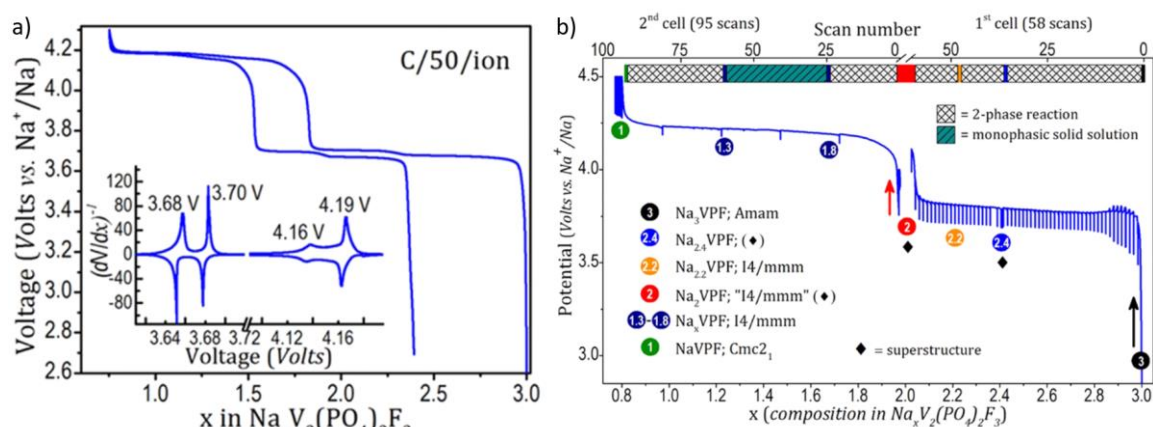


Figure 10: a) galvanostatic electrochemical cycling of $\text{Na}_3\text{V}_2(\text{PO}_4)_2\text{F}_3$ // Na battery at C/50 rate. b) potential-composition electrochemical curves obtained upon Na^+ extraction from $\text{NaV}_2(\text{PO}_4)_2\text{F}_3$ with the zone of biphasic reaction and solid-solution reaction indicated in the upper bar and its related composition shown at the left side. Adapted from ref [94].

A typical galvanostatic charge and discharge curves of NVPF₃ vs Na^+/Na is like the **Figure 10a**) with generally flat plateaus indicating a biphasic reaction. At first sight, the two plateaus of equal length at 3.7 V and 4.2 V indicate the presence of one intermediated phase $\text{Na}_2\text{V}^{3+}\text{V}^{4+}(\text{PO}_4)_2\text{F}_3$. Bianchini et al. used high angular and intensity resolution synchrotron radiation diffraction to reveal the further details of the structural change of NVPF₃ during deintercalation of sodium ions (**Figure 10b**). They found that the lower voltage region (3.7 V) reveals three biphasic reactions involving two intermediate phases, $\text{Na}_{2.4}\text{V}_2(\text{PO}_4)_2\text{F}_3$ and $\text{Na}_{2.2}\text{V}_2(\text{PO}_4)_2\text{F}_3$. At the end of the first plateau, the phase $\text{Na}_2\text{V}_2(\text{PO}_4)_2\text{F}_3$ is obtained, revealing a possible super-structure due to sodium ordering and/or charge ordering. Nevertheless, the accurate crystal structure is not determined up to now and an average unit cell in the tetragonal I 4/mmm is often considered. The higher voltage region (at 4.2 V) illustrates a biphasic reaction

upon which $\text{Na}_2\text{V}_2(\text{PO}_4)_2\text{F}_3$ progressively disappears, giving rise to a wide solid solution of compositions $\text{Na}_x\text{V}_2(\text{PO}_4)_2\text{F}_3$ ($1.8 \leq x \leq 1.3$). Finally, the end member of solid solution refined in the I4/mmm phase give rise to $\text{NaV}_2(\text{PO}_4)_2\text{F}_3$ with a space group of Cmc2_1 upon further desodiation. Rietveld refinement of this latter phase reveals the presence of mixed valence state $\text{V}^{3+} - \text{V}^{5+}$ in every $\text{V}_2\text{O}_8\text{F}_3$ bi-octahedron.^[94]

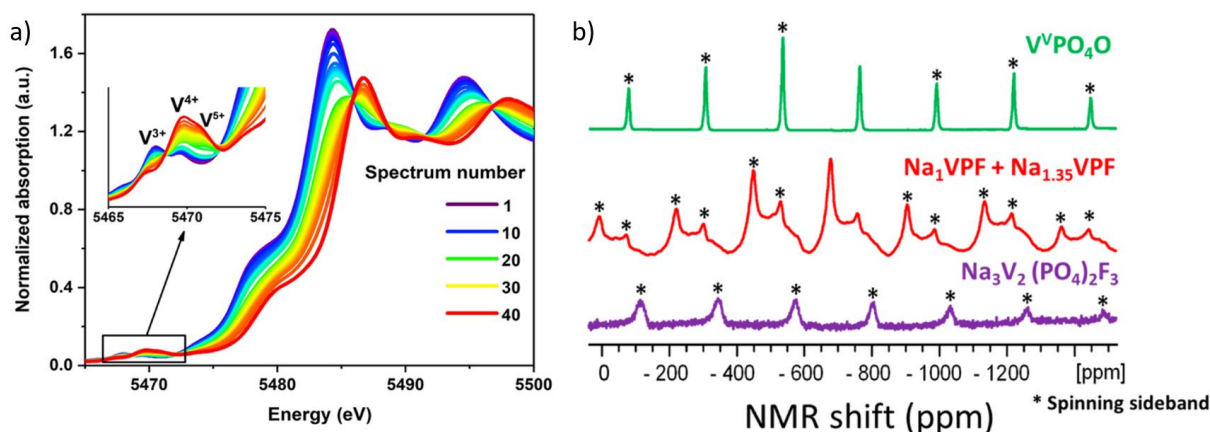


Figure 11: a) Operando vanadium K edge XANES spectra collected during the charge. Inset shows the evolution of the pre-edge signal (adapted from ref^[93]); b) ^{51}V MAS NMR spectra of the electrochemically oxidized compound (red, $\text{Na}_1\text{VPF} = \text{NaV}_2(\text{PO}_4)_2\text{F}_3$ and $\text{Na}_{1.35}\text{VPF} = \text{Na}_{1.35}\text{V}_2(\text{PO}_4)_2\text{F}_3$), the raw material $\text{Na}_3\text{V}_2(\text{PO}_4)_2\text{F}_3$ (purple), and $\text{V}^{\text{V}}\text{PO}_4\text{O}$ (green) (adapted from ref^[92]).

These processes were also studied by operando X-ray absorption spectroscopy (**Figure 11a**) by Broux et al. and Nguyen et al.^[95,96] The vanadium absorption edge, at around 5485 eV corresponding to the $1s \rightarrow 4p$ transition, is related to the valence state of the transition metal. And for pre-edge signals, the energy positions and intensity distributions represent the electronic structure and the local structural environment. The shift of the main absorption edge toward higher energy is consistent with the oxidation of V^{3+} and the pre-edge evolution to higher energy can be attributed to the progressive oxidation and distortion of the local environment. The disproportionation of two V^{4+} to V^{3+} and V^{5+} found by Bianchini et al. was also proved by the ^{51}V MAS NMR spectra after the deintercalation of one Na^+ (**Figure 11b**).^[95] and the DFT calculation of Long et al.^[97]

As we can see, there is only two sodium that can be extracted from the host structure in a normal functioning battery demonstrating an energy density of around 500 Wh/kg.^[98] To increase this latter, one interesting method is to insert another sodium into the host structure to form $\text{Na}_4\text{V}_2(\text{PO}_4)_2\text{F}_3$. Zhang et al. uses ball milling to insert the additional sodium.^[99] However, in the article, all the electrochemical tests were carried on the composite of $\text{Na}_{3.5}\text{V}_2(\text{PO}_4)_2\text{F}_3$, the

real performance of only $\text{Na}_4\text{V}_2(\text{PO}_4)_2\text{F}_3$ is unknown. And only 3 Na^+ can be extracted from the composite and still only two of them can be reinserted with a distorted host structure.^[99]

Another research direction is to further extract the third sodium which could theoretically lead to a better electrochemical performance to ~ 800 Wh/kg. However, the last Na^+ can only be removed at ~ 4.95 V beyond the stability window of usual electrolyte according to the calculation of Xu et al.^[100] This high working voltage is due to the stability of the strong Coulombic attraction between sodium ions and the polyanions. They then suggested a switch of F to less electronegative Cl to facilitate the extraction of Na^+ .^[100] Unfortunately, this hypothesis has not been verified by experiments yet.

Intriguingly, Yan et al. extracted the third Na with a prolonged charging time at high potential with a new formed disordered NVPF phase.^[101] Up to three Na were extracted at 4.75 V (contradicts the calculated results obtained before) and reinserted at 1.6 V vs Na^+/Na with a reversible capacity of 200 mAh/g. However, this capacity improvement might also stem from the decomposition of electrolyte because the number of extracted sodium ion at 4.75 V is fewer than that inserted at 1.6 V (**Figure 12**). Besides, due to the extra discharge capacity coming at a low potential, a 40% increase in capacity yields only a 15% benefit in energy density. This high potential charge also makes the original space group of Amam changed to I4/mmm for NVPF with significantly broadened and shortened peaks with the confirmation of results of synchrotron XRD and ^{31}P NMR, and can never be restored to its original state.^[101]

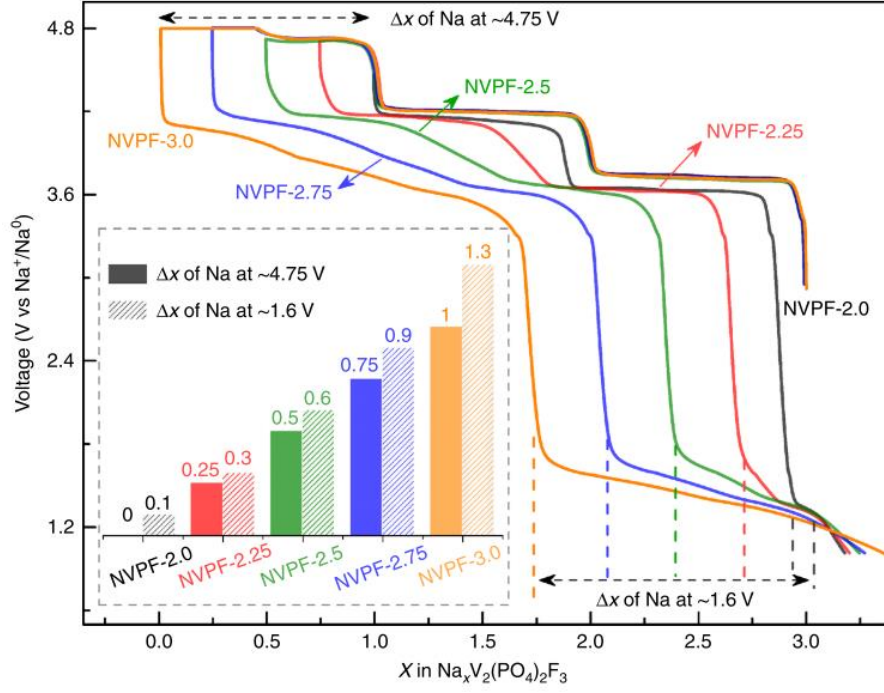


Figure 12: Galvanostatic electrochemical cycling of $\text{Na}_3\text{V}_2(\text{PO}_4)_2\text{F}_3 // \text{Na}$ with potential range from 1.6 V to 4.75 V. The inset demonstrates the Na ions extracted at ~ 4.75 V and the Na ions reinserted at ~ 1.6 V.

Element substitution

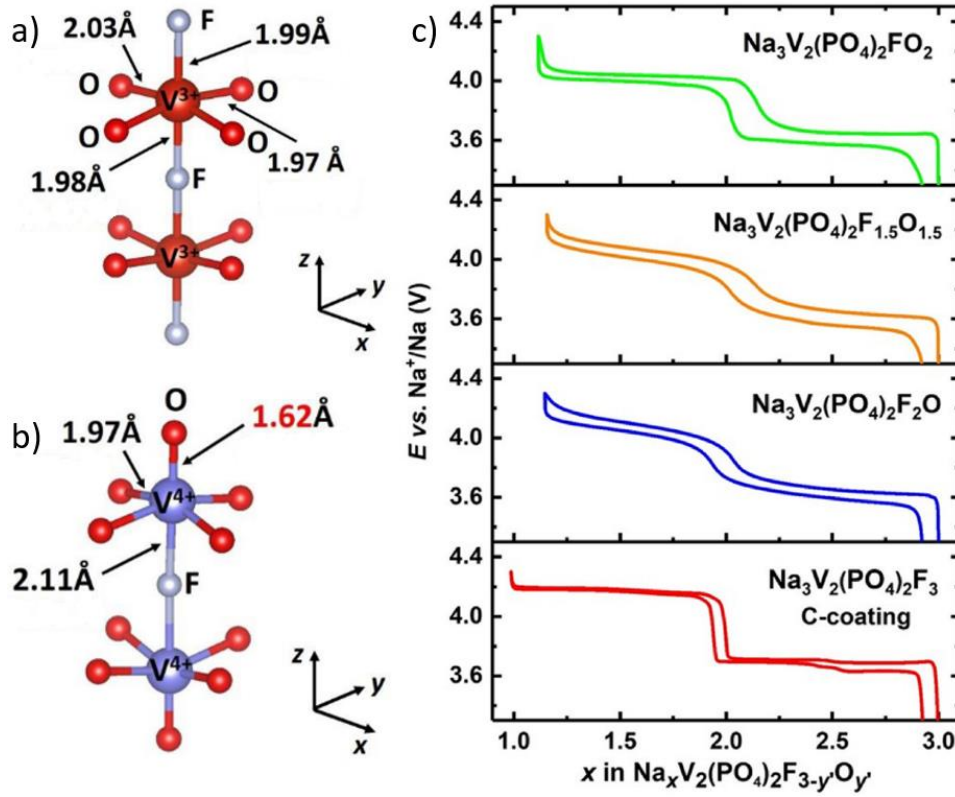


Figure 13: crystal structure of the bi-octahedral of a) $\text{Na}_3\text{V}_2(\text{PO}_4)_2\text{F}_3$ and of b) $\text{Na}_3\text{V}_2(\text{PO}_4)_2\text{FO}_2$ adapted from *ref*^[102]. c) Voltage composition curve of the $\text{Na}_3\text{V}^{3+}_{2-y}\text{V}^{4+}_y(\text{PO}_4)_2\text{F}_{3-y}\text{O}_y$ ($0 \leq y \leq 2$) adapted from *ref*^[103].

The most usual substitution element is F to O accompanied by the oxidation state change of vanadium to form $\text{Na}_3\text{V}^{3+}_{2-y}\text{V}^{4+}_y(\text{PO}_4)_2\text{F}_{3-y}\text{O}_y$ (NVPFO_y) ($0 \leq y \leq 2$) (**Figure 13a and b**). Park et al. firstly synthesized a series of NVPFO_y and found that all the materials present different but close average potential from 3.76 V to 3.9 V and similar specific capacity without significant tendency according to the oxygen variation. Furthermore, the different cell parameter, Na-vacancy and F/O distribution resulted in distinct voltage-composition curves.^[104] This found was further confirmed by the team of Croguennec et al.^[103,105] The cell parameter *c* decreases continuously with more disordered Na^+ distribution as the replacement from F to O. The charge compensation of this element substitution is attained by the continuous oxidation of vanadium and the formation of vanadyl bonds. Meanwhile, the O substituted NVPF clearly present sloping S shape voltage-composition signatures which indicate a continuous Na^+ de-intercalation and re-intercalation solid solution mechanisms from/in the structure during charge/discharge (**Figure 13c**).^[103,105] For the $\text{Na}_3\text{V}_2(\text{PO}_4)_2\text{F}_3$, when three Na^+ are extracted, the V^{3+} should be oxidized to possess an average oxidation state of +4.5. But for the more substituted NVPFO_y , the smaller the space in which vanadium can be oxidized. Meanwhile, after the extraction of more than two sodium ions in $\text{Na}_3\text{V}_2(\text{PO}_4)_2\text{F}_3$, the changed electrochemical curves signify that the crystal structure is modified (**Figure 14a**). In contrast, the unvaried electrochemical curves for NVPFO_y after the first cycle indicate a much better stability when the materials are overcharged (**Figure 14b**).^[103]

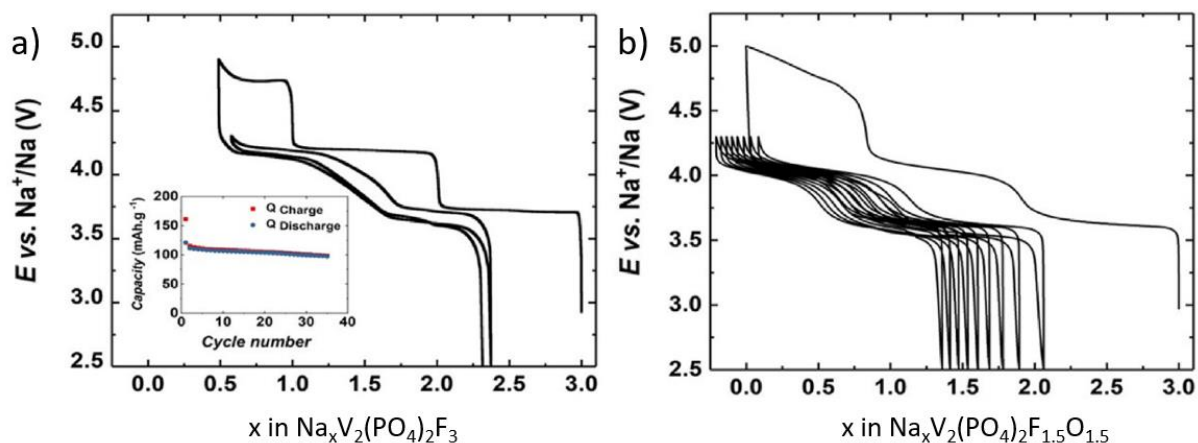


Figure 14: The electrochemical profile recorded for the half-cell $\text{Na}/\text{Na}_3\text{V}_2(\text{PO}_4)_2\text{F}_3$ during the first and the second cycles, charged up to 5.0 V vs. Na^+/Na during the first cycle. The inset corresponds to charge/discharge capacities as a function of the cycle number.

The stability improvement of O^{2-} substitution make the insertion of the 4th Na^+ possible to form Na_4VPFO_2 by lowering the potential to 1 V.^[106] The origin of the 4th sodium in insertion for NVPFO_2 is related to the strong screening effect of O^{2-} anions which compensates the electrostatic repulsion between the Na^+ ions and the strong stability of NVPFO_2 . However, the

additional sodium reversibly insertion/extraction happens at ~ 1.6 V.^[106] The low potential strongly limits the energy density obtained by another sodium ions insertion and it may also decompose the electrolyte, leading to significantly reduced cycling stability as found by Peng et al.^[107] But it still helps to decrease the sodium loss at the non sodium metal negative electrode during the first charge/discharge cycle.

The effectiveness of oxygen replacement in the improvement of the NVPF electrodes was also proved by Qi et al. who synthesized a series of NVPFO_y materials which present more than 90 mAh/g at 2C rate for over 1200 cycles.^[108]

Although, as mentioned before, the substitution of F to Cl predicted by Xu et al. through theoretical calculation should strongly enhance the energy density to around 800 Wh/kg, this assumption has not been verified by experiments yet.^[100]

Another common substitution choice is to dope other low-cost elements in vanadium. Among various metals, Al has attracted a great deal of interest due to its low cost, eco-friendliness, and ability to stabilize materials when charged and discharge. Pineda-Aguilar et al. doped the claimed pristine NVPF with 5% Al, and found the electrochemical performance was slightly better against lithium negative electrode.^[109] However, the NVPF material was probably partially oxidized (i.e. with O²⁻ substitution) since the charging/discharging curves were sloping indicating the solid solution mechanisms as mentioned before in the part of O doping. Olchowka et al. successfully increased the content of Al to form the Na₃V_{1.5}Al_{0.5}(PO₄)₂F₃ through a sol-gel process. They found the substitution of Al for V has minor effect on average potential than the F/O substitution with 3% theoretical gravimetric capacity increase for reversible exchange of 2 sodium ions.^[110] The 10% Y-doped NVPF Na₃V_{2-x}Y_x(PO₄)₃F₃/C (x=0.1) materials delivered a discharge capacity around 120 mAh/g at rate of 0.5C and even 80 mAh/g even at 50C might because of the larger ionic radius of Y providing a larger transport tunnel for Na⁺ diffusion. Furthermore, the weaker Y-O bonds compared to that of vanadium also facilitates the intrinsic electronic conductivity. As for the active elements which will also have redox reaction during the extraction/insertion of sodium ions, there is also researches on this type of doping to increase enhance the performance of NVPF. Compared to the vanadium, the amount of doping is typically very low, therefore the voltage platform is not observed. One doping example is the Titanium doping with +2, +3, +4 valence states. Yi et al. selected the titanium from +2 to +4 with different doping concentration from 0 to 20% in NVPF and they found the doping can have a significant impact on the morphology and electrochemical

performance of NVPF. The 10% Ti^{2+} substitution demonstrates the best rate capability of ~ 100 mAh/g at 40C.^[111] There is also a variety of other elements doping reported like Chromium^[112], Zirconium^[113,114], Gallium^[115], Manganese^[116] etc. In general, the substitution amount of Vanadium to other metal is always low, from 1% to 20% maximum. In particular, it improves the high rate capability at more than 10C probably thanks to the related structure strengthening.

Another substitution method is to replace the Na for other similar alkaline elements. Li et al. inserted Potassium into NVPF to improve the electrochemical performance to 120 mAh/g at 1C and this material remained 90 mAh/g at 10C after 1600 charging/discharging cycles because of the broadened Na^+ pathways after the bigger potassium doping.^[117] Kosova et al. also synthesized sodium lithium mixed $\text{Na}_{3-x}\text{Li}_x\text{V}_2(\text{PO}_4)_2\text{F}_3$ with good electrochemical performance and they thought the reason comes from the formation of surface impurity phase including V_2O_3 which has high electronic conductivity.^[118] Partheeban et al. reported an interesting solid state flux techniques using NaCl-LiF fluxes to form the $\text{Na}_{2.4}\text{Li}_{0.6}\text{V}_2(\text{PO}_4)_2\text{F}_{2.5}\text{O}_{0.5}$ crystals.^[119]

Synthesis

Generally, the NVPFO_y material family was synthesized by solid state synthesis which usually leads to the bulk and uncontrolled morphology. Although high energy consumption caused by several high temperature annealing process is a huge disadvantage, its easy control of O^{2-}/F^- ratio and straightforward operating characteristics have led to widespread use. In the previous year, many new synthesis methods appeared in the published articles, such as sol-gel methods, hydrothermal/solvothermal methods, ball-milling, spark plasma sintering and spray-drying methods. These methods gradually increased in proportion across studies due to their flexible synthesis conditions leading to different particle sizes and controlled morphologies. The sol-gel method is composed of mixing vanadium resource, fluorine resource and phosphorus resource with oxalic/citric acid for several hours to form a gel and then sintering the dried gel to get the carbon coated NVPF.^[110,120,121] The hydrothermal/solvothermal method is consist of adding all the mixed raw materials into an autoclave followed by low temperature heat treatment while adding or removing carbon sources as research needed.^[108,122–125] Spray-drying method is similar to sol-gel method. The difference lies only in the fact that the annealing of dry gel becomes the calcination of precursor after spray-drying.^[126–128] Ball-milling synthesis method is a combination of hydrothermal/solvothermal synthesis with a ball-milling process to coat final product with carbon.^[129] Spark plasma sintering and traditional solid state synthesis are extremely similar, but it can reduces the hours of high-temperature processing to ten or

twenty minutes.^[130] Compared to the conventional solid-state synthesis which cause usually agglomeration and limit the rate performance, sol-gel method and hydrothermal/solvothermal synthesis are promising to construct well designed structure and homogeneous element doping.

Morphology

In addition to the element doping, morphology is another well-known condition which can improve the final electrochemical performance because of the related specific area contact to electrolyte and the ion diffusion pathways. A larger surface area leads to better electrolyte contact i.e. higher material utilization and shorter diffusion paths then increase the rate capacity. Thus, plenty of morphologies at different sizes were synthesized to research this effect on NVPF such as the nanospheres/microspheres^[128,131,132], hollow aggregated particles^[122,125,133], nanocubes/microcubes^[134–136], nanoflowers^[123,137], platelets^[138] and many other special morphologies^[108,124,139–143]. However, many of the results in these studies were not influenced solely by morphologies. Synthesized NVPF materials are often accompanied by unavoidable oxidation i.e. oxygen doping due to the hydrothermal conditions (NVPF becomes actually NVPFO_y) or carbon coating. Different compositions of NVPF and the carbon coating also have great impact on the final electrochemical performance. Meanwhile, the performance is also influenced by the electrode formulation especially the carbon content and active material mass loading as well as the electrolyte used. With all the variables, it is difficult to strip the impact of morphologies alone. Thus, although nano-structuration improves high rate performance, a comparison of the literature between the different morphologies is not reliable considering the different experimental conditions used during electrochemical tests.

Carbon-coating

Carbon modifications are the most powerful method that enhance the existing NVPF's electrochemical performance. The coating of carbon layer can firstly enhance the synergic diffusion between electron and ions and protect the active material from the reaction with electrolyte thanks to its corrosion stability. Moreover, the carbon can also serve as a buffer for the tiny volume changes during the extraction/insertion of sodium ions.^[144] Most of the carbon resource can be classed into three kinds: amorphous carbon^[145], carbon nanotube^[126], graphene^[83,135] and reduced graphene oxide^[133,146]. All of the previously mentioned materials with excellent rate performance have been carbon coated. However, it should be pointed out

that the carbon coating layer can merely ameliorate the surface electron conductivity, and it is helpless to the conductivity of inner particles.^[144]

Characterization techniques

In this thesis, the NVPFO_y was synthesized primarily through solvothermal method. This method results in uncontrollable variations in the oxygen content of the finished product (details of which are discussed in the next chapters), and thus requires various methods to determine its exact composition. Most of the characterization techniques in this thesis refer to the results of the previous studies of Long Nguyen in the team.

Thus, the characterization techniques used in the thesis are briefly described here.

XRD: As the most common test for determining the phase purity of substances, the use of XRD is unavoidable in NVPFO_y . In addition to fitting the value of parameter c as mentioned before by Rietveld refinement to know the exact composition of NVPFO_y , the degree of oxidation of vanadium ($\text{V}^{3+}/\text{V}^{4+}$) can also be detected by shifting of (002) peak for NVPFO_y . The higher the degree of oxidation, the more the (002) peak shifts to the right, since different oxidation degrees of this material mainly affect parameter c (**Figure 15 inset**). This will be used several times in later chapters.

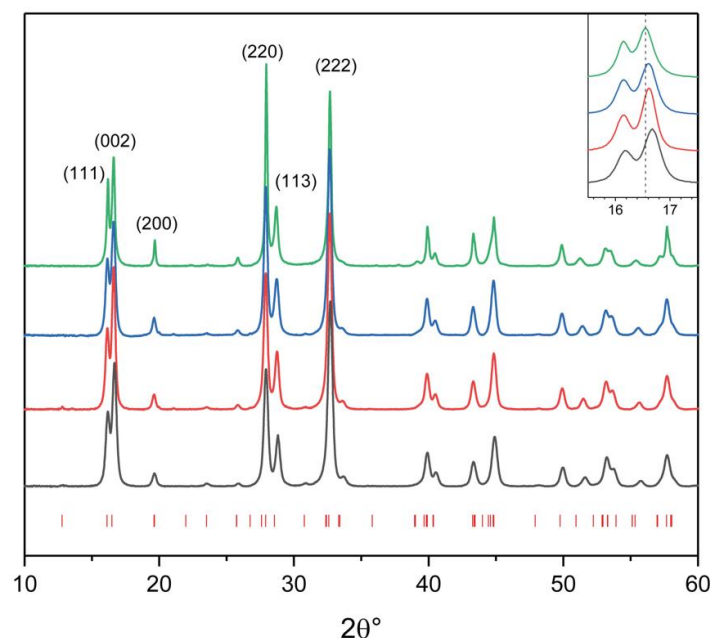


Figure 15: XRD for materials of $\text{NVPFO}_{0.80}$ (green), $\text{NVPFO}_{1.35}$ (blue), $\text{NVPFO}_{1.60}$ (red) and NVPFO_2 (black) with inset of zoom of (002) peak adapted from Chapter III

IR: the key for infrared spectroscopy in the detection of oxidation degree of vanadium is based on its capacity to identify the $\text{V}=\text{O}$ vibrational band. The vibration of the $\text{V}=\text{O}$ bond located at

$\sim 920 \text{ cm}^{-1}$ and $\sim 940 \text{ cm}^{-1}$ which corresponds to two a little different bonds groups of $\text{O}=\text{V}^{4+}-\text{F}-\text{V}^{4+}=\text{O}$ and $\text{O}=\text{V}^{3+}-\text{F}-\text{V}^{3+}-\text{F}$ as shown in the **Figure 16**. This hypothesis was proposed by Long et al.^[103] The intensity of the two peaks varies with the degree of oxidation of vanadium and will be discussed in detail in Chapter III.

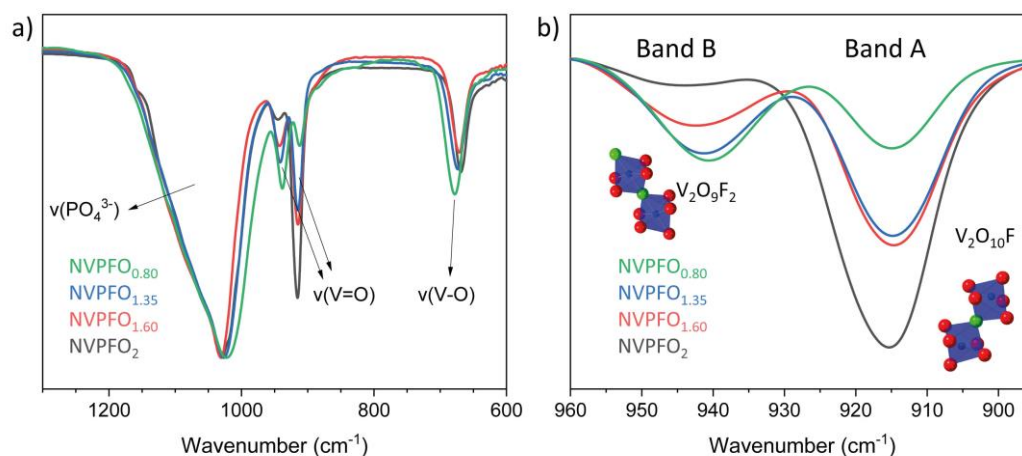


Figure 16: a) Comparison of IR spectra of NVPFO_{0.80}, NVPFO_{1.35}, NVPFO_{1.60} and NVPFO₂ in the wavenumber range of 600-1300 cm⁻¹. b) Zoom of the V=O vibration. Red ball: oxygen, blue ball: vanadium, green ball: fluorine. Images are adapted from Chapter III.

NMR: ²³Na and ³¹P solid-state NMR is very sensitive in the investigation of vanadium oxidation degree through the probe of their environment. The different vanadium presented around the phosphorus and sodium causes various signal. For example, the pure NVPF₃ should have just one major resonance peak at 6000 ppm corresponds to the P(OV³⁺)₄ local environment, while the pure NVPFO₂ possesses the single resonance at ~ 0 ppm attributed to the P(OV⁴⁺)₄ environment in the ³¹P solid-state NMR spectroscopy (**Figure 17**). In ²³Na solid-state NMR, NVPF₃ presents a major peak at ~ 140 ppm for the Na(V³⁺)₂ environment, and NVPFO₂ presents a major peak at ~ 80 ppm for the Na(V⁴⁺)₂ environment (**Figure 17**). These two spectroscopies will be used and discussed in the Chapter II and Chapter IV.

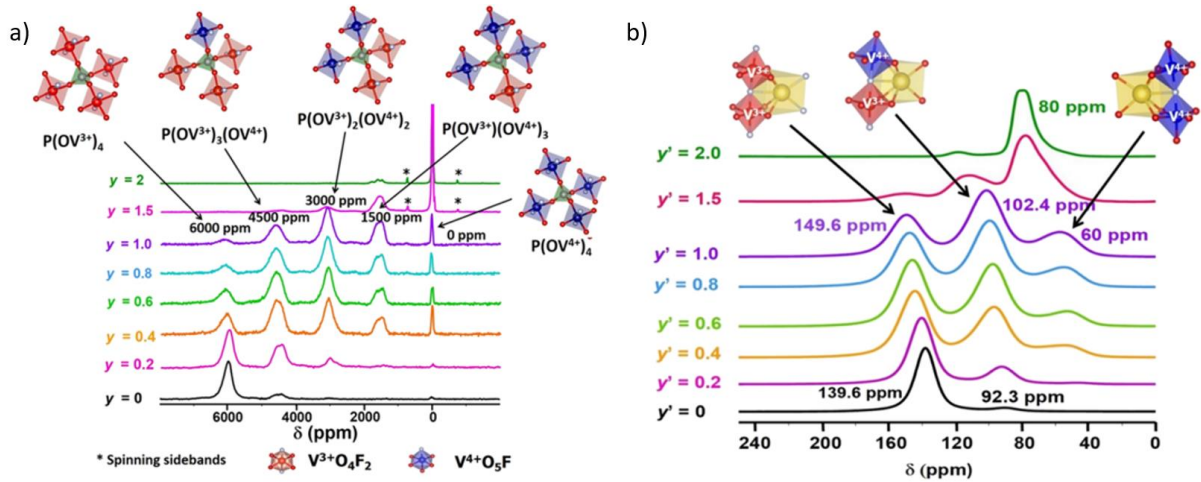


Figure 17: a): ^{31}P solid-state NMR spectroscopy for NVPFO_y and b): ^{23}Na solid-state NMR spectroscopy for NVPFO_y . Images adapted from ref^[102].

XPS: although the XPS (x-ray photoelectron spectroscopy) is a surface-sensitive quantitative spectroscopic technique, it can still give an idea of the oxidation degree of vanadium according to the related binding energy. As shown in **Figure 18**, if the degree of oxidation of vanadium is higher, then its signal peaks of $\text{V}2\text{p}_{1/2}$ and $\text{V}2\text{p}_{3/2}$ are more left-shifted presenting a greater binding energy with NVPFO_2 at ~ 524.6 eV and ~ 517.24 eV and NVPF_3 at ~ 523.71 eV and 516.64 eV.

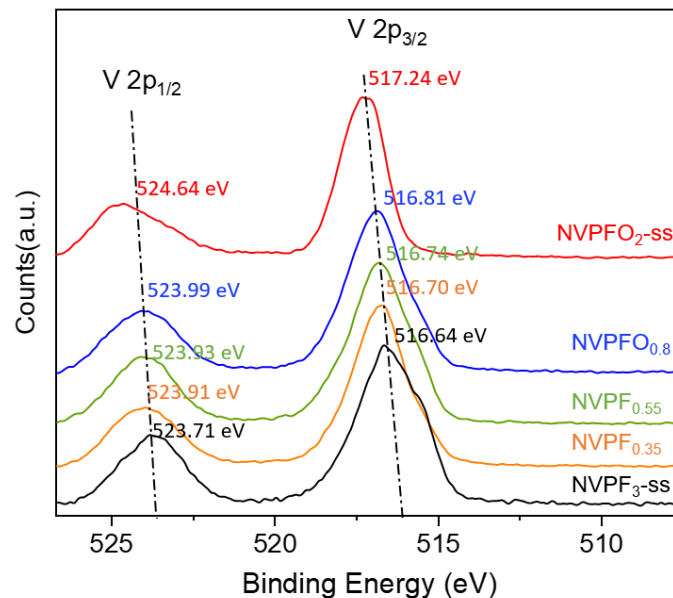


Figure 18: XPS spectra for $\text{V}2\text{p}$ orbital for NVPF_3 , $\text{NVPFO}_{0.35}$, $\text{NVPFO}_{0.55}$, $\text{NVPFO}_{0.8}$ and NVPFO_2 adapted from the Chapter II.

Raman: Raman spectroscopy is another good and simple method used firstly in this work to investigate the local environments of the NVPFO_y materials. This method was only applied to verify the existence of carbon coating before. The $\text{V}=\text{O}$ vibration is situated at $\sim 940\text{ cm}^{-1}$ and

the broad band at $\sim 1050 \text{ cm}^{-1}$ is characteristic of phosphate vibrations. The intensity of the V=O peak increases continuously with the concentration of V^{4+} (**Figure 19a**). Meanwhile, the intensity of the V-O bond at $\sim 530 \text{ cm}^{-1}$ is gradually decreasing and accompanied by a right ward shift from 525 to 532 cm^{-1} with the increase of vanadium oxidation degree (**Figure 19b**).

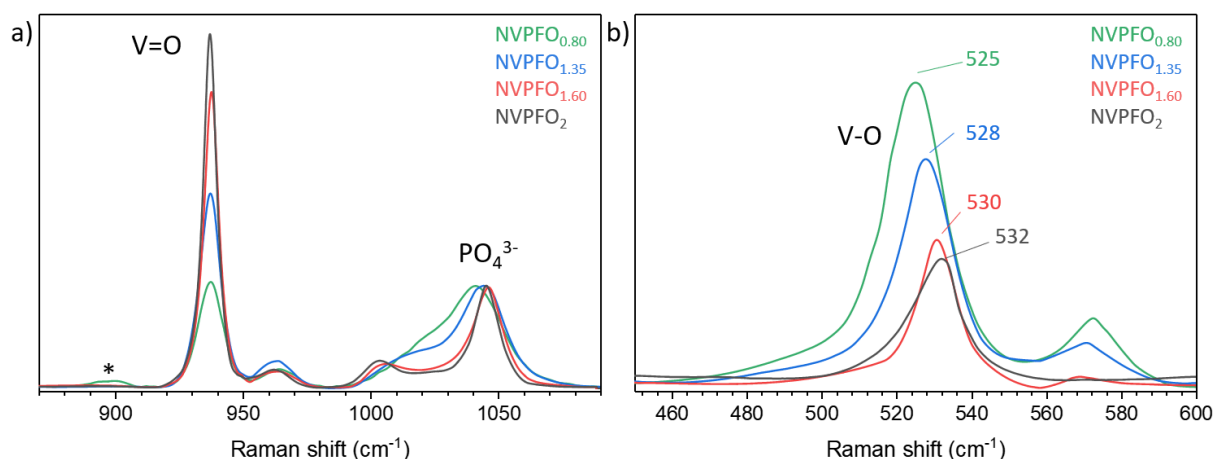


Figure 19: Raman spectra collected for NVPFO_{0.80}, NVPFO_{1.35}, NVPFO_{1.60} and NVPFO₂: The intensities of the spectra were normalized to the signal attributed to the vibration of phosphate groups adapted from the Chapter III.

5. Conclusion

As a positive electrode material widely used in SIBs, one of the alternative technologies to LIBs. NVPFO_y has shown excellent performance and has attracted extensive research. The combing through bibliography reveals that there is no rigorous interpretation of the influence of the morphology and composition of this material family on the final electrochemical performance. Therefore, as stated in the previous general introduction, the next chapters will focus on these aspects and consist of:

- ✚ Synthesizing NVPFO_y materials with different morphologies through well controlled synthesis condition with the same precursors and investigating the morphologies' influence on electrochemical capacity while trying keeping other condition unchanged.
- ✚ Starting from one performant morphology found in the first part and researching the composition effect (different O²⁻ substitution percent in NVPFO_y) on electrochemical performance.
- ✚ Understanding the morphology impact through a stricter comparison than the first part, with all the materials at the NVPFO₂ composition.

- ✚ A new deep eutectic solvent synthesis method to synthesize NVPFO_y with special morphology and carbon coating.

References:

- [1] NASA GISS, “Data.GISS: GISS Surface Temperature Analysis: Analysis Graphs and Plots,” can be found under https://data.giss.nasa.gov/gistemp/graphs_v4/, **2016**.
- [2] Robert Rohde, *Berkeley Earth* **2019**.
- [3] “European Climate Law | Climate Action,” can be found under https://ec.europa.eu/clima/policies/eu-climate-action/law_en, **n.d.**
- [4] European Environment Agency, “EEA greenhouse gas - data viewer — European Environment Agency,” can be found under <https://www.eea.europa.eu/data-and-maps/data/data-viewers/greenhouse-gases-viewer>, **2018**.
- [5] B. Global, *Statistical Review of World Energy - Global*, **2020**.
- [6] H. Ritchie, M. Roser, *Our World Data* **2020**.
- [7] M. S. Whittingham, A. H. Thompson, *J. Chem. Phys.* **1975**, 62, 1588.
- [8] M. S. Whittingham, *Science* (80-.). **1976**, 192, 1126–1127.
- [9] K. Mizushima, P. C. Jones, P. J. Wiseman, J. B. Goodenough, *Mater. Res. Bull.* **1980**, 15, 783–789.
- [10] A. k. Padhi, K. S. Nanjundaswamy, J. B. Goodenough, *J. Electrochem. Soc.* **1997**, 144, 1188.
- [11] A. Yoshino, K. Sanekata, T. Nakajima, *United States Patent*, **1987**.
- [12] C. Liu, Z. G. Neale, G. Cao, *Mater. Today* **2016**, 19, 109–123.
- [13] B. Swain, *Sep. Purif. Technol.* **2017**, 172, 388–403.
- [14] C. Liu, J. Lin, H. Cao, Y. Zhang, Z. Sun, *J. Clean. Prod.* **2019**, 228, 801–813.
- [15] D. Larcher, J. M. Tarascon, *Nat. Chem.* **2015**, 7, 19–29.
- [16] R. J. Clément, P. G. Bruce, C. P. Grey, *J. Electrochem. Soc.* **2015**, 162, A2589–A2604.
- [17] N. Yabuuchi, K. Kubota, M. Dahbi, S. Komaba, *Chem. Rev.* **2014**, 114, 11636–11682.
- [18] P. Ge, M. Foulletier, *Solid State Ionics* 28-30, **1988**.

- [19] D. A. Stevens, J. R. Dahn, *J. Electrochem. Soc.* **2001**, *148*, A803.
- [20] Y. Wen, K. He, Y. Zhu, F. Han, Y. Xu, I. Matsuda, Y. Ishii, J. Cumings, C. Wang, *Nat. Commun.* **2014**, *5*, 1–10.
- [21] B. Jache, P. Adelhelm, *Angew. Chemie - Int. Ed.* **2014**, *53*, 10169–10173.
- [22] V. Simone, A. Boulineau, A. de Geyer, D. Rouchon, L. Simonin, S. Martinet, *J. Energy Chem.* **2016**, *25*, 761–768.
- [23] A. Ponrouch, A. R. Goñi, M. R. Palacín, *Electrochem. commun.* **2013**, *27*, 85–88.
- [24] Y. Nishi, *Chem. Rec.* **2001**, *1*, 406–413.
- [25] E. Irisarri, A. Ponrouch, M. R. Palacin, *J. Electrochem. Soc.* **2015**, *162*, A2476–A2482.
- [26] Y. X. Wang, S. L. Chou, H. K. Liu, S. X. Dou, *Carbon N. Y.* **2013**, *57*, 202–208.
- [27] Y. Xu, E. M. Lotfabad, H. Wang, B. Farbod, Z. Xu, A. Kohandehghan, D. Mitlin, *Chem. Commun.* **2013**, *49*, 8973–8975.
- [28] A. Rudola, K. Saravanan, C. W. Mason, P. Balaya, *J. Mater. Chem. A* **2013**, *1*, 2653–2662.
- [29] J. Xu, C. Ma, M. Balasubramanian, Y. S. Meng, *Chem. Commun.* **2014**, *50*, 12564–12567.
- [30] A. Rudola, K. Saravanan, S. Devaraj, H. Gong, P. Balaya, *Chem. Commun.* **2013**, *49*, 7451–7453.
- [31] H. Kim, J. Hong, K.-Y. Park, H. Kim, S.-W. Kim, K. Kang, *Chem. Rev.* **2014**, *114*, 11788–11827.
- [32] Y. Shen, B. Liu, X. Liu, J. Liu, J. Ding, C. Zhong, W. Hu, *Energy Storage Mater.* **2021**, *34*, 461–474.
- [33] R. Selim, P. Bro, *J. Electrochem. Soc.* **1974**, *121*, 1457.
- [34] Y. Takada, R. Fujii, K. Matsuo, *TANSO* **1983**, *1983*, 120–123.
- [35] A. Ponrouch, E. Marchante, M. Courty, J. M. Tarascon, M. R. Palacín, *Energy Environ. Sci.* **2012**, *5*, 8572–8583.
- [36] R. Fong, U. von Sacken, J. R. Dahn, *J. Electrochem. Soc.* **1990**, *137*, 2009.
- [37] K. Xu, *Chem. Rev.* **2004**, *104*, 4303–4417.

- [38] M. Dahbi, T. Nakano, N. Yabuuchi, S. Fujimura, K. Chihara, K. Kubota, J.-Y. Son, Y.-T. Cui, H. Oji, S. Komaba, *ChemElectroChem* **2016**, *3*, 1856–1867.
- [39] H. Nakagawa, S. Izuchi, K. Kuwana, T. Nukuda, Y. Aihara, *J. Electrochem. Soc.* **2003**, *150*, A695.
- [40] N. Zhu, K. Zhang, F. Wu, Y. Bai, C. Wu, **2021**, DOI 10.34133/2021/9204217.
- [41] J. S. Moreno, M. Armand, M. B. Berman, S. G. Greenbaum, B. Scrosati, S. Panero, *J. Power Sources* **2014**, *248*, 695–702.
- [42] Y. Tominaga, K. Yamazaki, *Chem. Commun.* **2014**, *50*, 4448–4450.
- [43] A. Ponrouch, D. Monti, A. Boschini, B. Steen, P. Johansson, M. R. Palacín, *J. Mater. Chem. A* **2014**, *3*, 22–42.
- [44] K. Chayambuka, G. Mulder, D. L. Danilov, P. H. L. Notten, *Adv. Energy Mater.* **2018**, *8*, 1–49.
- [45] J. Y. Hwang, S. T. Myung, Y. K. Sun, *Chem. Soc. Rev.* **2017**, *46*, 3529–3614.
- [46] C. Delmas, C. Fouassier, P. Hagenmuller, *Phys. B+C* **1980**, *99*, 81–85.
- [47] K. Kubota, S. Komaba, *J. Electrochem. Soc.* **2015**, *162*, A2538.
- [48] L. W. Shacklette, T. R. Jow, L. Townsend, *J. Electrochem. Soc.* **1988**, *135*, 2669.
- [49] K. Takada, H. Sakurai, E. Takayama-Muromachi, F. Izumi, R. A. Dilanian, T. Sasaki, *Nat. 2003 4226927* **2003**, *422*, 53–55.
- [50] Y. Fang, X.-Y. Yu, X. W. (David) Lou, *Angew. Chemie Int. Ed.* **2017**, *56*, 5801–5805.
- [51] J. Zhao, L. Zhao, N. Dimov, S. Okada, T. Nishida, *J. Electrochem. Soc.* **2013**, *160*, A3077.
- [52] A. Caballero, L. Hernán, J. Morales, L. Sánchez, J. S. Peña, M. A. G. Aranda, *J. Mater. Chem.* **2002**, *12*, 1142–1147.
- [53] W. Zuo, X. Liu, J. Qiu, D. Zhang, Z. Xiao, J. Xie, F. Ren, J. Wang, Y. Li, G. F. Ortiz, W. Wen, S. Wu, M. S. Wang, R. Fu, Y. Yang, *Nat. Commun.* **2021**, *12*, 1–11.
- [54] S. Komaba, C. Takei, T. Nakayama, A. Ogata, N. Yabuuchi, *Electrochem. commun.* **2010**, *12*, 355–358.
- [55] J. J. Ding, Y. N. Zhou, Q. Sun, Z. W. Fu, *Electrochem. commun.* **2012**, *22*, 85–88.
- [56] H. Yoshida, N. Yabuuchi, S. Komaba, *Electrochem. commun.* **2013**, *34*, 60–63.

- [57] P. Vassilaras, A. J. Toumar, G. Ceder, *Electrochem. commun.* **2014**, 38, 79–81.
- [58] N. Yabuuchi, M. Kajiyama, J. Iwatate, H. Nishikawa, S. Hitomi, R. Okuyama, R. Usui, Y. Yamada, S. Komaba, *Nat. Mater.* **2012**, 11, 512–517.
- [59] N. Yabuuchi, M. Yano, H. Yoshida, S. Kuze, S. Komaba, *J. Electrochem. Soc.* **2013**, 160, A3131–A3137.
- [60] I. Hasa, D. Buchholz, S. Passerini, B. Scrosati, J. Hassoun, *Adv. Energy Mater.* **2014**, 4, 1400083.
- [61] M. Sathiya, Q. Jacquet, M.-L. Doublet, O. M. Karakulina, J. Hadermann, J.-M. Tarascon, *Adv. Energy Mater.* **2018**, 8, 1702599.
- [62] Q. Wang, S. Mariyappan, J. Vergnet, A. M. Abakumov, G. Rousse, F. Rabuel, M. Chakir, J.-M. Tarascon, *Adv. Energy Mater.* **2019**, 9, 1901785.
- [63] S. Mariyappan, T. Marchandier, F. Rabuel, A. Iadecola, G. Rousse, A. V. Morozov, A. M. Abakumov, J.-M. Tarascon, *Chem. Mater.* **2020**, 32, 1657–1666.
- [64] M. Duffiet, M. Blangero, P. E. Cabelguen, C. Delmas, D. Carlier, *J. Phys. Chem. Lett.* **2018**, 9, 5334–5338.
- [65] S. P. D. E. La, M. Condensee, **2019**.
- [66] A. Manthiram, J. B. Goodenough, *J. Power Sources* **1989**, 26, 403–408.
- [67] X. Xiang, K. Zhang, J. Chen, *Adv. Mater.* **2015**, 27, 5343–5364.
- [68] C. Masquelier, L. Croguennec, *Chem. Rev.* **2013**, 113, 6552–6591.
- [69] P. Barpanda, G. Oyama, S. Nishimura, S.-C. Chung, A. Yamada, *Nat. Commun.* **2014**, 5, 4358.
- [70] A. Plewa, A. Kulka, D. Baster, J. Molenda, *Solid State Ionics* **2019**, 335, 15–22.
- [71] M. Casas-Cabanas, V. V. Roddatis, D. Saurel, P. Kubiak, J. Carretero-González, V. Palomares, P. Serras, T. Rojo, *J. Mater. Chem.* **2012**, 22, 17421–17423.
- [72] K. Zaghib, J. Trottier, P. Hovington, F. Brochu, A. Guerfi, A. Mauger, C. M. Julien, *J. Power Sources* **2011**, 196, 9612–9617.
- [73] D. Saurel, M. Galceran, M. Reynaud, H. Anne, M. Casas-Cabanas, *Int. J. Energy Res.* **2018**, 42, 3258–3265.
- [74] Y. Fang, Q. Liu, L. Xiao, X. Ai, H. Yang, Y. Cao, *ACS Appl. Mater. Interfaces* **2015**, 7, 17977–17984.

- [75] Y. Zhu, Y. Xu, Y. Liu, C. Luo, C. Wang, *Nanoscale* **2012**, 5, 780–787.
- [76] S. Ping Ong, V. L. Chevrier, G. Hautier, A. Jain, C. Moore, S. Kim, X. Ma, G. Ceder, **n.d.**, DOI 10.1039/c1ee01782a.
- [77] C. Li, X. Miao, W. Chu, P. Wu, D. G. Tong, *J. Mater. Chem. A* **2015**, 3, 8265–8271.
- [78] K. T. Lee, T. N. Ramesh, F. Nan, G. Botton, L. F. Nazar, *Chem. Mater.* **2011**, 23, 3593–3600.
- [79] H. Kim, R. A. Shakoor, C. Park, S. Y. Lim, J. S. Kim, Y. N. Jo, W. Cho, K. Miyasaka, R. Kahraman, Y. Jung, J. W. Choi, *Adv. Funct. Mater.* **2013**, 23, 1147–1155.
- [80] S. J. Lim, D. W. Han, D. H. Nam, K. S. Hong, J. Y. Eom, W. H. Ryu, H. S. Kwon, *J. Mater. Chem. A* **2014**, 2, 19623–19632.
- [81] C. G. Delmas, R. Olazcuaga, F. Cherkaoui, R. Brochu, G. Le Flem, *Chem. Informationsd.* **1979**, 10, DOI 10.1002/chin.197902041.
- [82] Z. Jian, L. Zhao, H. Pan, Y. S. Hu, H. Li, W. Chen, L. Chen, *Electrochem. commun.* **2012**, 14, 86–89.
- [83] Y. H. Jung, C. H. Lim, D. K. Kim, *J. Mater. Chem. A* **2013**, 1, 11350–11354.
- [84] Y. Jiang, Z. Yang, W. Li, L. Zeng, F. Pan, M. Wang, X. Wei, G. Hu, L. Gu, Y. Yu, *Adv. Energy Mater.* **2015**, 5, 1402104.
- [85] X. Rui, W. Sun, C. Wu, Y. Yu, Q. Yan, *Adv. Mater.* **2015**, 27, 6670–6676.
- [86] F. Chen, V. M. Kovrugin, R. David, O. Mentré, F. Fauth, J. N. Chotard, C. Masquelier, *Small Methods* **2019**, 3, 1–9.
- [87] W. Zhou, L. Xue, X. Lü, H. Gao, Y. Li, S. Xin, G. Fu, Z. Cui, Y. Zhu, J. B. Goodenough, *Nano Lett.* **2016**, 16, 7836–7841.
- [88] M. V. Zakharkin, O. A. Drozhzhin, I. V. Tereshchenko, D. Chernyshov, A. M. Abakumov, E. V. Antipov, K. J. Stevenson, *ACS Appl. Energy Mater.* **2018**, 1, 5842–5846.
- [89] F. Lalère, V. Seznec, M. Courty, R. David, J. N. Chotard, C. Masquelier, *J. Mater. Chem. A* **2015**, 3, 16198–16205.
- [90] F. Lalère, V. Seznec, M. Courty, J. N. Chotard, C. Masquelier, *J. Mater. Chem. A* **2018**, 6, 6654–6659.

- [91] J. M. Le Meins, M. P. Crosnier-Lopez, A. Hemon-Ribaud, G. Courbion, *J. Solid State Chem.* **1999**, *148*, 260–277.
- [92] M. Bianchini, N. Brisset, F. Fauth, F. Weill, E. Elkaim, E. Suard, C. Masquelier, L. Croguennec, *Chem. Mater.* **2014**, *26*, 4238–4247.
- [93] S. T. Dacek, W. D. Richards, D. A. Kitchaev, G. Ceder, *Chem. Mater.* **2016**, *28*, 5450–5460.
- [94] M. Bianchini, F. Fauth, N. Brisset, F. Weill, E. Suard, C. Masquelier, L. Croguennec, *Chem. Mater.* **2015**, *27*, 3009–3020.
- [95] T. Broux, T. Bamine, L. Simonelli, L. Stievano, F. Fauth, M. Ménétrier, D. Carlier, C. Masquelier, L. Croguennec, *J. Phys. Chem. C* **2017**, *121*, 4103–4111.
- [96] L. H. B. Nguyen, A. Iadecola, S. Belin, J. Olchowka, C. Masquelier, D. Carlier, L. Croguennec, *J. Phys. Chem. C* **2020**, *124*, 23511–23522.
- [97] L. H. B. Nguyen, P. Sanz Camacho, T. Broux, J. Olchowka, C. Masquelier, L. Croguennec, D. Carlier, *Chem. Mater.* **2019**, *31*, 9759–9768.
- [98] A. Ponrouch, R. Dedryvère, D. Monti, A. E. Demet, J. M. Ateba Mba, L. Croguennec, C. Masquelier, P. Johansson, M. R. Palacín, *Energy Environ. Sci.* **2013**, *6*, 2361–2369.
- [99] B. Zhang, R. Dugas, G. Rousse, P. Rozier, A. M. Abakumov, J. M. Tarascon, *Nat. Commun.* **2016**, *7*, 1–9.
- [100] M. Xu, P. Xiao, S. Stauffer, J. Song, G. Henkelman, J. B. Goodenough, *Chem. Mater.* **2014**, *26*, 3089–3097.
- [101] G. Yan, S. Mariyappan, G. Rousse, Q. Jacquet, M. Deschamps, R. David, B. Mirvaux, J. W. Freeland, J.-M. Tarascon, *Nat. Commun.* **2019**, *10*, 585.
- [102] L. H. B. Nguyen, P. Sanz Camacho, T. Broux, J. Olchowka, C. Masquelier, L. Croguennec, D. Carlier, *Chem. Mater.* **2019**, *31*, 9759–9768.
- [103] L. H. B. Nguyen, T. Broux, P. S. Camacho, D. Denux, L. Bourgeois, S. Belin, A. Iadecola, F. Fauth, D. Carlier, J. Olchowka, C. Masquelier, L. Croguennec, *Energy Storage Mater.* **2019**, *20*, 324–334.
- [104] Y. U. Park, D. H. Seo, H. Kim, J. Kim, S. Lee, B. Kim, K. Kang, *Adv. Funct. Mater.* **2014**, *24*, 4603–4614.

- [105] T. Broux, T. Bamine, F. Fauth, L. Simonelli, W. Olszewski, C. Marini, M. Ménétrier, D. Carlier, C. Masquelier, L. Croguennec, *Chem. Mater.* **2016**, 28, 7683–7692.
- [106] M. Bianchini, P. Xiao, Y. Wang, G. Ceder, *Adv. Energy Mater.* **2017**, 7, 1700514.
- [107] M. Peng, D. Zhang, X. Wang, D. Xia, Y. Sun, G. Guo, *Chem. Commun.* **2019**, 55, 3979–3982.
- [108] Y. Qi, L. Mu, J. Zhao, Y. S. Hu, H. Liu, S. Dai, *Angew. Chemie - Int. Ed.* **2015**, 54, 9911–9916.
- [109] N. Pineda-Aguilar, V. J. Gallegos-Sánchez, E. M. Sánchez, L. C. Torres-González, L. L. Garza-Tovar, *J. Sol-Gel Sci. Technol.* **2017**, 83, 405–412.
- [110] J. Olchowka, L. H. B. Nguyen, T. Broux, P. Sanz Camacho, E. Petit, F. Fauth, D. Carlier, C. Masquelier, L. Croguennec, *Chem. Commun.* **2019**, 55, 11719–11722.
- [111] H. Yi, M. Ling, W. Xu, X. Li, Q. Zheng, H. Zhang, *Nano Energy* **2018**, 47, 340–352.
- [112] A. Criado, P. Lavela, C. Pérez-Vicente, G. F. Ortiz, J. L. Tirado, *J. Electroanal. Chem.* **2020**, 856, 113694.
- [113] M. Wang, K. Wang, X. Huang, T. Zhou, H. Xie, Y. Ren, *Ceram. Int.* **2020**, 46, 28490–28498.
- [114] C. Guo, J. Yang, Z. Cui, S. Qi, Q. Peng, W. Sun, L.-P. Lv, Y. Xu, Y. Wang, S. Chen, *J. Energy Chem.* **2021**, DOI 10.1016/j.jechem.2021.06.015.
- [115] I. L. Matts, S. Dacek, T. K. Pietrzak, R. Malik, G. Ceder, *Chem. Mater.* **2015**, 27, 6008–6015.
- [116] Y. Zhang, S. Guo, H. Xu, *J. Mater. Chem. A* **2018**, 6, 4525–4534.
- [117] L. Li, X. Liu, L. Tang, H. Liu, Y. G. Wang, *J. Alloys Compd.* **2019**, 790, 203–211.
- [118] N. V. Kosova, D. O. Rezepova, *J. Power Sources* **2018**, 408, 120–127.
- [119] T. Partheeban, B. Senthilkumar, V. Aravindan, S. Madhavi, M. Sasidharan, *ACS Appl. Energy Mater.* **2021**, DOI 10.1021/acsaem.0c02622.
- [120] Q. Liu, X. Meng, Z. Wei, D. Wang, Y. Gao, Y. Wei, F. Du, G. Chen, *ACS Appl. Mater. Interfaces* **2016**, 8, 31709–31715.
- [121] Q. Liu, D. Wang, X. Yang, N. Chen, C. Wang, X. Bie, Y. Wei, G. Chen, F. Du, *J. Mater. Chem. A* **2015**, 3, 21478–21485.

- [122] X. Shen, J. Zhao, Y. Li, X. Sun, C. Yang, H. Liu, Y. S. Hu, *ACS Appl. Energy Mater.* **2019**, 2, 7474–7482.
- [123] Y. Qi, L. Mu, J. Zhao, Y. S. Hu, H. Liu, S. Dai, *J. Mater. Chem. A* **2016**, 4, 7178–7184.
- [124] Y. Qi, J. Zhao, C. Yang, H. Liu, Y.-S. Hu, *Small Methods* **2018**, 3, 1800111.
- [125] A. Mukherjee, T. Sharabani, I. Perelshtein, M. Noked, *Batter. Supercaps* **2020**, 3, 52–55.
- [126] N. Eshraghi, S. Caes, A. Mahmoud, R. Cloots, B. Vertruyen, F. Boschini, *Electrochim. Acta* **2017**, 228, 319–324.
- [127] Y. Cao, Y. Liu, D. Zhao, X. Xia, L. Zhang, J. Zhang, H. Yang, Y. Xia, *ACS Sustain. Chem. Eng.* **2020**, 8, 1380–1387.
- [128] C. Shen, H. Long, G. Wang, W. Lu, L. Shao, K. Xie, *J. Mater. Chem. A* **2018**, 6, 6007–6014.
- [129] H. Yi, L. Lin, M. Ling, Z. Lv, R. Li, Q. Fu, H. Zhang, Q. Zheng, X. Li, *ACS Energy Lett.* **2019**, 4, 1565–1571.
- [130] A. Nadeina, P. Rozier, V. Seznec, *Energy Technol.* **2020**, 8, 1901304.
- [131] J. Xun, Y. Zhang, H. Xu, *Inorg. Chem. Commun.* **2020**, 115, 107884.
- [132] J. Zhao, L. Mu, Y. Qi, Y. S. Hu, H. Liu, S. Dai, *Chem. Commun.* **2015**, 51, 7160–7163.
- [133] P. Du, K. Mi, F. Hu, X. Jiang, D. Wang, X. Zheng, *New J. Chem.* **2020**, 44, 12985–12992.
- [134] Y. Cai, X. Cao, Z. Luo, G. Fang, F. Liu, J. Zhou, A. Pan, S. Liang, *Adv. Sci.* **2018**, 5, DOI 10.1002/advs.201800680.
- [135] H. Jin, J. Dong, E. Uchaker, Q. Zhang, X. Zhou, S. Hou, J. Li, G. Cao, *J. Mater. Chem. A* **2015**, 3, 17563–17568.
- [136] C. Zhu, C. Wu, C. C. Chen, P. Kopold, P. A. Van Aken, J. Maier, Y. Yu, *Chem. Mater.* **2017**, 29, 5207–5215.
- [137] A. Mukherjee, T. Sharabani, R. Sharma, S. Okashy, M. Noked, *Batter. Supercaps* **2020**, 3, 510–518.
- [138] J. Olchowka, L. H. B. Nguyen, E. Petit, P. S. Camacho, C. Masquelier, D. Carlier, L. Croguennec, *Inorg. Chem.* **2020**, 59, 17282–17290.

- [139] Z. Tong, Y. Qi, J. Zhao, L. Liu, X. Shen, H. Liu, *Waste and Biomass Valorization* **2018**, *11*, 2201–2209.
- [140] Y. Hou, K. Chang, Z. Wang, S. Gu, Q. Liu, J. Zhang, H. Cheng, S. Zhang, Z. Chang, Z. Lu, *Sci. China Mater.* **2019**, *62*, 474–486.
- [141] M. Xu, L. Wang, X. Zhao, J. Song, H. Xie, Y. Lu, J. B. Goodenough, *Phys. Chem. Chem. Phys.* **2013**, *15*, 13032–13037.
- [142] J. Z. Guo, P. F. Wang, X. L. Wu, X. H. Zhang, Q. Yan, H. Chen, J. P. Zhang, Y. G. Guo, *Adv. Mater.* **2017**, *29*, 1–8.
- [143] Z. Y. Gu, J. Z. Guo, Y. Yang, H. Y. Yu, X. T. Xi, X. X. Zhao, H. Y. Guan, X. He, X. L. Wu, *Inorg. Chem. Front.* **2019**, *6*, 988–995.
- [144] L. Zhu, H. Wang, D. Sun, Y. Tang, H. Wang, *J. Mater. Chem. A* **2020**, *8*, 21387–21407.
- [145] T. Broux, F. Fauth, N. Hall, Y. Chatillon, M. Bianchini, T. Bamine, J. B. Leriche, E. Suard, D. Carlier, Y. Reynier, L. Simonin, C. Masquelier, L. Croguennec, *Small Methods* **2019**, *3*, 1–12.
- [146] L. Zhu, Q. Zhang, D. Sun, Q. Wang, N. Weng, Y. Tang, H. Wang, *Mater. Chem. Front.* **2020**, *4*, 2932–2942.

Chapter II: Effect of the particles morphology on the electrochemical performance of $\text{Na}_3\text{V}_2(\text{PO}_4)_2\text{F}_{3-y}\text{O}_y$

As mentioned in the previous chapter, NVPFO_y has been synthesized by various synthesis approaches, leading to a wild variety of different particles sizes and morphologies. However, the conductive coating applied to these materials, in addition to the various experimental conditions to evaluate the electrochemical performance, make impossible, from the literature's work, to accurately compare and evaluate the particle's size and morphology influences on the energy storage performance. At the same time, the F/O ratio ("y" parameter) can hardly be controlled during low temperature synthesis, which may lead to unexpected fluorine for oxygen substitution, and subsequently inevitably affects the understanding of morphologies variation impact. Indeed, the real composition is often overlooked in the literature and approximated to $\text{Na}_3\text{V}_2(\text{PO}_4)_2\text{F}_3$.

In this chapter, different morphologies were obtained with as little change as possible in the composition of $\text{Na}_3\text{V}_2(\text{PO}_4)_2\text{F}_{3-y}\text{O}_y$ (NVPFO_y) through our efforts in synthesis. The detailed research and discussion process will be shown in the following article. This article has been accepted in Batteries & Supercaps and chosen to be the cover article.

<https://doi.org/10.1002/batt.202100179>



Effect of the particles morphology on the electrochemical performance of $\text{Na}_3\text{V}_2(\text{PO}_4)_2\text{F}_{3-y}\text{O}_y$

Runhe Fang ^[a,d], Jacob Olchowka ^{[b,d,e]*}, Chloé Pablos ^[b,c,d], Paula Sanz Camacho ^[b], Dany Carlier ^[b,d,e], Laurence Croguennec ^[b,d,e], Sophie Cassaignon^{[a,d]*}

[a] Sorbonne Université, CNRS Laboratoire Chimie de la Matière Condensée de Paris, LCMCP, UMR 7574, 4 Place Jussieu, 75005 Paris, France

E-mail: sophie.cassaignon@sorbonne-universite.fr

[b]CNRS, Univ. Bordeaux, Bordeaux INP, ICMCB UMR 5026, 33600 Pessac, France

E-mail: jacob.olchowka@icmcb.cnrs.fr

[c] Laboratoire de Réactivité et de Chimie des Solides, Université de Picardie Jules Verne, CNRS-UMR 7314, F-80039 Amiens Cedex 1, France

[d] RS2E, Réseau Français sur le Stockage Electrochimique de l'Energie, CNRS 3459, 80039 Amiens Cedex 1, France.

[e] ALISTORE-ERI European Research Institute, CNRS 3104, 80039 Amiens Cedex 1, France

Among all the positive electrode materials explored for Na-ion batteries, the family of $\text{Na}_3\text{V}^{\text{III}}_{2-y}(\text{V}^{\text{IV}}\text{O})_y(\text{PO}_4)_2\text{F}_{3-y}$ (NVPFO_y) has attracted extensive attention for its high operating voltage and structural stability. In order to promote better performance at high rates, it appears interesting to consider the correlation between NVPFO_y's composition, morphology (size and shape) and electrochemical properties. Here, solvothermal syntheses were considered in order to obtain a series of NVPFO_y compounds showing different morphologies (such as nanospheres, flakes, cylindrical aggregates or desert-roses) by playing on different synthesis parameters like water/ethanol ratio, stoichiometry of the precursors' mixture, heating rate, and the presence or not of a surfactant. Four compounds presenting different morphology have been fully characterized by X-ray diffraction, scanning electron microscopy, transmission electron microscopy, infrared, NMR and XPS spectroscopies. Their electrochemical properties are studied using electrodes rich in active material to better observe the influence of the morphology on the energy storage performance and are compared to those of $\text{Na}_3\text{V}_2(\text{PO}_4)_2\text{F}_3$ and

$\text{Na}_3\text{V}_2(\text{PO}_4)_2\text{FO}_2$ reference materials obtained by solid-state synthesis and with shapeless morphology.

KEYWORDS: morphology design; Na-ion batteries; $\text{Na}_3\text{V}_2(\text{PO}_4)_2\text{F}_3$; $\text{Na}_3(\text{VO})_2(\text{PO}_4)_2\text{F}$; polyanions; synthesis design.

1. Introduction

Nowadays, lithium-ion batteries (LIBs) are widely used in mobile phones, laptops, electric vehicles, and energy storage stations.^[1] However, in the context of today's rapid development of electric vehicles and the increasing demand of energy storage devices for grid application, the uneven distribution of lithium resources in the earth's crust raises concerns about its stable cost and supply. Among the possible alternative technologies, sodium-ion battery is considered to be currently the most reliable and environmentally friendly one. The very high abundance, wide distribution and low cost of sodium conjugated to similar working principle as that of already commercialized LIBs, contribute to a rapid development of sodium-ion batteries.^[2,3] These last years, a range of layered metal oxide and polyanionic materials have been intensively investigated as positive electrode materials.^[4-9] Among the polyanionic ones, the NASICON $\text{Na}_3\text{V}_2(\text{PO}_4)_3$ and the sodium vanadium oxyfluoride phosphate family, $\text{Na}_3\text{V}^{3+}_{2-y}\text{V}^{4+}_y(\text{PO}_4)_2\text{F}_{3-y}\text{O}_y$ (NVPFO_y) ($0 \leq y \leq 2$), have attracted extensive attention for their structural stability and low volume change upon the reversible extraction of 2 Na^+ per formula unit. However, due to the higher reversible capacity and average extraction potential (128 mAh.g⁻¹ vs. 118 mAh.g⁻¹ and ~3.9 V vs 3.4 V (vs. Na^+/Na) for $\text{Na}_3\text{V}_2(\text{PO}_4)_2\text{F}_3$ and $\text{Na}_3\text{V}_2(\text{PO}_4)_3$ respectively), NVPFO_y family exhibits stronger perspective in term of application.^[10-16] For instance, Broux et al. reported excellent long-term cycling stability and high-rate performance for prototype cells made of carbon coated $\text{Na}_3\text{V}_2(\text{PO}_4)_2\text{F}_3$ versus hard carbon.^[10] Their 75 Wh/kg 18650 prototype cells exhibited 80% of capacity retention after 4000 cycles at 1C rate.

$\text{Na}_3\text{V}^{3+}_{2-y}\text{V}^{4+}_y(\text{PO}_4)_2\text{F}_{3-y}\text{O}_y$ ($0 \leq y \leq 2$) has a three-dimensional framework built of $\text{V}_2\text{O}_8\text{F}_{3-y}\text{O}_y$ bi-octahedral units linked together by phosphate groups via oxygen atoms, and the highly mobile Na ions occupy the tunnel sites along the $[110]$ and $[1\bar{1}0]$ directions.^[17] The presence of isolated vanadium bi-octahedra in the structure induces a poor intrinsic electronic conductivity ($\sim 10^{-12} \text{ S.cm}^{-1}$) which strongly affects the high-rate capacity retention.^[18] To face this problem, the main approaches studied in the literature consist in combining NVPFO_y with conductive carbon based material to synthesize composites or in decreasing particles size to

facilitate the accessibility of electrolyte to the electrode surface and shorten ion and electron transport pathways.^[19–21] For instance, dealing with this last approach, it was shown that nanosizing carbon coated-NVPP by mechanical activation improves high rate capacity and cycling stability.^[22] Although it is well known that particle's size and morphology influence the energy storage performance and a lot of particle shapes can be obtained, such as nano or microspheres^[23–25], hollow spheres^[19,26,27], nano or microcubes^[28–30], nano-flowers^[31,32], platelets^[33] and other special morphologies^{[34–39],[40]}, it is still unclear which particle's morphology allows to reach the best high-rate performance and if the synthesis method influences the electrochemical properties. Indeed, different electrode formulations, nature of electrolytes, active mass loadings, carbon coatings or conductive additives make very complicated a simple comparison between all the studies reported in the literature.

In this work, in order to learn more about the effect of particle shape on the electrochemical performance, energy-saving solvothermal method was used to prepare a series of $\text{Na}_3\text{V}^{3+}_{2-y}\text{V}^{4+}_y(\text{PO}_4)_2\text{F}_{3-y}\text{O}_y$ compounds showing different morphologies. The same precursors were used whatever the synthesis conditions in order to try to minimize the impact on the F/O composition. The electrochemical tests were performed on electrodes rich in active material and with high mass loading to better observe the influence of the morphology by attenuating the effect of the carbon black additive, and to be close to the practical conditions. These results were compared to those obtained for $\text{Na}_3\text{V}^{3+}_2(\text{PO}_4)_2\text{F}_3$ and $\text{Na}_3\text{V}^{4+}_2(\text{PO}_4)_2\text{FO}_2$ synthesized by conventional solid-state synthesis.

2. Results and discussions

2.1 Structural and morphological characterization

The XRD patterns of all compounds, presented in **Figure 1a**, confirm the successful syntheses of phases that belong to the $\text{Na}_3\text{V}^{3+}_{2-y}\text{V}^{4+}_y(\text{PO}_4)_2\text{F}_{3-y}\text{O}_y$ family. The lattice parameters determined from the Rietveld refinement of the XRD data, taking into account the structural model already described in details in reference [13], are gathered in **Table 1** and the results of the refinement are reported for each compound in **Figure 2**. Additionally, the elemental

chemical analyses, determined by ICP-OES, reveal cationic ratio very close to the expected ones for this series of $\text{Na}_3\text{V}^{3+}_{2-y}\text{V}^{4+}_y(\text{PO}_4)_2\text{F}_{3-y}\text{O}_y$ compounds ($\text{Na}/\text{V}/\text{P} = 1.5/1/1$) (**Table 2**).

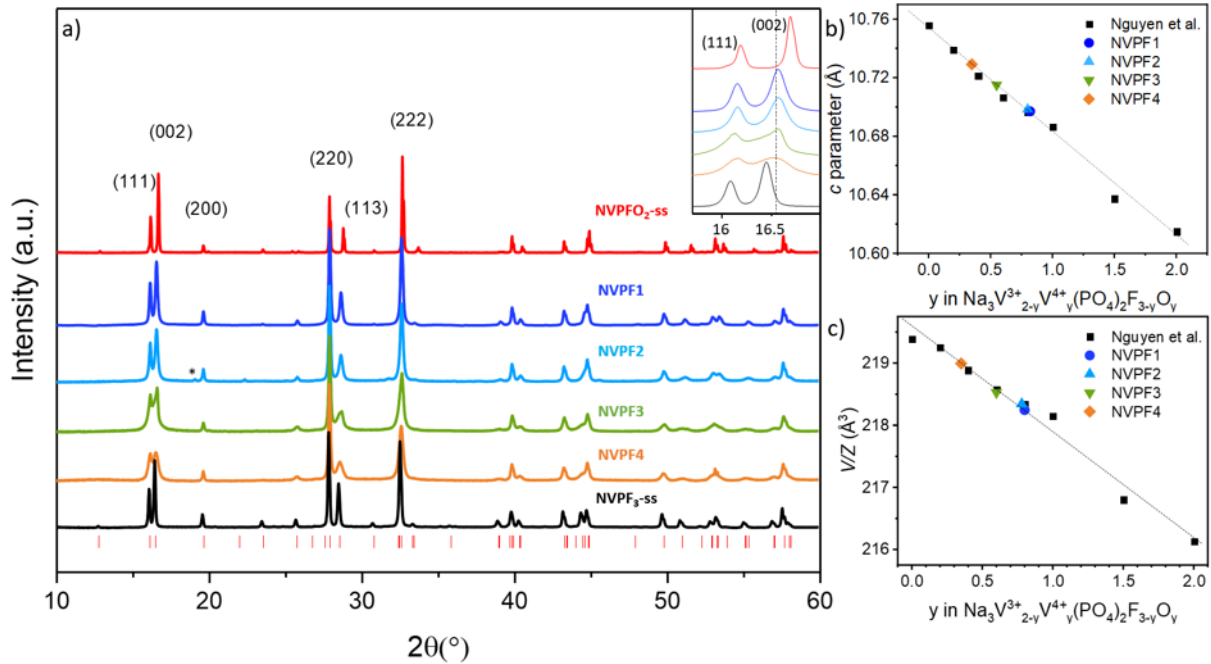
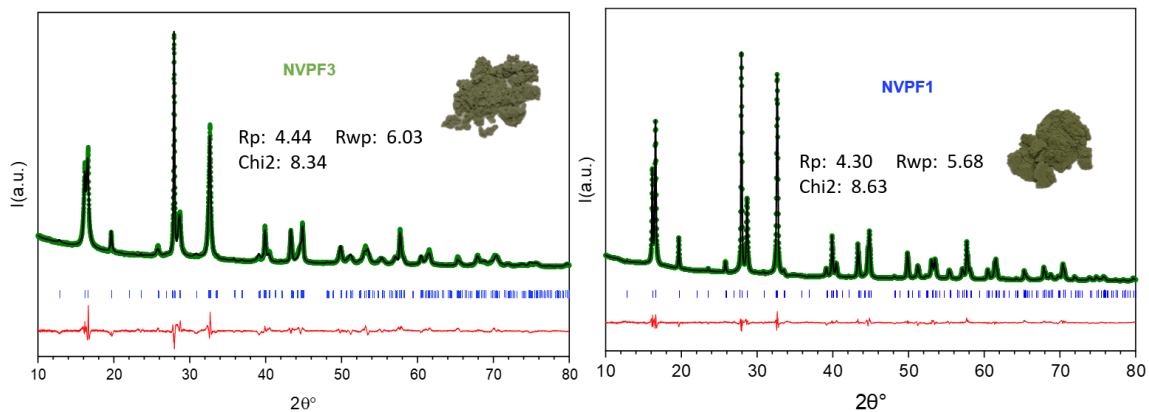


Figure 1: a) XRD patterns of all compounds: from top to bottom are respectively given that of the reference NVPFO_{2-ss}, NVPF1, NVPF2, NVPF3, NVPF4 and the second reference NVPF_{3-ss}. The inset shows an enlargement of (111) and (002) reflections. The red ticks correspond to theoretical positions for Na₃V₂(PO₄)₂F₃ as reported in ICDD 00-066-0322 and the small star for NVPF2 diagram corresponds to a reflection peak that may belong to traces of residual Pluronic acid; Comparison of b) the c cell parameters and c) V/Z values (V/Z being the cell volume per formula unit) determined by Rietveld refinement to those already reported. [13,41,42] The dash lines give the evolution of these parameters as a function of “y” in Na₃V₂(PO₄)₂F_{3-y}O_y. [13]

Table 1: Lattice parameters obtained by the Rietveld refinement, coherent domain sizes along the (220) and (002) directions and chemical composition determined for all the NVPFO_y materials

	a(Å)	b(Å)	c(Å)	V/Z(Å ³)	(220) (nm)	(002) (nm)	Formula	Space group
NVPF1	9.0331(1)	9.0374(1)	10.6970(1)	218.31(1)	61	67	Na ₃ V ³⁺ _{1.20} V ⁴⁺ _{0.80} (PO ₄) ₂ F _{2.20} O _{0.80}	Amam
NVPF2	9.0339(1)	9.0368(1)	10.6983(1)	218.34(1)	60	56	Na ₃ V ³⁺ _{1.20} V ⁴⁺ _{0.80} (PO ₄) ₂ F _{2.20} O _{0.80}	Amam
NVPF3	9.0316(1)	9.0344(1)	10.7150(1)	218.53(1)	55	35	Na ₃ V ³⁺ _{1.45} V ⁴⁺ _{0.55} (PO ₄) ₂ F _{2.45} O _{0.55}	Amam
NVPF4	9.0347(2)	9.0387(2)	10.7291(2)	219.00(2)	57	30	Na ₃ V ³⁺ _{1.65} V ⁴⁺ _{0.35} (PO ₄) ₂ F _{2.65} O _{0.35}	Amam
NVPFO _{2-ss}	9.0330(1)	9.0330(1)	10.6137(2)	216.51(1)	60	65	Na ₃ V ₂ (PO ₄) ₂ FO ₂	P4 ₂ /mnm
NVPF _{3-ss}	9.0304(1)	9.0437(1)	10.7490(1)	219.46(1)	76	101	Na ₃ V ₂ (PO ₄) ₂ F ₃	Amam



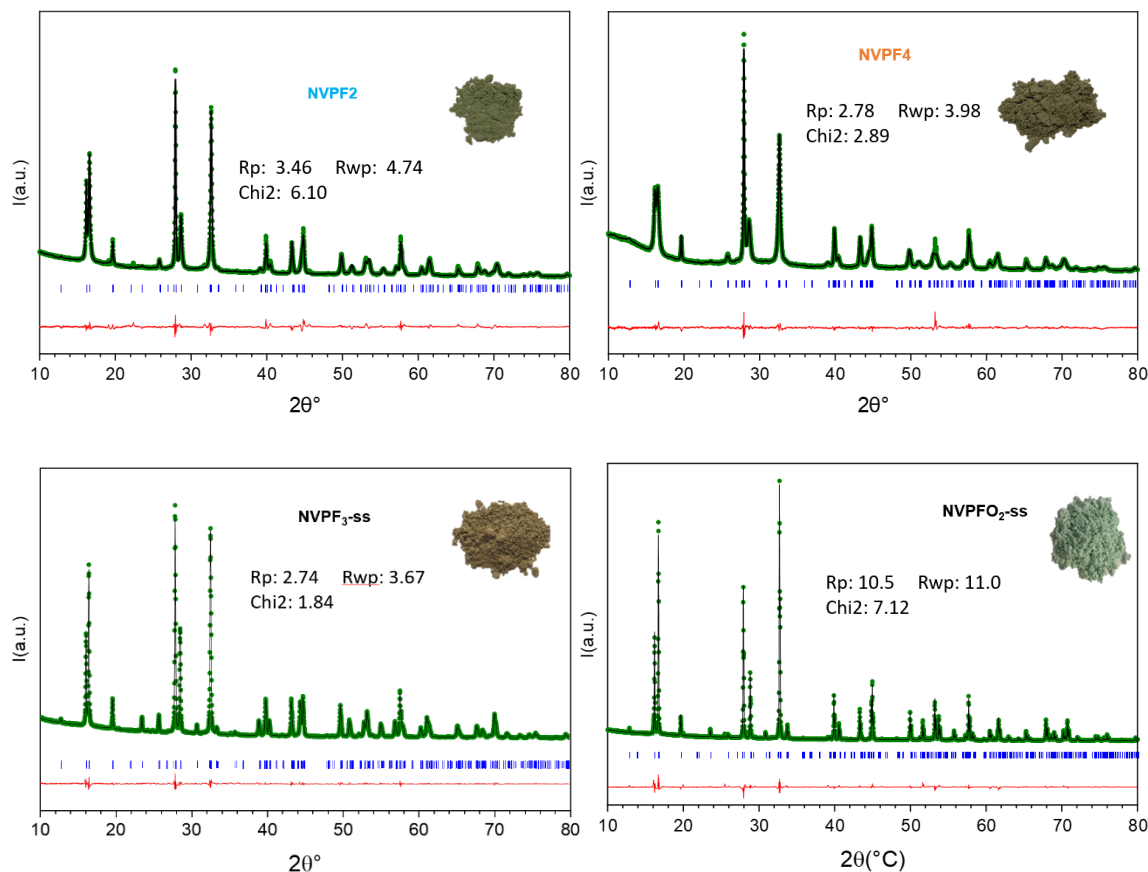


Figure 2: Rietveld refinement of the XRD data and photograph of the powder in inset for the different compounds NVPF1, NVPF2, NVPF3 and NVPF4, in comparison with NVPF₃-ss and NVPFO₂-ss. Green dots are experimental intensities, the black line is drawn from calculated pattern and the red line is the difference between the experimental and calculated patterns. Blue sticks correspond to Bragg positions.

The determination of the cell parameters allows a good estimation of the O²⁻ for F⁻ substitution: the smaller the cell volume and *c* cell parameter (experimentally observed with a shift of (002) diffraction peak to higher diffraction angles), the higher is the content in oxygen in Na₃V₂(PO₄)₂F_{3-y}O_y.^[13,42–44] Indeed, the substitution of O²⁻ for F⁻ induces the vanadium oxidation (V³⁺ to V⁴⁺) for charge compensation, along with the formation of vanadyl bonds (V=O)²⁺ and leads to a solid solution between the two end-members, Na₃V³⁺₂(PO₄)₂F₃ and Na₃V⁴⁺₂O₂(PO₄)₂F. As the vanadyl bonds are localized along the *c*-axis (**Figure 3**) (in the *Amam* space group), the replacement of long ionic V-F bonds (~2 Å) by short covalent V=O bonds (~1.6 Å) induces a decrease of the *c* cell parameter. As shown in **Figure 1b-c** and **Figure 4**, the compounds NVPF1 and NVPF2 are characterized by the higher oxygen contents, similar for both of them and in good agreement with the chemical composition Na₃V³⁺_{1.20}V⁴⁺_{0.80}(PO₄)₂F_{2.20}O_{0.80} (*i.e.* *y* = 0.8). The compound NVPF3 is less oxidized and shows the composition Na₃V³⁺_{1.45}V⁴⁺_{0.55}(PO₄)₂F_{2.45}O_{0.55} (*y* = 0.55), whereas the compound NVPF4 is even less oxidized with the composition Na₃V³⁺_{1.65}V⁴⁺_{0.35}(PO₄)₂F_{2.65}O_{0.35} (*y* = 0.35) (**Table 1**). It appears thus that a partial oxidation of the V³⁺ precursor takes place in the

conditions used during the solvothermal syntheses due to presence of oxidative solvent. It clearly shows the difficulty to control the oxygen content (vanadium oxidation state) by using solvothermal approach.^[45]

Table 2: Cationic ratio determined by ICP-OES

	NVPF1	NVPF2	NVPF3	NVPF4
Na/V/P	1.49 : 1 : 1.00	1.47 : 1 : 0.97	1.39 : 1 : 1.10	1.46 : 1 : 1.01

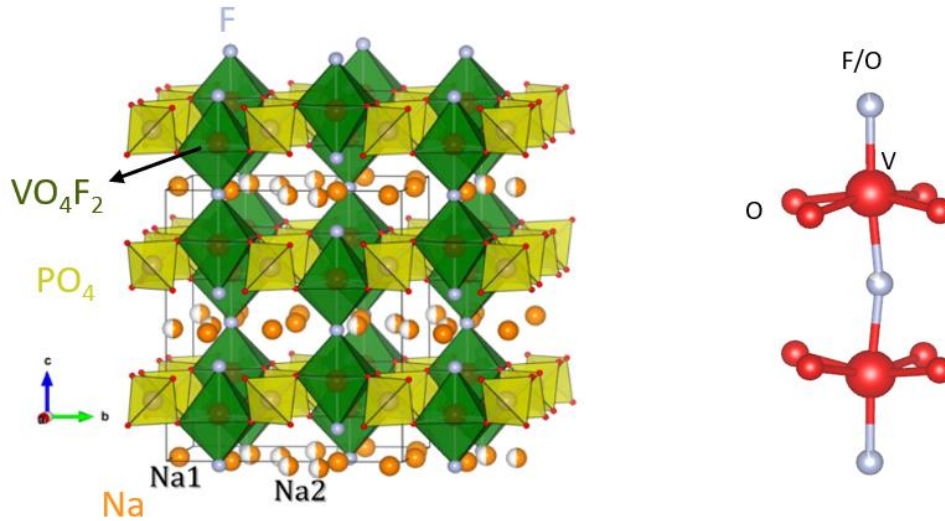


Figure 3: Structure of $\text{Na}_3\text{V}_2(\text{PO}_4)_2\text{F}_3$ and on the right, a focus on the bi-octahedral $\text{V}_2\text{O}_8\text{F}_3$ structure. In the $\text{Na}_3\text{V}^{3+}_{2-y}\text{V}^{4+}_y(\text{PO}_4)_2\text{F}_{3-y}\text{O}_y$ the two fluorine atoms localized at the extremity of the bi-octahedral unit can be substituted by oxygen generating short vanadyl bonds ($d_{\text{V}=\text{O}} = 1.6 \text{ \AA}$) instead of long V-F bonds ($d_{\text{V}-\text{F}} = 2 \text{ \AA}$). This figure is adapted from Figure 1(a) in reference1. The V-F and V=O bonds are pointing along the c-axis.

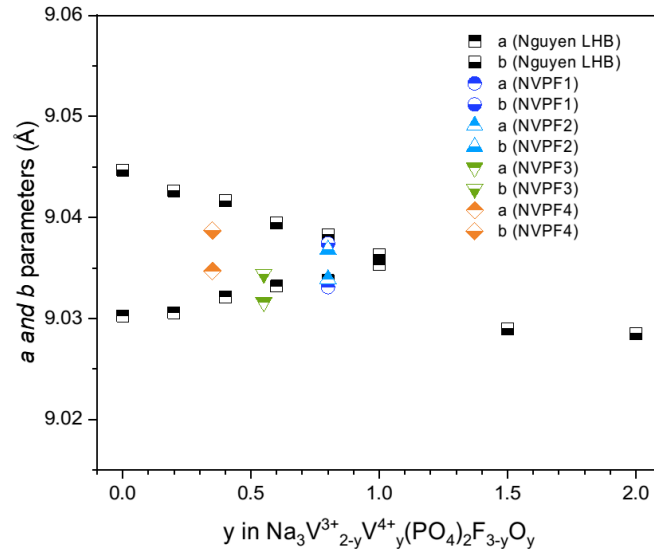


Figure 4: Cell parameters a and b for the materials NVPF1, NVPF2, NVPF3 and NVPF4, compared to those reported by Nguyen et al. for the series $\text{Na}_3\text{V}^{3+}_{2-y}\text{V}^{4+}_y(\text{PO}_4)_2\text{F}_{3-y}\text{O}_y$. The oxygen content ' y ' was deduced from the c parameter and the volume. This figure is adapted from Figure 3 in reference2.

Further, the presence of vanadyl bonds (V=O) and mixed V^{3+}/V^{4+} valence state (also written as $V^{3+}/(V=O)^{2+}$) were confirmed by infrared, ^{23}Na NMR and X-Ray photoelectron spectroscopies. The IR spectra of all these compounds obtained by solvothermal syntheses are compared in **Figure 5a**. They exhibit vibrational bands at 680 cm^{-1} and 1080 cm^{-1} , which respectively correspond to the stretching modes of vanadium oxygen bond $\nu(\text{V-O})$ and phosphate groups $\nu(\text{PO}_4^{3-})$. Additionally, the spectra reveal two peaks at ~ 910 and 940 cm^{-1} characteristic of the vibrations generated by a vanadyl bond (**Figure 5a**).^[13,46,47] These peaks are, as expected, very intense for $\text{NVPFO}_2\text{-ss}$ and not observed for $\text{NVPF}_3\text{-ss}$, characterized for this latter by the composition $\text{Na}_3\text{V}^{3+}_2(\text{PO}_4)_2\text{F}_3$ (i.e. without any vanadyl bond $(\text{V=O})^{2+}$).

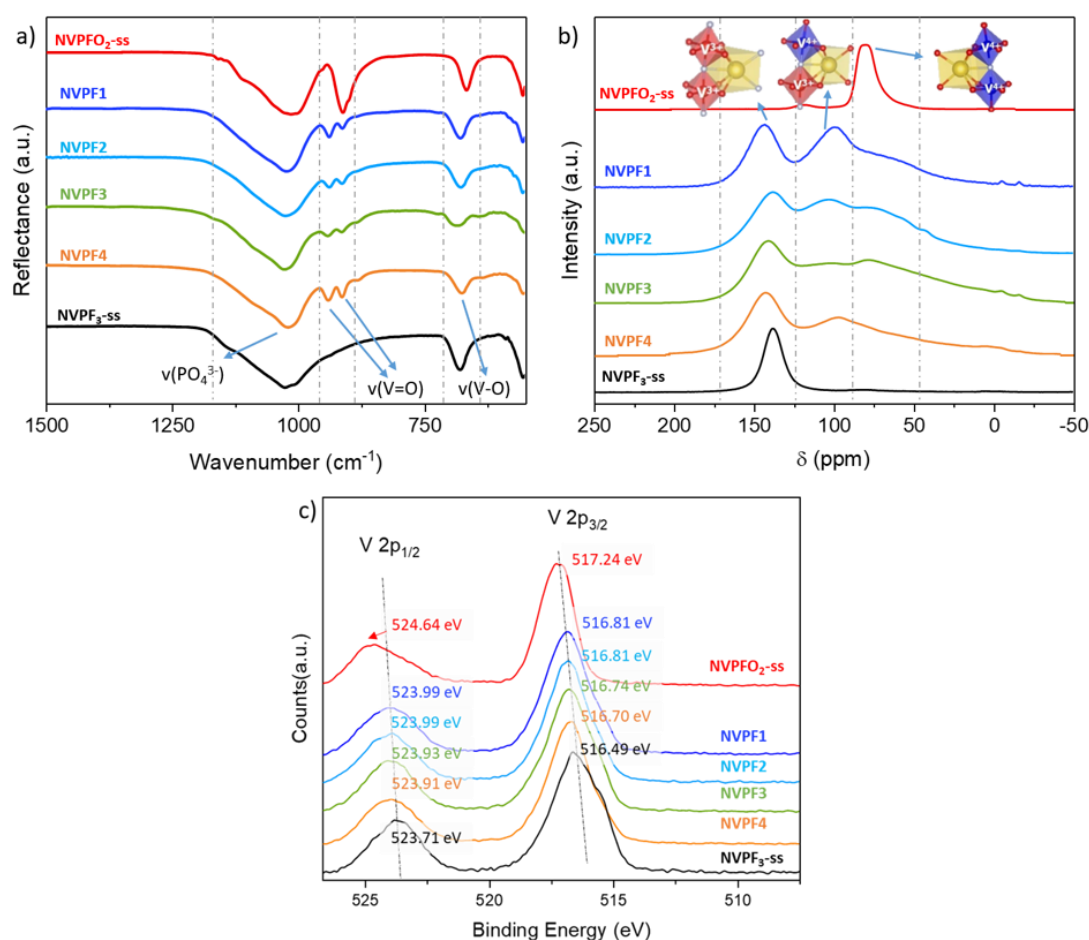


Figure 5: a) Comparison of the IR spectra of all the studied NVPFO_y materials in the wavenumber range of 550-1500 cm^{-1} . b) ^{23}Na ss-NMR spectra recorded for all compounds. The fitting results of ^{23}Na ss-NMR are reported Figure S4. c) XPS spectra of V 2p orbital

The ^{23}Na ss-NMR spectra recorded for all compounds are given in **Figure 5b**. Three main signals can be detected at ~ 70 ppm, ~ 100 ppm and ~ 140 ppm and indicate the presence of hyperfine interactions between the ^{23}Na nuclei and the paramagnetic $V^{3+,4+}$ ions present in their close environments. According to previous works, the more positively shifted signal is attributed to

the presence of two V^{3+} in close vicinity with a Na^+ ($Na(OV^{3+})_2$ environment) whereas the lower Fermi contact shift at ~ 70 ppm corresponds to the interaction of two V^{4+} with a Na^+ ($Na(OV^{4+})_2$ environment).^[42–44,48] The intermediate signal at ~ 100 ppm corresponds to a $Na(OV^{4+})(OV^{3+})$ local environment. The presence of these three broad signals for NVPF1, NVPF2, NVPF3 and NVPF4 thus confirms the mixed V^{3+}/V^{4+} vanadium oxidation state.^[48,49] Moreover, by fitting the spectra, we found the presence of a 4th signal with an even lower paramagnetic shift (between 20 – 39 ppm, as shown in **Figure 6**), which may originate from environment where Na^+ is in close interaction with only one vanadium. These environments could come from the surface defects probably enhanced by the nanosizing of the particles, as we will see in the next part. Nevertheless, the higher intensity of the signal measured at ~ 140 ppm compared to those at ~ 100 and ~ 70 ppm observed for NVPF4 and NVPF3, indicates that the vanadium average oxidation degree is closer to V^{3+} and confirms the trend composition determined by XRD.

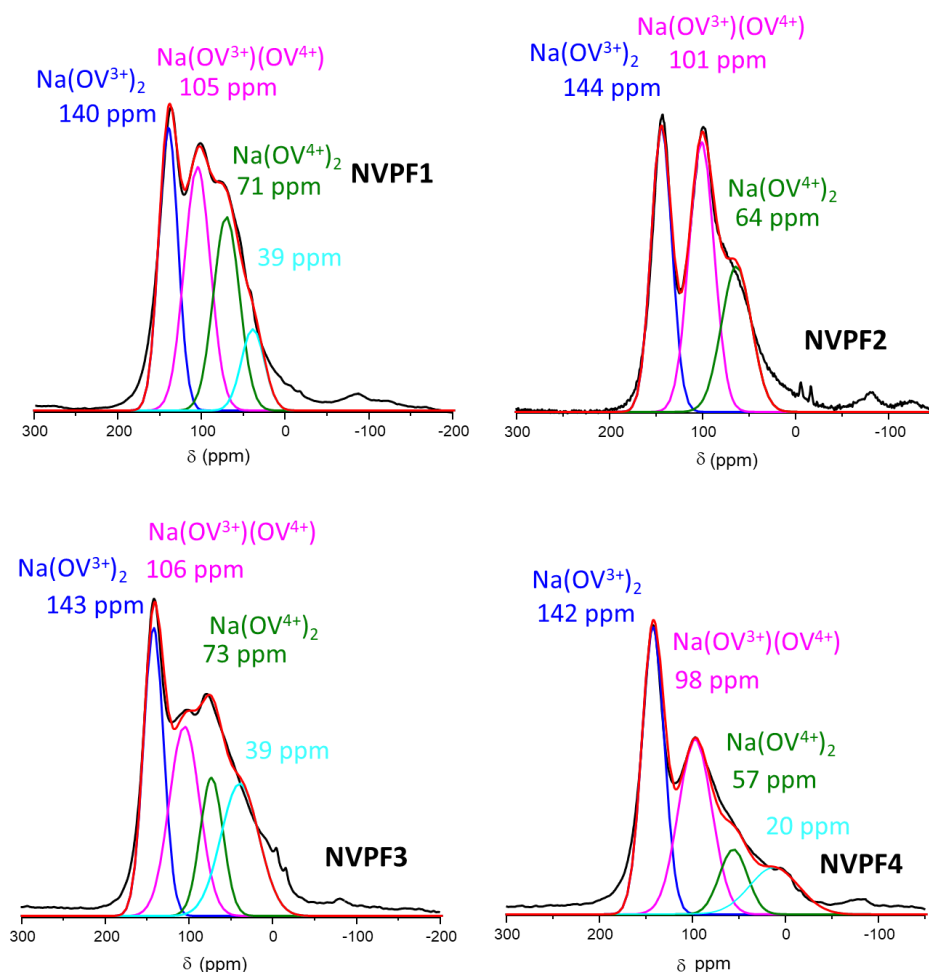


Figure 6: Fitting of ^{23}Na ss-NMR spectra, some small impurity resonances exist also in NVPF1 and NVPF3 around 0 ppm, which is still under characterization. A 4th signal with a low paramagnetic shift (cyan curve), can be tentatively attributed to Na^+ in close interaction with only one V, $Na(OV^{4+})$, maybe due to the surface defects enhanced by the nanosizing of our materials. The 4th signal is less intense for NVPF2 and less shifted (around 20

ppm) for NVPF4. The negative shifts are associated to rotation bands and the fitting were performed using DmFIT program.

The vanadium oxidation state has also been evaluated by XPS analyses (**Figure 5c**). The V2p spectrum of NVPFO₂-ss reference exhibits two broad components at 517.24 eV and 524.77 eV coming from V2p_{3/2} and V2p_{1/2} transitions, respectively, and which are consistent with results expected for V⁴⁺ in such polyanionic materials.^[35] On the other hand, NVPF₃-ss demonstrates that the binding energies of V2p_{3/2} and V2p_{1/2} are located at 516.49 eV and 523.71 eV, in good agreement with a vanadium in its trivalent state in such polyanionic materials.^[35] All the compounds obtained by solvothermal reaction have V2p_{3/2} and V2p_{1/2} binding energies in between those of the two references, confirming the mixed V³⁺/V⁴⁺ valence state and in very good agreement with the vanadium mean oxidation state deduced from changes in the cell parameters determined from XRD patterns analysis.

As it can be seen in the SEM and TEM images (**Figure 7**, and for more details **Figure 8** and **Figure 9** in supplementary information), various particle morphologies generated by different aggregation / organization of similar nanoscale primary particles (**Table 1**) were successfully obtained by slightly adjusting synthesis conditions while maintaining the same synthesis precursors (**Table 5**). Indeed, increasing the amount of phosphoric acid does not only change the acidity of the reaction medium, but also modify the complexation process of the particle surface, which allows to stabilize a large extent of different particle's morphologies. The addition of the surfactant Pluronic F127 also allows to control the growth of the primary particles and the way they aggregate to form the final cylindrical-shape secondary particles. Ethanol, with its smaller surface tension compared to water, also allows to modify the shape of the primary and secondary particles by playing with the concentration of ethanol in water/ethanol solutions. Finally, the slower ramp-up curve allows for a more continuous change in temperature in the reaction media and thus, a more homogeneous nucleation and aggregation for the formation of controlled particles' size.

Synthesis using stoichiometric ratio (i.e. according to the molar ratio of 1 for the vanadium precursor, 1.5 for sodium fluorine and 1 for phosphoric acid) reacted at 180°C for ten hours leads to the formation of spherical nanoparticles of around 300 nm (NVPF1, **Figure 7a-b** and **Figure 9**). Under the influence of Pluronic F127 surfactant in a more concentrated ethanol solution media, and with a gentler heating profile, the particles grow into micron-sized cylindrical aggregates composed of flakes around 2-3 µm (NVPF2, **Figure 7c-d** and **Figure 9**).

Interestingly, despite different synthesis conditions used to prepare NVPF1 and NVPF2, a negligible impact was observed on their chemical composition and on their coherent domains' size, which was determined using Scherrer formula (**Table 1**). The addition of surfactant certainly orients the aggregation of primary particles to the stacking of the basal faces, which show a smaller surface energy. On the contrary, increasing the molar ratio of H_3PO_4 and NaF versus that of vanadium acetylacetonate affects both the oxygen content and the morphology as shown by the comparison of NVPF1 and NVPF4. The spherical nanoparticles of NVPF1 become micrometric aggregates similar to desert roses for NVPF4 (**Figure 7g-h and Figure 8**), and the excess of phosphoric acid is most probably limiting the vanadium oxidation during the synthesis of the latter. Furthermore, in the absence of Pluronic F127 conjugated to a higher amount of H_3PO_4 , the aggregates of flakes observed for NVPF2 lose their cylindrical-shape microstructure to form rounded flake (around 2-3 μm length) for NVPF3 (**Figure 7e-f**). Finally, an excess of NaF and H_3PO_4 used for the synthesis of NVPF3 and NVPF4 leads to the formation of small coherent domains along the [002] direction close to 30-35 nm, whereas larger ones are observed for NVPF1 and NVPF2 with ~ 65 nm and ~ 55 nm respectively (**Table 1**). It is worth mentioning that platelet-like shape particles are obtained with different thicknesses for NVPF2 (ca. 100 nm), NVPF3 (ca. 100 nm) and NVPF4 (ca. 50 nm), and that all the morphologies prepared in these solvothermal conditions are very different from that observed for $\text{Na}_3\text{V}_{2-y}(\text{PO}_4)_2\text{F}_{3-y}\text{O}_y$ synthesized by solid state method and showing big and irregular aggregates made of ill-defined particles fused together (**Figure 8**). The results of specific surface area (SSA) measured for all compounds are given in **Table 3** and the SSA trend fits well to the different morphologies that are compared.

Table 3: Specific surface area for the five compounds studied in this work.

	NVPF1	NVPF2	NVPF3	NVPF4
BET (m^2/g)	10.77(6)	1.74(1)	2.47(2)	21.19(4)

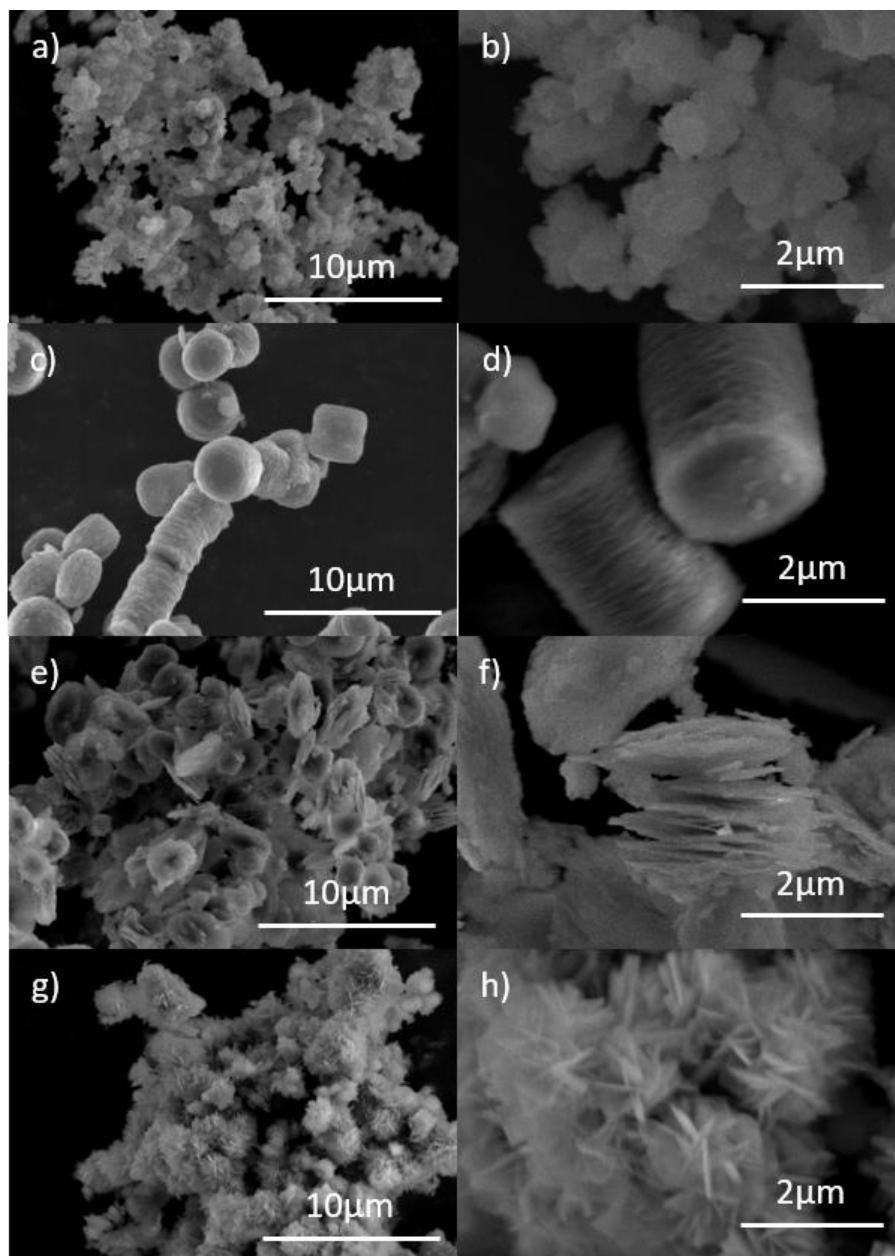


Figure 7: SEM images of all studied materials: a-b) NVPF1, c-d) NVPF2, e-f) NVPF3, and g-h) NVPF4

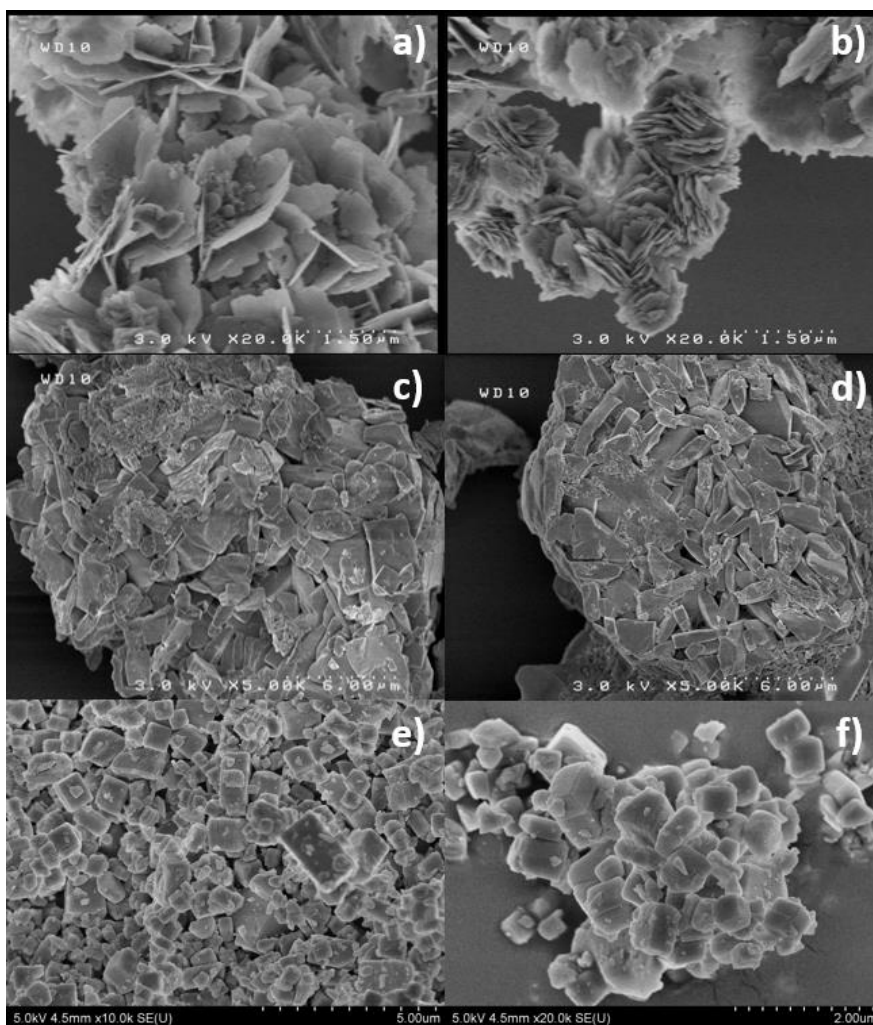


Figure 8: SEM images a) b): at greater magnification for NVPF4, which present aggregates of thin flakes leading to desert rose's morphology. c) d): NVPF2-ss. e) f): NVPF3-ss

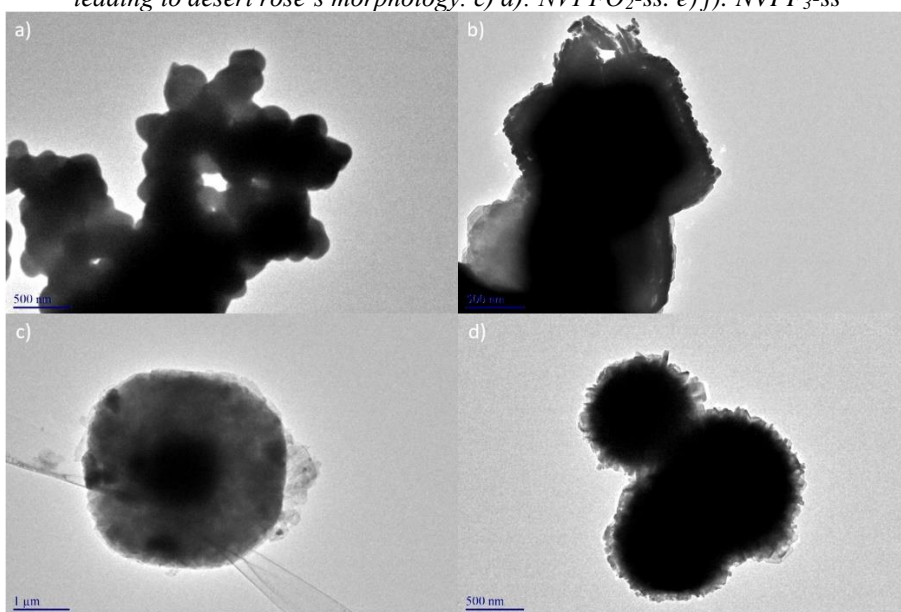


Figure 9: TEM images of a) NVPF1 b) NVPF2 c) NVPF3 and d) NVPF4.

In order to study further the morphology of the different samples, high resolution TEM was performed to determine the flakes' orientation in NVPF3 and NVPF4 (**Figure 10**). The flakes

observed in NVPF3 were found to exhibit (00 l) crystallographic planes through fringe calculation, in good agreement with an orientation of the nanoplatelets along the c -axis (**Figure 10a**). As the Na⁺ ions diffuse in channels situated in the (ab) plane, perpendicular to the orientation of the primary particles, it could be expected that the stacking of nanosheets, forming the flakes, would make Na⁺ insertion/extraction difficult.^[11] Similarly, the platelets that compose the sand-roses are also orientated along (00 l) planes, however this time their special aggregation leads to an easy access to the nanoplatelets' surface and should thus favor good Na⁺ diffusion (**Figure 10b**). The orientation determined for the platelets is in good agreement with the work of Yi et al. that also found 2D NVPF platelets oriented along (00 l) planes through fringe calculation.^[50]

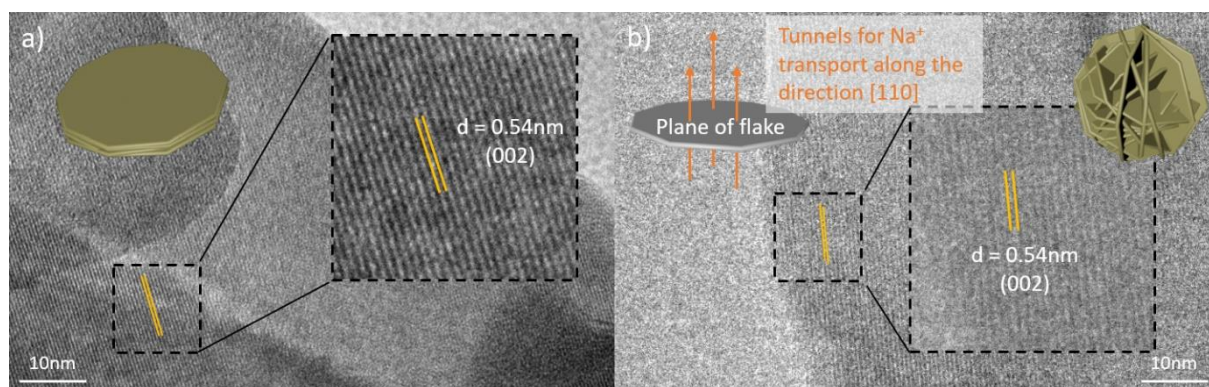


Figure 10: TEM images of the flakes of a) NVPF3 and b) NVPF4 with 3D models and schematic.

2.2 Electrochemical properties

The electrochemical behavior and reaction kinetics were investigated for the four samples by galvanostatic charge/discharge (GCD) experiments and cyclic voltammetry (CV) in coin-type half-cells versus metallic Na, and were compared to those obtained for NVPF₃-ss and NVPFO₂-ss. Although the materials prepared by solvothermal approach are not carbon coated, electrodes were prepared such as to contain a high mass loading (~ 6 mg/cm²), with 88 wt.% of active material, 7 wt.% of carbon and 5 wt.% of PVDF as binder, in order to be close to practical conditions and better observe the influence of the materials' morphology. **Figure 11a-d** show the GDC profiles of the 1st, 2nd and 5th cycles obtained at a cycling rate of C/20 in the potential range 2.5-4.3 V vs. Na⁺/Na. As expected, due to the mixed valence state of vanadium with the presence of V³⁺ and (V=O)²⁺ in NVPF1, NVPF2, NVPF3 and NVPF4, their electrochemical curves are characterized by two slopping “plateaus” showing thus the succession of two solid-solution composition domains upon Na⁺ extraction/insertion. On the contrary, the NVPF₃-ss and NVPFO₂-ss (**Figure 12**) exhibit well defined plateaus revealing the reversible extraction of

Na⁺ ions through a succession of biphasic reactions mainly.^[17] The difference between these desodiation mechanisms can be clearly identified on the first derivative curve of the 5th cycles (**Figure 11e**). The broad peaks confirm the S-shape profile (*i.e.* solid solution type reaction) and the sharp and intense peaks observed at 3.69 V, 3.72 V, 4.20 V for NVPF₃-ss and 3.64 V, 4.02 V for NVPFO₂-ss agree with successive biphasic reactions (**Figure 11e** and **Figure 13**). **Figure 11e** also reveals that the average oxidation potentials are similar for the four materials prepared by solvothermal syntheses (~ 3.65 and ~ 4.13 V), showing thus that the oxygen content has a very limited impact on the Na⁺ extraction potential in the composition range $0.35 \leq y \leq 0.8$ with y in Na₃V³⁺_{2-y}V⁴⁺_y(PO₄)₂F_{3-y}O_y. As shown by Nguyen *et al.*, the redox couples V⁴⁺/V³⁺ and (V=O)³⁺/(V=O)²⁺ are activated simultaneously upon Na⁺ extraction in these four electrode materials.^[51] On the contrary, the absence of covalent vanadyl bonds in NVPF₃-ss leads to higher average Na⁺ extraction potential (~ 3.7 and ~ 4.2 V). At C/20 all the materials display low polarization in Na cells, however NVPF1 and NVPF4 exhibit higher specific capacity: 114 mAh/g and 108 mAh/g respectively (as determined from the 2nd cycle), versus 99 mAh/g and 86 mAh/g for NVPF3 and NVPF2 and 86 mAh/g and 70 mAh/g for NVPF₃-ss and NVPFO₂-ss (**Figure 14** and **Figure 12**). It seems that the stacking of nanosheets into flakes (NVPF3) or into cylinders (NVPF2) is detrimental to performance as expected from HRTEM analyses. Indeed, the sodium diffusion channels are perpendicular to their basal surface and their random stacking (no oriented aggregation) limits sodium insertion. Indeed, contrary to nanosphere (NVPF1) or nanoflower (NVPF4) morphologies, this stacking may prevent a good contact between the primary particles and the electrolyte that limits the participation of the “active material” to the electrochemical activity. To get more information, the materials were tested at different current densities, from C/20 up to 2C (**Figure 15a**). Once again, NVPF1 shows the best specific capacities at high rates, far ahead NVPF4 this time. This implies that nanosphere morphology (NVPF1) allows reaching better ionic and/or electronic kinetics than the desert rose morphology composed of randomly oriented flakes (NVPF4). It is also interesting to notice that NVPF3 shows a better capacity retention than NVPF2 at higher rate than C/5, which may suggest that further micro-structuration of flakes into cylindrical aggregates prevents a good ionic diffusion. Indeed, the random orientation of the stacking flakes is more likely to cause misalignment of the sodium pathway at the junction of the flakes and thus slow down the Na⁺ transport. Similar observation was reported by Shen *et al.*, who observed that discharge capacity becomes higher when the microstructure becomes looser.^[19] It is also noted that NVPF1 and NVPF2 determined with the same chemical composition Na₃V³⁺_{1.20}V⁴⁺_{0.80}(PO₄)₂F_{2.20}O_{0.80} exhibit respectively the best and the worst high rate capacities among the nanostructured

materials, which confirms the strong influence of morphology on the electrochemical performance. Compared to $\text{NVPF}_{3\text{-ss}}$ and $\text{NVPFO}_{2\text{-ss}}$, all the materials obtained by solvothermal method present better capacity, which highlights the great potential of the solvothermal synthesis method and the influence of the synthesis approach. Meanwhile, the less fluoridated $\text{NVPFO}_{2\text{-ss}}$ presents worst performance, suggesting the increase of O/F ratio is not the major reason for the electrochemical performance improvement of NVPF_1 .

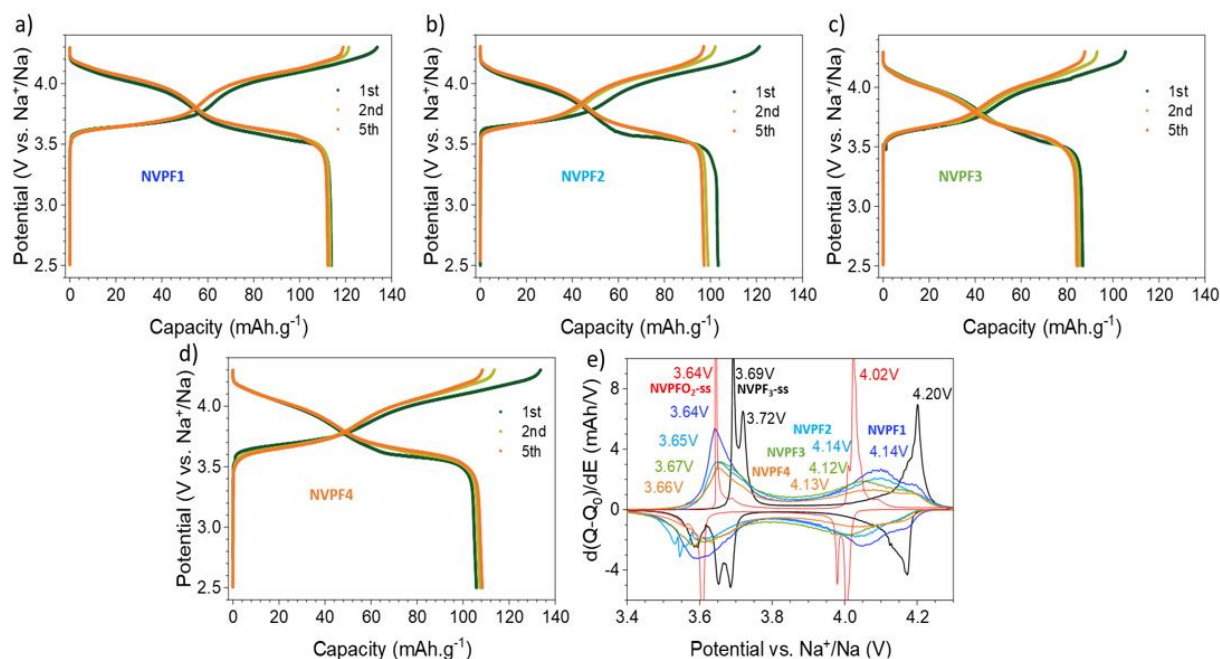


Figure 11: a-d) Galvanostatic charge and discharge curves obtained for all the NVPFO_y materials at the cycling rate of C/20. e) Associated derivative curves of the 5th cycles.

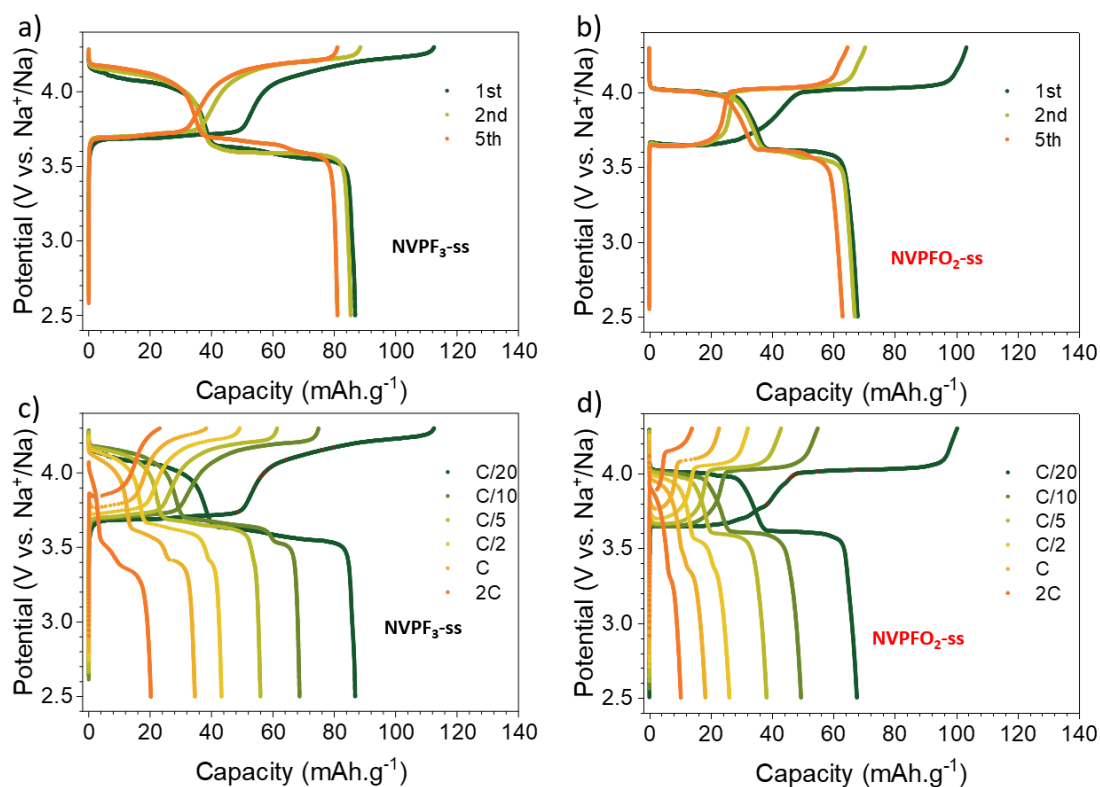


Figure 12: a) b) galvanostatic charge and discharge curves obtained for NVPF₃-ss and NVPFO₂-ss at C/20; c) d): Charge and discharge curves of NVPF₃-ss NVPFO₂-ss at different cycling rates, from C/20 to 2C.

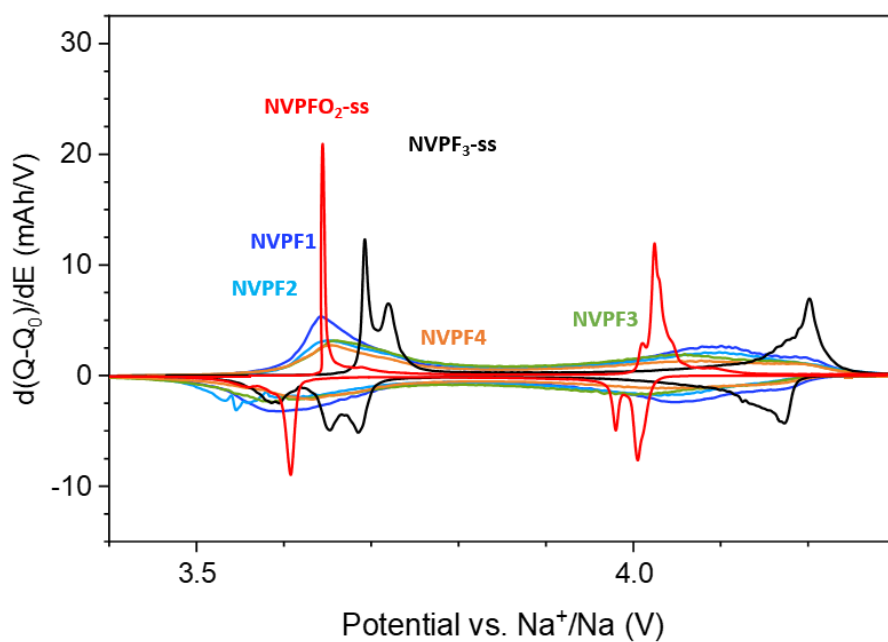


Figure 13: First derivative curves of the 5th cycle for NVPF1, NVPF2, NVPF3, NVPF4 and the two NVPF₃ and NVPFO₂ references.

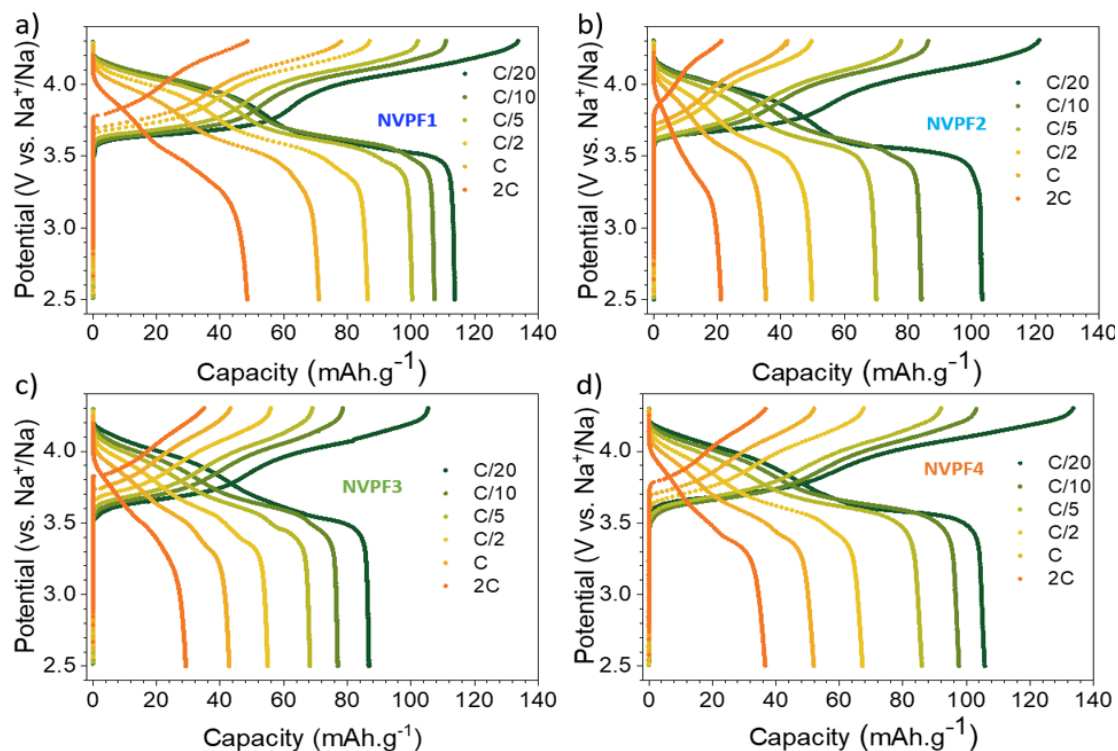


Figure 14: a-d) Charge and discharge curves of NVPF_{O_y} materials at different cycling rates, from C/20 to 2C.

Finally, the recovering of the original performance at C/10 after cycling at high rates reveals the good structural stability for all phases and implies that the capacity decrease upon higher current comes from limited kinetics (**Figure 15a**).

According to **Figure 15b**, all the compounds show a capacity retention higher than 80% after 200 cycles at C/10 and an initial specific capacity higher than 80 mAh/g. NVPF1 showing a controlled granulometry with independent particles of 300 nm delivers the best performance, with an initial specific capacity of 110 mAh/g and a capacity retention of about 91% after 200 cycles.

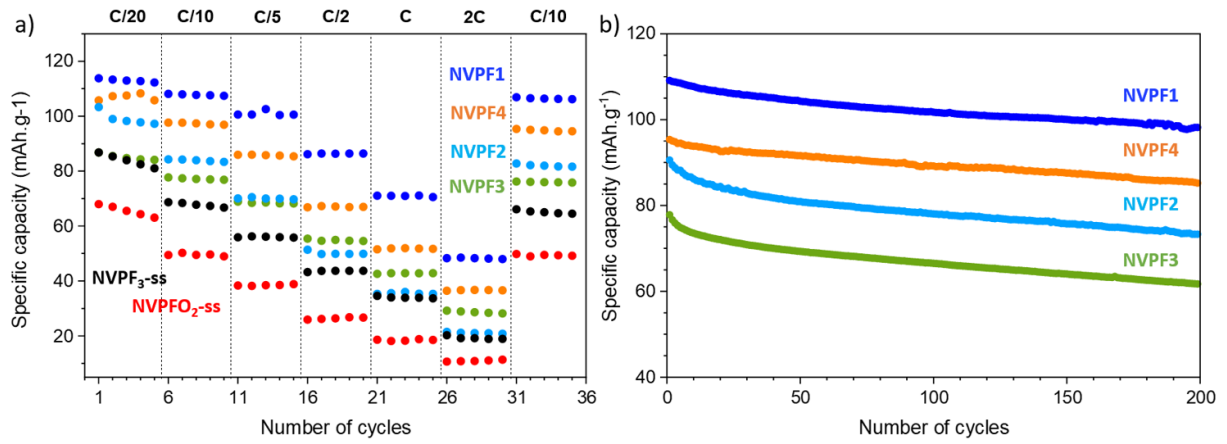


Figure 15: a) Rate capabilities obtained for all the studied materials at various rates from C/20 to 2C. b) Cycling performance of all the NVPFO_y materials prepared without any carbon coating, comparison at a current rate of C/10.

In order to investigate more deeply the influence of the morphology on the ionic diffusion, CV analysis was used to analyze the Na⁺ migration kinetics in NVPFO_y materials at various scan rates from 0.025 mV/s to 0.8 mV/s and in the potential range 2.5-4.3 V vs. Na⁺/Na, the upper cut-off voltage being limited to 4.3 V to avoid any possible electrolyte degradation. For all the materials, two reversible oxidation peaks, corresponding to the two pseudo-plateaus observed in GCD mode, can be observed at low scan rate. It can be seen that the height and area of these peaks continuously increase with the increasing rate. Simultaneously the polarization also increases which shifts the high potential oxidation peak out of the selected electrochemical window. Thus, the second oxidation/reduction was not complete and only the behavior of the first oxidation named O1 and its corresponding reduction (R₁) was further analyzed. **Figure 16** illustrates the evolution of the peak current (*i_p*) versus the square root of the scan rate (*v*^{1/2}). The linear profiles demonstrate excellent fitting results and indicate that the electrochemical reactions of all the materials are based on diffusion-controlled processes for Na⁺ intercalation/deintercalation. Based on the above CV measurements and linear fitting results, the apparent ion diffusion coefficient (**Table 4**) can be determined from the Randles-Sevcik equation. Based on the CV measurements (**Figure 16**) and linear fitting results, the apparent ion diffusion coefficient can be determined from the Randles-Sevcik equation.

$$i_p = 0.4463 nFAC \left(\frac{nFvD}{RT} \right)^{\frac{1}{2}}$$

Where *i_p* is the maximum current, *n* is the number of electrons transferred in the redox event (*n*=1), *A* is the electrode area (cm²), *F* is the Faraday constant, *C* is the concentration of Na⁺ (2.91.10⁻⁴ mol/cm³), *v* is the scan rate, *R* is the gas constant and *T* is the temperature in Kelvin.

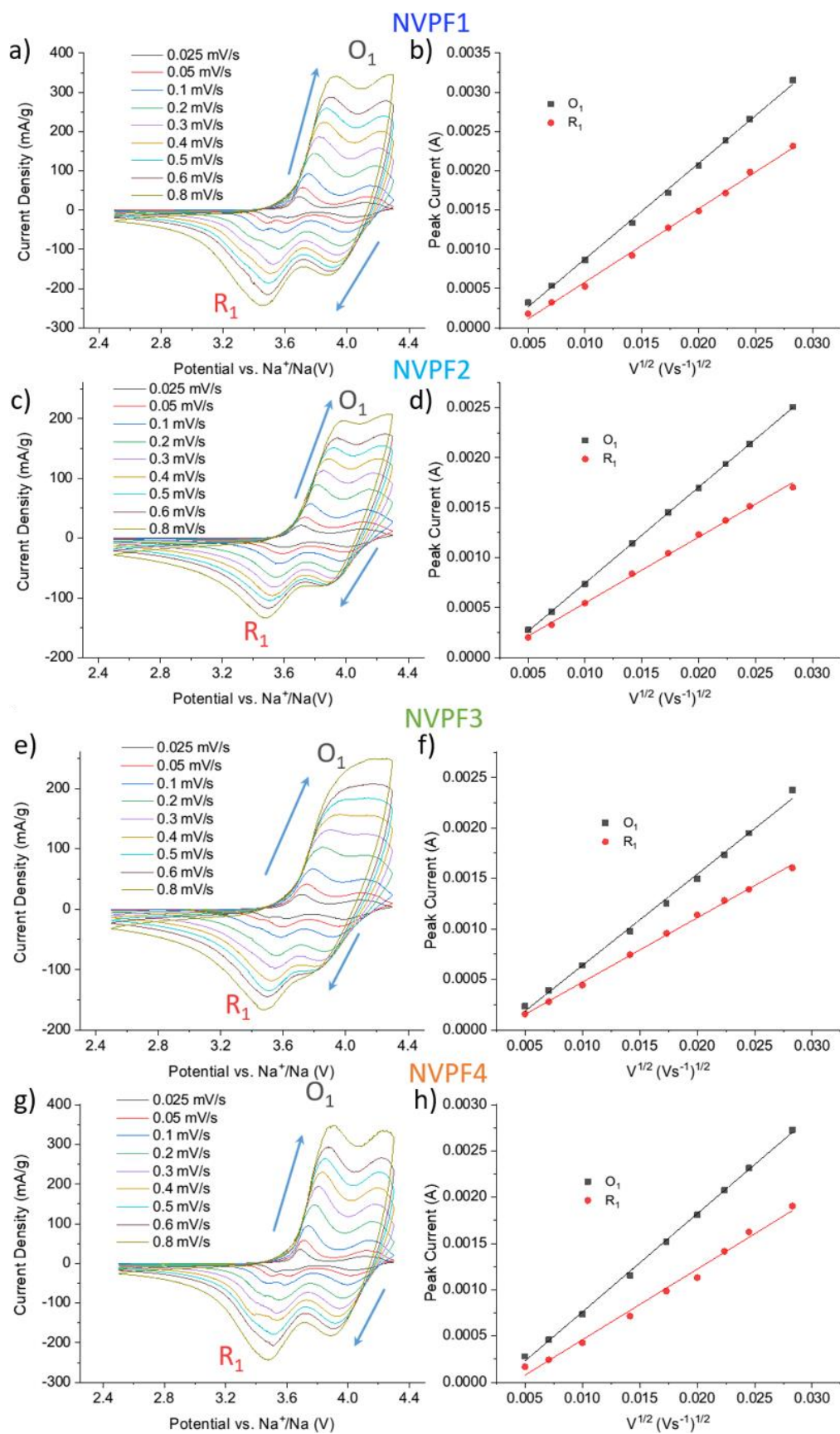


Figure 16: a-h) CV curves at different scan rates and the corresponding linear fitting curves between the peak current (i_p) and the square root of the scan rate ($v^{1/2}$): a-b) NVPF1, c-d) NVPF2, e-f) NVPF3, g-h) NVPF4.

Table 4: Diffusion coefficients determined for the four different samples.

D (cm ² s ⁻¹)	NVPF1	NVPF2	NVPF3	NVPF4
O1	1.60×10 ⁻¹¹	9.99×10 ⁻¹²	8.82×10 ⁻¹²	1.22×10 ⁻¹¹
R1	9.46×10 ⁻¹²	4.72×10 ⁻¹²	4.39×10 ⁻¹²	6.30×10 ⁻¹²

First of all, it can be seen that the diffusion coefficient determined upon reduction process is always lower than that upon oxidation reaction, which shows that Na⁺ can be more easily extracted than re-intercalated. The one determined for NVPF1 presents the highest diffusion coefficient (1.60×10⁻¹¹ cm².s⁻¹), nearly one order of magnitude higher than that for NVPFO₂-ss reference (**Figure 17**), and reveals very promising diffusion abilities considering the absence of coating and the electrode formulation chosen. Then, NVPF4, NVPF2 and NVPF3 possess diffusion coefficient of 1.22×10⁻¹¹ cm².s⁻¹, 9.99×10⁻¹² cm².s⁻¹ and 8.82×10⁻¹² cm².s⁻¹ respectively. These values are consistent with those reported in literature and even sometimes higher than for carbon-coated NVPF materials^[19,23,52,53] (e.g. 6.366×10⁻¹² cm².s⁻¹ for NVPF@C reported by Shen et al.^[23]). Finally, these results confirm the energy storage performance measured previously and demonstrate that the nanosphere morphology of NVPF1 facilitates the ionic diffusion and generates thus better kinetics compared to those of agglomeration of platelets within flakes, sand-rose flowers or cylinders' morphologies.^[10,54]

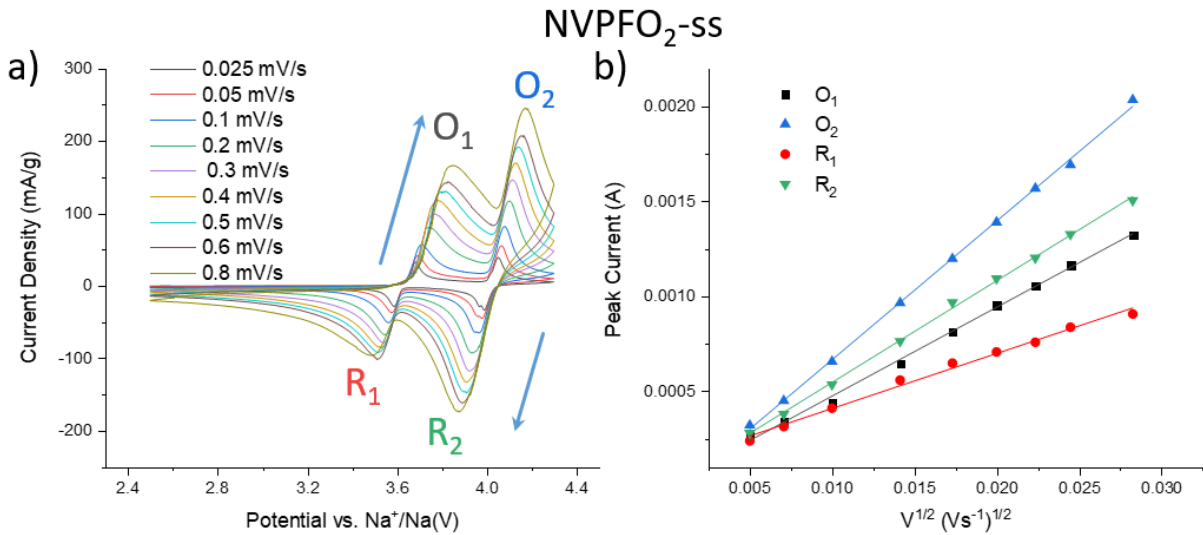


Figure 17: CV curves at different scan rates and the corresponding linear fitting curves between the peak current (*ip*) and the square root of the scan rate ($v^{1/2}$) for NVPFO₂-ss. Corresponding diffusion coefficient is O₁: 2.37×10⁻¹² and R₁: 9.08×10⁻¹³.

3. Conclusion

A series of $\text{Na}_3\text{V}^{3+}_{2-y}\text{V}^{4+}_y(\text{PO}_4)_2\text{F}_{3-y}\text{O}_y$ materials with different morphologies (nanosphere, micrometric flake, cylindrical agglomerate and sand-rose) were obtained by controlling the precursors' molar ratio, the ethanol concentration in the water/ethanol mixture and the heating rate during solvothermal syntheses, but also by adding a surfactant. Through a series of thorough characterization, the anionic composition in oxygen and fluorine and the structure were determined for the different compounds, found to belong to the $\text{Na}_3\text{V}^{3+}_{2-y}\text{V}^{4+}_y(\text{PO}_4)_2\text{F}_{3-y}\text{O}_y$ family with $0.35 \leq y \leq 0.8$. The electrochemical measurements disclose that the O/F ratio has a limited influence on the average oxidation potential within the composition range $0.35 \leq y \leq 0.8$ in $\text{Na}_3\text{V}^{3+}_{2-y}\text{V}^{4+}_y(\text{PO}_4)_2\text{F}_{3-y}\text{O}_y$, whereas the V^{3+} -rich $\text{Na}_3\text{V}_2(\text{PO}_4)_2\text{F}_3$ compound exhibits a higher average potential of ~ 0.1 V due to the absence of covalent vanadyl bonds. This study has demonstrated that particles morphology has a strong influence on the energy storage performance. It was shown that the misaligned stacking of nanosheets grown perpendicularly to the Na^+ diffusion channels prevents for a fast Na^+ diffusion. On the other hand, sand rose and especially nanosphere morphologies, which allow for an easy access to the Na^+ diffusion channels situated in the (ab) crystallographic plane, exhibit the best high rate performance and should be favored in future works.

4. Experimental Section

4.1 Materials preparation

The $\text{Na}_3\text{V}^{3+}_{2-y}\text{V}^{4+}_y(\text{PO}_4)_2\text{F}_{3-y}\text{O}_y$ compounds were prepared by one step solvothermal reaction, by adding required amounts of vanadium acetylacetonate (Sigma-Aldrich; $\geq 97\%$), sodium fluoride (Prolabo; 98%) and phosphoric acid (VWR; 85%). Starting from these precursors, numerous different morphologies were obtained under different synthesis conditions. In this work, four of them that exhibit homogeneous morphologies were chosen to be studied more in details. As described in **Table 5**, different synthesis parameters were explored: the molar ratio of the precursors (the amount of NaF and H_3PO_4 were adjusted whereas the concentration of vanadium acetylacetonate was kept around 0.2 mol.L^{-1}), the nature of the solution (water/ethanol mixtures), the use of the surfactant additive Pluronic F127 (Sigma-Aldrich) and the thermal treatment conditions. Indeed, the precursor solution was heated at 180°C in a Teflon Parr autoclave, for 10 h with different heating rates (**Table 5**). Depending on the experimental conditions, polycrystalline powders with different green shades were recovered after several washing steps by centrifugation (first with ethanol then with distilled water), and a final drying in vacuum at 60°C overnight. A wide variety of $\text{Na}_3\text{V}^{3+}_{2-y}\text{V}^{4+}_y(\text{PO}_4)_2\text{F}_{3-y}\text{O}_y$ compounds with

different morphologies were obtained by playing on the experimental parameters. In this study, we selected four samples showing different and homogeneous morphology as well as well crystallized particles and we do not consider samples showing heterogeneous particles morphology or amorphous parts.

Besides, $\text{Na}_3\text{V}^{3+}_2(\text{PO}_4)_2\text{F}_3$ (NVPF₃-ss) and $\text{Na}_3\text{V}^{4+}_2(\text{PO}_4)_2\text{FO}_2$ (NVPFO₂-ss) material synthesized by solid state approach according to reference [13] and were used as references for comparison.^{[13][55]}

Table 5: Detailed synthesis method and parameters of all the studied materials.

Type	Vanadium acetylacetonate	Sodium fluorine	Phosphoric acid	Water/ethanol solution	Additive	Heating rate	T	Time
NVPF1	1	1.5	1	50%/50%	X	Directly in oven	180°C	10H
NVPF2	1	1.5	1	10%/90%	Pluronic F127	1°C/min	180°C	10H
NVPF3	1	1.67	1.5	10%/90%	X	0.5°C/min	180°C	10H
NVPF4	1	1.67	1.5	50%/50%	X	Directly in oven	180°C	10H

4.2 Characterization techniques

X-ray diffraction (XRD) measurements were carried out by using a BRUKER D8 ADVANCE diffractometer in θ - θ configuration, equipped with a Cu $\text{K}_{\alpha 1,2}$ X-ray source. The acquisition was performed in the 2θ angular range of $10^\circ - 140^\circ$ with a step size of 0.0197° . The Rietveld refinements were performed using the FullProf Suite.^[56]

Scanning electron microscopy (SEM) images were taken without any conductive deposition by a Hitachi Model S-3400N microscope.

Transmission electron microscopy (TEM) was carried out with the Tecnai spirit G2 microscope.

The chemical analysis of the Na, P and V contents was performed by inductively coupled plasma-optical emission spectroscopy (ICP-OES) using a Varian Model 720-ES spectrometer, after a complete dissolution of the powders into a concentrated hydrochloric acid (HCl) solution.

Fourier transformed infrared (FT-IR) spectra were recorded by using a PerkinElmer Spectrum 400 FT-IR/FT-NIR spectrometer in the wavenumber range of $400 - 4000 \text{ cm}^{-1}$ (mid-IR).

^{23}Na ss-NMR spectra were acquired using a Bruker Advance III 500WB spectrometer equipped with an 11.7 T wide bore magnet (operating at Larmor frequency of 132.3 MHz for ^{23}Na).

Experiments were performed using a conventional 2.5 mm MAS probe with a 30 kHz MAS rate. In each case, a short pulse length of 1 μ s corresponding to a selective $\pi/8$ pulse was employed. The spectral width was set to 1 MHz and the recycle delay to $D_0 = 0.2$ s, which was long enough to avoid T_1 saturation effects. Chemical shifts are referenced relative to an aqueous 1 mol.L⁻¹ solution of NaCl solution ($\delta(^{23}\text{Na}) = 0$ ppm).

All the ^{23}Na ss-NMR spectra were deconvoluted using DmFIT program.^[57] In the cases where the signals were very thin, individual Lorentzian peaks were used, while a combination of Gaussian-Lorentzian 0.5 were used when broad peaks were observed.

X-ray photoelectron spectroscopy (XPS) spectra were obtained by using an Omicron Argus X-ray photoelectron spectrometer with a 280 W electron beam power and a monochromated AlK α radiation source (1486.6 eV). Binding energies were calibrated against the C 1s binding energy at 284.8 eV.

BET surface area measurements were carried out on Micromeritics ASAP 2010 after 150 °C overnight drying.

The electrochemical properties of the materials were tested in CR2032-type coin cells. The positive electrodes were prepared as a mixture containing the active material, carbon black, and polyvinylidene fluoride (PVDF) in NMP (N-Methyl-2-pyrrolidone) with the ratio of 88/7/5 (by wt.%). After an hour of thorough mixing, the black ink was casted as a flat film by doctor blade on an aluminum foil and dried in an oven at 60°C. Disks were cut, then pressed under 5 tons and finally dried overnight at 80°C under vacuum. A homemade electrolyte containing a 1 mol.L⁻¹ solution of NaPF₆ (Strem Chemical; 99%) in ethylene carbonate and dimethyl carbonate (EC/DMC = 1/1) with 2 wt.% of fluoroethylene carbonate (FEC) was used for all the electrochemical tests. The assembled cells were cycled in galvanostatic mode, from C/20 to 2C cycling rates between 2.5 and 4.3 V vs. Na⁺/Na. The theoretical capacity being 128 mAh.g⁻¹ (corresponding to 2 Na⁺ reversibly extracted from NVPF), the rate C/20 corresponds to the exchange of 2 Na⁺ in 20 hours. The electrodes have a typical active mass loading around 6 mg.cm⁻².

Acknowledgement

The authors thank the Materials Physics and Chemistry Doctoral School (ED397) of Sorbonne University for the funding of Runhe FANG's PhD thesis, as well as the financial support of

Région Nouvelle Aquitaine, of the French National Research Agency (STORE-EX Labex Project ANR-10-LABX-76-01) and of the European Union's Horizon 2020 research and innovation program under grant agreement No 875629 (NAIMA project). The authors also thank Emmanuel PETIT, Cathy DENAGE, Eric LEBRAUD (ICMCB) and Antoine MICHE (Sorbonne University) for their technical support.

Reference

- [1] J. B. Goodenough, Y. Kim, *Chem. Mater.* **2010**, 22, 587–603.
- [2] Y. S. Hu, S. Komaba, M. Forsyth, C. Johnson, T. Rojo, *Small Methods* **2019**, 3, 2–3.
- [3] I. Hasa, S. Mariyappan, D. Saurel, P. Adelhelm, A. Y. Kuposov, C. Masquelier, L. Croguennec, M. Casas-Cabanas, *J. Power Sources* **2021**, 482, 228872.
- [4] B. V. Rami Reddy, R. Ravikumar, C. Nithya, S. Gopukumar, *J. Mater. Chem. A* **2015**, 3, 18059–18063.
- [5] F. Lalère, V. Seznec, M. Courty, R. David, J. N. Chotard, C. Masquelier, *J. Mater. Chem. A* **2015**, 3, 16198–16205.
- [6] A. Ponrouch, R. Dedryvère, D. Monti, A. E. Demet, J. M. Ateba Mba, L. Croguennec, C. Masquelier, P. Johansson, M. R. Palacín, *Energy Environ. Sci.* **2013**, 6, 2361–2369.
- [7] W. Zhou, L. Xue, X. Lü, H. Gao, Y. Li, S. Xin, G. Fu, Z. Cui, Y. Zhu, J. B. Goodenough, *Nano Lett.* **2016**, 16, 7836–7841.
- [8] F. Chen, V. M. Kovrugin, R. David, O. Mentré, F. Fauth, J. N. Chotard, C. Masquelier, *Small Methods* **2019**, 3, 1–9.
- [9] C. Delmas, D. Carlier, M. Guignard, *Adv. Energy Mater.* **2021**, 11, 2001201.
- [10] T. Broux, F. Fauth, N. Hall, Y. Chatillon, M. Bianchini, T. Bamine, J. B. Leriche, E. Suard, D. Carlier, Y. Reynier, L. Simonin, C. Masquelier, L. Croguennec, *Small Methods* **2019**, 3, 1–12.
- [11] G. Fang, Z. Wu, J. Zhou, C. Zhu, X. Cao, T. Lin, Y. Chen, C. Wang, A. Pan, S. Liang, *Adv. Energy Mater.* **2018**, 8, 1–10.
- [12] C. Masquelier, L. Croguennec, *Chem. Rev.* **2013**, 113, 6552–6591.
- [13] L. H. B. Nguyen, T. Broux, P. S. Camacho, D. Denux, L. Bourgeois, S. Belin, A. Iadecola, F. Fauth, D. Carlier, J. Olchowka, C. Masquelier, L. Croguennec, *Energy Storage Mater.* **2019**, 20, 324–334.
- [14] C. Zhu, K. Song, P. A. Van Aken, J. Maier, Y. Yu, *Nano Lett.* **2014**, 14, 2175–2180.
- [15] K. Saravanan, C. W. Mason, A. Rudola, K. H. Wong, P. Balaya, *Adv. Energy Mater.* **2013**, 3, 444–

450.

- [16] Z. Jian, L. Zhao, H. Pan, Y. S. Hu, H. Li, W. Chen, L. Chen, *Electrochem. commun.* **2012**, *14*, 86–89.
- [17] M. Bianchini, N. Brisset, F. Fauth, F. Weill, E. Elkaim, E. Suard, C. Masquelier, L. Croguennec, *Chem. Mater.* **2014**, *26*, 4238–4247.
- [18] L. Zhu, H. Wang, D. Sun, Y. Tang, H. Wang, *J. Mater. Chem. A* **2020**, *8*, 21387–21407.
- [19] X. Shen, J. Zhao, Y. Li, X. Sun, C. Yang, H. Liu, Y. S. Hu, *ACS Appl. Energy Mater.* **2019**, *2*, 7474–7482.
- [20] A. Criado, P. Lavela, G. Ortiz, J. L. Tirado, C. Pérez-Vicente, N. Bahrou, Z. Edfouf, *Electrochim. Acta* **2020**, *332*, 1–8.
- [21] A. R. Iarchuk, D. V. Sheptyakov, A. M. Abakumov, **2021**, *10*, 26.
- [22] D. O. Semykina, M. A. Kirsanova, Y. M. Volkovich, V. E. Sosenkin, N. V. Kosova, *J. Solid State Chem.* **2021**, *297*, 122041.
- [23] C. Shen, H. Long, G. Wang, W. Lu, L. Shao, K. Xie, *J. Mater. Chem. A* **2018**, *6*, 6007–6014.
- [24] J. Xun, Y. Zhang, H. Xu, *Inorg. Chem. Commun.* **2020**, *115*, 107884.
- [25] J. Zhao, L. Mu, Y. Qi, Y. S. Hu, H. Liu, S. Dai, *Chem. Commun.* **2015**, *51*, 7160–7163.
- [26] A. Mukherjee, T. Sharabani, I. Perelshtein, M. Noked, *Batter. Supercaps* **2020**, *3*, 52–55.
- [27] P. Du, K. Mi, F. Hu, X. Jiang, D. Wang, X. Zheng, *New J. Chem.* **2020**, *44*, 12985–12992.
- [28] Y. Cai, X. Cao, Z. Luo, G. Fang, F. Liu, J. Zhou, A. Pan, S. Liang, *Adv. Sci.* **2018**, *5*, DOI 10.1002/advs.201800680.
- [29] H. Jin, J. Dong, E. Uchaker, Q. Zhang, X. Zhou, S. Hou, J. Li, G. Cao, *J. Mater. Chem. A* **2015**, *3*, 17563–17568.
- [30] C. Zhu, C. Wu, C. C. Chen, P. Kopold, P. A. Van Aken, J. Maier, Y. Yu, *Chem. Mater.* **2017**, *29*, 5207–5215.
- [31] A. Mukherjee, T. Sharabani, R. Sharma, S. Okashy, M. Noked, *Batter. Supercaps* **2020**, *3*, 510–518.
- [32] Y. Qi, L. Mu, J. Zhao, Y. S. Hu, H. Liu, S. Dai, *J. Mater. Chem. A* **2016**, *4*, 7178–7184.
- [33] J. Olchowka, L. H. B. Nguyen, E. Petit, P. S. Camacho, C. Masquelier, D. Carlier, L. Croguennec, *Inorg. Chem.* **2020**, *59*, 17282–17290.
- [34] Y. Qi, J. Zhao, C. Yang, H. Liu, Y.-S. Hu, *Small Methods* **2018**, *3*, 1800111.

- [35] Z. Tong, Y. Qi, J. Zhao, L. Liu, X. Shen, H. Liu, *Waste and Biomass Valorization* **2018**, *11*, 2201–2209.
- [36] Y. Hou, K. Chang, Z. Wang, S. Gu, Q. Liu, J. Zhang, H. Cheng, S. Zhang, Z. Chang, Z. Lu, *Sci. China Mater.* **2019**, *62*, 474–486.
- [37] Y. Qi, L. Mu, J. Zhao, Y. S. Hu, H. Liu, S. Dai, *Angew. Chemie - Int. Ed.* **2015**, *54*, 9911–9916.
- [38] M. Xu, L. Wang, X. Zhao, J. Song, H. Xie, Y. Lu, J. B. Goodenough, *Phys. Chem. Chem. Phys.* **2013**, *15*, 13032–13037.
- [39] J. Z. Guo, P. F. Wang, X. L. Wu, X. H. Zhang, Q. Yan, H. Chen, J. P. Zhang, Y. G. Guo, *Adv. Mater.* **2017**, *29*, 1–8.
- [40] Z. Y. Gu, J. Z. Guo, Y. Yang, H. Y. Yu, X. T. Xi, X. X. Zhao, H. Y. Guan, X. He, X. L. Wu, *Inorg. Chem. Front.* **2019**, *6*, 988–995.
- [41] R. A. Shakoor, D. H. Seo, H. Kim, Y. U. Park, J. Kim, S. W. Kim, H. Gwon, S. Lee, K. Kang, *J. Mater. Chem.* **2012**, *22*, 20535–20541.
- [42] T. Broux, T. Bamine, F. Fauth, L. Simonelli, W. Olszewski, C. Marini, M. Ménétrier, D. Carlier, C. Masquelier, L. Croguennec, *Chem. Mater.* **2016**, *28*, 7683–7692.
- [43] Y. U. Park, D. H. Seo, H. Kim, J. Kim, S. Lee, B. Kim, K. Kang, *Adv. Funct. Mater.* **2014**, *24*, 4603–4614.
- [44] P. Serras, V. Palomares, J. Alonso, N. Sharma, J. M. López Del Amo, P. Kubiak, M. L. Fdez-Gubieda, T. Rojo, *Chem. Mater.* **2013**, *25*, 4917–4925.
- [45] D. Semykina, O. Podgornova, N. Kosova, *Mater. Today Proc.* **2020**, *25*, 497–500.
- [46] F. Sauvage, E. Quarez, J. M. Tarascon, E. Baudrin, *Solid State Sci.* **2006**, *8*, 1215–1221.
- [47] J. Olchowka, L. H. B. Nguyen, T. Broux, P. Sanz Camacho, E. Petit, F. Fauth, D. Carlier, C. Masquelier, L. Croguennec, *Chem. Commun.* **2019**, *55*, 11719–11722.
- [48] L. H. B. Nguyen, P. Sanz Camacho, T. Broux, J. Olchowka, C. Masquelier, L. Croguennec, D. Carlier, *Chem. Mater.* **2019**, *31*, 9759–9768.
- [49] C. Li, M. Shen, X. Lou, B. Hu, *J. Phys. Chem. C* **2018**, *122*, 27224–27232.
- [50] H. Yi, L. Lin, M. Ling, Z. Lv, R. Li, Q. Fu, H. Zhang, Q. Zheng, X. Li, *ACS Energy Lett.* **2019**, *4*, 1565–1571.
- [51] L. H. B. Nguyen, A. Iadecola, S. Belin, J. Olchowka, C. Masquelier, D. Carlier, L. Croguennec, *J. Phys. Chem. C* **2020**, *124*, 23511–23522.
- [52] Q. Liu, D. Wang, X. Yang, N. Chen, C. Wang, X. Bie, Y. Wei, G. Chen, F. Du, *J. Mater. Chem. A*

2015, 3, 21478–21485.

[53] F. Li, Y. Zhao, L. Xia, Z. Yang, J. Wei, Z. Zhou, *J. Mater. Chem. A* **2020**, 8, 12391–12397.

[54] A. Ponrouch, E. Marchante, M. Courty, J. M. Tarascon, M. R. Palacín, *Energy Environ. Sci.* **2012**, 5, 8572–8583.

[55] N. Hall, S. Boulineau, L. Croguennec, S. Launois, C. Masquelier, L. Simonin, *United States Pat.* **2018**.

[56] J. Rodríguez-Carvajal, *Phys. B Phys. Condens. Matter* **1993**, 192, 55–69.

[57] D. Massiot, F. Fayon, M. Capron, I. King, S. Le Calvé, B. Alonso, J. O. Durand, B. Bujoli, Z. Gan, G. Hoatson, *Magn. Reson. Chem.* **2002**, 40, 70–76.

Additional Information

As mentioned in the article, many other morphologies were obtained besides these four shapes selected for a complete study. Several of these shapes and the conditions for their synthesis are listed below:

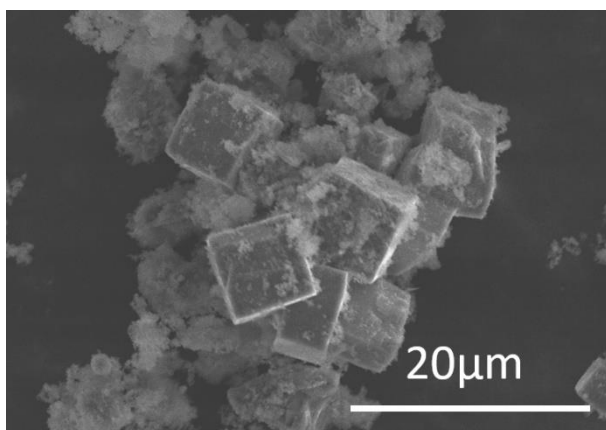


Figure 18: The mixture of $V(acac)_3$, NaF and H_3PO_4 with molar ratio of 1:1.67:1.5 in H_2O :Ethanol = 10%:90% solution heated directly at $120^\circ C$ oven for 10h. However, due to the amorphous parts, also detected by XRD, this type of sample did not proceed to the electrochemical testing phase. Based on this sample, the synthesis condition started to be modified and a series of different morphologies were obtained.

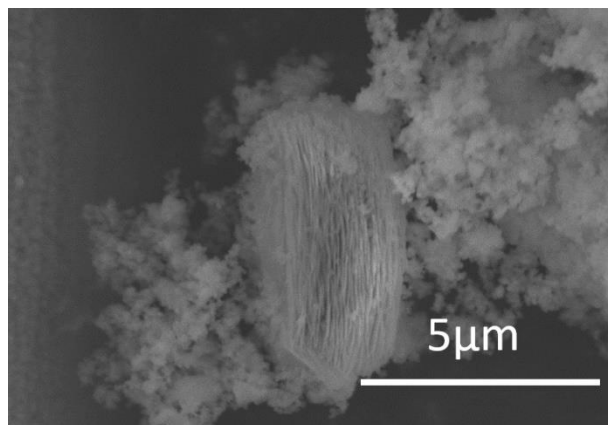


Figure 19: The mixture of $V(acac)_3$, NaF and H_3PO_4 with molar ratio of 1:1.67:1.5 in H_2O :Ethanol = 15%:85% solution was heated directly at $120^\circ C$ for 10h. This sample was obtained by varying the ethanol concentration compared to the previous synthesis parameter, however, the large number of amorphous parts also prevented it from being further characterized.

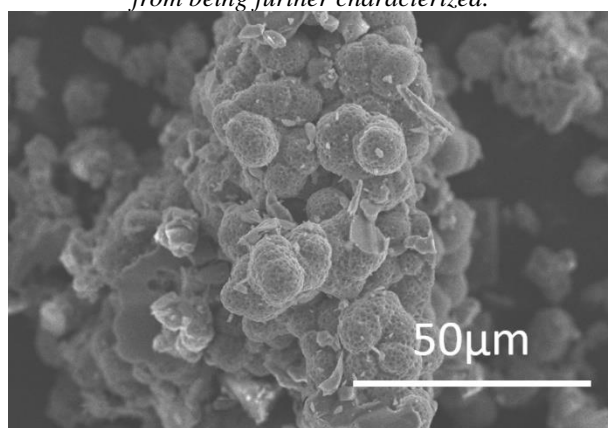


Figure 20: The mixture of $V(acac)_3$, NaF and H_3PO_4 with molar ratio of 1:1.67:1.5 in H_2O :Ethanol = 100%:0% solution heated at $180^\circ C$ for 10h. To solve the problem of the large number of amorphous parts obtained under $120^\circ C$. In order to reduce the amorphous parts, the reaction temperature was increased and the two special shapes covered in this chapter were obtained. This sample synthesized with 100% water was also not further characterized because the homogeneity of the particles is not very good.

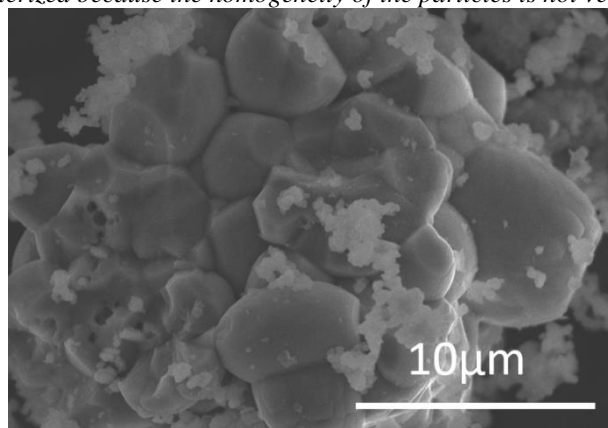


Figure 21: The mixture of $V(acac)_3$, NaF and H_3PO_4 with molar ratio of 1:1.67:1.5 and 0.025 mmol citric acid as additives in H_2O :Ethanol = 50%:50% solution heated at $180^\circ C$ for 10h. Before trying F127, citric acid was also tried in the reaction. However, the morphology of the resulting samples was not very homogeneous and the crystallinity was not comparable to other samples.

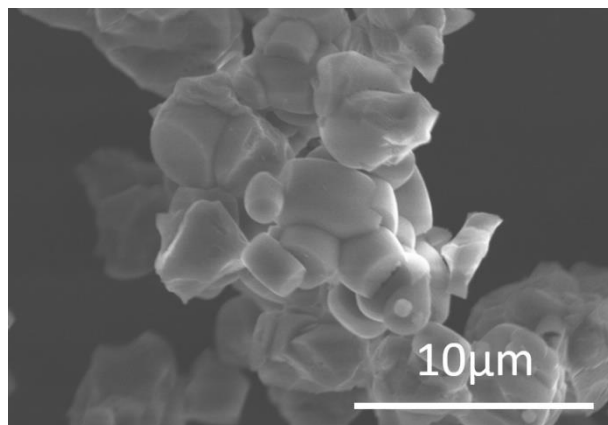


Figure 22: The mixture of Na_3VO_4 , NaF and H_3PO_4 with molar ratio of 1:1.7:3 in H_2O :Ethanol = 100%:0% solution heated at 180 °C for 1h in microwave oven. The samples synthesized by microwave oven give nice cylindrical structures, but some particles seem to be broken for some reason and do not form cylinders. Due to the lack of time, the morphological changes and the subsequent electrochemical properties were not studied.

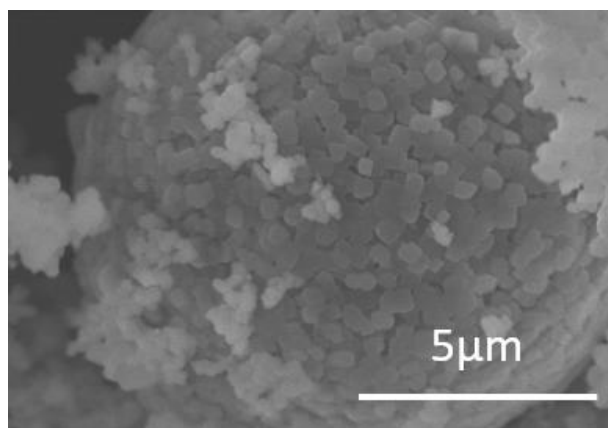


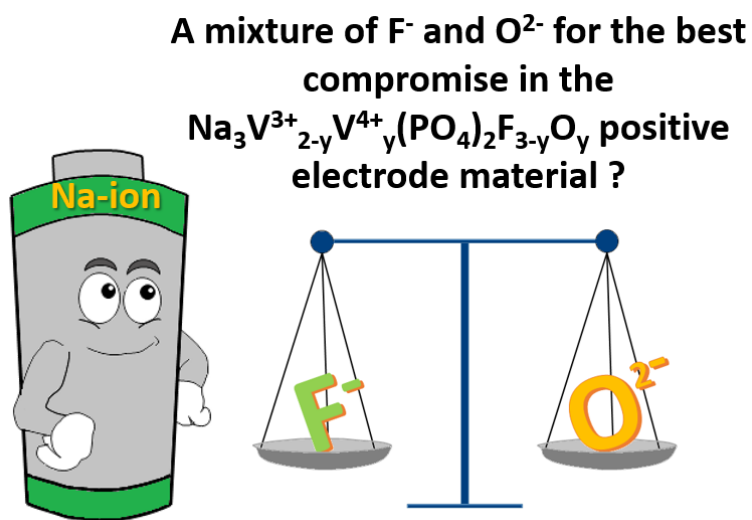
Figure 23: The mixture of $\text{V}(\text{acac})_3$, NaF and $\text{NH}_4\text{H}_2\text{PO}_4$ with ratio of 1:3:2 in water:DMF = 60%:40% solution heated at 180 °C for 10h in normal oven. As mentioned before the effect of the change of solution on the morphology is significant. Thus, further DMF solution was tested. This compound was also not further characterized because of its homogeneity (presence of small particles around the micrometric sphere).

In summary, these samples were not able to be assembled in half-cells and to test their electrochemical properties due to the lack of time and the homogeneity of some morphologies.

**Chapter III Impact of the F⁻ for O²⁻
substitution in Na₃V₂(PO₄)₂F_{3-y}O_y on
their transport properties and
electrochemical performance**

In last chapter, we found the great impact of morphologies on the final electrochemical performance. Among these morphologies, nanosphere has the most significant improvement. Besides, given the F^-/O^{2-} substitution effect on the electrochemical property mentioned in Chapter 1, the related influence of this ratio change, i.e. the final vanadium oxidation degree variation, on the final electrochemical performance needs to be further investigated.

To minimize the effect of changes in synthesis conditions on the final nanosphere particles, the only variable is the proportion of vanadium acetylacetonate in the precursor against its vanadyl counterpart. Raman spectroscopy was firstly carried out on the series of $Na_3V_{2-y}V^{4+}_y(PO_4)_2F_{3-y}O_y$ ($0 \leq y \leq 2$) nanospheres to reveal the V^{3+}/V^{4+} evolution. And these NVPFO_y compound were then characterized through impedance and galvanostatic measurement.



This article is deposited to ACS applied energy material and is under review.

Impact of the F⁻ for O²⁻ substitution in Na₃V₂(PO₄)₂F_{3-y}O_y on their transport properties and electrochemical performance

Runhe Fang ^{a,d}, Jacob Olchowka ^{b,d,e,*}, Chloé Pablos ^{b,c,d}, Rafaël Bianchini Nuernberg ^b, Laurence Croguennec ^{b,d,e}, Sophie Cassaignon ^{a,d,*}

^a Sorbonne Université, CNRS, Laboratoire Chimie de la Matière Condensée de Paris, LCMCP, UMR 7574, 4 Place Jussieu, 75005 Paris, France

^b CNRS, Univ. Bordeaux, Bordeaux INP, ICMCB UMR 5026, 33600 Pessac, France

^c Laboratoire de Réactivité et de Chimie des Solides, Université de Picardie Jules Verne, CNRS-UMR 7314, F-80039 Amiens Cedex 1, France

^d RS2E, Réseau Français sur le Stockage Electrochimique de l'Energie, CNRS 3459, 80039 Amiens Cedex 1, France.

^e ALISTORE-ERI European Research Institute, CNRS 3104, 80039 Amiens Cedex 1, France

The series of polyanionic compounds Na₃V₂(PO₄)₂F_{3-y}O_y ($0 \leq y \leq 2$) attracts much attention as positive electrode material for Na-ion batteries, because of its high operating potential and stable cycling performance. A series of nanospherical Na₃V₂(PO₄)₂F_{3-y}O_y (NVPFO_y) materials with $y = 0.8, 1.35, 1.6$ and 2 was synthesized using a solvothermal reaction and changes in the vanadium average oxidation state were fully characterized combining analyses by infrared spectroscopy and X-ray diffraction. Raman spectroscopy, beyond checking for the absence of a carbon coating, was in fact used for its sensitivity to the vanadium environment and turn out to be an efficient characterization technique to estimate the oxygen content within the Na₃V^{3+_{2-y}}V^{4+_y}(PO₄)₂F_{3-y}O_y family. The impact of the oxygen content on the transport properties was evaluated by impedance spectroscopy. The material with $y = 1.35$ demonstrates the smallest electrical resistivity in the series, as well as the best rate capability and cyclability upon long-term cycling, despite no carbon coating and a high mass loading positive electrode.

KEYWORDS: Na-ion batteries; Polyanionic positive electrode materials; Na₃V₂(PO₄)₂F₃; Na₃(VO)₂(PO₄)₂F; Transport properties; Raman spectroscopy.

* Corresponding authors:

S. Cassaignon (sophie.cassaignon@sorbonne-universite.fr)

J. Olchowka (jacob.olchowka@icmcb.cnrs.fr)

1. Introduction

As the climate problem grows, the European Union, like many political entities all over the world, proposed to reach the climate-neutral by 2050, which means reaching net zero greenhouse gas emissions with the help of European climate law.^[1] This ambition inevitably requires reducing the consumption of fossil fuel energy and strongly enhances solar and wind energy production. However, due to their intermittent character, these latter can be efficient only when coupled with performant energy storage devices that can store the excess of production and reinject it into the grid during peak demands. Sodium-ion batteries are believed to be a reliable and environmentally friendly energy storage system to respond this problem.^[2–4] Among all the materials tested as positive electrode materials, such as layered oxides and polyanionic ones, the series of $\text{Na}_3\text{V}^{3+}_{2-y}\text{V}^{4+}_y(\text{PO}_4)_2\text{F}_{3-y}\text{O}_y$ ($0 \leq y \leq 2$) (NVPFO_y) is one of the most promising due to its high operating voltage, long cycling stability and low volume changes upon the extraction/insertion of two Na^+ ions per formula unit.^[5–8]

The three-dimensional framework of this family is made of $\text{V}_2\text{O}_8\text{F}_{3-y}\text{O}_y$ bi-octahedral units interlinked together by PO_4 tetrahedra that allows efficient 2D Na^+ diffusion within tunnels along the $[110]$ and $[1\bar{1}0]$ directions.^[9] Unfortunately, although the phosphates contribute largely to stabilize the structure during cycling, they isolate the metal ions that begets a rather poor intrinsic electronic conductivity which reduces significantly the performance, especially at high rates. Such as it was done for LiFePO_4 , many remedies are proposed to improve the rate capabilities, such as combining NVPFO_y with conductive carbon source (carbon coating, carbon nanotube, graphene etc.),^[10–16] performing an elemental substitution (Al, Fe, Mn etc.)^[17–20], and designing nanostructured morphologies^[13,21–24]. However, few studies have been done to evaluate the intrinsic conductivity within the $\text{Na}_3\text{V}^{3+}_{2-y}\text{V}^{4+}_y(\text{PO}_4)_2\text{F}_{3-y}\text{O}_y$ series depending on oxygen content. Broux et al. demonstrated that a low partial substitution of O^{2-} for F^- (when the composition changes from $\text{Na}_3\text{V}_2(\text{PO}_4)_2\text{F}_3$ ($y = 0$) to $\text{Na}_3\text{V}_2(\text{PO}_4)_2\text{F}_{2.5}\text{O}_{0.5}$ ($y = 0.5$)) could improve both the electronic and ionic conductivities (at 95°C, from 1.22×10^{-10} to 3.76×10^{-10} S.cm^{-1} and 4.98×10^{-10} to 6.38×10^{-10} S.cm^{-1} , respectively).^[25] Park et al. performed high temperature measurements (> 430 K) and estimated, by interpolation, a room temperature electrical conductivity close to 2.4×10^{-12} S.cm^{-1} for $\text{Na}_3\text{V}_2(\text{PO}_4)_2\text{F}_{1.4}\text{O}_{1.60}$ ($y = 1.60$).^[26] Similarly, it is reported that the O^{2-} for F^- substitution improves the ionic conductivity of Na^+ and stabilizes the structure during the overcharge.^[27,28] Dealing with electrochemical performances, Qi et al. reported that higher rate capability is achieved for $\text{Na}_3\text{V}^{3+}_2(\text{PO}_4)_2\text{FO}_2$ (y

= 2) compared to $\text{Na}_3\text{V}^{4+}_2(\text{PO}_4)_2\text{F}_3$ ($y = 0$), possibly due to a faster Na^+ diffusion^[29]. However, few is known whether a mixed $\text{V}^{3+}/\text{V}^{4+}$ pristine composition could be of benefit or not for high rate charge/discharge.

In this work, four compounds of the $\text{Na}_3\text{V}^{3+}_{2-y}\text{V}^{4+}_y(\text{PO}_4)_2\text{F}_{3-y}\text{O}_y$ series, and possessing different O/F ratios, were synthesized using a solvothermal reaction. Their chemical composition was carefully determined by X-ray diffraction and a combination of spectroscopic techniques, whereas microscopy imaging confirmed that the same spherical morphology was obtained for all the members of the series. Electrochemical impedance spectroscopy analyses and electrochemical tests were performed, also at high rates and upon long range cycling, to investigate the influence of the chemical composition of NVPFO_y on their electronic conductivity and energy storage performance. Moreover, these analyses were carried out on electrodes with high mass loading of active material (88 wt.%) prepared without any carbon coating, with the aim to better determine the oxygen content impact on the electrochemical properties in conditions as close as possible to practical conditions.

2. Experimental Section

2.1 Materials preparation

A series of $\text{Na}_3\text{V}^{3+}_{2-y}\text{V}^{4+}_y(\text{PO}_4)_2\text{F}_{3-y}\text{O}_y$ (NVPFO_y) compounds was prepared via an easy one-step solvothermal reaction. First, appropriate amounts (molar ratio) of vanadium acetylacetonate (Sigma-Aldrich; $\geq 97\%$) ($\text{V}(\text{acac})_3$), vanadyl acetylacetonate (Sigma-Aldrich; $\geq 97\%$) ($\text{VO}(\text{acac})_3$), sodium fluoride (Prolabo; 98%) and phosphoric acid (VWR; 85%) were introduced into 100 mL Teflon Parr autoclave containing an equimolar mixture water/ethanol (**Table 1**) and stirred for 10 min. Then, the mixtures were heated in an oven at 180°C during 10 h. Finally, polycrystalline powders, presenting various shades of green (**Figure 1**), were retrieved through complete cleaning by centrifugation (firstly with ethanol, then with distilled water) and a full drying in vacuum at 60°C overnight. As detailed in **Table 1**, stoichiometric amount of NaF and H_3PO_4 were used according to reference^[30] in order to obtain nanospherical morphology, which shows extremely promising performance. The phase obtained from the precursors' molar ratio of 0.25 $\text{VO}(\text{acac})_2$: 0.75 $\text{V}(\text{acac})_3$ possesses, according to the Rietveld refinement and spectroscopic studies, similar composition to $\text{NVPFO}_{0.8}$ (see **Figure 2** for more details). Thus, due to a rather oxidative environment, these synthesis conditions would lead to a minimum average oxidation state of 3.4 for vanadium in the final product, with at least 0.8

V^{4+} among 2 per formula unit. The vanadium oxidation during solvothermal synthesis was already observed in our previous work.^[30]

Table 1: Detailed molar ratios and synthesis conditions used to prepare all the studied materials.

Type	$VO(acac)_2$	$V(acac)_3$	NaF	H_3PO_4	Ethanol solution	T	Time
$NVPFO_{0.80}$	0	1	1.5	1	50%	180°C	10H
$NVPFO_{1.35}$	0.50	0.50	1.5	1	50%	180°C	10H
$NVPFO_{1.60}$	0.75	0.25	1.5	1	50%	180°C	10H
$NVPFO_2$	1	0	1.5	1	50%	180°C	10H

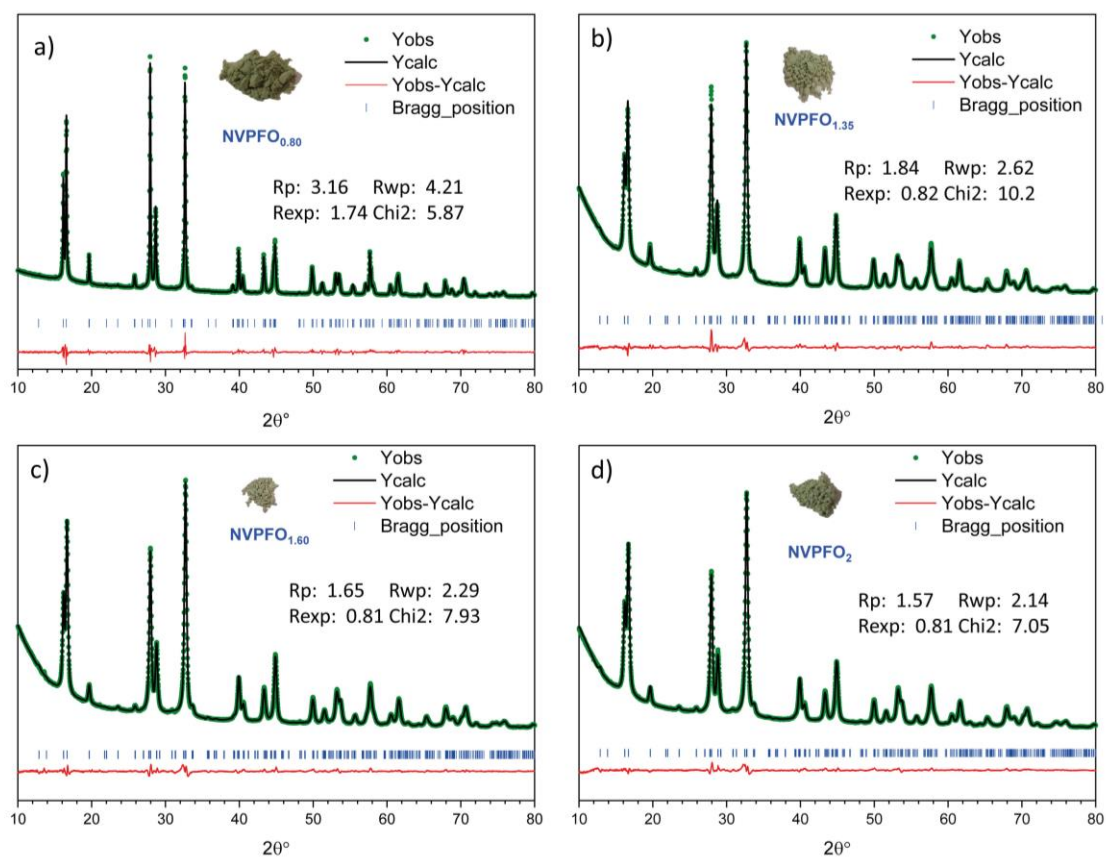


Figure 1: Rietveld refinement of the XRD data for the different compounds $NVPFO_{0.80}$, $NVPFO_{1.35}$, $NVPFO_{1.60}$ and $NVPFO_2$.

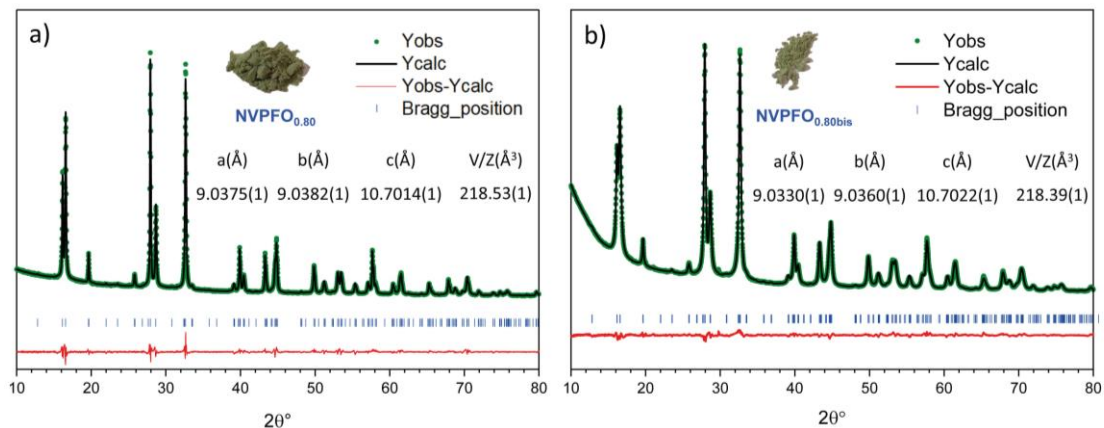


Figure 2: The cell parameter comparison of the NVPFO0.80 and NVPFO0.80bis.

2.2 Characterization techniques

X-ray diffraction (XRD) measurements were carried out by using a BRUKER D8 ADVANCE diffractometer in θ - θ configuration, equipped with a Cu $K_{\alpha 1,2}$ X-ray source. The acquisition was performed in the 2θ angular range of $10^\circ - 140^\circ$ with a step size of 0.0197° . The Rietveld refinements were performed using the FullProf Suite.^[31]

Scanning electron microscopy (SEM) images were taken without any conductive deposition by a Hitachi Model S-3400N microscope and SEM-FEG (field emission gun) images were obtained on a Hitachi SU-70 microscope. Transmission electron microscopy (TEM) analyses were carried out with the Tecnai spirit G2 microscope. The powder was sonificated for 20 min in ethanol before the analysis.

Fourier transformed infrared (FT-IR) spectra were recorded by using a PerkinElmer Spectrum 400 FT-IR/FT-NIR spectrometer in the wavenumber range of $400 - 4000 \text{ cm}^{-1}$ (mid-IR). Raman spectra were obtained with a confocal LabRAM HR Evolution micro-spectrometer from Horiba, using a 633 nm laser source. They were collected in the range $100 - 1300 \text{ cm}^{-1}$, using a 10.6 mm (NA 0.5) focal length lens and with an acquisition time of 20 s and 40 accumulations. Additional acquisitions were performed between $450 - 600 \text{ cm}^{-1}$ and $850 - 1100 \text{ cm}^{-1}$ in order to reach a better resolution in these wavenumber ranges.

X-ray photoelectron spectroscopy (XPS) spectra were collected through Omicron Argus X-ray photoelectron spectrometer with a 280 W electron beam power and a monochromated AlK α

radiation source (1486.6 eV). The binding energy scale were calibrated from the C 1s peak at 284.8 eV.

The transport properties of $\text{Na}_3\text{V}_2(\text{PO}_4)_2\text{F}_{3-y}\text{O}_y$ compounds were investigated by electrochemical impedance spectroscopy (EIS). For this purpose, the powders were mixed with camphor (about 2 wt.%) and pressed into pellets of 13 mm diameter applying 200 MPa by means of a uniaxial press. Subsequently, the pellets were heat-treated at 250 °C for 1 h under air to evaporate the camphor. Then, gold electrodes were sputtered on their parallel opposite faces to ensure electrical contact. EIS measurements were performed at OCP using a Solartron 1260 Impedance/Gain Phase Analyzer in the frequency range between 1 MHz and 1 Hz, with an applied root mean square voltage of 100 mV, 10 points per decade and 20 measures per point. The measurements were carried out in air, using a two-probe sample-holder and over the temperature range of 100 - 300 °C.

The electrochemical performances of the materials were tested in CR2032-type coin cells. The positive electrodes were prepared as a mixture containing the active material, carbon black, and polyvinylidene fluoride (PVDF) in NMP (N-Methyl-2-pyrrolidone) with the ratio of 88/7/5 (by wt.%). After an hour of thorough mixing, the black ink was casted as a flat film by doctor blade on an aluminum foil and dried in an oven at 60°C. Disks were cut, then pressed under 5 tons and finally dried overnight at 80°C under vacuum. A homemade electrolyte containing a 1 mol.L⁻¹ solution of NaPF₆ (Strem Chemical; 99%) in ethylene carbonate and dimethyl carbonate (EC/DMC = 1/1) with 2 wt.% of fluoroethylene carbonate (FEC) was used for all the electrochemical tests. The assembled cells were cycled in galvanostatic mode, from C/20 to 2C cycling rates between 2.5 and 4.3 V vs. Na⁺/Na. The theoretical capacity being 128 mAh.g⁻¹ (corresponding to 2 Na⁺ reversibly extracted from NVPFO₂), the rate C/20 corresponds to the exchange of 2 Na⁺ in 20 hours. The electrodes have a typical active mass loading around 6 mg.cm⁻². The tests were performed several time and **Figure 3** shows an example of reproducibility.

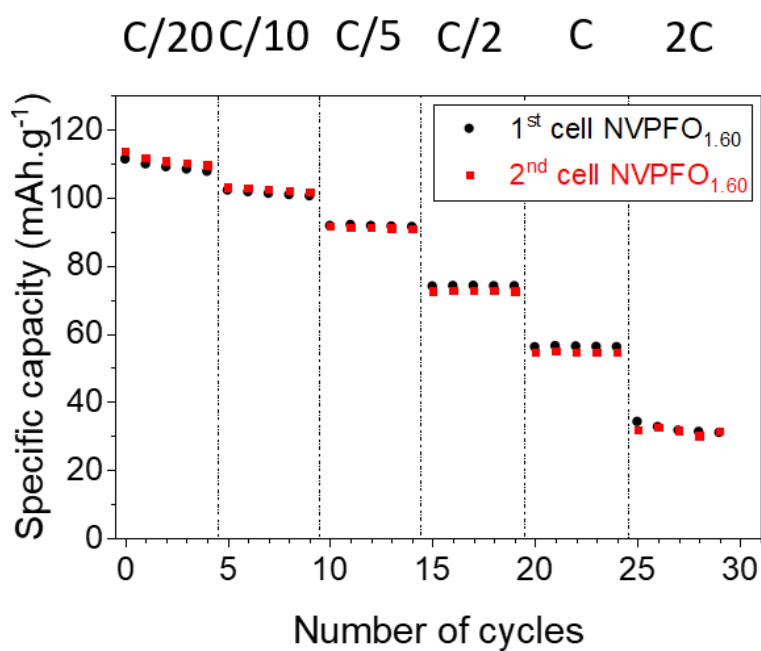


Figure 3: Illustration of the reproducibility of the electrochemical performance obtained for NVPFO_{1.6}.

3. Results and discussions

3.1 Structural and morphological characterization

The XRD patterns obtained for all the compounds synthesized by solvothermal method indicate the successful syntheses of pure phases that belong to the solid solution Na₃V³⁺_{2-y}V⁴⁺_y(PO₄)₂F_{3-y}O_y (**Figure 4a**). The lattice parameters determined from the Rietveld refinement are reported in **Table 2** and the results of these refinements are presented in **Figure 1**.^[9,27]

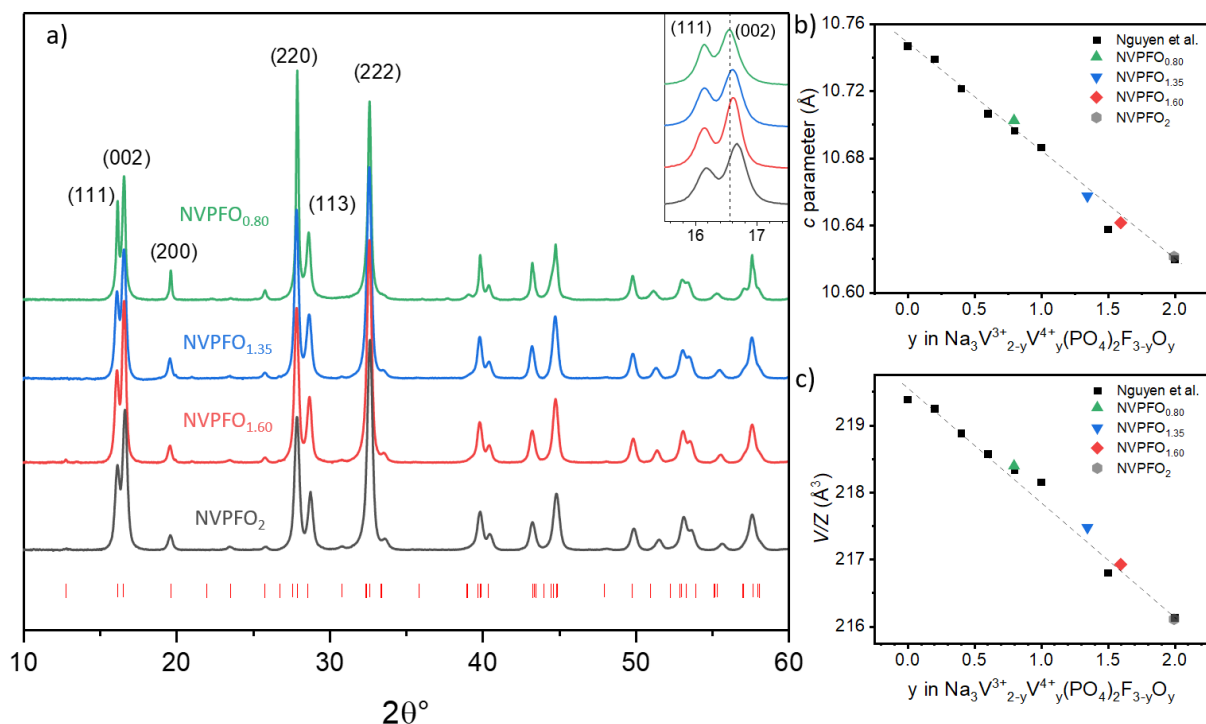


Figure 4: a) X-ray diffraction patterns of NVPFO_{0.80}, NVPFO_{1.35}, NVPFO_{1.60} and NVPFO₂. The red ticks correspond to theoretical positions as reported in ICDD 00-066-0322. b-c) Comparison of the *c*-cell parameters and V/Z values (V/Z being the cell volume per formula unit) as determined for these four compounds by Rietveld refinement with those already reported in ref^[27]. The dash lines give the evolution of these parameters as a function of *y* in Na₃V₂(PO₄)₂F_{3-y}O_y.

The structure of Na₃V₂(PO₄)₂F₃ is built from V₂O₈F₃ bi-octahedral units linked to each other by phosphate groups to generate a 3D framework. Each bi-octahedron is composed by two VO₄F₂ octahedra sharing a common fluorine. The fluorine atoms are in apical positions (along the *c*-axis) and the oxygen atoms in the equatorial plane.^[32] The substitution of F⁻ anions that are pointing outside the bi-octahedra by O²⁻ induces vanadium oxidation from V³⁺ to V⁴⁺ and formation of short covalent V=O bonds (~1.6 Å) instead of long ionic V-F bonds (~2 Å) (**Figure 5**). Thus, as reported by Park et al. and Nguyen et al., it is possible to determine the chemical composition of the NVPFO_y family members from the *c*-cell parameter and V/Z value, the cell volume per formula unit, due to their linear evolution within the solid solution Na₃V³⁺_{2-y}V⁴⁺_y(PO₄)₂F_{3-y}O_y (0 ≤ *y* ≤ 2).^[8,27] For instance, in **Figure 4a** (insert), it can be clearly seen a shift of the (002) reflection to higher 2θ values when increasing the ratio of V⁴⁺/V³⁺ precursors, which according to Bragg law leads to a decrease of the *c*-cell parameter. Based on the lattice parameters determined from Rietveld refinement, the syntheses lead to the preparation of Na₃V³⁺_{1.20}V⁴⁺_{0.80}(PO₄)₂F_{2.20}O_{0.80} (NVPFO_{0.80}), Na₃V³⁺_{1.65}V⁴⁺_{1.35}(PO₄)₂F_{1.65}O_{1.35} (NVPFO_{1.35}), Na₃V³⁺_{1.40}V⁴⁺_{1.60}(PO₄)₂F_{1.40}O_{1.60} (NVPFO_{1.60}) and Na₃V⁴⁺₂(PO₄)₂FO₂ (NVPFO₂) (**Table 2**, **Figures 4a-c** and **Figure 1**). It can be noticed that due to the oxidative character of the solvent (water/ethanol mixture), V³⁺ is partially oxidized during the synthesis, which leads

to compounds with vanadium mean oxidation state higher to the one expected from the reactants' ratio. This oxidation in hydrothermal conditions was already reported in several works and highlights the difficulty to precisely control the chemical composition within this polyanionic series, especially for F⁻-rich members.^[30,33–35]

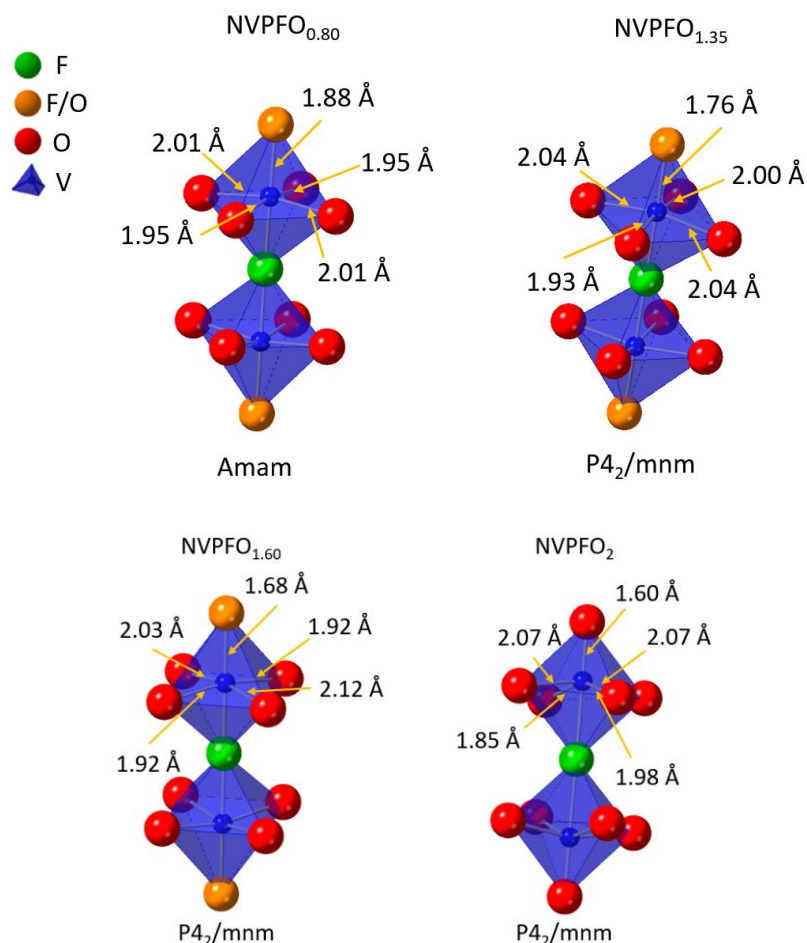


Figure 5: Illustration of bond distance changes from the composition $NVPFO_{0.80}$ to the composition $NVPFO_2$. Table 2: Lattice parameters obtained by the Rietveld refinement of the XRD patterns, coherent domain sizes along the (220) and (002) directions, and chemical compositions determined for all the $NVPFO_y$ materials.

	a (Å)	b (Å)	c (Å)	V/Z (Å ³)	(220) (nm)	(002) (nm)	Formula	Space group
$NVPFO_{0.80}$	9.0375(1)	9.0382(1)	10.7014(1)	218.53(1)	44	34	$Na_3V^{3+}_{1.20}V^{4+}_{0.80}(PO_4)_2F_{2.20}O_{0.80}$	Amam
$NVPFO_{1.35}$	9.0347(1)	9.0347(1)	10.6571(2)	217.47(1)	28	23	$Na_3V^{3+}_{0.65}V^{4+}_{1.35}(PO_4)_2F_{1.65}O_{1.35}$	P4 ₂ /mnm
$NVPFO_{1.60}$	9.0299(1)	9.0299(1)	10.6412(2)	216.92(1)	25	26	$Na_3V^{3+}_{0.40}V^{4+}_{1.60}(PO_4)_2F_{1.40}O_{1.60}$	P4 ₂ /mnm
$NVPFO_2$	9.0215(1)	9.0215(1)	10.6210(3)	216.10(1)	22	24	$Na_3V^{4+}_2(PO_4)_2FO_2$	P4 ₂ /mnm

Infrared spectroscopy measurements reveal the presence of bands at $\sim 675\text{ cm}^{-1}$ and $\sim 1050\text{ cm}^{-1}$ corresponding to the vibrations of V-O bonds and phosphate groups respectively. Additionally, bands associated to vanadyl bonds are observed for the four compounds with the systematic presence of sharp signals at 915 and 940 cm^{-1} , characteristic of the vibrations generated by covalent V=O bonds (**Figure 6a**). Nguyen et al. suggested that the presence of these two $\nu_{V=O}$

bands is consistent with two different local environments for the vanadyl bond.^[27] The band at 940 cm⁻¹ (Band B) would correspond to a V⁴⁺=O bond with a V³⁺-F bond opposite along the axis of the bi-octahedral unit, whereas the one at 915 cm⁻¹ (Band A) involves the presence of two V⁴⁺=O bonds in the same bi-octahedra. Thus, the relative intensity observed between the two V=O vibration bands tends to match the variation of the vanadium average oxidation state determined by X-ray diffraction: the higher the Band A (V⁴⁺-V⁴⁺ bi-octahedra) / Band B (V⁴⁺-V³⁺ bi-octahedra) ratio, the higher the vanadium mean oxidation state (**Figure 6b**).

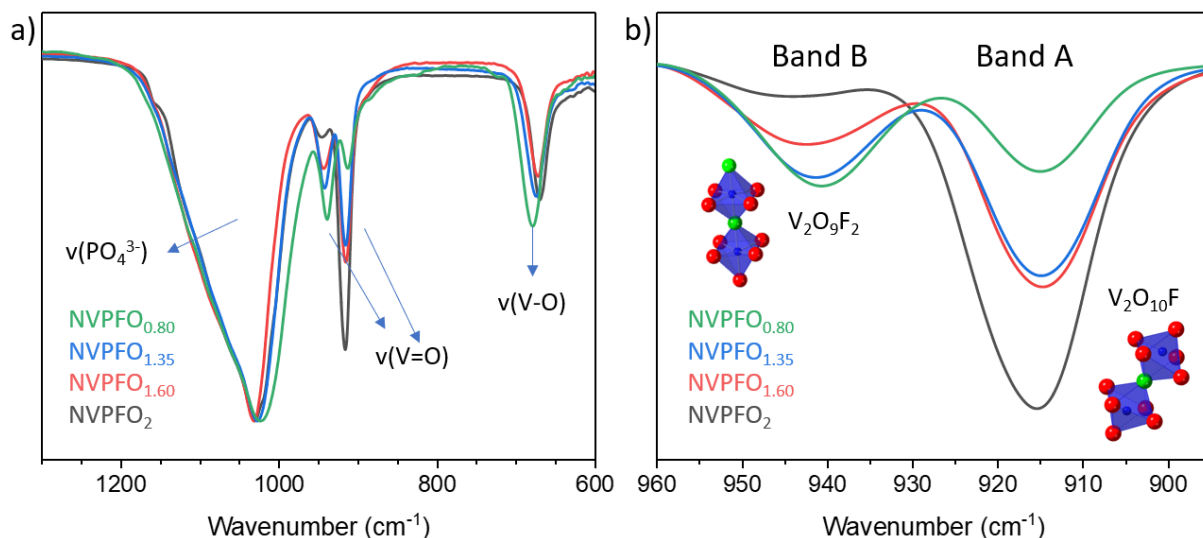


Figure 6: FTIR spectroscopy analyses: a) The intensities of the spectra were normalized to the signal attributed to vibration of phosphate groups at ~1050 cm⁻¹ to highlight the evolution of the intensities attributed to the vibrations of V=O bond, depending on its concentration, and b) Focus between 890 and 960 cm⁻¹ to better observe the evolution of V=O bonds.

Complementary to Infrared spectroscopy, Raman spectroscopy is another efficient method to probe the local environments within materials.^[36] To the best of our knowledge, this technique is, up to now, used mainly to characterize graphitization degree of the carbon coating applied on NVPFO_y to enhance the electronic conductivity of the electrode material,^[22,37] whereas it could give precious information on vanadium environment. **Figure 7** exhibits the Raman spectra of all compounds obtained with a 633 nm laser source between 100 and 1300 cm⁻¹, while **Figure 8** shows the enlarged areas that will be discussed here more in details. On **Figure 8a**, the signal around 940 cm⁻¹ is attributed to V=O vibrations whereas the broad band at ~1050 cm⁻¹ is characteristic of phosphate vibrations.^[38,39] This attribution is supported by absence of band at 940 cm⁻¹ for Na₃V₂(PO₄)₂F₃ which does not possess vanadyl bond (**Figure 9**). Within NVPFO_y series, the intensity of the peak at 940 cm⁻¹ increases continuously with the concentration of vanadyl bonds as determined from X-ray diffraction, which demonstrates the possibility to estimate whether the composition is V³⁺-rich or V⁴⁺=O-rich by analyzing the

intensity ratio between the vanadyl and phosphate bands (**Table 3**). Additionally, the low intensity signal at 900 cm^{-1} (* in the **Figure 8a**) observed for $\text{NVPFO}_{0.80}$ disappears for the more oxidized compositions, which may reveal a change in structure symmetry. This is in perfect agreement with the work of Nguyen et al., which reported a clear orthorhombic distortion in NVPFO_y series for $y \leq 1$, whereas a tetragonal symmetry could be considered for phases with $y > 1$.^[27] Besides, the intensity of the vibration peak generated by V-O bond (**Figure 8b**) is gradually decreasing and accompanied by a right ward shift from 525 to 532 cm^{-1} with the increase of vanadium mean oxidation state.^[38] Indeed, this linear displacement can be perfectly explained by the increase of $\text{V}^{n+}\text{-O}$ bond covalency upon metal ion oxidation and the position of the band can thus be used to estimate the vanadium mean oxidation state and hence the chemical formula within the solid solution (**Figure 10**). Thus, Raman spectroscopy appears to be an efficient complementary technique to confirm the $\text{Na}_3\text{V}^{3+}_{2-y}\text{V}^{4+}_y(\text{PO}_4)_2\text{F}_{3-y}\text{O}_y$ ($0 \leq y \leq 2$) composition deduced by X-ray diffraction and although theoretical calculations would be needed to attribute each signal, it could help to alleviate doubts about symmetry in this series.^[9]

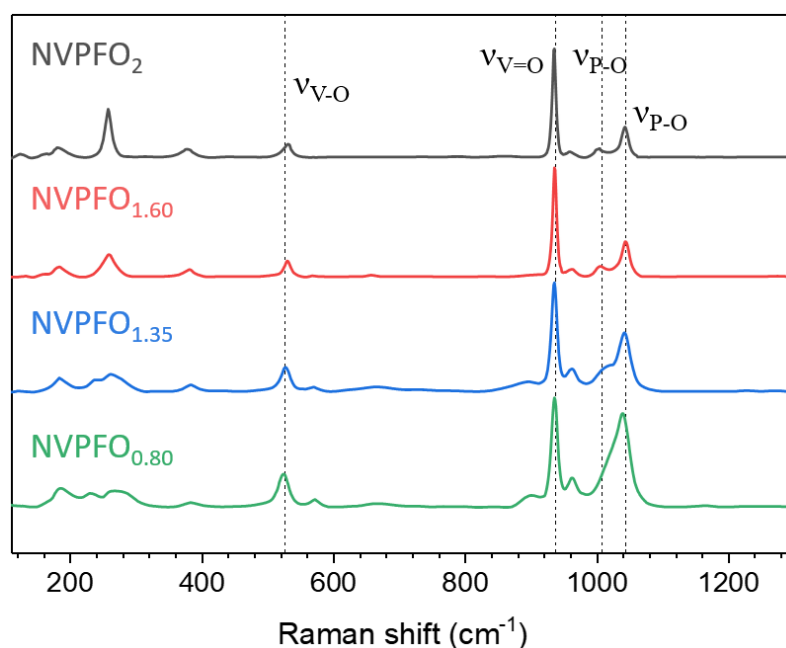


Figure 7: All Raman spectra from 100 cm^{-1} to 1300 cm^{-1} . The spectra were corrected to remove the background. The absence of signal after 1150 cm^{-1} confirmed the absence of carbon in the compounds (absence of D-band, see Figure S5)^[22].

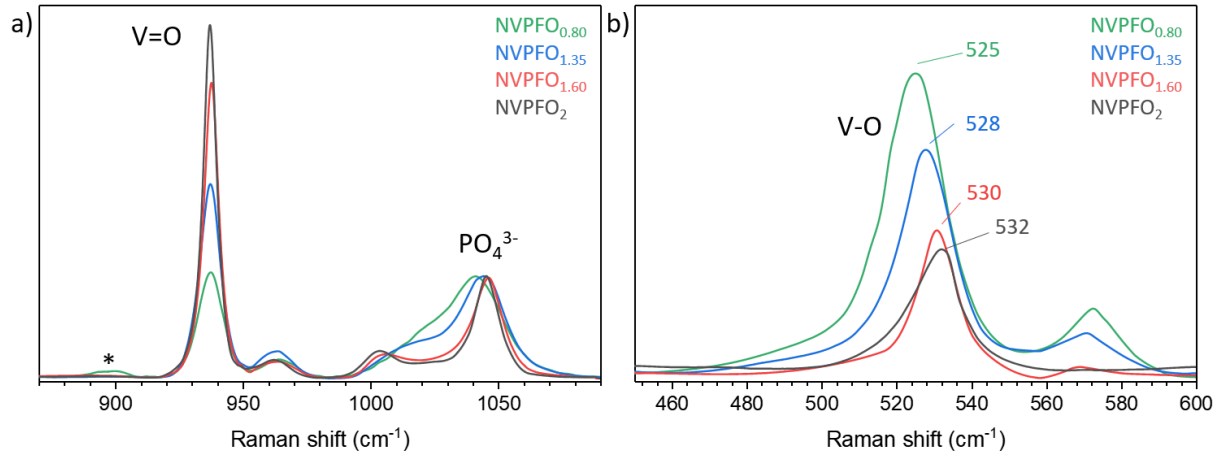


Figure 8: a) Raman spectra collected for $\text{NVPFO}_{0.80}$, $\text{NVPFO}_{1.35}$, $\text{NVPFO}_{1.60}$ and NVPFO_2 : The intensities of the spectra were normalized to the signal attributed to the vibration of phosphate groups at $\sim 1050 \text{ cm}^{-1}$ to highlight the evolution of the intensity attributed to the vibration of V=O bond depending on its concentration, and b) focus between 450 and 600 cm^{-1} to observe the evolution of the band attributed to vibration of V-O bonds.

Table 3: Absolute intensity ratios of the V=O vibration and PO_4^{3-} vibration for all the materials studied

	$\text{NVPFO}_{0.80}$	$\text{NVPFO}_{1.35}$	$\text{NVPFO}_{1.60}$	NVPFO_2
Intensity ratio	1.04	1.90	2.90	3.49
$v_{\text{V=O}} : v_{\text{P-O}}$				

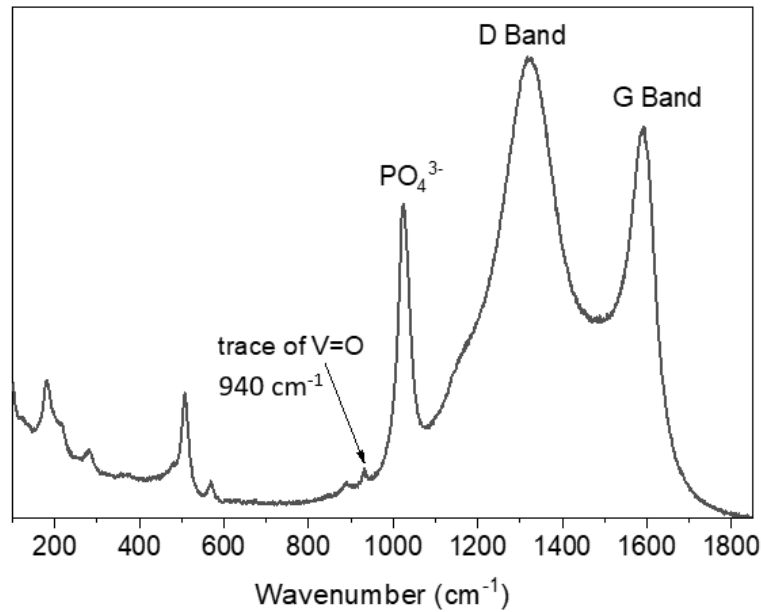


Figure 9: Raman spectrum of carbon-coated $\text{Na}_3\text{V}_2(\text{PO}_4)_2\text{F}_3$ ($y=0$). The electrode material was synthesized through the method proposed by Hall et al.^[40] This spectrum confirms the absence of carbon in the series studied in this work (absence of signal around $1150\text{-}1300 \text{ cm}^{-1}$ as shown in Figure S4) and endorses the attribution of the signal at 940 cm^{-1} to vanadyl bond vibration since this signal nearly disappears for $\text{Na}_3\text{V}^{3+}_2(\text{PO}_4)_2\text{F}_3$. Indeed, as reported previously, a small amount of vanadyl type defects is always identified, which explains the detection of the signal at 940 cm^{-1} .^[27]

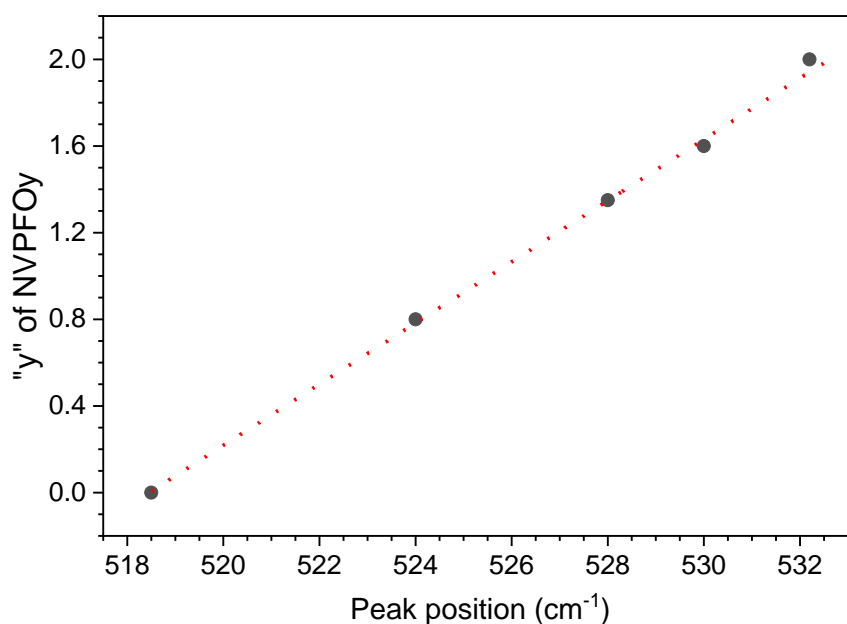


Figure 10: y of $\text{NVPF}O_y$ variation versus the migration of the V-O peak position. The linear fitting in red clearly demonstrates a linear shift of the peak according to the chemical formulae. The position of V-O band for NVPF ($y=0$) is measured from the spectrum reported Figure 9.

SEM images (**Figure 11**) show that all the compounds unveil micrometric aggregates made of spherical particles with diameters distributed between 200 and 400 nm and present very similar particle size distribution according to the histogram illustrating the statistics of particle sizes (**Figure 12**). Complementary analyses by high resolution SEM-FEG reveal that these spherical particles are mainly composed of smaller spheres of about 30 nm diameter. Furthermore, HRTEM analyses (**Figure 13**) and spacing measurements of lattice fringes confirm that these primary particles of 20-30 nm are $\text{NVPF}O_y$ crystallites, which perfectly fits to the crystallite size determined by XRD using Scherrer equation (**Table 2**).

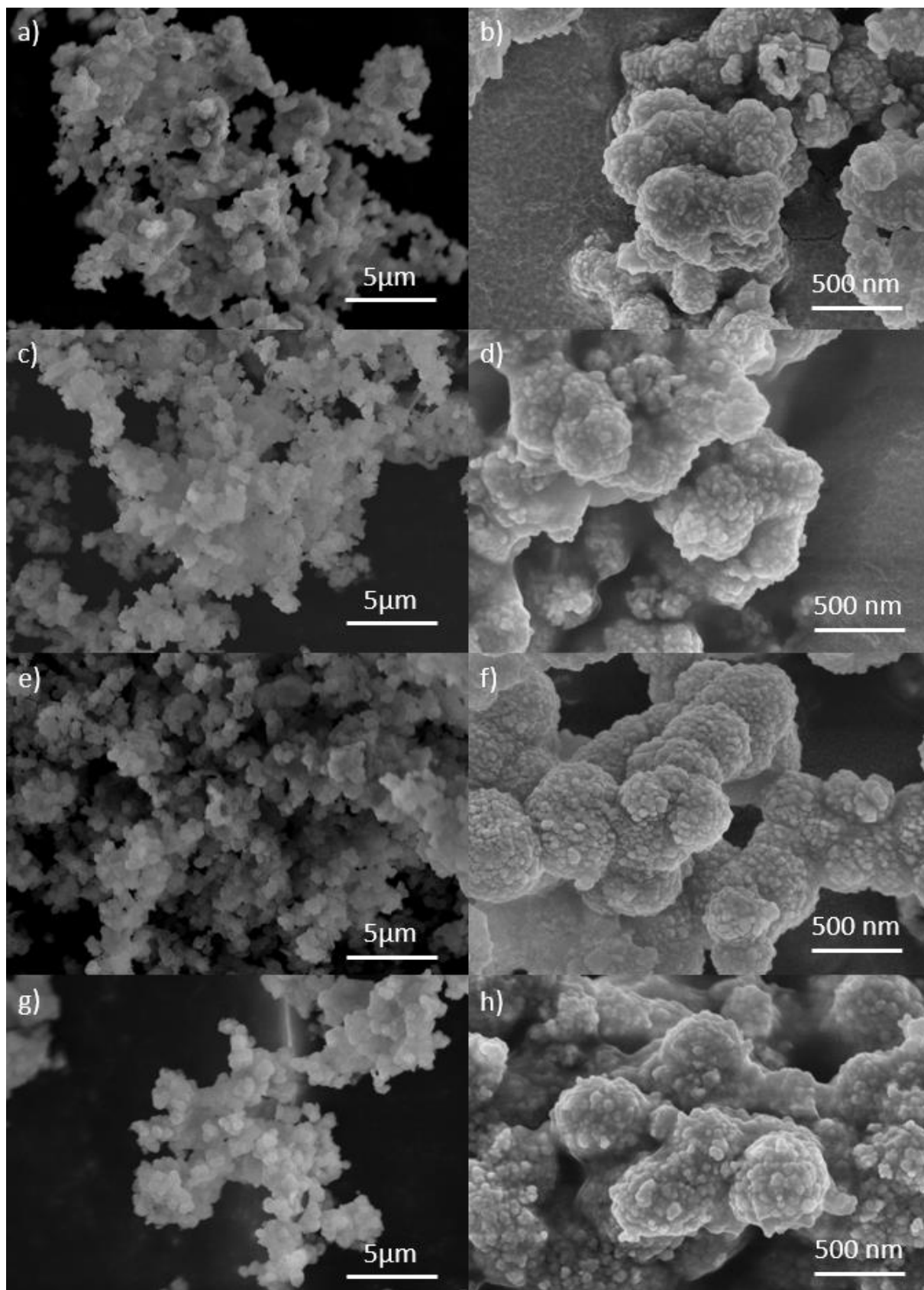


Figure 11: SEM images of a) $\text{NVPFO}_{0.80}$, c) $\text{NVPFO}_{1.35}$, e) $\text{NVPFO}_{1.60}$, and g) NVPFO_2 . The corresponding SEM-FEG images of b) $\text{NVPFO}_{0.80}$, d) $\text{NVPFO}_{1.35}$, f) $\text{NVPFO}_{1.60}$, and h) NVPFO_2 .

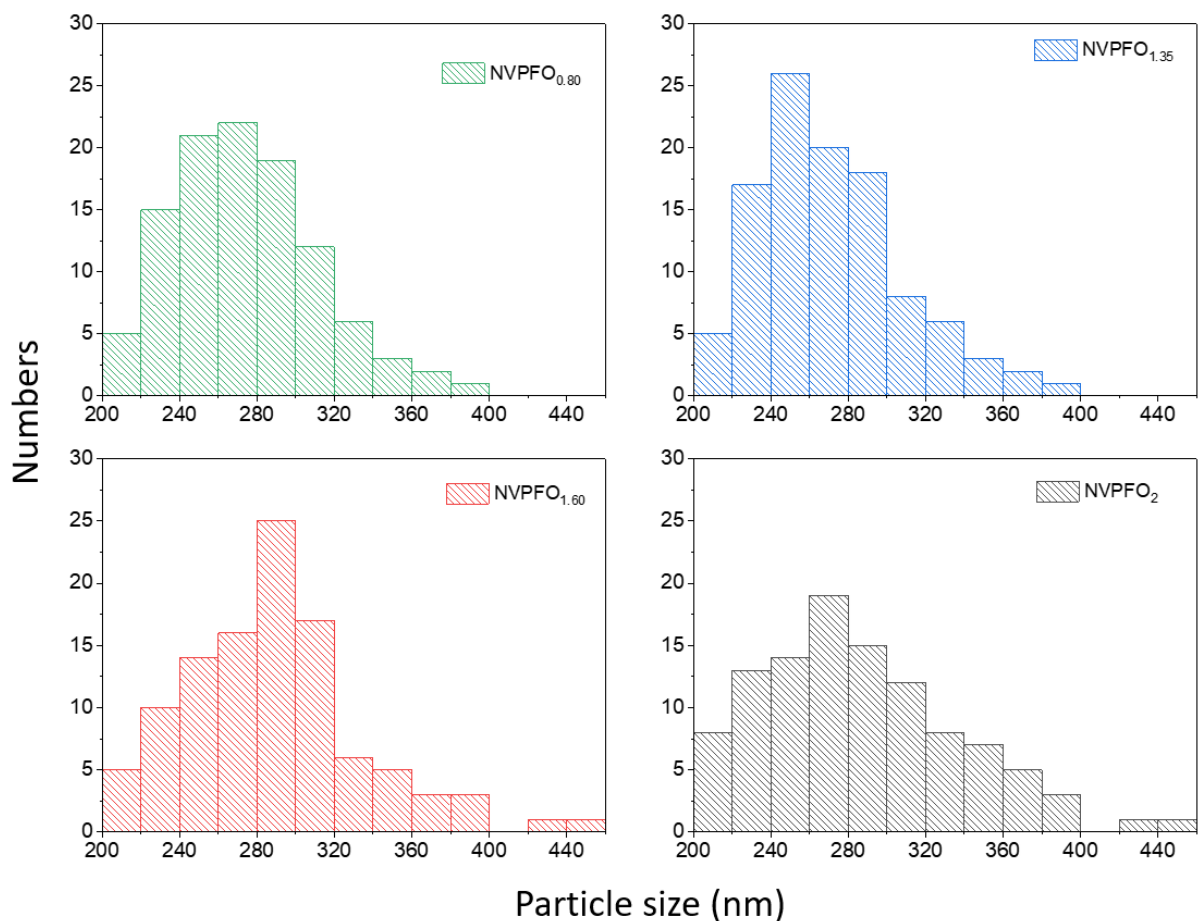


Figure 12: Statistics of particle size distribution for all the materials. For each material 106 particles were measured.

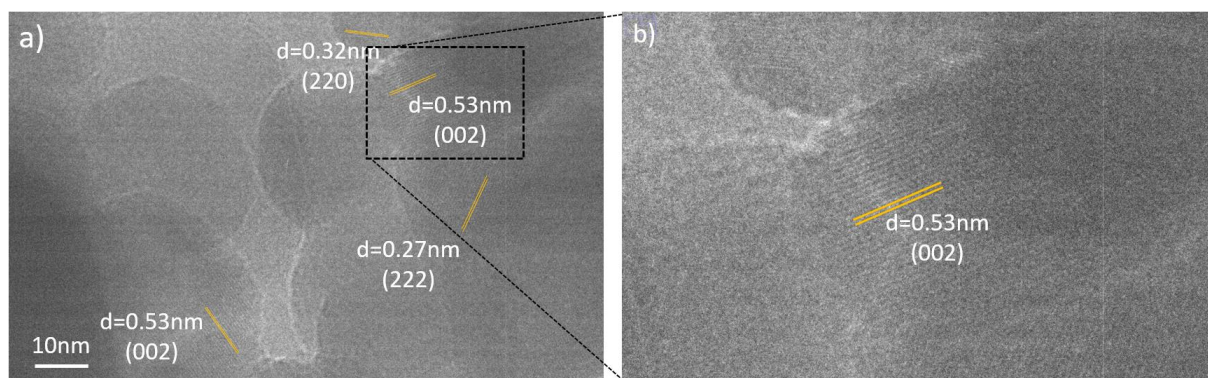


Figure 13: a) and b) HRTEM for NVPFO_{1.35}

The different lattice fringes observed by HRTEM (0.27 nm (222), 0.32 nm (220), 0.53 nm (002) and 0.55 nm (111)) confirm the good crystallinity of the small primary particles of NVPFO_{1.35}. Moreover, the observation of various crystalline lattices (**Figure 13**) suggests the absence of preferential orientation and may weight in favor of crystallite's spherical shape. Similar results are obtained for the rest of the NVPFO_y series and are presented in **Figure 14**.

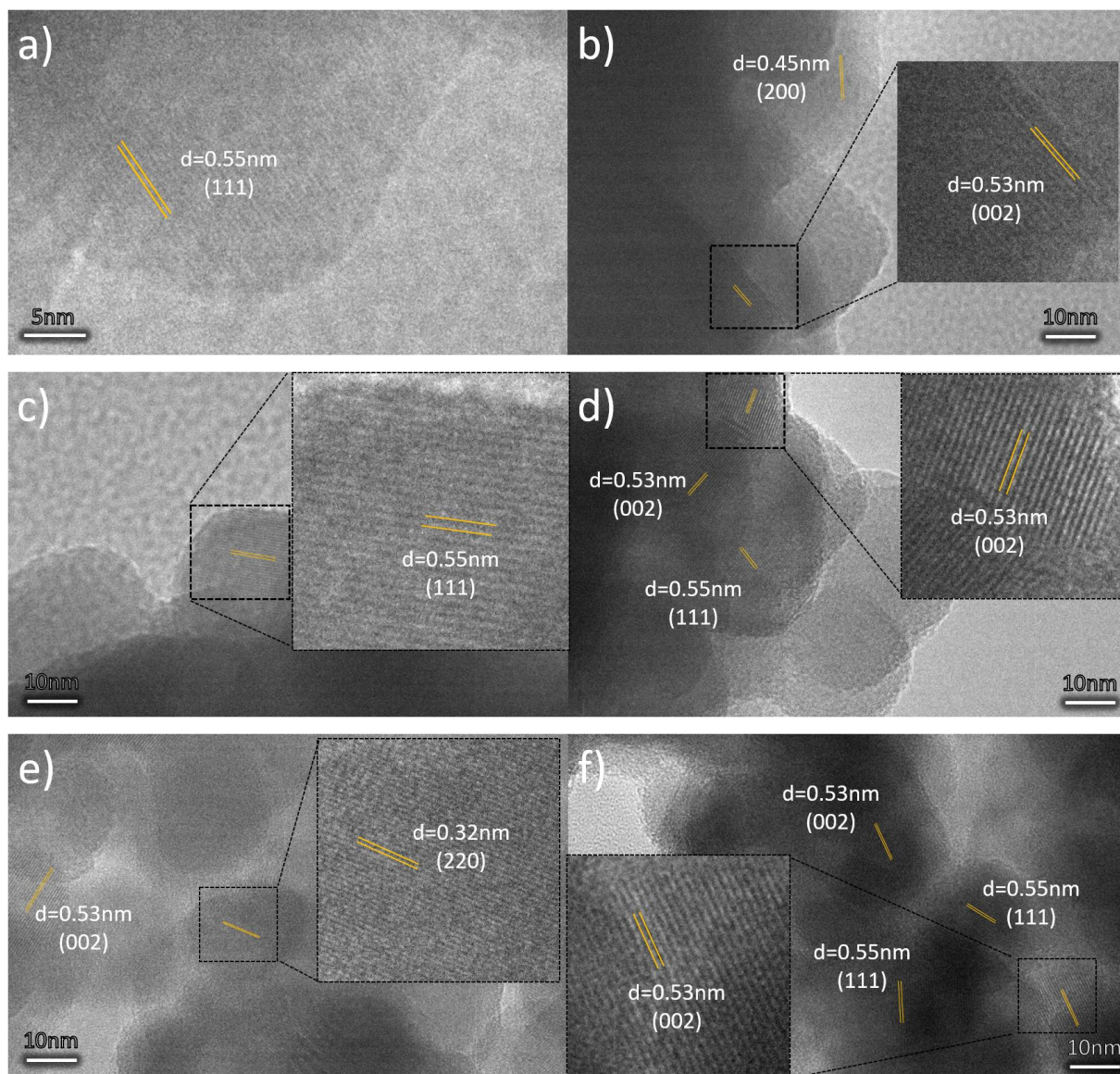


Figure 14: HRTEM images of a-b) $\text{NVPFO}_{0.80}$ c-d) $\text{NVPFO}_{1.60}$ and e-f) NVPFO_2

3.2 Transport and Electrochemical properties

Thus, this NVPFO_y series of compounds presenting different chemical compositions while preserving a very similar particle's size and morphology represents an ideal case to study the effect of the oxygen content on the transport properties. A first analysis of the complex impedance data of the NVPFO_y compounds reveals quite similar electrical behavior in all studied samples. **Figure 15** depicts complex impedance plots for each compound recorded at 200 °C. Here, the complex impedance data (Z^*) have already been normalized regarding the shape factor (l/A , thickness over area) of each sample according to the relation $Z_s^* = Z^* \cdot A/l$, given rise to the specific impedance (Z_s^*). Due to very similar particle's size and morphology, this approach allows to compare the samples directly and their overall electrical resistivity can be promptly read at the low-frequency intercept of the impedance data on the axis representing

the real part of specific impedance (Z_s').^[41] A common feature in the electrical behavior is the distorted semi-circles probably caused by a jointly contribution of grains and grain boundaries at high and middle-frequency ranges, respectively.^[25,42] The deconvolution of these contributions applying a suitable equivalent circuit to fit the impedance data unveils that the grain impedance response is about one order of magnitude higher than that of the grain boundaries (**Figure 16**).^[25] However, the deconvolution procedure is not possible for all samples nor all temperatures of measurements due to the very similar electrical relaxation processes of grains and grain boundaries. In this case, only the overall impedance of the samples can be determined but it should be mostly controlled by the impedance of the grains (**Figure 16**). As shown in **Figure 15**, NVPFO_{1.35} compound presents the highest conductivity among the NVPFO_y compounds investigated. Another similar aspect in the impedance response obtained at 200 °C for this series, is the absence of polarization phenomenon (ion-blocking effect) characterized by a steep increase of the imaginary part of impedance (Z_s'') at low-frequency range, which is the main signature of an ionic conductor.^[43,44] Therefore, it is reasonable to assume that the nanometric NVPFO_y compounds investigated here are mostly electronic conductors at this temperature (200 °C).

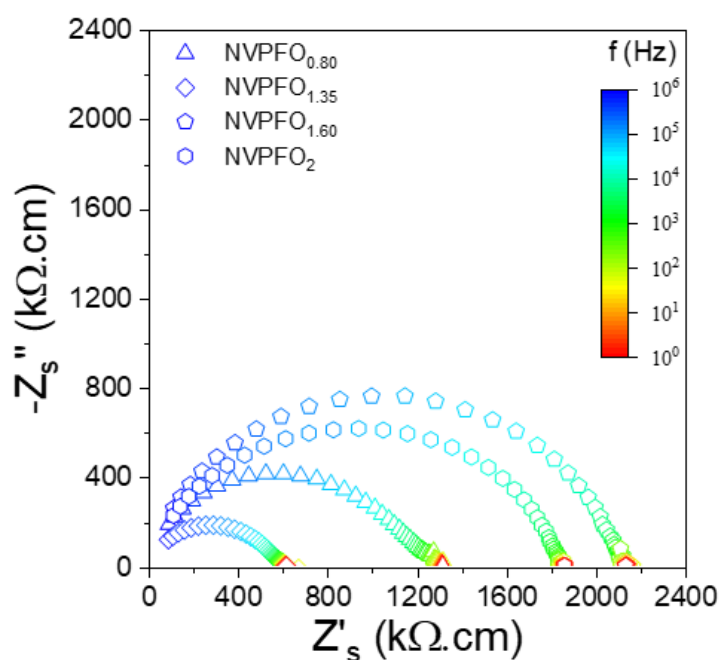


Figure 15: EIS analyses of the $\text{Na}_3\text{V}_2(\text{PO}_4)_2\text{F}_{3-y}\text{O}_y$ compounds performed at 200°C, namely, NVPFO_{0.80}, NVPFO_{1.35}, NVPFO_{1.60} and NVPFO₂. The complex impedance data shown here have already been normalized regarding the shape factor of each sample for comparison purposes.

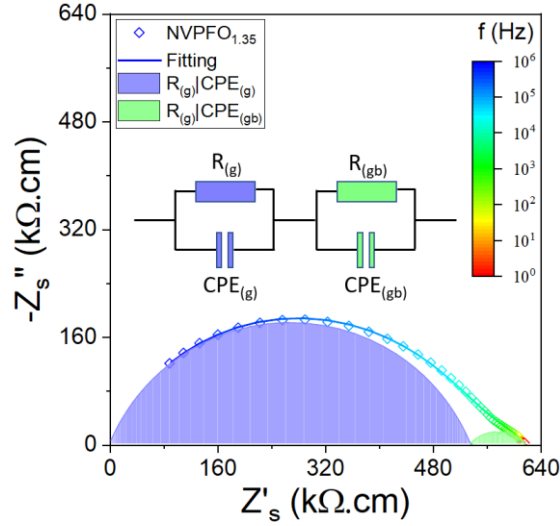


Figure 16: Deconvolution of grain and grain boundary contributions of complex impedance data recorded at 200 °C for NVPFO_{1.35} sample. The complex impedance data shown here have already been normalized regarding the shape factor of the sample. The shown equivalent circuit is used for impedance data fitting. Acronyms *R* and *CPE* represent resistive and constant phase elements whereas *g* and *gb* stand for grain and grain boundary contributions, respectively. The obtained effective specific capacitances or the relative permittivity are typical from grain (1.4 pF.cm⁻¹ or 15) and grain boundary (470 pF.cm⁻¹ or 5329^[45]) contributions.

However, when the electrical behavior of these compounds is analyzed as function of the temperature, a more intricate impedance behavior is unfolded. **Figure 17** displays the dependence on frequency of the real (Z'_s) and imaginary ($-Z''_s$) parts of the impedance of the series of materials in the whole range of temperatures investigated (100-300°C). Again, the electrical resistivity can be promptly read on the left y axis at the low frequency plateau because the impedance data have been normalized by the shape factor of each sample. With respect to the imaginary part of impedance, the $-Z''_s$ peak shifts to higher frequencies as the temperature is increased. This behavior is due to the drop in the electrical resistivity with the temperature which increases the relaxation frequency (f) of the semicircle that is inversely proportional to the resistance (R) and capacitance (C) of the sample ($f \sim 1/RC$).^[41] Although in the middle-frequency range (10-100Hz), interferences of the electrical wiring in the measurement room increases the dispersion of measurements, the overall trend of evolution is not influenced. Nonetheless, the most important feature that differs the samples is spotted at low-frequency range (1-10 Hz), where the polarization phenomenon should arise.^[43,44] NVPFO_{0.80} (**Figure 17a**) and NVPFO_{1.35} (**Figure 17b**) samples present a typical behavior of an electronic conductor, since from the high-frequency $-Z''_s$ peak, the imaginary part, decreases continuously with the frequency, until low frequencies, for all temperatures. No polarization is observed, as expected if the main charge carriers in the sample are electrons, when the electrodes used in the measurement (gold in this case) present electronic conductivity several orders of magnitude higher than the analyzed sample. On the other hand, NVPFO_{1.60} (**Figure 17c**) and NVPFO₂

(**Figure 17d**) samples exhibit at high temperatures an increasing of $-Z_s''$ in the low-frequency range, evidencing a polarization behavior. This feature is typical for an ion conductor, and it is caused by the blockage of mobile ions in the metallic electrodes. Therefore, at high temperatures ($> 180^\circ\text{C}$) the ionic contribution for these two samples is likely to be as important as the electronic one.^[43,44]

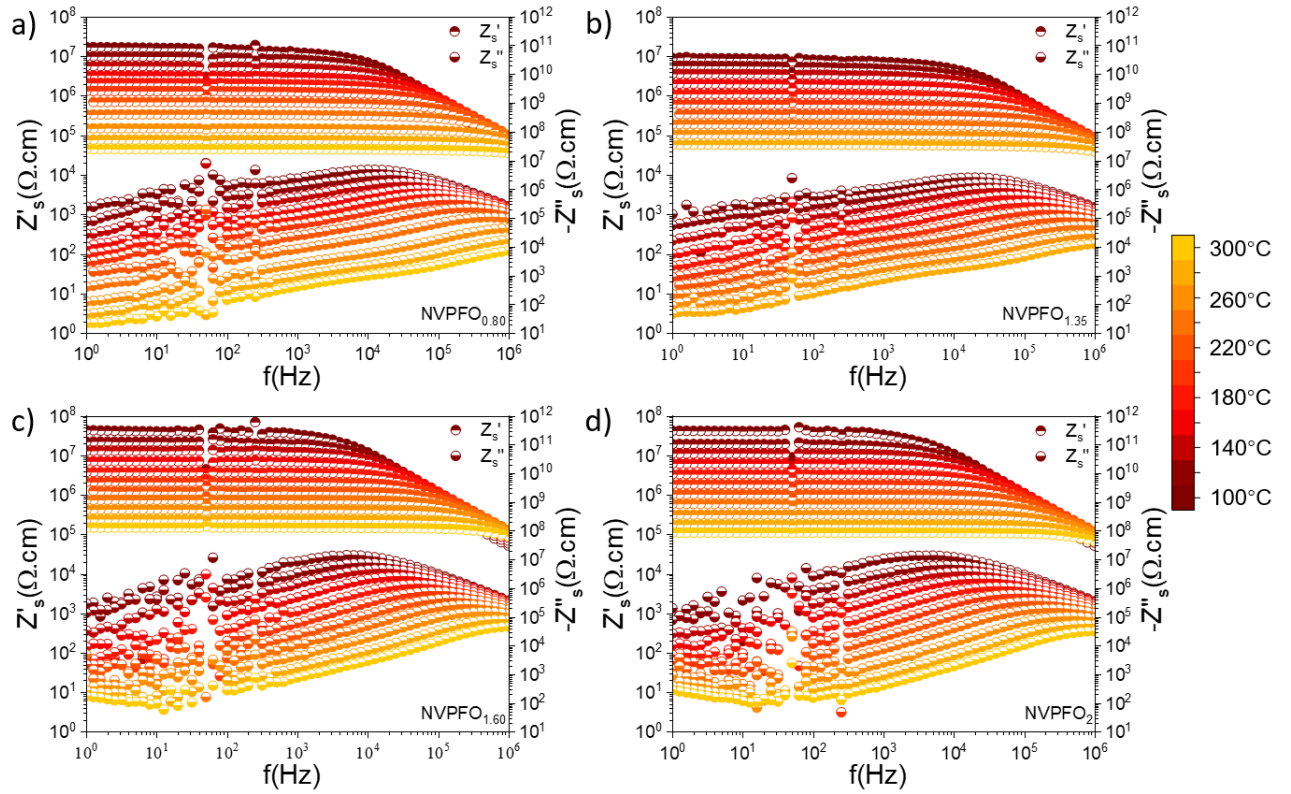


Figure 17: Dependence on frequency of the real (half up filled symbol) and imaginary (half down filled symbol) parts of impedance of the a) $\text{NVPFO}_{0.80}$, b) $\text{NVPFO}_{1.35}$, c) $\text{NVPFO}_{1.60}$ and d) NVPFO_2 samples. The real and imaginary parts of impedance have already been normalized regarding the shape factor of the samples.

Finally, the electrical conductivity dependence on the inverse of temperature (**Figure 18**) is plotted applying the linearized form of the Arrhenius-like relation (Eq. 1), which is mostly used for ionic conductors but sometimes also applied for electronic conductors.^[44,46,47]

$$\sigma T = \sigma_0 \exp\left(\frac{-E_a}{k_B T}\right) \quad (1)$$

Here, σ_0 is the pre-exponential factor, E_a is the activation energy for ionic conductivity, k_B is the Boltzmann constant, and T is the absolute temperature. Following this methodology, the linear fit slope is proportional to the activation energy, which therefore provides access to the energetic barrier of the mechanism responsible for the electrical transport.^[47] **Figure 18** exhibits the Arrhenius-like plots of the overall electrical conductivity of the NVPFO_y compounds

investigated in this work as well as those reported in literature by Broux et al.^[25] Overall, the dependence of the electrical conductivity on temperature for the nanometric NVPFO_y compounds seems to present a low ($T < 180^\circ\text{C}$) and a high ($T > 180^\circ\text{C}$) temperature regime due to the dominating electronic transport at low temperatures and the mixed ionic-electronic conducting behavior at higher temperatures. The activation energy of the high temperature regime is considerably higher than the low-temperature one for all nanometric NVPFO_y samples (**Table 4**). However, when the samples are compared at the same temperature regime, the activation energy of nanometric NVPFO_y samples are nearly the same if uncertainties are considered (**Table 4**). Even though, the NVPFO_{1.35} sample presents the highest overall conductivity in the entire investigated temperature range. Two activation energy regimes have been also visualized for the micrometric NVPFO_y compounds reported in literature.²⁵ Nevertheless, the transition on this last case takes place around the temperature of 130°C and it has been attributed to a structural change induced by a mobility of the Na⁺ ions on a ring. Besides, in the low temperature regime, the micrometric NVPFO_y compounds reported in literature show much lower conductivity and higher activation energy than the nanometric NVPFO_y compounds studied in this work (**Table 4**).^[25] Indeed, NVPFO_{1.35} possess, at 100°C , an electrical conductivity nearly two order of magnitude higher than the micrometric NVPFO_y reported in the literature, which clearly demonstrates the advantage of particle's downsizing to improve electrical transport. Besides, these micrometric NVPFO_y compounds were mostly ionic conductors on the contrast with the nanometric compounds of this investigation. Nonetheless, the high temperature polarization phenomenon spotted in the impedance response of samples NVPFO_{1.60} (**Figure 17c**) and NVPFO₂ (**Figure 17d**) is in good agreement with the literature data, once above 180°C the ionic conductivity of the micrometric compounds is in the same order of magnitude of the electronic conductivity of the nanometric compounds reported here. As a final point, NVPFO_{1.35} and NVPFO_{0.80} exhibit the best electronic conductivities within the investigated series. Besides the fact that V³⁺/V⁴⁺ bi-octahedra does not form continuous chains throughout the structure, which probably hinder the electronic transport, the decreasing of the particles size to nanometric scale are likely to created additional energy levels on the band gap of these compounds due to surface disorder, fostering the electronic transport. After the high temperature impedance measurement, the NVPFO_{1.35} was characterized again with XRD to check for its structure. The invariant peaks' position confirms that the material retains its original crystal structure (**Figure 19**).

Table 4: Activation energy for all the materials with temperature dividing point at $\sim 180^\circ\text{C}$ for nanometric NVPFO_y ($y = 0.8, 1.35, 1.6$ and 2) and at $\sim 130^\circ\text{C}$ for micrometric NVPFO_y ($y = 1$ and 0)^[25].

Samples		NVPFO_2	$\text{NVPFO}_{1.60}$	$\text{NVPFO}_{1.35}$	$\text{NVPFO}_{0.80}$	NVPFO_1	NVPFO_0
Activation	Low-T	0.43(3)	0.43(3)	0.42(3)	0.42(1)	0.87(1)	0.97(5)
Energy (eV)	High-T	0.69(2)	0.65(2)	0.69(2)	0.79(4)	0.69(1)	0.77(1)

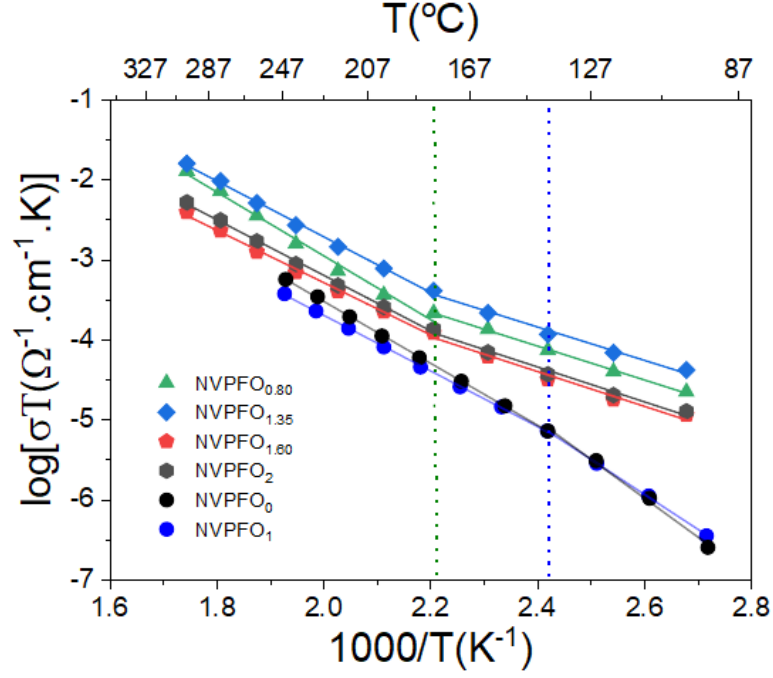


Figure 18: Arrhenius-like plots of the dependence of the overall electrical conductivity of NVPFO_y compounds on the inverse temperature. Black and deep blue points correspond to literature data for $\text{Na}_3\text{V}_2(\text{PO}_4)_2\text{F}_3$ and $\text{Na}_3\text{V}_2(\text{PO}_4)_2\text{F}_2\text{O}$ sintered samples of micrometric grain size, respectively^[25].

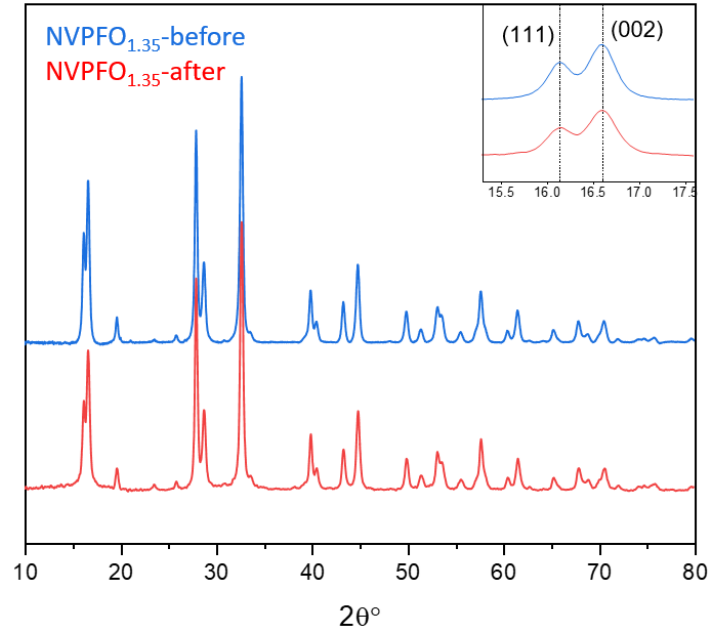


Figure 19: Comparison of the XRD patterns collected for $\text{NVPFO}_{1.35}$, before and after the impedance measurement, with inset of enlarged (111) and (002) peaks.

Figures 20a-d demonstrate the Galvanostatic charge and discharge curves profiles of the 1st, 2nd, and 5th cycles obtained at C/20 in the potential range 2.5-4.3 V vs. Na⁺/Na. The four electrode materials present two “pseudo-plateaus” of equivalent length characteristic of the NVPFO_y family^[7,8,33,48] and a very low polarization indicating a good diffusion process of Na⁺ ions within the materials and the electrodes. All of them exhibit a first charge capacity of 126 mAh.g⁻¹ indicating the extraction of two Na⁺ (the theoretical capacity for NVPFO₂ is 130 mAh.g⁻¹) and show comparable first cycle irreversible capacity losses, leading thus to similar reversible capacities around 114 mA.h.g⁻¹. As it could be expected from the mixed V³⁺/V⁴⁺ initial composition, the electrochemical curves of NVPFO_{0.80}, NVPFO_{1.35} and NVPFO_{1.60} are composed by two rather slopping “plateaus” indicating that the Na⁺ intercalation/de-intercalation is mainly driven by monophasic reaction.^[27] On the other hand, NVPFO₂ exhibits more horizontal plateaus that suggests the presence of biphasic reaction upon the reversible desodiation.^[49] These different reaction mechanisms are supported by the corresponding first derivative curves presented in **Figure 20e** which reveals intense and narrow peaks for NVPFO₂ versus rather broad and less defined peaks for the other members of the series.^[23] From a practical point of view, the solid solution reaction usually leads to a smoother potential jump between the two pseudo-plateaus and could attenuate the heat generated due to the phase transition that is detrimental to long-term cycling.^[49,50] Meanwhile, it could be observed that the average redox potential of the second pseudo-plateau tends to rise with the increase of fluorine content due to the more ionic character of V-F bond compared to V=O one (**Figure 20e**). On the other hand, the average oxidation potential for the lower voltage plateau is less affected by composition and could not be linked to the fluorine content (**Figure 20e**).

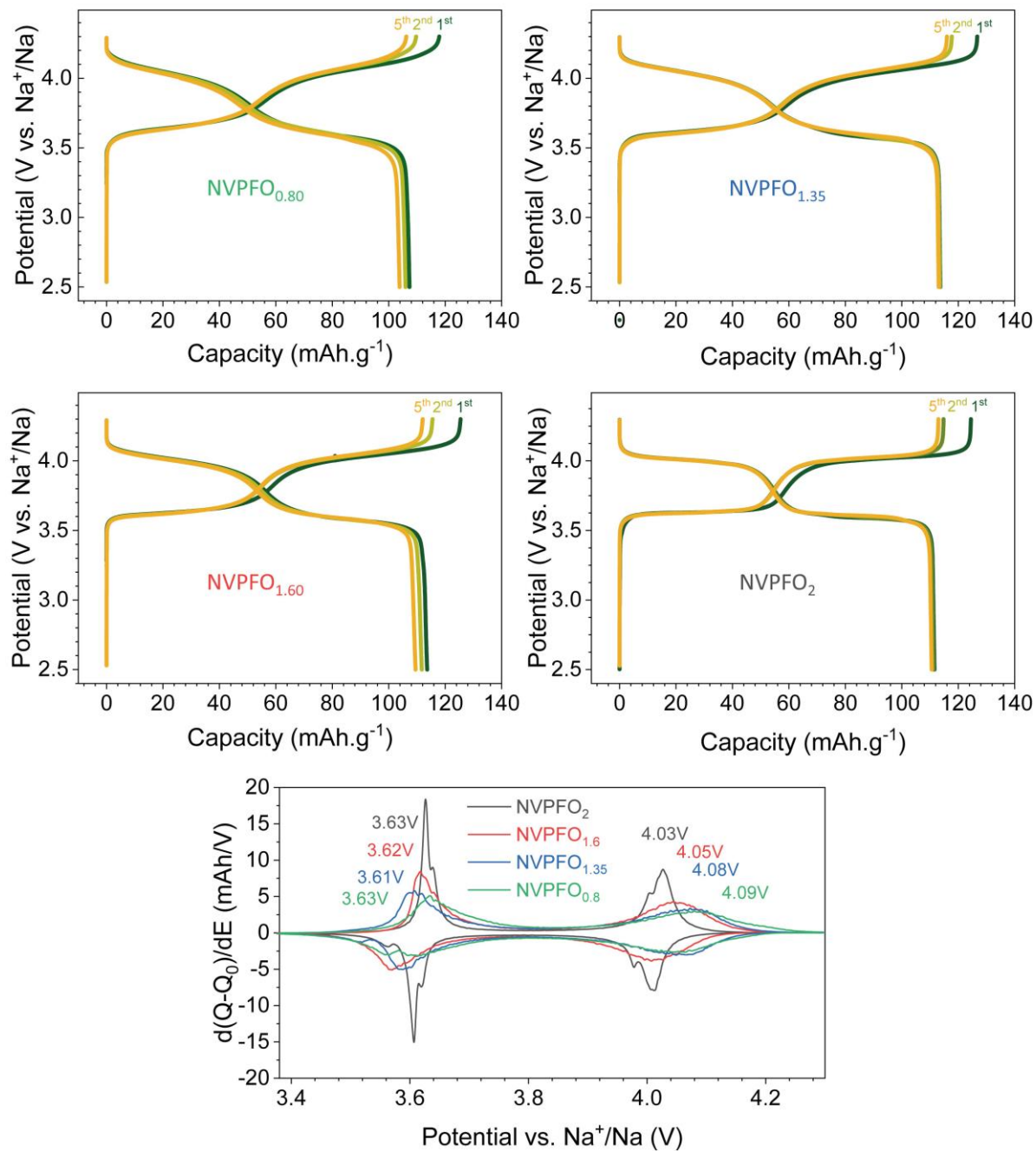


Figure 20: a-d) Galvanostatic charge and discharge curves obtained in half-cell for all the NVPFO_y electrode materials at the cycling rate of C/20. All the electrodes were prepared with 88 wt.% of active materials, 7 wt.% of carbon black, and 5 wt.% of PVDF in order to better observe the effect of composition change of NVPFO_y. e) First derivative curves corresponding to the 5th cycle performed at C/20.

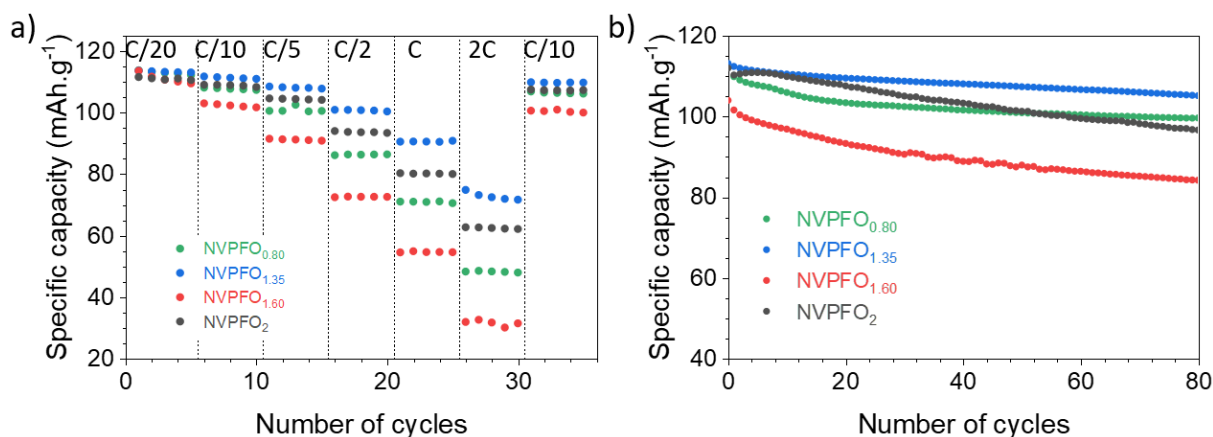


Figure 21: a) Specific (reversible) capacities obtained for all the studied electrode materials at various C-rates from C/20 to 2C. b) Long term cycling performance of all the NVPFO_y materials prepared without any carbon coating at C/10. It represents cycling time between 1200 and 1500 hours depending on the electrode materials.

Although at low current densities all the electrode materials could nearly reach their theoretical capacities, the capacity retention differs within the series when the charges/discharges become faster (**Figure 21a** and **Figure 22**). For example, NVPFO_{1.35} exhibits ~90 mAh.g⁻¹ at 1C while only 80 mAh.g⁻¹, 70 mAh.g⁻¹ and 50 mAh.g⁻¹ are measured for NVPFO₂, NVPFO_{0.80} and NVPFO_{1.60} respectively. There is no straightforward trend between the rate performance and the oxygen content within the series, however, as for the transport properties it can be noticed that $\text{Na}_3\text{V}^{3+}_{0.65}\text{V}^{4+}_{1.35}(\text{PO}_4)_2\text{F}_{1.65}\text{O}_{1.35}$ exhibits the best results and $\text{Na}_3\text{V}^{3+}_{0.40}\text{V}^{4+}_{1.60}(\text{PO}_4)_2\text{F}_{1.40}\text{O}_{1.60}$ the worst ones. Nevertheless, a direct correlation between electronic conductivity of the pristine materials and C-rate performances is not possible since the galvanostatic measurements involve Na⁺ extraction/insertion and hence, the composition as well as the vanadium mean oxidation state change upon cycling. It is important to notice that after testing the rate performance, the full capacity is recovered at C/10 for all series, which indicates that all the materials reveal good structural stability and the capacity drop at higher current density is only due to kinetic limitations.

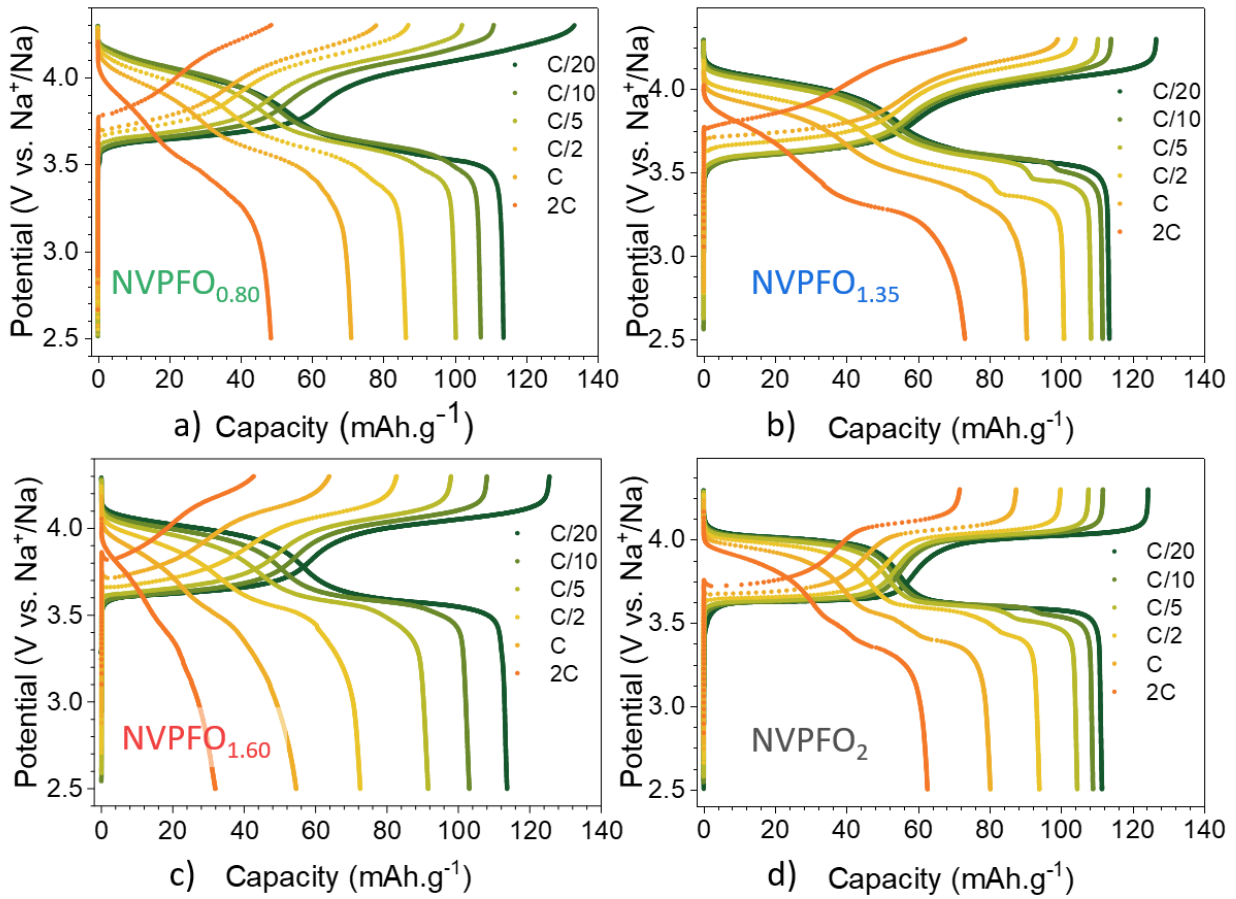


Figure 22: Charge and discharge curves of NVPFO_y materials at different cycling rates, from C/20 to 2C.

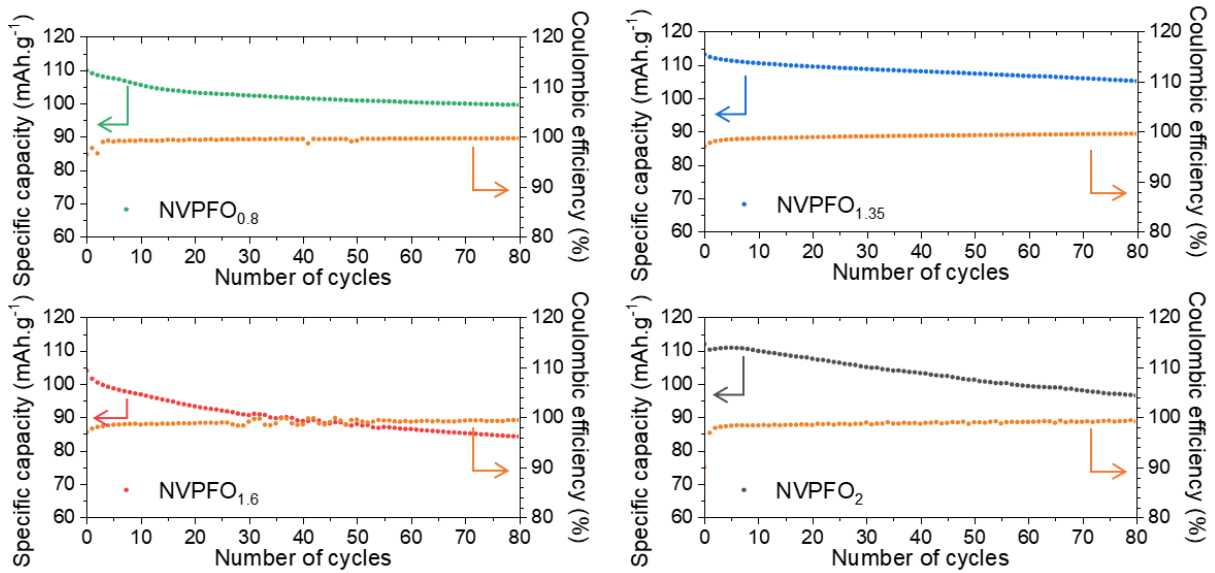


Figure 23: Long range cycling performance (specific capacity and Coulombic efficiency) at C/10 for NVPFO_y

As represented **Figure 21b** and **Figure 23**, all the materials exhibit a capacity retention higher than 80% after 80 cycles at C/10 and an initial specific capacity higher than 100 mAh.g^{-1} . Once again, $\text{Na}_3\text{V}^{3+}_{0.65}\text{V}^{4+}_{1.35}(\text{PO}_4)_2\text{F}_{1.65}\text{O}_{1.35}$ demonstrates the best performance with an initial specific capacity of 115 mAh.g^{-1} and a capacity retention rate of 91% after 80 cycles which also

confirms the good structural stability upon long-term cycling. Finally, considering the active mass rich formulation and high mass loading of the electrode as well as the absence of carbon-coating, NVPFO_{1.35} with nano-spherical morphology reveals extremely favorable energy storage performance.

4. Conclusion

To summarize, four compounds that belong to the $\text{Na}_3\text{V}^{3+}_{2-y}\text{V}^{4+}_y(\text{PO}_4)_2\text{F}_{3-y}\text{O}_y$ ($0 < y < 2$) family, and possessing different O^{2-}/F^- ratios (“y” parameter), were obtained through a low temperature solvothermal synthesis. They all possess the same nanospherical morphology that represents an ideal series to investigate the impact of the oxygen content (or $\text{V}^{3+}/\text{V}^{4+}$ initial ratio) on the electronic conductivity as well as on the energy storage performance. The structure of each compound was determined carefully by Rietveld refinement and the O^{2-} content trend was confirmed by Infrared spectroscopy. Besides, Raman spectroscopy is for the first time reported for this series and reveals to be an efficient characterization technique to estimate the oxygen content within the $\text{Na}_3\text{V}^{3+}_{2-y}\text{V}^{4+}_y(\text{PO}_4)_2\text{F}_{3-y}\text{O}_y$ family. This work also shows the great impact of particle downsizing on the electronic conductivity that is improved by more than two order of magnitude compared to their bulk counterpart. Moreover, it was demonstrated that a high amount of mixed $\text{V}^{3+}/\text{V}^{4+}$ bi-octahedra most probably favors the electronic mobility. In this work, $\text{Na}_3\text{V}^{3+}_{1.65}\text{V}^{4+}_{1.35}(\text{PO}_4)_2\text{F}_{1.65}\text{O}_{1.35}$ ($y = 1.35$) and $\text{Na}_3\text{V}^{3+}_{1.20}\text{V}^{4+}_{0.80}(\text{PO}_4)_2\text{F}_{2.20}\text{O}_{0.80}$ ($y = 0.80$) show the lowest electronic resistivity with $9 \times 10^6 \, \Omega \cdot \text{cm}$ and $2 \times 10^7 \, \Omega \cdot \text{cm}$ respectively at 100°C . $\text{Na}_3\text{V}^{3+}_{1.65}\text{V}^{4+}_{1.35}(\text{PO}_4)_2\text{F}_{1.65}\text{O}_{1.35}$ ($y = 1.35$) also presents the best rate capacity retention and stability upon long-term cycling. Finally, this study reveals that the intrinsic properties of NVPFO_y materials could be improved by tailoring the oxygen content and mixed $\text{V}^{3+}/\text{V}^{4+}$ polyanionic electrode material should be further investigated to reach the best energy storage performance.

Acknowledgements

The authors thank the Materials Physics and Chemistry Doctoral School (ED397) of Sorbonne University for the funding as well as the financial support of Région Nouvelle Aquitaine, of the French National Research Agency (STORE-EX Labex Project ANR-10-LABX-76-01) and of the European Union’s Horizon 2020 research and innovation program under grant agreement No 875629 (NAIMA project).

References

- [1] “European Climate Law | Climate Action,” can be found under https://ec.europa.eu/clima/policies/eu-climate-action/law_en, **n.d.**
- [2] Y. S. Hu, S. Komaba, M. Forsyth, C. Johnson, T. Rojo, *Small Methods* **2019**, 3, 2–3.
- [3] I. Hasa, S. Mariyappan, D. Saurel, P. Adelhelm, A. Y. Kuposov, C. Masquelier, L. Croguennec, M. Casas-Cabanas, *J. Power Sources* **2021**, 482, 228872.
- [4] J. M. Tarascon, *Joule* **2020**, 4, 1616–1620.
- [5] T. Broux, F. Fauth, N. Hall, Y. Chatillon, M. Bianchini, T. Bamine, J. B. Leriche, E. Suard, D. Carlier, Y. Reynier, L. Simonin, C. Masquelier, L. Croguennec, *Small Methods* **2019**, 3, 1–12.
- [6] G. Yan, R. Dugas, J.-M. Tarascon, *J. Electrochem. Soc.* **2018**, 165, A220–A227.
- [7] M. Bianchini, P. Xiao, Y. Wang, G. Ceder, *Adv. Energy Mater.* **2017**, 7, 1700514.
- [8] Y. U. Park, D. H. Seo, H. Kim, J. Kim, S. Lee, B. Kim, K. Kang, *Adv. Funct. Mater.* **2014**, 24, 4603–4614.
- [9] M. Bianchini, N. Brisset, F. Fauth, F. Weill, E. Elkaim, E. Suard, C. Masquelier, L. Croguennec, *Chem. Mater.* **2014**, 26, 4238–4247.
- [10] Y. Zhu, E. Xu, J. Zhang, J. Quan, H. Wang, Z. Sun, Y. Jiang, *ACS Appl. Energy Mater.* **2021**, 4, 3952–3961.
- [11] L. Li, X. Liu, L. Tang, H. Liu, Y. G. Wang, *J. Alloys Compd.* **2019**, 790, 203–211.
- [12] H. Li, X. Zhang, Z. Zhao, Z. Hu, X. Liu, G. Yu, *Energy Storage Mater.* **2020**, 26, 83–104.
- [13] C. Shen, H. Long, G. Wang, W. Lu, L. Shao, K. Xie, *J. Mater. Chem. A* **2018**, 6, 6007–6014.
- [14] F. Li, Y. Zhao, L. Xia, Z. Yang, J. Wei, Z. Zhou, *J. Mater. Chem. A* **2020**, 8, 12391–12397.
- [15] H. Jin, J. Dong, E. Uchaker, Q. Zhang, X. Zhou, S. Hou, J. Li, G. Cao, *J. Mater. Chem. A* **2015**, 3, 17563–17568.

- [16] J. Xun, Y. Zhang, H. Xu, *Inorg. Chem. Commun.* **2020**, *115*, 107884.
- [17] J. Olchowka, L. H. B. Nguyen, T. Broux, P. Sanz Camacho, E. Petit, F. Fauth, D. Carlier, C. Masquelier, L. Croguennec, *Chem. Commun.* **2019**, *55*, 11719–11722.
- [18] L. H. B. Nguyen, J. Olchowka, S. Belin, P. Sanz Camacho, M. Duttine, A. Iadecola, F. Fauth, D. Carlier, C. Masquelier, L. Croguennec, *ACS Appl. Mater. Interfaces* **2019**, *11*, 38808–38818.
- [19] A. R. Iarchuk, D. V Sheptyakov, A. M. Abakumov, *ACS Appl. Energy Mater.* **2021**, *4*, 5007–5014.
- [20] W. Liu, H. Yi, Q. Zheng, X. Li, H. Zhang, *J. Mater. Chem. A* **2017**, *5*, 10928–10935.
- [21] X. Shen, J. Zhao, Y. Li, X. Sun, C. Yang, H. Liu, Y. S. Hu, *ACS Appl. Energy Mater.* **2019**, *2*, 7474–7482.
- [22] Y. Cai, X. Cao, Z. Luo, G. Fang, F. Liu, J. Zhou, A. Pan, S. Liang, *Adv. Sci.* **2018**, *5*, DOI 10.1002/advs.201800680.
- [23] J. Olchowka, L. H. B. Nguyen, E. Petit, P. S. Camacho, C. Masquelier, D. Carlier, L. Croguennec, *Inorg. Chem.* **2020**, *59*, 17282–17290.
- [24] Y. Qi, J. Zhao, C. Yang, H. Liu, Y.-S. Hu, *Small Methods* **2018**, *3*, 1800111.
- [25] T. Broux, B. Fleutot, R. David, A. Brüll, P. Veber, F. Fauth, M. Courty, L. Croguennec, C. Masquelier, *Chem. Mater.* **2018**, *30*, 358–365.
- [26] Y. U. Park, D. H. Seo, H. S. Kwon, B. Kim, J. Kim, H. Kim, I. Kim, H. I. Yoo, K. Kang, *J. Am. Chem. Soc.* **2013**, *135*, 13870–13878.
- [27] L. H. B. Nguyen, T. Broux, P. S. Camacho, D. Denux, L. Bourgeois, S. Belin, A. Iadecola, F. Fauth, D. Carlier, J. Olchowka, C. Masquelier, L. Croguennec, *Energy Storage Mater.* **2019**, *20*, 324–334.
- [28] S. T. Dacek, W. D. Richards, D. A. Kitchaev, G. Ceder, *Chem. Mater.* **2016**, *28*, 5450–5460.
- [29] Y. Qi, L. Mu, J. Zhao, Y. S. Hu, H. Liu, S. Dai, *Angew. Chemie - Int. Ed.* **2015**, *54*, 9911–9916.
- [30] R. Fang, J. Olchowka, C. Pablos, P. S. Camacho, D. Carlier, L. Croguennec, S.

- Cassaignon, *Batter. Supercaps* **2021**, DOI 10.1002/batt.202100179.
- [31] J. Rodríguez-Carvajal, *Phys. B Phys. Condens. Matter* **1993**, 192, 55–69.
 - [32] J. M. Le Meins, M. P. Crosnier-Lopez, A. Hemon-Ribaud, G. Courbion, *J. Solid State Chem.* **1999**, 148, 260–277.
 - [33] P. Serras, V. Palomares, J. Alonso, N. Sharma, J. M. López Del Amo, P. Kubiak, M. L. Fdez-Gubieda, T. Rojo, *Chem. Mater.* **2013**, 25, 4917–4925.
 - [34] P. R. Kumar, K. Kubota, Y. Miura, M. Ohara, K. Gotoh, S. Komaba, *J. Power Sources* **2021**, 493, 229676.
 - [35] D. Semykina, O. Podgornova, N. Kosova, *Mater. Today Proc.* **2020**, 25, 497–500.
 - [36] R. Baddour-Hadjean, J. P. Pereira-Ramos, *Chem. Rev.* **2010**, 110, 1278–1319.
 - [37] A. Criado, P. Lavela, G. Ortiz, J. L. Tirado, C. Pérez-Vicente, N. Bahrou, Z. Edfouf, *Electrochim. Acta* **2020**, 332, 1–8.
 - [38] F. D. Hardcastle, I. E. Wachs, *J. Phys. Chem.* **1991**, 95, 5031–5041.
 - [39] C. J. Antony, A. Aatiq, C. Y. Panicker, M. J. Bushiri, H. T. Varghese, T. K. Manojkumar, *Spectrochim. Acta - Part A Mol. Biomol. Spectrosc.* **2011**, 78, 415–419.
 - [40] N. Hall, S. Boulineau, L. Croguennec, S. Launois, C. Masquelier, L. Simonin, *United States Pat.* **2018**.
 - [41] D. R. Cassar, R. F. Lancelotti, R. Nuernberg, M. L. F. Nascimento, A. M. Rodrigues, L. T. Diz, E. D. Zanotto, *J. Chem. Phys.* **2017**, 147, 014501.
 - [42] O. R. K. Montedo, R. B. Nuernberg, R. H. Piva, J. Jiusti, S. Arcaro, D. H. Piva, *Ceram. Int.* **2021**, 47, 21358–21366.
 - [43] R. B. Nuernberg, N. M. P. Machado, M. Malki, M. Neyret, *J. Nucl. Mater.* **2021**, 546, 152777.
 - [44] M. C. Ungureanu, M. Lévy, J. L. Souquet, *Ionics* 1998 43 **1998**, 4, 200–206.
 - [45] J. T. S. Irvine, D. C. Sinclair, A. R. West, *Adv. Mater.* **1990**, 2, 132–138.
 - [46] J.-L. Souquet, *Encycl. Glas. Sci. Technol. Hist. Cult.* **2021**, 453–463.
 - [47] R. B. Nuernberg, *Ionics* 2019 265 **2019**, 26, 2405–2412.

- [48] T. Broux, T. Bamine, F. Fauth, L. Simonelli, W. Olszewski, C. Marini, M. Ménétrier, D. Carlier, C. Masquelier, L. Croguennec, *Chem. Mater.* **2016**, 28, 7683–7692.
- [49] N. Sharma, P. Serras, V. Palomares, H. E. A. Brand, J. Alonso, P. Kubiak, M. Luisa Fdez-Gubieda, T. Rojo, *Chem. Mater.* **2014**, 26, 3391–3402.
- [50] J. Huang, L. A. Blanquer, J. Bonefacino, E. Logan, D. Alves, D. Corte, C. Delacourt, B. Gallant, S. Boles, J. Dahn, H.-Y. Tam, *Nat. Energy* **n.d.**, 2020, DOI 10.1038/s41560-020-0665-yi.

**Chapter IV: Nanosizing and ionic
liquid particle's coating: two ways to
improve transport properties of
 $\text{Na}_3\text{V}_2(\text{PO}_4)_2\text{FO}_2$ electrode material**

In the previous section, the nanospherical of $\text{Na}_3\text{V}_2(\text{PO}_4)_2\text{FO}_2$ was successfully synthesized through the solvothermal methods. Thus, that is interesting to compare this NVPFO_2 with other NVPFO_2 materials, which are synthesized through various methods with different morphologies to further understand the impact of morphologies on the final electrochemical performance because of the easy control of NVPFO_2 composition.

In this chapter, $\text{Na}_3\text{V}_2(\text{PO}_4)_2\text{FO}_2$ will be synthesized by three different synthesis method and the resulting polycrystalline materials will be compared from the structural/morphological point of view and also in term of related electrochemical performance. More especially, the effect of nanosizing and ionic liquid coating on the transport properties will be investigated and discussed in the following chapter.

Nanosizing and ionic liquid particle's coating: two ways to improve transport properties of $\text{Na}_3\text{V}_2(\text{PO}_4)_2\text{FO}_2$ electrode material

1. Introduction

Human-induced climate problem is already impacting the weather and producing extreme climate in every inhabited region across the world such as the frequent heatwaves, heavy precipitation, droughts and tropical cyclones.^[1] The main solution is based on limiting the cumulative CO_2 and other greenhouse gas emissions. To do so, one of the major methods is to reduce and convert the share of fossil fuels-based power station, led by coal-fired power plants, to alternative energy like solar and wind energy accompanied with performant energy storage systems, which can store the additional power during peak periods and supply it to the grid during low hours to reduce burden on the electric grid. Other than the relatively rare lithium based battery, sodium ion battery is an environmentally friendly and reliable choice.^[2–4] Polyanionic materials attracts much attention because of the advantages like high average operating potential and structure stability. Within this category, the most studied polyanionic materials are $\text{Na}_3\text{V}_2(\text{PO}_4)_3$ (NVP)^[5,6] and $\text{Na}_3\text{V}^{3+}_{2-y}\text{V}^{4+}_y(\text{PO}_4)_2\text{F}_{3-y}\text{O}_y$ (NVPFO_y).^[7,8] The second one is even promising because of its higher energy density around 500 Wh.kg^{-1} compared to for NVP. $\text{Na}_3\text{V}^{4+}_2(\text{PO}_4)_2\text{FO}_2$ (NVPFO₂, $y=2$), the most oxidized member of NVPFO_y family, has also a high working potential, although the extraction of the second Na^+ is performed at slightly lower voltage than for $\text{Na}_3\text{V}^{3+}_2(\text{PO}_4)_2\text{F}_3$ (NVPF, $y=0$) (4 V against 4.2 V vs Na/Na^+). Their good structural stability can endure long cycling and minor volume changes during the intercalation and deintercalation of sodium ions.^[9,10]

The $\text{Na}_3\text{V}_2(\text{PO}_4)_2\text{FO}_2$ is composed of $\text{V}_2\text{O}_{10}\text{F}$ bi-octahedral units which are connected by PO_4 groups. In this three-dimensional structure, the channels along the $[110]$ and $[1\bar{1}0]$ directions allow efficient diffusion of sodium ions.^[11] Although, the robust structure supported by the PO_4^{3-} groups leads to stable long cycling capability, the isolated transition metal in this structure result in rather low intrinsic electronic conductivity.^[12] Thus, the NVPFO₂ and NVPF suffer significant capacity loss at high rate charging/discharging. In recent years, plenty of methods were proposed to tackle this problem, such as the application of a carbon coating (carbon nanotube, reduced graphene oxide or amorphous carbon),^[13–16] transition metal dopings (Al,

Cr, Mn, Y, Zr, Ga...)^[17–22] and morphology design (flower, sand rose, nano/micro-sphere, nano/micro-cubes...)^[23–28] etc. Among the various methods, the morphology control is often carried out by hydrothermal/solvothermal synthesis.^[28,29] However, due to the inevitable oxidation of Vanadium(III) during the heat treatment period under normal atmosphere within autoclave, the final composition could not be controlled.^[28,30–32] Indeed, the analysis of morphology improvement on electrochemical performance and related comparison were often performed under the wrong condition.

In this work, in order to avoid these undesired oxidation processes and control well all the different conditions during the Na half-cell assembly process, various NVPFO₂ with three morphologies were synthesized through solid state, ionothermal and solvothermal methods. The final V⁴⁺ oxidation state was meticulously confirmed by X-ray diffraction and different spectroscopic techniques. The influence of different morphologies on electronic and ionic conductivities as well as on the electrochemical performance were investigated through the electrochemical impedance spectroscopy and electrochemical tests.

2.1 Materials preparation

NVPFO₂ materials were synthesized through three different methods. The NVPFO₂-Iono was obtained by ionothermal synthesis. α -VOPO₄·2H₂O and NaF (Prolabo; 98%) (molar ratio of 2/3) were placed in Teflon Parr autoclave with 6 mL of EMI-TFSI (1-ethyl-3-methylimidazolium bis(trifluoromethylsulfonyl)imide) (Lolitec) and heated at 220 °C for 10 hours, similarly to the conditions described in our previous work.^[33] The polycrystalline powder was recovered by centrifugation and washing with ethanol. NVPFO₂-Nano was produced by solvothermal synthesis. A stoichiometric mixture of vanadyl acetylacetonate (Sigma-Aldrich; $\geq 97\%$), NaF, H₃PO₄ (VWR; 85%) (molar ratio of 1/1.5/1) was placed in a Teflon Parr autoclave with a mixture 50% ethanol / 50% distilled water and heated at 180°C for 10 hours. NVPFO₂-Bulk was prepared by solid-state reaction using stoichiometric amounts of VPO₄, VOPO₄, NaF and Na₂CO₃ (Merck) at 550°C during 2 hours.^[34] VPO₄ and VOPO₄ were obtained from VOPO₄·2H₂O homemade precursor. First, VOPO₄·2H₂O was obtained by heating 5g of V₂O₅ (Sigma-Aldrich) in a mixture of 40 mL of phosphoric acid, 110 mL of nitric acid (Sigma-Aldrich) and 130 mL of distilled water at 100 °C during 3 hours. The freshly obtained VOPO₄·2H₂O was dehydrated and reduced under argon/hydrogen flow at 890 °C during 2 hours to synthesize VPO₄.

2.2 Characterization techniques

X-ray diffraction (XRD) measurements were carried out by using a BRUKER D8 ADVANCE diffractometer in θ - θ configuration, equipped with a Cu $K_{\alpha 1,2}$ X-ray source. The acquisition was performed in the 2θ angular range of $10^\circ - 140^\circ$ with a step size of 0.0197° . The Rietveld refinements were performed using the FullProf Suite.^[35]

The chemical analysis of the Na, P and V contents was performed by inductively coupled plasma-optical emission spectroscopy (ICP-OES) using a Varian Model 720-ES spectrometer, after complete dissolution of the powders into concentrated hydrochloric acid solution.

Scanning electron microscopy (SEM) images were taken without any conductive deposition by a Hitachi Model S-3400N microscope. And SEM-FEG (field emission gun) images were on Hitachi SU-70.

Transmission electron microscopy (TEM) was carried out with the Tecnai spirit G2 microscope. The powder was sonicated for 20 min in ethanol before the analysis.

Fourier transformed infrared (FT-IR) spectra were recorded by using a PerkinElmer Spectrum 400 FT-IR/FT-NIR spectrometer in the wavenumber range of $400 - 4000\text{ cm}^{-1}$ (mid-IR).

Raman spectra acquired with a confocal LabRAM HR Evolution micro-spectrometer from Horiba, using a 633-nm laser source. Raman spectra were collected in the range $100\text{--}1300\text{ cm}^{-1}$, using a 10.6 mm (NA 0.5) focal length lens and with acquisition time of 20 s and 40 accumulations.

X-ray photoelectron spectroscopy (XPS) spectra were collected through Omicron Argus X-ray photoelectron spectrometer for an applied power of 280 W and a monochromated AlK α radiation source (1486.6 eV). Charge correction was done by calibrating the C 1s peak at a binding energy of 284.8 eV.

The electrical properties of $\text{Na}_3\text{V}_2(\text{PO}_4)_2\text{FO}_2$ compounds were investigated by electrochemical impedance spectroscopy (EIS). For this purpose, the powders were mixed with camphor (about 2 % wt.) and pressed into pellets of 13 mm diameter applying 200 MPa by means of a uniaxial press, except for sample “NVPFO₂-Iono” which has been pressed without camphor. Subsequently, the other pellets were heat-treated at 250°C for 1 h under air to evaporate the camphor. Indeed, contrary to the two others samples, NVPFO₂-Iono could be well pelletized

without camphor. Moreover, the evaporation of camphor at 250 °C will also decompose the IL. Then, gold electrodes were sputtered on their parallel opposite faces to ensure electrical contact. EIS measurements were performed employing a Solartron 1260 Impedance/Gain Phase Analyzer in the frequency range between 1 MHz and 1 Hz, with an applied root mean square voltage of 100 mV, 10 points per decade and 20 measures per points. Impedance of all the samples were measured under heating and cooling in air on a two-probe sample holder and over the temperature range of 100 - 300 °C. Among them, NVPFO₂-Iono was left at 300 °C for 6h to completely remove the IL and then entered into the cooling process.

The electrochemical performances of the materials were tested in CR2032-type coin cells. The positive electrodes were prepared as a mixture containing the active material, carbon black, and polyvinylidene fluoride (PVDF) in NMP (N-Methyl-2-pyrrolidone) with the ratio of 88/7/5 (by wt.%). After an hour of thorough mixing, the black ink was casted as a flat film by doctor blade on an aluminum foil and dried in an oven at 60°C. Disks were cut, then pressed under 5 tons and finally dried overnight at 80 °C under vacuum. A homemade electrolyte containing a 1 mol/L solution of NaPF₆ (Strem Chemical; 99%) in ethylene carbonate and dimethyl carbonate (EC/DMC = 1/1) with 2 wt.% of fluoroethylene carbonate (FEC) was used for all the electrochemical tests. The assembled cells were cycled in galvanostatic mode, from C/20 to 2C cycling rates between 2.5 and 4.3 V vs. Na⁺/Na. The theoretical capacity being 130 mAh/g (corresponding to 2 Na⁺ reversibly extracted from NVPFO₂), the rate C/20 corresponds to the exchange of 2 Na⁺ in 20 hours. The electrodes have a typical active mass loading around 5 mg/cm². Galvanostatic intermittent titration technique (GITT) measurements have been performed after three formation cycles at C/20, and consisted of a series of 30 min galvanostatic charge/discharge at C/25 followed by a relaxation up to 1 mV/h between 2.5 and 4.3 V.

3 Results and discussions

3.1 Structural and morphological characterization

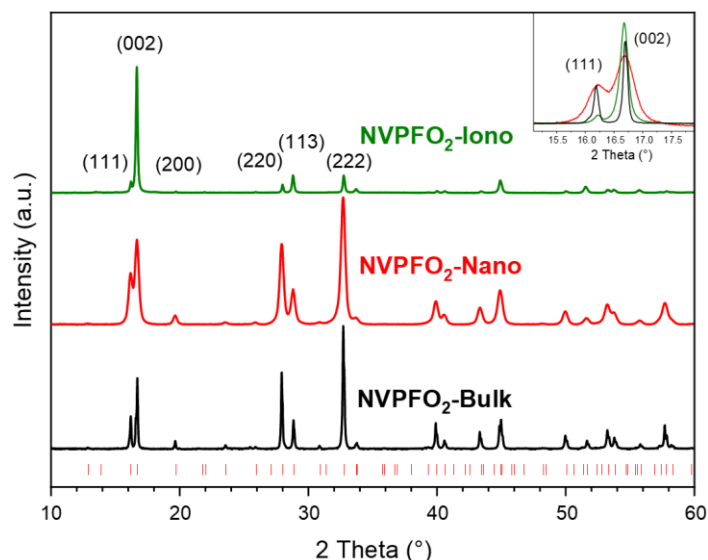


Figure 1: X-ray diffraction patterns of NVPFO₂-Iono (green curve), NVPFO₂-Nano (red curve) and NVPFO₂-Bulk (black curve). The red ticks correspond to theoretical positions as reported in ICDD 01-083-7199. The inset shows the enlargement of (111) and (002) reflections.

The powder XRD patterns illustrated in **Figure 1** and the Rietveld refinements presented in **Figure 2** confirm that the three synthesis methods (Solid-state reaction, Solvothermal and Ionothermal) lead to the synthesis of pure Na₃V⁴⁺₂(PO₄)₂FO₂ (NVPFO₂) phase. In this work, these NVPFO₂ materials are refined in the “average” space group P4₂/mnm, due to the limited resolution of the laboratory equipment. For each compound, all the diffraction peaks could be indexed in the space group P4₂/mnm and the lattice parameters, reported **Table 1**, are in good agreement to those of Na₃V⁴⁺₂(PO₄)₂FO₂, the end member composition of the Na₃V³⁺_{2-y}V⁴⁺_y(PO₄)₂F_{3-y}O_y (0 ≤ y ≤ 2) solid solution.^[7] Indeed, with Synchrotron data, Nguyen et al. found that a ordering of Na⁺ happens along the crystallographic *b* and *c* axes and the accurate NVPFO₂ structure should be described in the monoclinic P2₁/m space group with a modulation vector $q = \frac{1}{2} b^* + \frac{1}{2} c^*$.^[7]

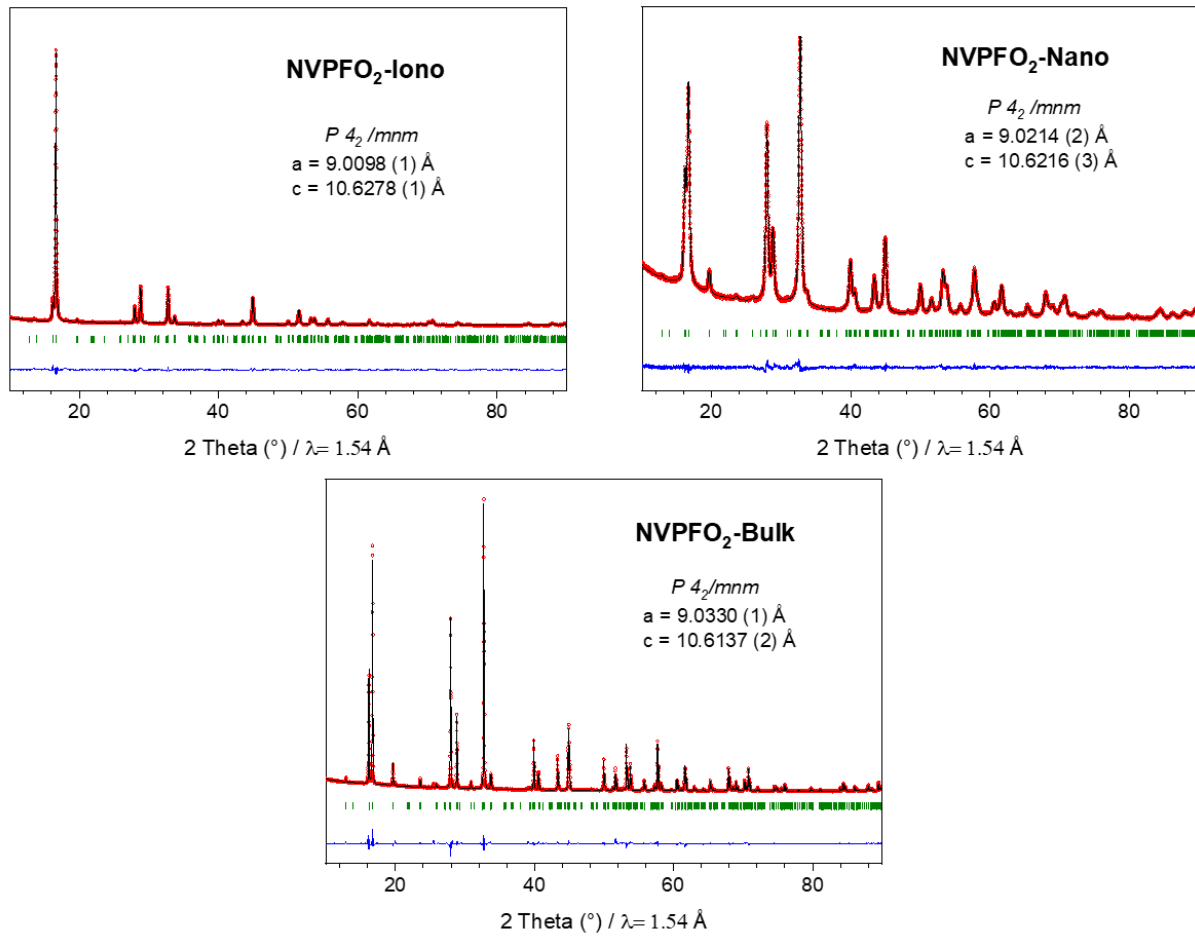


Figure 2: Rietveld refinement of NVPFO₂-Iono, NVPFO₂-Nano and NVPFO₂-Bulk.

Table 1: Lattice parameters obtained by the Rietveld refinement of the XRD patterns, coherent domain sizes along the (220) and (002) directions

	a (Å)	c (Å)	(220) (nm)	(002) (nm)	Space group
NVPFO ₂ -Iono	9.0098(1)	10.6278(1)	52	52	P42/mnm
NVPFO ₂ -Nano	9.0214(2)	10.6216(3)	23	21	P42/mnm
NVPFO ₂ -Bulk	9.0330(1)	10.6137(2)	64	70	P42/mnm

Additionally, ICP analyses confirm the expected cationic ratio (**Table 2**). A comparison of the X-ray diagrams (**Figure 1**) clearly shows differences in the diffraction peaks width and relative intensities, suggesting huge variations of crystallite size and then particles size and/or morphology within the series of NVPFO₂. Indeed, compared to NVPFO₂-Nano and NVPFO₂-Bulk, the very intense (002) reflection observed for NVPFO₂-Iono suggests an oriented (secondary) particles growth in the (ab) plane leading to platelet (2D) morphology.

Furthermore, the dissimilar diffraction peak broadening, highlighted in the inset of the **Figure 1**, unveils disparate crystallite size caused by the different synthesis conditions. The coherent domains calculated using Scherrer equation are reported **Table 1** and reveal that high temperature solid state reaction lead to the biggest primary particles (~70 nm) whereas the solvothermal synthesis to the smallest ones (~ 20 nm). Moreover, the similar coherent domains calculated with (002) and (220) reflections suggest an isotropic crystal growth for all synthesis routes. Finally, it is possible that the internal strains generated by the different crystallite size or crystallite agglomeration are responsible of the slightly different lattice parameters within the NVPFO₂ series (**Table 1** and **Figure 2**).

Table 2: Cationic ratio determined by ICP-OES

ICP	NVPFO ₂ -lono	NVPFO ₂ -Nano	NVPFO ₂ -Bulk
Na/V/P	2.9 : 2 : 2	2.95 : 2 : 2	2.9 : 2 : 2

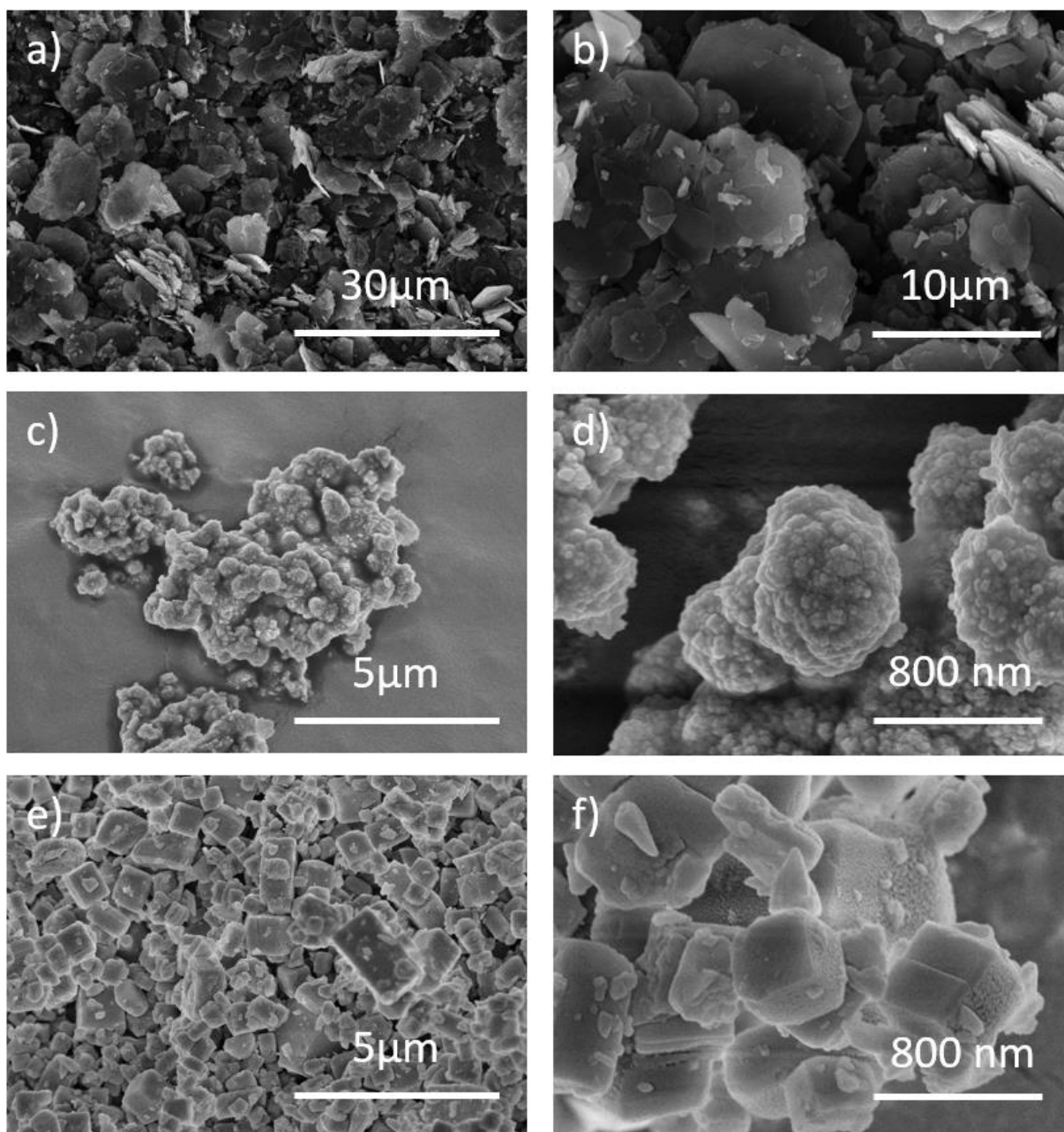


Figure 3: a), b) SEM images of NVPFO₂-iono. c), d) SEM-FEG images of NVPFO₂-nano; e), f) SEM-FEG images of NVPFO₂-bulk.

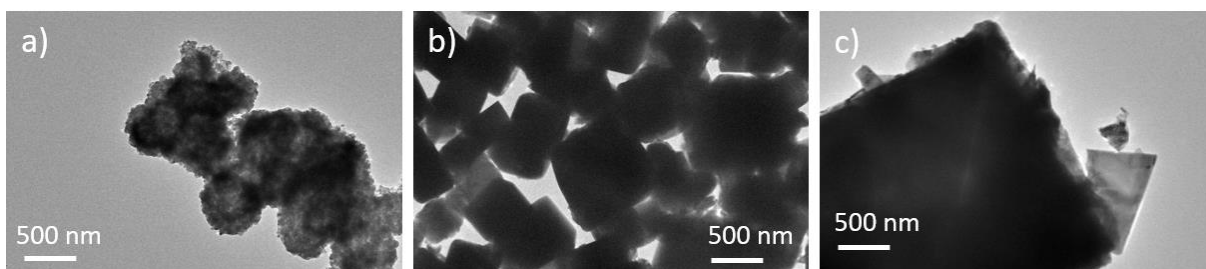


Figure 4: TEM images of all the NVPFO₂ materials a): NVPFO₂-Nano, b): NVPFO₂-Bulk, c): NVPFO₂-Iono.

SEM, SEM-FEG (**Figure 3**) and TEM images (**Figure 4**) further confirm the various morphologies of NVPFO₂ materials obtained by different syntheses methods. The NVPFO₂-

Iono, which is obtained by topochemical reaction from layered α -VOPO₄·2H₂O,^[33] is characterized by aggregated flakes with an average length around 5-10 μ m and thickness of 100-200 nm (**Figure 3 a-b**). The small fragments that can be distinguished probably comes from the break of big flakes. HRTEM analyses further revealed that the platelets exhibit (220) crystallographic planes through lattice fringes (**Figure 5**) which perfectly fits to the exalted intensity of (002) diffraction peak obtained by XRD. Thus, it can be concluded that the Na⁺ diffusion channels along the [110] and [1 $\bar{1}$ 0] directions are situated in the plan of the flake (**Figure 6**). NVPFO₂-Nano synthesized through solvothermal method presents quite different morphology (**Figure 3c-d**). It is characterized by aggregates made of randomly agglomerated spherical secondary particles of diameter ~500 nm. These latter are constructed with smaller primary particles around 30 nm which are in good agreement with the crystallite size determined by XRD (**Table 1**). The different lattice fringes observed by HRTEM (**Figure 5**) for NVPFO₂-Nano (0.32 nm (220), 0.53 nm (002) and 0.55 nm (111)) support the spherical morphology of the small primary particles and the absence of preferential orientation. Finally, the shape of NVPFO₂-Bulk obtained by the high temperature solid-state method approximates to cubes varying from hundreds of nanometers to several micrometers (**Figure 3e-f**). The tiny particles on the surface of these cubes come from the gold coating to better observe the morphology at high magnification due to the relatively poor electronic conductivity of the NVPFO₂ material. Moreover, the thickness of NVPFO₂-Bulk cubes makes the lattice fringes measurement impossible.

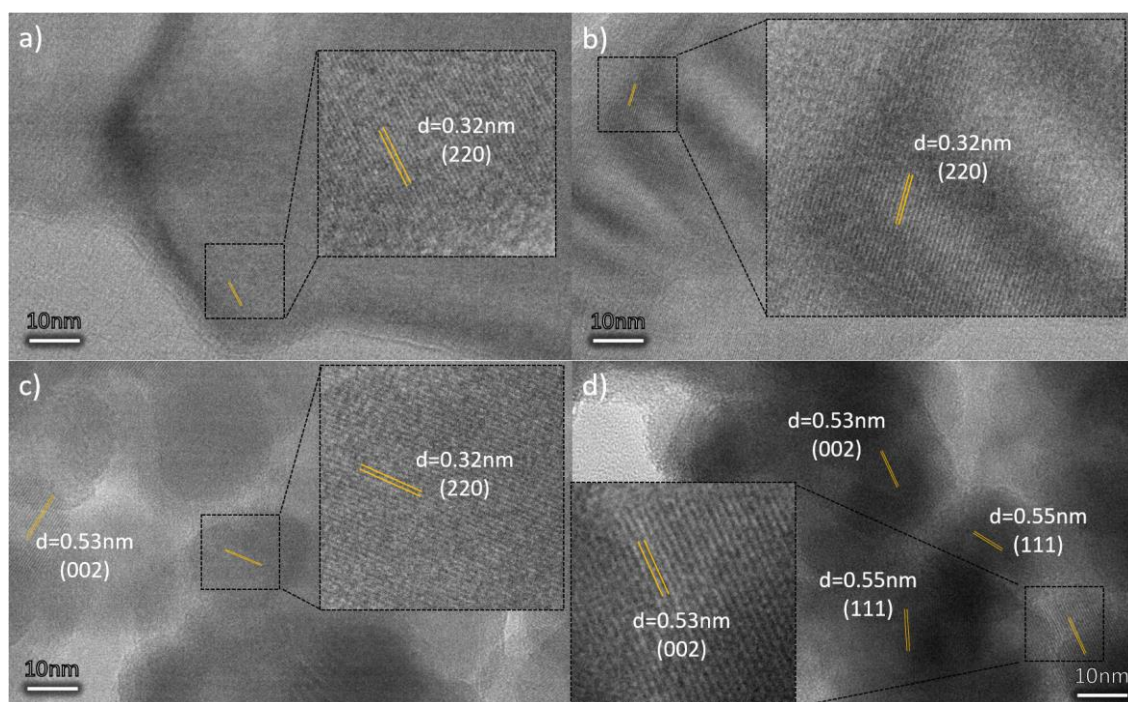


Figure 5: a), b): HRTEM for NVPFO₂-Iono; c), d): HRTEM for NVPFO₂-Nano

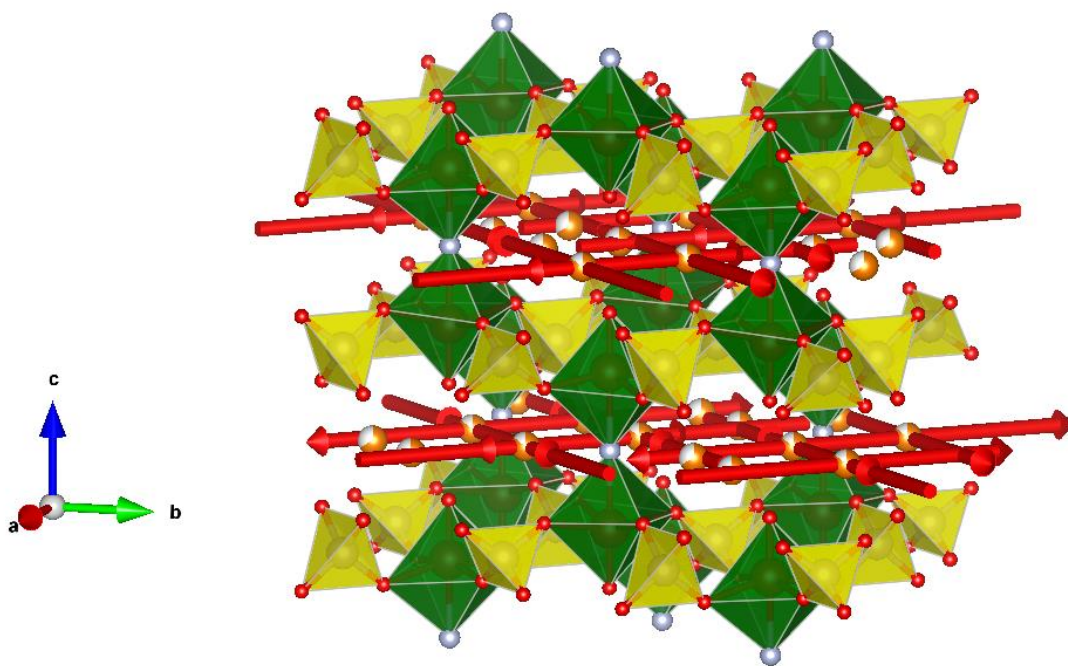


Figure 6: Illustration of $\text{Na}_3\text{V}_2(\text{PO}_4)\text{FO}_2$ crystal structure, the vanadium octahedra are depicted in green, the phosphate in yellow and sodium ion in orange/grey. The sodium diffusion channels are represented by red arrow and correspond to $[110]$ and $[1-10]$ direction in the (ab) plane.

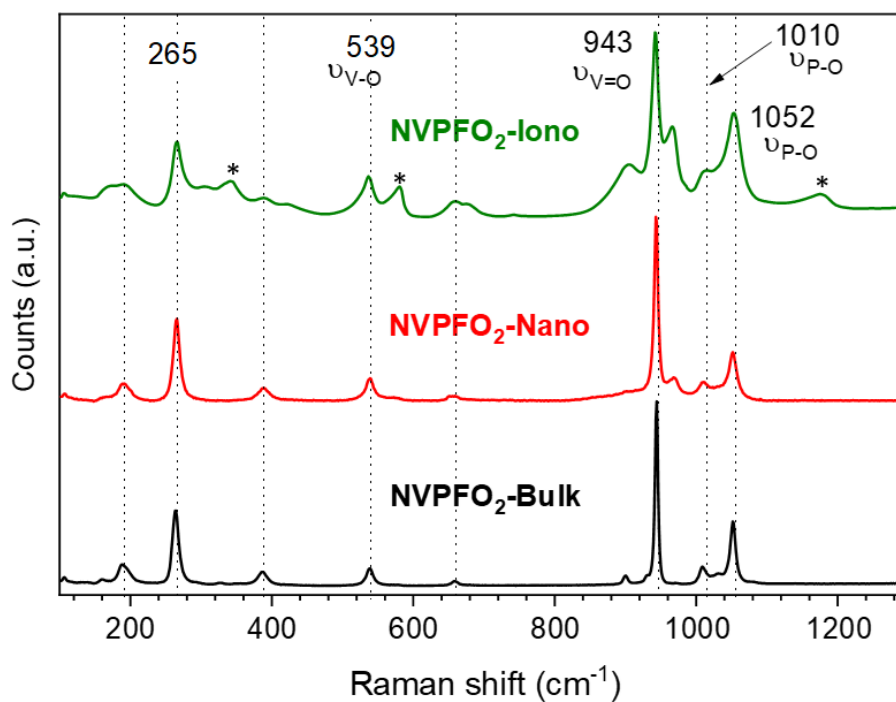


Figure 7: Raman spectra of $\text{NVPFO}_2\text{-Iono}$ (green), $\text{NVPFO}_2\text{-Nano}$ (red) and $\text{NVPFO}_2\text{-Iono}$ (black).

The series of NVPFO_2 was further characterized by various spectroscopic techniques to probe the Na, P and V local environments and confirm the composition deduced from Rietveld refinements. As illustrated on the Raman spectra **Figure 7**, all materials possess the typical signature of $\text{Na}_3\text{V}_2(\text{PO}_4)\text{FO}_2$ with peaks at 539 cm^{-1} , 943 cm^{-1} , 1010 cm^{-1} and 1052 cm^{-1}

attributed to the vibrations of V-O, V=O and phosphate groups.^[36,37] As reported in our previous work on the topochemical reaction mechanism happening during the ionothermal synthesis of NVPFO₂, the ionic liquid functionalizes the particles' surface to create an IL coating, which can be seen as an “artificial Solid Electrolyte Interface”.^[33] This latter, which in some cases stabilize the electrode material upon cycling and favors ionic adsorption on the surface and/or alkaline diffusion through the material,^[38–40] is observed on NVPFO₂-Iono spectrum. Indeed, the band marked with a star are in rather good agreement with those measured for EMI TFSI ionic liquid.^[41–44]

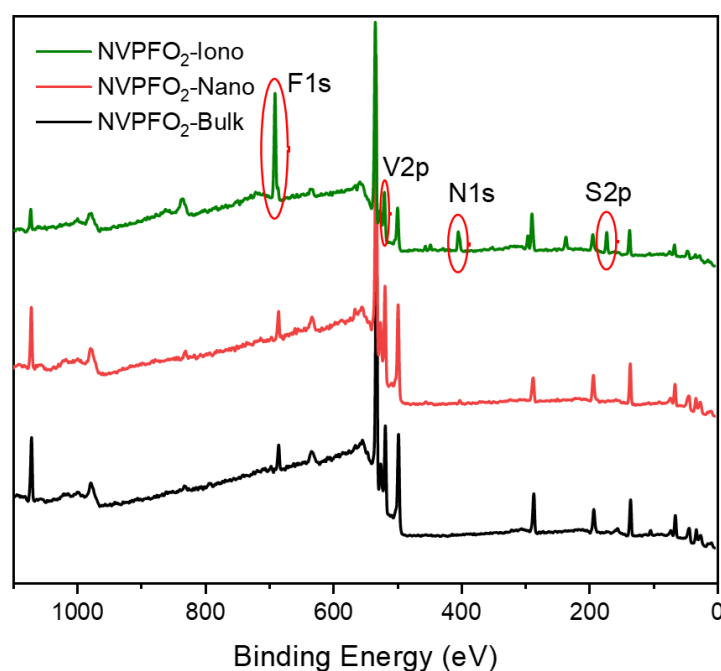


Figure 8: XPS survey of all the NVPFO₂ materials

IL can also be detected on the surface of NVPFO₂-Iono through XPS analysis that reveal the presence of N1s and S2p peaks originated from imidazolium ring and TFSI respectively (**Figure 8**). Meanwhile, the F1s spectra (**Figure 9a**) clearly show a signal at 684.1 eV for all the compounds, corresponding to the fluorine in the polyanionic materials whereas NVPFO₂-Iono presents a second peak at 688.6 eV which is the agreement with the presence of CF₃ from EMI TFSI.^[39,45,46] However, this IL coating does not seem to affect the inorganic core phase. The V2p XPS spectra of the NVPFO₂ series are presented **Figure 9b** and the spectrum of each compound exhibits two broad peaks at 517.2 eV and 524.8 eV corresponding to the V 2p_{3/2} and V 2p_{1/2} transitions. These binding energies are consistent with the expected ones for this polyanionic material with V⁴⁺ environment and demonstrate for NVPFO₂-Iono that the IL coating does not affect the electronic structure of vanadium present near the surface.^[47]

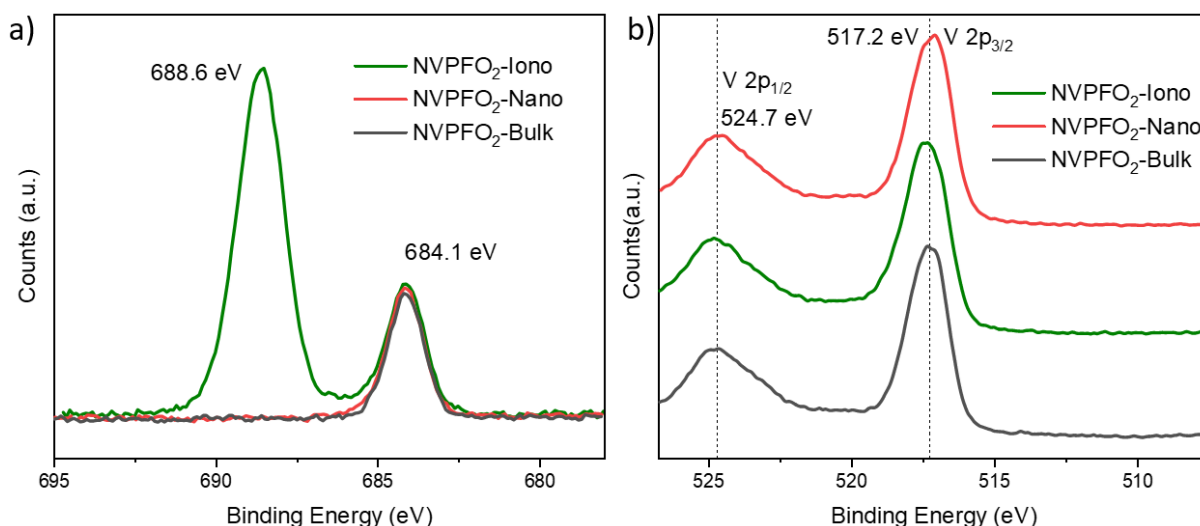


Figure 9: a) XPS spectra of F1s orbital and b) V 2p orbital for all the NVPFO₂ materials with different morphologies

For all compounds, the ²³Na ss-NMR spectrum (**Figure 10a**) reveals a main peak at ~77 ppm, which is generated by the fine interaction between the Na⁺ and the paramagnetic V⁴⁺ and is characteristic of Na(OV⁴⁺)₂ environment.^[48,49] The absence of signals at higher isotropic shift confirms the absence of V³⁺ in these phases and validates the Na₃V⁴⁺₂(PO₄)FO₂ composition.^[10,30,34,48] Meanwhile, the broader signal for NVPFO₂-Nano is the consequence of particles downsizing. ³¹P ss-NMR spectra obtained for all NVPFO₂ show very intense diamagnetic signal at ~0 ppm corresponding to P(OV⁴⁺)₄ local environment (**Figure 10b**).^[50] Once again the absence of signal induced by Fermi contact shift at ~ 1500, 3000 ppm, 4500 ppm or 6000 ppm excludes the V³⁺ existence in the compounds.^[48,49] The enlarged area **Figure 10c** unfolds more details on the diamagnetic signal. Three distinct signals are observed for NVPFO₂-Bulk that most probably corresponds to the inequivalent local environments for phosphorus. On the other hand, the signals of NVPFO₂-Nano and NVPFO₂-Iono are broader, asymmetric and less resolved because of the strains brought by the morphology changes. The slight left ward shift of NVPFO₂-Iono diamagnetic signal is probably due to small local environmental difference which needs further study afterwards. Therefore, the use of different synthesis methods allows to obtain Na₃V⁴⁺₂(PO₄)FO₂ materials with extremely different particles size, with and without coating, offering thus an ideal series to study the size and coating effects on the transport properties and energy storage performance.

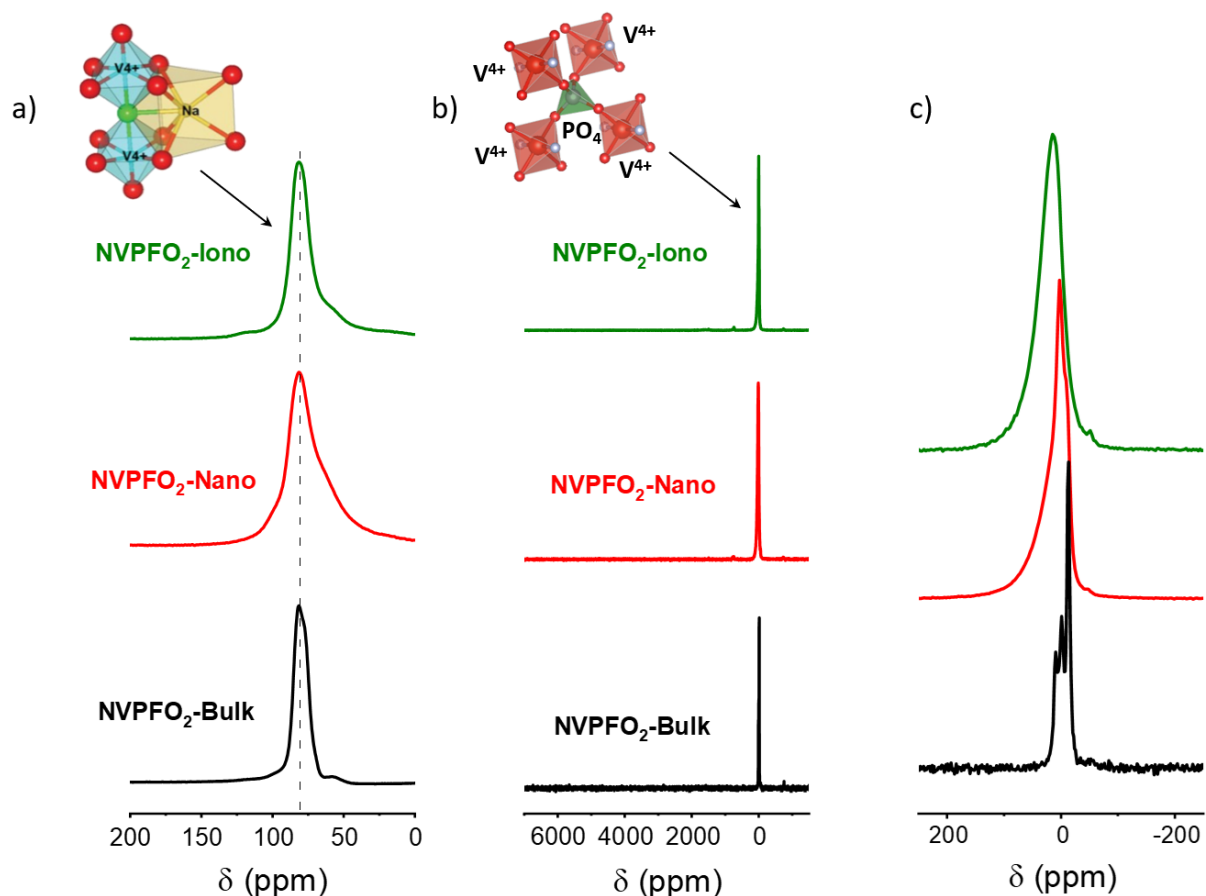


Figure 10: a) ^{23}Na solid-state MAS NMR spectra of $\text{NVPFO}_2\text{-Iono}$, $\text{NVPFO}_2\text{-Nano}$ and $\text{NVPFO}_2\text{-Iono}$; b) ^{31}P solid-state MAS NMR spectra of these NVPFO_2 materials and c) zoom on the diamagnetic signal of ^{31}P NMR.

3.2 Transport kinetics and energy storage performance

The energy storage performance of the three $\text{Na}_3\text{V}_2(\text{PO}_4)_2\text{FO}_2$ samples were first evaluated by cyclic voltammetry and galvanostatic measurements in half-cell configuration. The electrode formulation (88 wt% active material / 7 wt% carbon black / 5 wt% PVDF) and the mass loading of $\sim 5 \text{ mg/cm}^2$ are expected to emphasize on the influence of the different NVPFO_2 electrode materials. **Figures 11a-c** show the galvanostatic charge-discharge curves obtained within potential windows 2.5 - 4.3V vs Na^+/Na at different current intensities, whereas the reversible capacity evolution depending on the C-rate is represented **Figure 11d**. All electrode materials exhibit two reversible plateaus or pseudo-plateaus at around 3.6 and 4 V vs Na^+/Na , attributed to the $\text{V}^{5+}/\text{V}^{4+}$ redox reaction induced by reversible Na^+ extraction and in perfect agreement with the values reported in the literature.^[7] At C/20, $\text{NVPFO}_2\text{-Nano}$ and $\text{NVPFO}_2\text{-Iono}$ exhibit similar reversible high capacities (113 mAh/g and 108 mAh/g respectively), close to the theoretical one. However, $\text{NVPFO}_2\text{-Nano}$ possesses a much better capacity retention when the charge rate increases up to 2C. Meanwhile, the discharge capacity of $\text{NVPFO}_2\text{-Bulk}$ already merely reaches 67 mAh/g at C/20 and quickly drops when the current becomes higher. The full

initial capacity recovering after several cycles of fast charge/discharge clearly shows that the difference in performance mainly originates from the kinetics limitations specific to the electrode material.

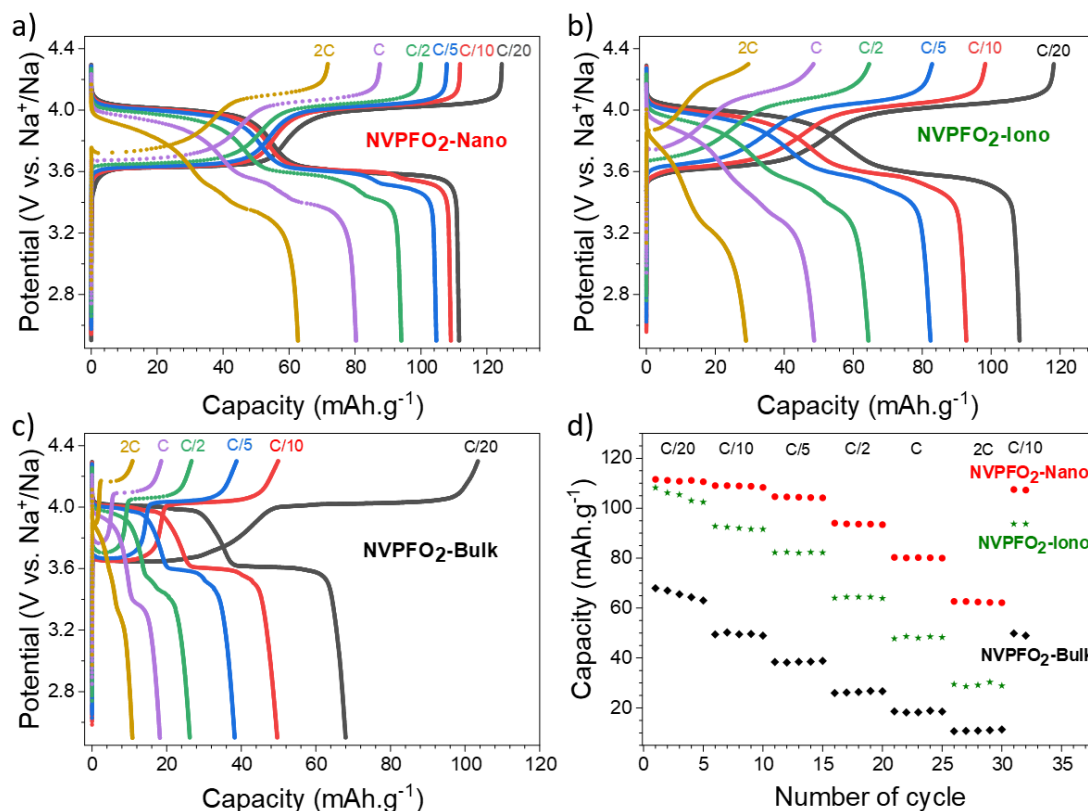


Figure 11: a)-c) Charge and discharge curves of all the NVPFO₂ materials at different cycling rates; d) rate capabilities obtained for all these materials, from C/20 to 2C.

This is supported by the evolution of the polarization when the charge rate increases as illustrated in **Figure 12** that shows the first derivative curves of the 2nd galvanostatic cycle performed at C/20 and C/5.

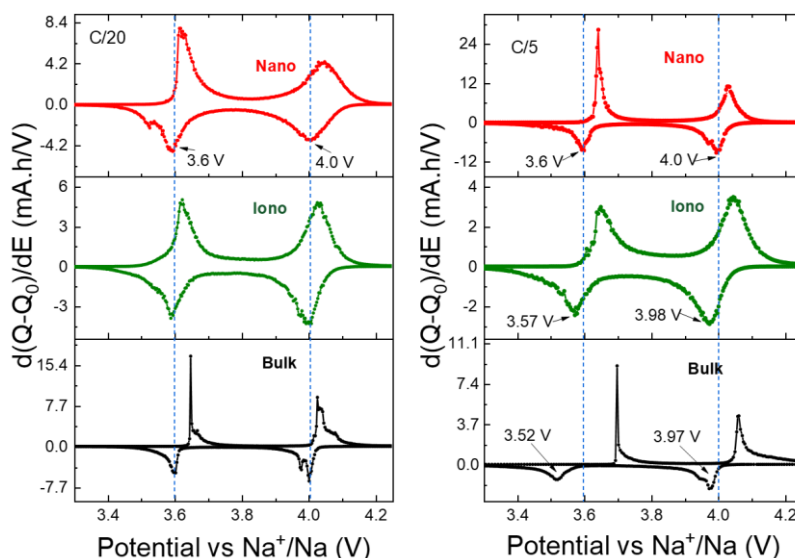


Figure 12: Derivative curves of all the NVPFO₂ materials at C-rate of C/20 and C/5.

At C/20, the discharge average redox potentials for all electrode materials are observed at 3.6 V and 4 V vs Na⁺/Na. These potentials remain unchanged for NVPFO₂-Nano when the charge rate increases to C/5, whereas the values drop to 3.57 V and 3.98 V for NVPFO₂-Iono and 3.52 V and 3.97 V for NVPFO₂-Bulk. Meanwhile, the ΔE_p (potential difference between charge/discharge) increase significantly for NVPFO₂-Iono and NVPFO₂-Bulk, which lead to a system slower kinetics, lower discharged average potential and thus lower energy density. These clearly show that the resistance R (sum of electrical and ionic resistance) follows the trend $R_{\text{Bulk}} > R_{\text{Iono}} > R_{\text{Nano}}$ and thus, strongly depends on the active material nature as it is the only variable parameter in this electrode series. Therefore, the transport properties were further investigated to get a deeper insight into the influence of the particles' size and IL coating.

Then, the complex impedance data of all the NVPFO₂ compounds reveals quite distinct electrical behaviors. **Figure 13** depicts complex impedance plots of each NVPFO₂ sample recorded at 200 °C under heating and also under cooling for NVPFO₂-Iono. Here, the complex impedance data (Z^*) have already been normalized regarding the shape factor (l/A , thickness over area) of each sample according to the relation $Z_s^* = Z^* \cdot A/l$ given rise to the specific impedance (Z_s^*). This approach allows a straight comparison between the impedance response of samples. For samples NVPFO₂-Bulk (**Figure 13b**) and NVPFO₂-Nano (**Figure 13a**), the overall electrical resistivity can be promptly read at the low-frequency intercept of the impedance data with the real part of the specific impedance (Z_s'). Thus, sample NVPFO₂-Bulk is about one order of magnitude more resistive than sample NVPFO₂-Nano. Indeed, sample NVPFO₂-Bulk is so resistive that its overall impedance is out of the equipment impedance range, so there is the dispersion of impedance data at low-frequency range. A common feature between the electrical behavior of these samples is the distorted semi-circles probably caused by a jointly contribution of grains and grain boundaries at high and middle-frequency ranges, respectively. On contrast, NVPFO₂-Ionic (**Figure 13c**) presents an impedance response completely distinct from the other samples and less resistive than sample NVPFO₂-Nano. Its impedance response is constituted by a high-frequency semicircle probably linked to the Na⁺ transport enhanced by the IL and a low-frequency highly depressed semicircle due to electrode polarization phenomenon. In theory, if the IL is rigidly attached on the surface of NVPFO₂ particles and only Na⁺ ions are mobile, a steep increase of the imaginary party of the impedance should take place in low-frequency range.^[39] Since this is not the case, we hypothesized that the ionic molecular species that constitute the IL could be also relatively mobile because of the high temperature employed for the impedance spectroscopy measurements. The electrical

resistivity related Na^+ transport can be roughly read at the middle frequency real part projection of the specific impedance (Z_s') between the two semicircles. Furthermore, once this sample is heated up to 300 °C and then cooled down, its electrical behavior changes entirely (**Figure 13d**) due to the degradation of the IL whereas the responses are the same for the two other electrode materials. In this case, the final electrical behavior of the NVPFO₂-Iono is much alike that of the NVPFO₂-Bulk, highly resistive and with two impedance contributions likely coming from grains and grain boundaries contributions.

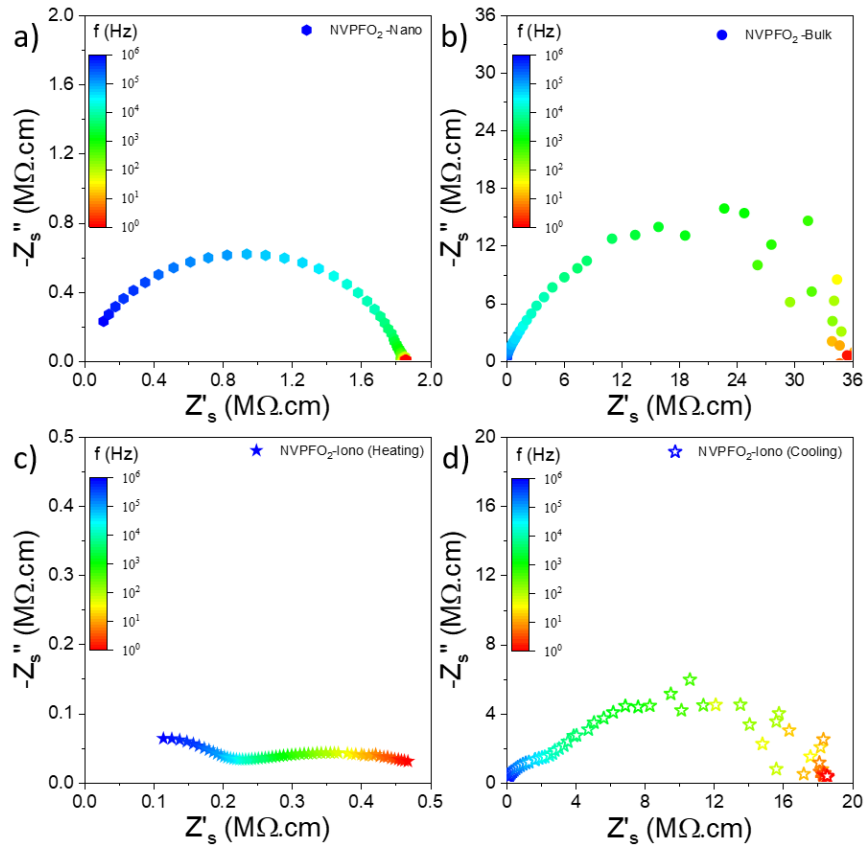


Figure 13: EIS analyses of $\text{Na}_3\text{V}_2(\text{PO}_4)_2\text{FO}_2$ samples at 200°C recorded under heating for NVPFO₂-Nano a) and NVPFO₂-Bulk b) as well as for NVPFO₂-Ionic under heating (c) and cooling (d). The complex impedance data shown here have already been normalized regarding the shape factor of each sample for comparison purposes.

The dependence of the overall electrical conductivity on the inverse of temperature is plotted by applying the linearized form of the Arrhenius-like relation (Eq. 1), which is mostly used for ionic conductors but sometimes also applied for electronic conductors.^[51–53]

$$\sigma T = \sigma_0 \exp\left(\frac{-E_a}{k_B T}\right) \quad (1)$$

Here, σ_0 is the pre-exponential factor, E_a is the activation energy for ionic conductivity, k_B is the Boltzmann constant, and T is the absolute temperature. Following this methodology, the linear fit slope is proportional to the activation energy, which therefore provides access to the

energetic barrier of the mechanism responsible for the electrical transport.^[53] **Figure 14** exhibits the Arrhenius-like plots of the overall electrical conductivity of the NVPFO₂ compounds synthesized under different conditions. Overall, the dependence of the electrical conductivity on temperature for the nanometric NVPFO₂ sample seems to present a low ($T < 180\text{ }^{\circ}\text{C}$) and a high ($T > 180\text{ }^{\circ}\text{C}$) temperature regime due to the dominating electronic transport at low temperatures and the mixed ionic-electronic conducting behavior at higher temperatures. The activation energy of the high temperature regime is considerably higher than the low-temperature one (**Figure 14**). Two activation energy regimes have been also visualized for the micrometric NVPFO₁ compounds reported in literature of Broux et al.^[54] Nevertheless, the transition on this last case takes place around the temperature of $130\text{ }^{\circ}\text{C}$ and it has been attributed to a structural change. Besides, in the low temperature regime, the micrometric NVPFO₁ compound reported in literature (and obtained by solid-state synthesis) shows much lower conductivity and higher activation energy than the NVPFO₂-Nano studied in this work (**Figure 14**). For example, the conductivity and activation energy for the NVPFO₁ reference are $\sim 10^{-10}\text{ S/cm}$ and 0.86 eV at $95\text{ }^{\circ}\text{C}$, while they are $3 \times 10^{-8}\text{ S/cm}$ and 0.43 eV for NVPFO₂-Nano at $100\text{ }^{\circ}\text{C}$.^[54] Likewise, NVPFO₂-Bulk in this study also presents electrical conductivity much lower and activation energy higher than the nanometric NVPFO₂ compounds. Thus, this result demonstrates the strong enhancement of electronic conductivity induced by particles downsizing.

On the other hand, the sample coated with the IL presents at low temperatures an overall conductivity even higher than the nanometric NVPFO₂ ($2.7 \times 10^{-7}\text{ S/cm}$ vs $3 \times 10^{-8}\text{ S/cm}$ at 100°C) and an equivalent activation within errors. However, above $220\text{ }^{\circ}\text{C}$ the conductivity drops considerably probably due to the IL decomposition. After six hours at $300\text{ }^{\circ}\text{C}$, the conductivity of the sample gradually decreases to less than its conductivity at $220\text{ }^{\circ}\text{C}$ (**Figure 14**). When the conductivity is measured under cooling, the activation energy is almost the double than under heating which suggesting a totally different conduction mechanism. Meanwhile, the differences in conductivity under heating and cooling regimes at $200\text{ }^{\circ}\text{C}$ is about two orders of magnitudes (**Figure 14**) and the electrical conductivity of NVPFO₂-Iono under cooling is in the same order of magnitude of NVPFO₂-Bulk. Moreover, the activation energy of NVPFO₂-Iono under cooling is the same of NVPFO₂-Bulk sample considering uncertainties, which indicates the strong ionic conductivity improvement brought by IL coating. Barpanda et al. have demonstrated a lithium conductivity enhancement by IL grafting for lithium fluoride sulfate compounds.^[39] Thus, it could be supposed that in our case Na^{+}

conductivity in NVPFO₂-Iono is strongly improved. The impedance of these two micrometric samples was so high that it was out of the range of the equipment.

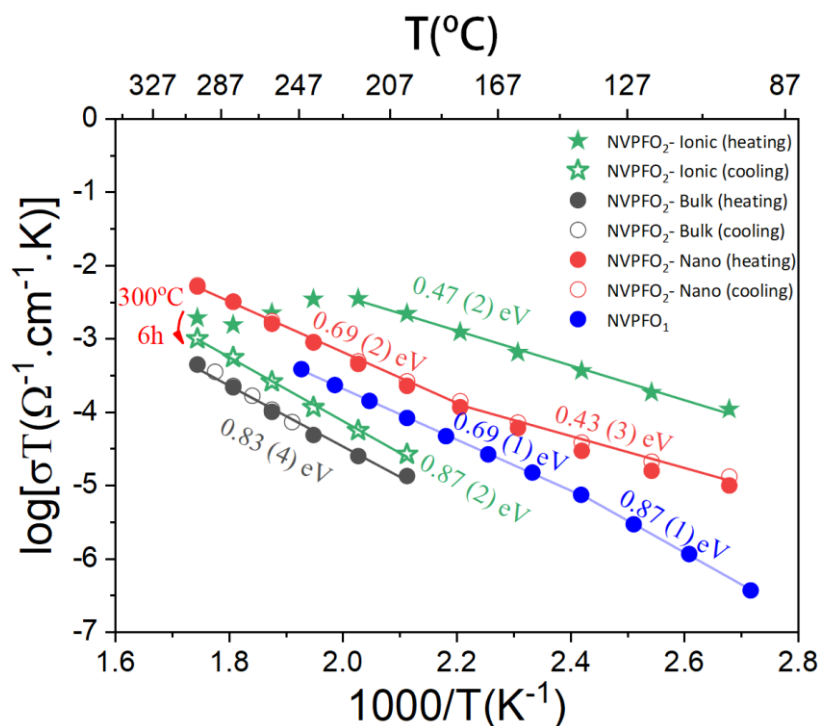


Figure 14: Arrhenius-like plots of the dependence of the overall electric conductivity on the inverse temperature for NVPFO₂ samples synthesized under distinct conditions.

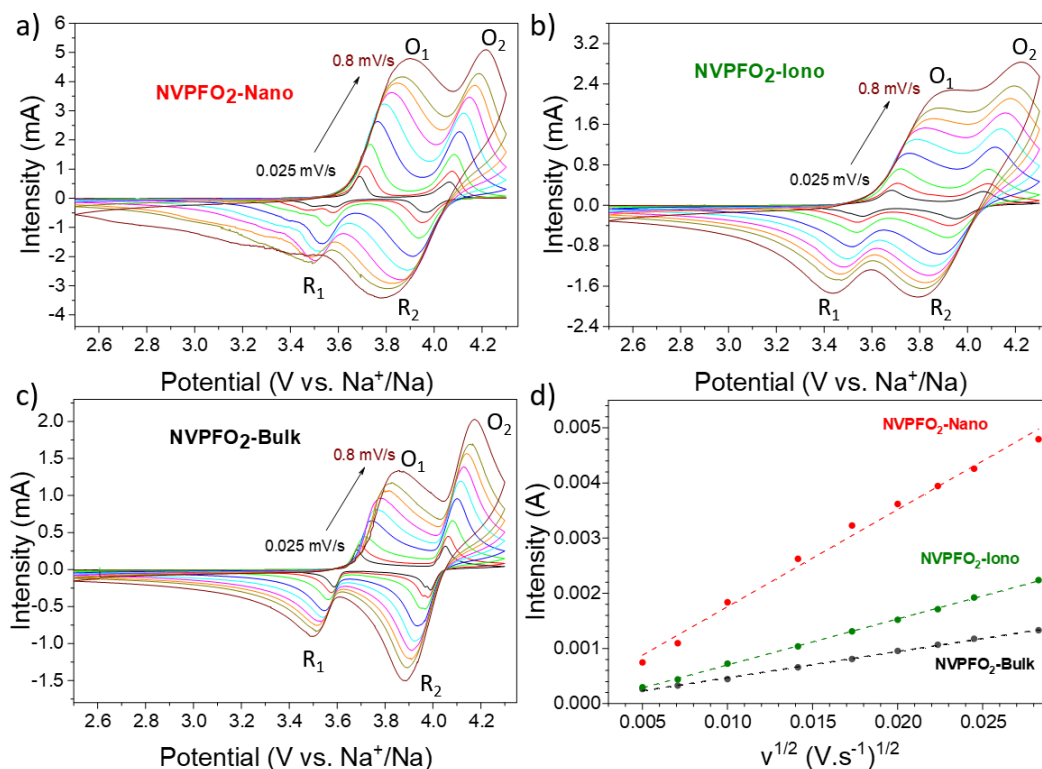


Figure 15: CV curves at different scan rates and the corresponding linear fitting curves between the peak current (i_p) and the square root of the scan rate ($v^{1/2}$) of O₁ peak for each compound.

The Na⁺ diffusion during redox reactions was then investigated through the CV analysis at various scan rates from 0.25 mV/s to 0.8 mV/s in the potential range between 2.5 V and 4.3 V vs Na⁺/Na to avoid possible electrolyte degradation (**Figure 15a-c**). All the NVPFO₂ materials present two oxidation and two reduction peaks, representing respectively the two plateaus in galvanostatic charge and discharge curves. Interestingly at high scan rate, the two oxidation and reduction peaks strongly overlap for NVPFO₂-Iono, which suggests the absence of Na⁺ ordering and a single-phase reaction mechanism. This could be explained by the enhanced Na⁺ conductivity determined by impedance spectroscopy. On the other hand, the overlap is globally less pronounced for NVPFO₂-Nano and even less for NVPFO₂-Bulk, which for instance exhibits two well-defined reduction peaks for all scan rate range. **Figure 15d** and **Figure 16** depicts the evolution of the peak current intensity (*i_p*) vs. the square root of the scan rate (*v*^{1/2}) that allows to estimate Na⁺ diffusion coefficients (**Table 3**) using Randles-Sevcik equation (**eq.2**).

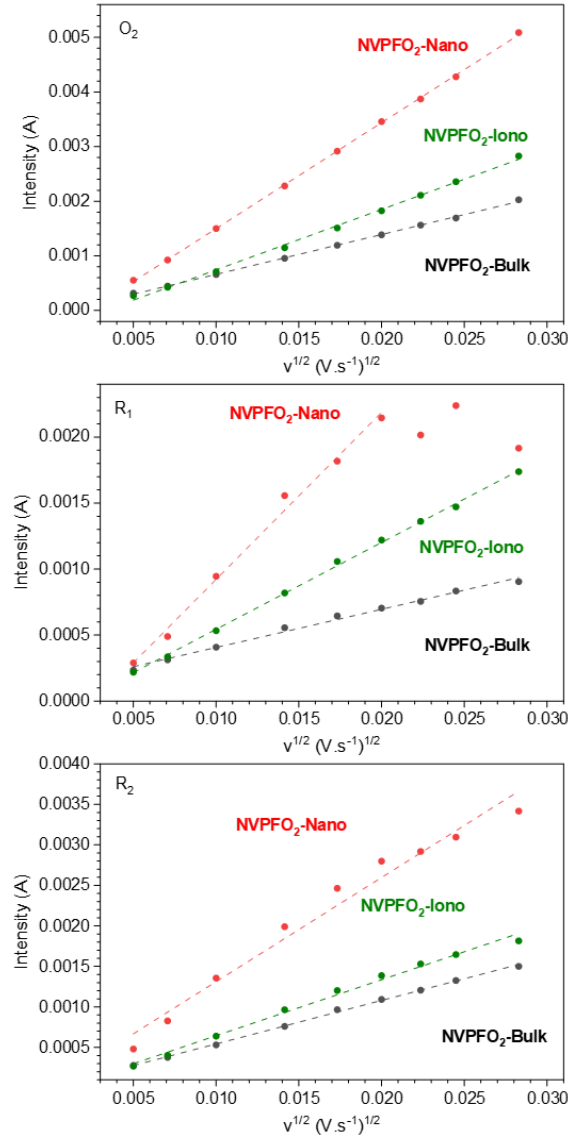


Figure 16: Linear fitting curves between the peak current and the square root of the scan rate of O_2 peak, R_1 peak and R_2 peak.

$$i_p = 0.4463nFAC \frac{nFvD^{\frac{1}{2}}}{RT} \quad (2)$$

Where i_p is the maximum current in A, n is the number of electrons transferred in the redox event ($n=1$), A is the electrode area (2 cm^2), F is the Faraday constant, C is the concentration of Na^+ (12 Na^+ in a unit cell of 866.75 \AA^3 lead to 0.02 mol/cm^3), v is the scan rate (V/s), R is the gas constant and T is the temperature in Kelvin.

Table 3: Diffusion coefficients calculated from CV curves using for Randles-Sevcik equation.

$D \text{ (cm}^2\text{s}^{-1}\text{)}$	NVPFO ₂ -Nano	NVPFO ₂ -Iono	NVPFO ₂ -Bulk
O_2	4.06×10^{-11}	1.32×10^{-11}	5.73×10^{-12}
O_1	3.28×10^{-11}	7.67×10^{-12}	2.43×10^{-12}
R_2	1.78×10^{-11}	5.16×10^{-12}	3.10×10^{-12}
R_1	1.73×10^{-11}	4.66×10^{-12}	1.08×10^{-12}

Nanospherical NVPFO₂-Nano presents the best diffusion capability with a 4.06×10^{-11} cm²/s at the O₂ oxidation peak, nearly one order of magnitude higher than the cubic NVPFO₂-Bulk with the result of 5.73×10^{-12} cm²/s. Quite surprisingly, the IL coated NVPFO₂ exhibits only intermediate diffusion coefficient during redox reactions (e.g. 1.32×10^{-11} cm²/s for the higher potential Na⁺ extraction) whereas a high ionic mobility was been measured by impedance spectroscopy. It is thus possible that the Na⁺ diffusion during redox processes is hindered by the low electronic conductivity as the method allows to estimate a diffusion coefficient during redox reaction process and doesn't probe the ionic mobility in a given phase. Besides, GITT measurements confirm this trend.

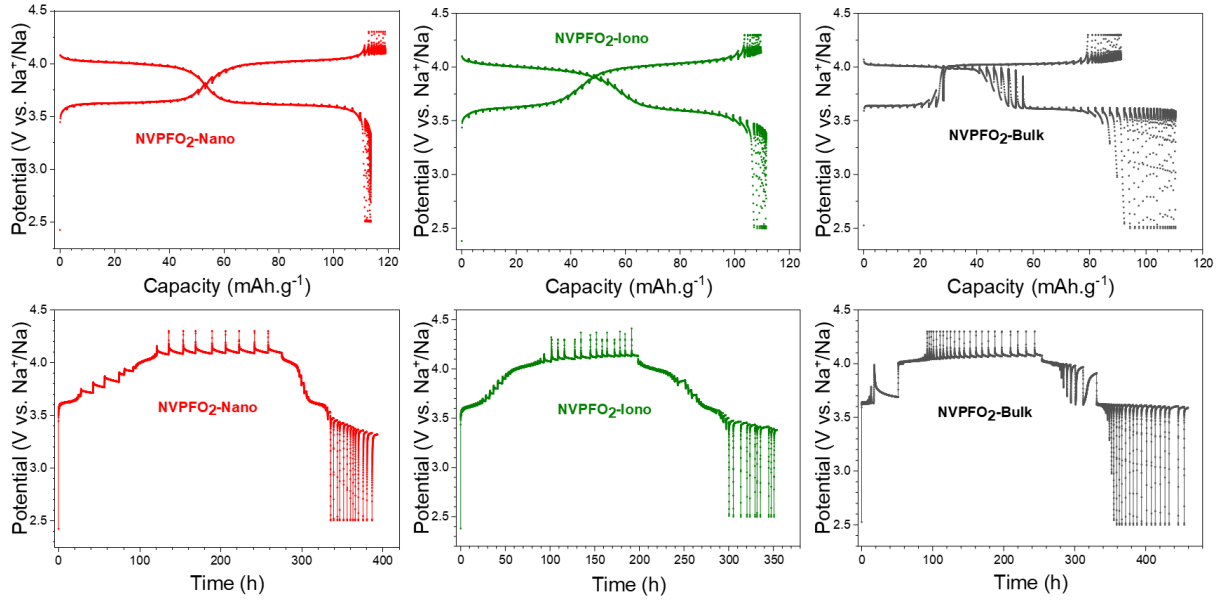


Figure 17: GITT results of the NVPFO₂ materials with Potential versus capacity and potential versus time.

On the basis of the GITT measurement (**Figure 17**), the chemical diffusion coefficients of sodium ions for the three materials were calculated by the following simplified formula (**eq.3**) with rather small pulse current and short time intervals.

$$D = \frac{4}{\pi\tau} \left(\frac{m_B V_M}{M_{BS}} \right)^2 \left(\frac{\Delta E_S}{\Delta E_T} \right)^2 \quad (3)$$

The slow changes of potential are associated to the diffusion of Na⁺ while the sharp potential rise or drop can be attributed to charge transfer and ohm resistance.^[43] GITT curves show for all the NVPFO₂ materials an increasingly larger overpotential towards the end of charge/discharge, implying a kinetically limited process. However, it is much more pronounced for NVPFO₂-Bulk than for the two others electrode materials. This overpotential can also be clearly identified during the potential jump between the first and the second plateaus for NVPFO₂-Bulk (**Figure 18c**). In practice this generates heat and can lead to the degradation of

long-term stability. On the other hand, for NVPFO₂-Nano and NVPFO₂-Iono, this variation is not obvious. More details comparison can be seen from the **Figure 18d** and calculated overpotential for each material in the inset. The overpotential for NVPFO₂-Nano is even smaller than the materials coated with IL.

Figure 18 depicts also the variation of the average diffusion coefficient along the charging/discharging process. Generally, all the compounds suffer a decrease in diffusion coefficient before the 50% state of charge/discharge followed by a small lift because of the easier sodium ion extraction process. Then, it continuously decreases until the state of full/none sodium ion. Both NVPFO₂-Nano and NVPFO₂-Iono possess much better coefficient diffusion than NVPFO₂-Bulk which confirms the previous results obtained by cyclic voltammetry.

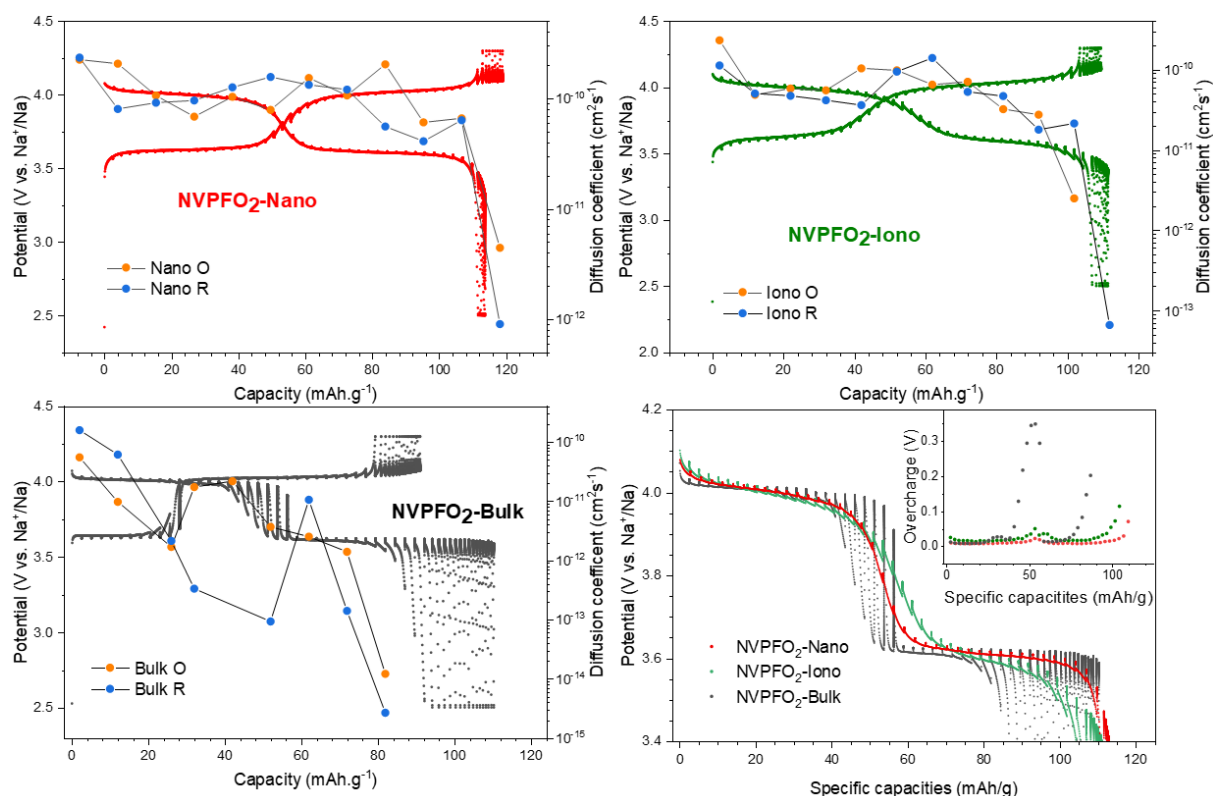


Figure 18: a), b) and c) GITT test results of the NVPFO₂ electrode obtained by different synthesis methods, showing the changes of $D_{app,Na}$ and potentials along with the GCD processes; d) GITT electrochemical discharge curves of all the NVPFO₂ materials. Inset: overpotential between discharge and relax intervals.

According to the **Figure 19a**, all the positive electrode materials present good reversible capacity retention after 100 cycles at C/5. NVPFO₂-Nano and NVPFO₂-Bulk exhibits still 96% of the initial capacity with 105 mAh.g⁻¹ and 40 mAh.g⁻¹ respectively whereas NVPFO₂-Iono has a capacity retention slightly higher than 90%. On the other hand, the coulombic efficiency of NVPFO₂-Bulk is not stable (**Figure 19b**). Starting from the 20th cycle, the positive electrode

suffers frequent coulombic efficiency lose that might be due to the electrolyte degradation and the formation of not electrochemically active byproducts.

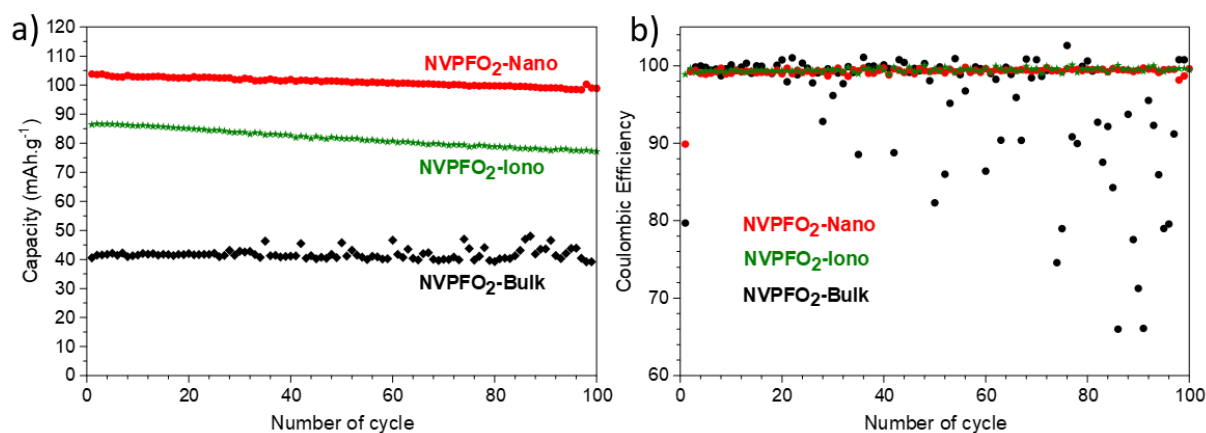


Figure 19: a) Evolution of reversible capacity upon long term cycling and b) coulombic efficiency of all the NVPFO₂ materials.

Bearing in mind the very promising performance presented by nanospherical NVPFO₂, a full cell NVPFO₂-Nano versus hard carbon was assembled and tested. Considering the electrode composition (88% active material / 7% C / 5% PVDF) and the mass loading, the full cell presents excellent performance with energy density of 319 Wh/kg at C/20 and 311 Wh/kg at C/10 (**Figure 20a**). For comparison, Iarchuk et al. reported the same energy density for NVPFO₂ but with electrodes containing only 70 % of active material loading.^[55] The rate capability of full cell is not as good as the half cell. When charging rate is increased to 2C, the capacity retention of the full cell decline to 60% (**Figure 20b**). This can also be observed through the Ragone plots, which demonstrates the variation of energy density along with the increase of power density (**Figure 20c**). The best energy density of 300 Wh/kg is presented at the power density of 16 W/kg and it decreases to around 180 Wh/kg at a power density of 650 W/kg. Meanwhile, the long cycling stability of full cell need further optimisation as the capacity retention is around 70% after 56 cycles (**Figure 21**).

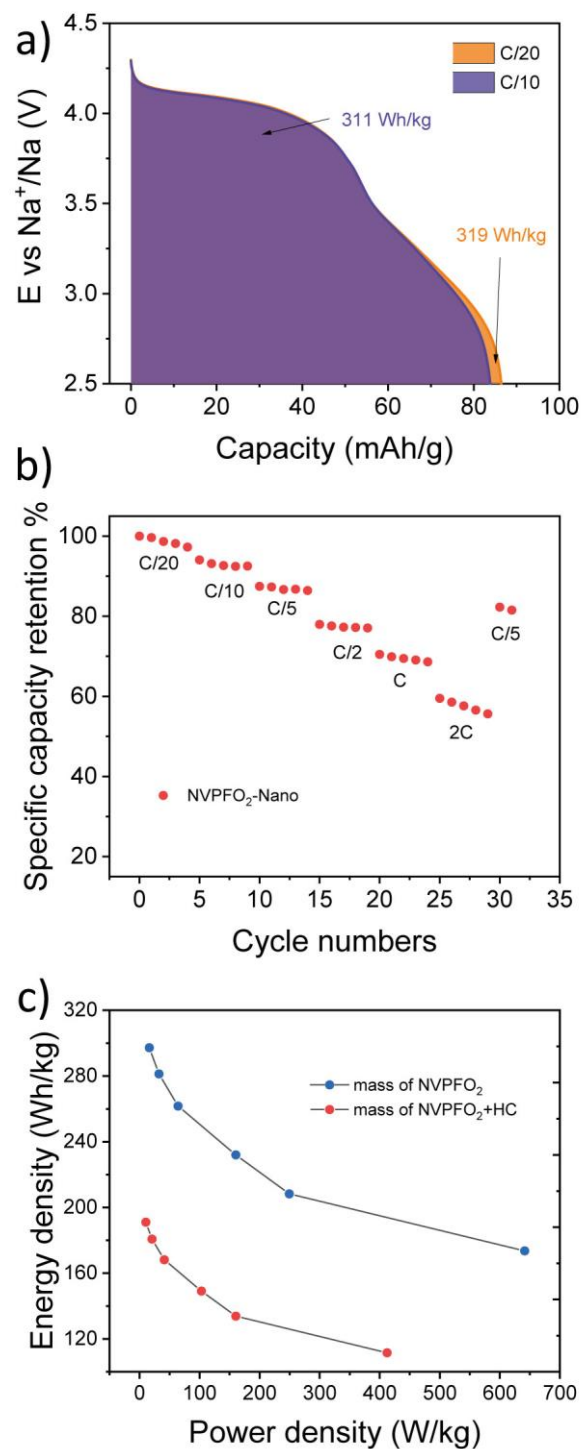


Figure 20: a) Energy density calculated for NVPFo₂-Nano at C/20 and C/10, b) percent of the specific capacity retention upon increasing C-rate and c) Ragone plots of the NVPFo₂-Nano full cell.

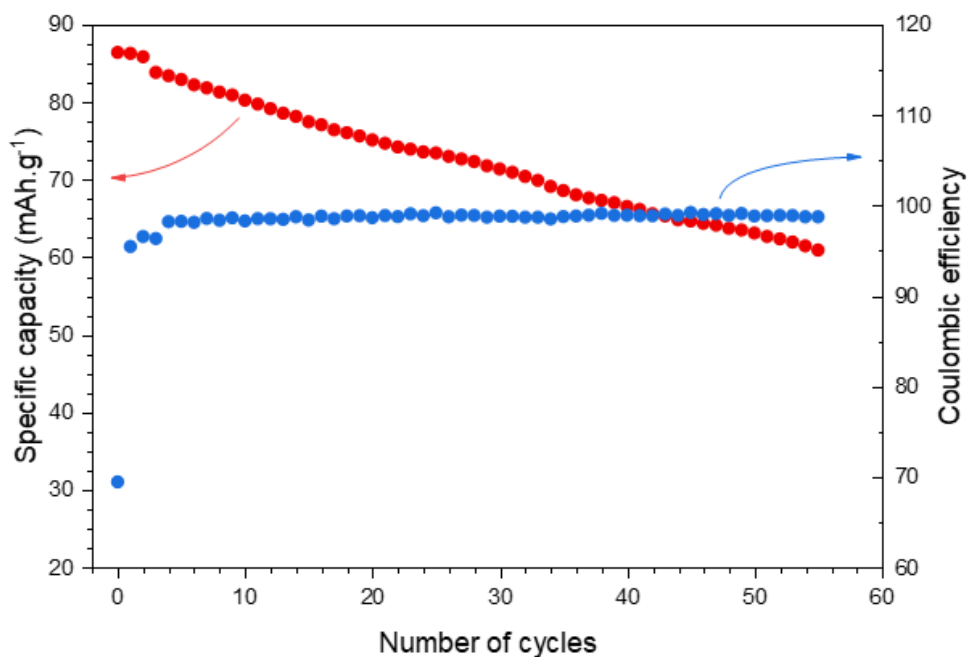


Figure 21: Evolution of reversible capacity upon long term cycling and the coulombic efficiency of the NVPFO₂-Nano vs. HC full cell.

4. Conclusion

In summary, NVPFO₂ electrode materials were synthesized through three different synthesis methods leading to a series of NVPFO₂ with different characteristics, which allows investigating separately particles' size impact and the effect of an IL coating on the electronic conductivity, diffusion capacity of Na⁺ and the energy storage performance. A set of spectroscopic characterization (NMR, XPS and Raman) confirms the Na₃V₂(PO₄)₂FO₂ composition for each compound and reveals that the ionic liquid coating on NVPFO₂-Iono does not affect the vanadium nor the sodium local environment. Impedance spectroscopy measurements demonstrate that particle's downsizing improves the electronic conductivity by more than two order of magnitude in the low temperature range whereas the IL coating strongly enhances the ionic mobility. For instance, NVPFO₂-Nano and NVPFO₂-Iono present conductivities around 3×10^{-8} S/cm and 2.5×10^{-7} S/cm at 100°C whereas the one of NVPFO₂-bulk is estimated below 10^{-10} S/cm. The broad and overlapping redox peaks on CV curves for NVPFO₂-Iono, in addition to the sloping profile on GCD curves, suggest the absence of Na⁺ ordering during cycling which may be due to the enhanced ionic mobility brought by the IL coating. Moreover, when NVPFO₂-Iono loses its IL coating upon thermal degradation, the conductivity and activation energy become similar to NVPFO₂-Bulk, which confirms the beneficial role of IL coating. Concerning energy storage performance, NVPFO₂-Nano demonstrates the best rate capacity retention confirming that a good electronic conductivity of

positive electrode materials is primordial for high rate cycling, and its absence cannot be fully compensated by improving the ionic diffusion. Besides NVPFO₂-Nano performance in full cell are very promising considering the absence of carbon-coating nor formulation optimization. Finally, it was shown that particles downsizing strongly increases the electronic conductivity whereas an ionic liquid coating enhances the ionic mobility, thus the next step would be to combined both approach to develop a more performant electrode material.

5. Reference

- [1] IPCC Working Group I, *Climate Change 2021: The Physical Science Basis*, **2021**.
- [2] Y. S. Hu, S. Komaba, M. Forsyth, C. Johnson, T. Rojo, *Small Methods* **2019**, 3, 2–3.
- [3] I. Hasa, S. Mariyappan, D. Saurel, P. Adelhelm, A. Y. Kuposov, C. Masquelier, L. Croguennec, M. Casas-Cabanas, *J. Power Sources* **2021**, 482, 228872.
- [4] J. M. Tarascon, *Joule* **2020**, 4, 1616–1620.
- [5] Ile Rousse, nald David, O. Mentre, M. Courty, C. Masquelier, *Chem. Mater* **2015**, 27, 54.
- [6] C. V. Manohar, K. A. Raj, M. Kar, M. Forsyth, D. R. MacFarlane, S. Mitra, *Sustain. Energy Fuels* **2018**, 2, 566–576.
- [7] L. H. B. Nguyen, T. Broux, P. S. Camacho, D. Denux, L. Bourgeois, S. Belin, A. Iadecola, F. Fauth, D. Carlier, J. Olchowka, C. Masquelier, L. Croguennec, *Energy Storage Mater.* **2019**, 20, 324–334.
- [8] M. Bianchini, F. Fauth, N. Brisset, F. Weill, E. Suard, C. Masquelier, L. Croguennec, *Chem. Mater.* **2015**, 27, 3009–3020.
- [9] M. Bianchini, P. Xiao, Y. Wang, G. Ceder, *Adv. Energy Mater.* **2017**, 7, 1700514.
- [10] Y. U. Park, D. H. Seo, H. Kim, J. Kim, S. Lee, B. Kim, K. Kang, *Adv. Funct. Mater.* **2014**, 24, 4603–4614.
- [11] M. Bianchini, N. Brisset, F. Fauth, F. Weill, E. Elkaim, E. Suard, C. Masquelier, L.

- Croguennec, *Chem. Mater.* **2014**, 26, 4238–4247.
- [12] L. Zhu, H. Wang, D. Sun, Y. Tang, H. Wang, *J. Mater. Chem. A* **2020**, 8, 21387–21407.
- [13] N. Eshraghi, S. Caes, A. Mahmoud, R. Cloots, B. Vertruyen, F. Boschini, *Electrochim. Acta* **2017**, 228, 319–324.
- [14] F. Li, Y. Zhao, L. Xia, Z. Yang, J. Wei, Z. Zhou, *J. Mater. Chem. A* **2020**, 8, 12391–12397.
- [15] L. Zhu, Q. Zhang, D. Sun, Q. Wang, N. Weng, Y. Tang, H. Wang, *Mater. Chem. Front.* **2020**, 4, 2932–2942.
- [16] T. Broux, F. Fauth, N. Hall, Y. Chatillon, M. Bianchini, T. Bamine, J. B. Leriche, E. Suard, D. Carlier, Y. Reynier, L. Simonin, C. Masquelier, L. Croguennec, *Small Methods* **2019**, 3, 1–12.
- [17] J. Olchowka, L. H. B. Nguyen, T. Broux, P. Sanz Camacho, E. Petit, F. Fauth, D. Carlier, C. Masquelier, L. Croguennec, *Chem. Commun.* **2019**, 55, 11719–11722.
- [18] A. Criado, P. Lavela, C. Pérez-Vicente, G. F. Ortiz, J. L. Tirado, *J. Electroanal. Chem.* **2020**, 856, 113694.
- [19] M. Wang, K. Wang, X. Huang, T. Zhou, H. Xie, Y. Ren, *Ceram. Int.* **2020**, 46, 28490–28498.
- [20] C. Guo, J. Yang, Z. Cui, S. Qi, Q. Peng, W. Sun, L.-P. Lv, Y. Xu, Y. Wang, S. Chen, *J. Energy Chem.* **2021**, DOI 10.1016/j.jechem.2021.06.015.
- [21] I. L. Matts, S. Dacek, T. K. Pietrzak, R. Malik, G. Ceder, *Chem. Mater.* **2015**, 27, 6008–6015.
- [22] Y. Zhang, S. Guo, H. Xu, *J. Mater. Chem. A* **2018**, 6, 4525–4534.
- [23] C. Shen, H. Long, G. Wang, W. Lu, L. Shao, K. Xie, *J. Mater. Chem. A* **2018**, 6, 6007–6014.
- [24] J. Xun, Y. Zhang, H. Xu, *Inorg. Chem. Commun.* **2020**, 115, 107884.
- [25] J. Zhao, L. Mu, Y. Qi, Y. S. Hu, H. Liu, S. Dai, *Chem. Commun.* **2015**, 51, 7160–7163.

- [26] A. Mukherjee, T. Sharabani, R. Sharma, S. Okashy, M. Noked, *Batter. Supercaps* **2020**, 3, 510–518.
- [27] Y. Qi, L. Mu, J. Zhao, Y. S. Hu, H. Liu, S. Dai, *J. Mater. Chem. A* **2016**, 4, 7178–7184.
- [28] R. Fang, J. Olchowka, C. Pablos, P. S. Camacho, D. Carlier, L. Croguennec, S. Cassaignon, *Batter. Supercaps* **2021**, DOI 10.1002/batt.202100179.
- [29] Y. Qi, J. Zhao, C. Yang, H. Liu, Y.-S. Hu, *Small Methods* **2018**, 3, 1800111.
- [30] P. Serras, V. Palomares, J. Alonso, N. Sharma, J. M. López Del Amo, P. Kubiak, M. L. Fdez-Gubieda, T. Rojo, *Chem. Mater.* **2013**, 25, 4917–4925.
- [31] P. R. Kumar, K. Kubota, Y. Miura, M. Ohara, K. Gotoh, S. Komaba, *J. Power Sources* **2021**, 493, 229676.
- [32] D. Semykina, O. Podgornova, N. Kosova, *Mater. Today Proc.* **2020**, 25, 497–500.
- [33] J. Olchowka, L. H. B. Nguyen, E. Petit, P. S. Camacho, C. Masquelier, D. Carlier, L. Croguennec, *Inorg. Chem.* **2020**, 59, 17282–17290.
- [34] T. Broux, T. Bamine, F. Fauth, L. Simonelli, W. Olszewski, C. Marini, M. Ménétrier, D. Carlier, C. Masquelier, L. Croguennec, *Chem. Mater.* **2016**, 28, 7683–7692.
- [35] J. Rodríguez-Carvajal, *Phys. B Phys. Condens. Matter* **1993**, 192, 55–69.
- [36] F. D. Hardcastle, I. E. Wachs, *J. Phys. Chem.* **1991**, 95, 5031–5041.
- [37] C. J. Antony, A. Aatiq, C. Y. Panicker, M. J. Bushiri, H. T. Varghese, T. K. Manojkumar, *Spectrochim. Acta - Part A Mol. Biomol. Spectrosc.* **2011**, 78, 415–419.
- [38] J. Olchowka, R. Invernizzi, A. Lemoine, J. Allouche, I. Baraille, D. Flahaut, L. Guerlou-Demourgues, *J. Electrochem. Soc.* **2020**, 167, 100527.
- [39] P. Barpanda, R. Dedryvère, M. Deschamps, C. Delacourt, M. Reynaud, A. Yamada, J.-M. Tarascon, *J. Solid State Electrochem.* **2012**, 16, 1743–1751.
- [40] J. Olchowka, T. Tailliez, L. Bourgeois, M. A. Dourges, L. Guerlou-Demourgues, *Nanoscale Adv.* **2019**, 1, 2240–2249.

- [41] R. Baddour-Hadjean, J. P. Pereira-Ramos, *Chem. Rev.* **2010**, *110*, 1278–1319.
- [42] A. Criado, P. Lavela, G. Ortiz, J. L. Tirado, C. Pérez-Vicente, N. Bahrou, Z. Edfouf, *Electrochim. Acta* **2020**, *332*, 1–8.
- [43] Y. Cai, X. Cao, Z. Luo, G. Fang, F. Liu, J. Zhou, A. Pan, S. Liang, *Adv. Sci.* **2018**, *5*, DOI 10.1002/advs.201800680.
- [44] K. Fujii, T. Fujimori, T. Takamuku, R. Kanzaki, Y. Umebayashi, S. I. Ishiguro, *J. Phys. Chem. B* **2006**, *110*, 8179–8183.
- [45] C. J. Jafta, X. G. Sun, H. Lyu, H. Chen, B. P. Thapaliya, W. T. Heller, M. J. Cuneo, R. T. Mayes, M. P. Paranthaman, S. Dai, C. A. Bridges, *Adv. Funct. Mater.* **2021**, *31*, 2008708.
- [46] T. Sugimoto, M. Kikuta, E. Ishiko, M. Kono, M. Ishikawa, *J. Power Sources* **2008**, *183*, 436–440.
- [47] Z. Tong, Y. Qi, J. Zhao, L. Liu, X. Shen, H. Liu, *Waste and Biomass Valorization* **2018**, *11*, 2201–2209.
- [48] L. H. B. Nguyen, P. Sanz Camacho, T. Broux, J. Olchowka, C. Masquelier, L. Croguennec, D. Carlier, *Chem. Mater.* **2019**, *31*, 9759–9768.
- [49] J. Olchowka, L. H. B. Nguyen, T. Broux, P. Sanz Camacho, E. Petit, F. Fauth, D. Carlier, C. Masquelier, L. Croguennec, *Chem. Commun.* **2019**, *55*, 11719–11722.
- [50] L. H. B. Nguyen, P. Sanz Camacho, T. Broux, J. Olchowka, C. Masquelier, L. Croguennec, D. Carlier, *Chem. Mater.* **2019**, *31*, 9759–9768.
- [51] M. C. Ungureanu, M. Lévy, J. L. Souquet, *Ionics 1998 43* **1998**, *4*, 200–206.
- [52] J.-L. Souquet, *Encycl. Glas. Sci. Technol. Hist. Cult.* **2021**, 453–463.
- [53] R. B. Nuernberg, *Ionics 2019 265* **2019**, *26*, 2405–2412.
- [54] T. Broux, B. Fleutot, R. David, A. Brüll, P. Veber, F. Fauth, M. Courty, L. Croguennec, C. Masquelier, *Chem. Mater.* **2018**, *30*, 358–365.
- [55] A. R. Iarchuk, D. V. Sheptyakov, A. M. Abakumov, *ACS Appl. Energy Mater.* **2021**, *4*,

5007–5014.

**Chapter V: Synthesis of polyanionic
electrode material $\text{Na}_3\text{V}_2(\text{PO}_4)_2\text{F}_{3-y}\text{O}_y$
in deep eutectic solvent**

In the previous chapter, many NVPFO_y with different morphologies were synthesized by a variety of reaction conditions. However, the synthesis conditions for the vast majority of special morphologies are based on the water/ethanol solution. Ionic liquids (ILs) outside of this solution system have shown equally attractive characteristics in the synthesis of various materials as mentioned in chapter IV. But, its high cost may limit its further use and development. The deep eutectic solvent usually composed of easy accessed organic compounds and presenting similar properties than ILs, was used in this chapter to synthesize the NVPFO_y material with very special morphology. The related characterization and electrochemical performance were also tested through various methods.

The data for this chapter is not complete and there is still a portion of the data from the comparison experiment being generated and processed. When this part of the experiment is completed, their results will be integrated into this article and published afterwards.

Synthesis of polyanionic electrode material $\text{Na}_3\text{V}_2(\text{PO}_4)_2\text{F}_{3-y}\text{O}_y$ in deep eutectic solvent

1. Introduction

As environmental concerns become more pressing, various types of energy storage technologies are emerging to complement renewable energy sources in order to move away from dependence on fossil fuels. Amid them, sodium ion batteries are well suited for such work as an economical alternative to lithium batteries.^[1] Among the various positive electrode materials for sodium ion batteries, such as polyanionic types, layered oxides, and Prussian blue analogues, $\text{Na}_3\text{V}^{3+}_{2-y}\text{V}^{4+}_y(\text{PO}_4)_2\text{F}_{3-y}\text{O}_y$ ($0 \leq y \leq 2$) (NVPFO_y) is a highly promising series of polyanionic materials possessing stable structure and high operating voltage.^[2] This excellent stability comes from the three-dimensional framework, which is assembled by $\text{V}_2\text{O}_8\text{F}_{3-y}\text{O}_y$ bi-octahedral units and PO_4 tetrahedra. The ensuing formation of sodium migration channels along the $[110]$ and $[1\bar{1}0]$ directions also facilitates the insertion and extraction of two sodium ions.^[3] This diffusion capability can be tuned through the substitution of F^- by O^{2-} from the $\text{Na}_3\text{V}_2(\text{PO}_4)_2\text{F}_3$ accompanied with the oxidation of V^{3+} to V^{4+} and the presence of more covalent vanadyl bonds, $\text{V}=\text{O}$.^[2,4,5] These oxidation degree and bond variation lead to a little bit decrease of the operating voltage and the improvement of structure stability.^[6,7]

The NVPFO_y material is traditionally synthesized through solid state synthesis. In recent years, many new synthetic methods have emerged, such as sol-gel method,^[8–10] hydrothermal/solvothermal method,^[11–15] spray-drying method^[16–18] and ionothermal method.^[19] Among them, ionothermal method which uses ionic liquids (IL) instead of conventional solvent has its unique advantages due to the template function of ionic liquids (ILs) and the surface functionalization like the protection of IL molecules at the surface of the electrode materials.^[20,21]

However, the high expense of ILs prevents its further use. Thus, the deep eutectic solvents (DESs) which are widely acknowledged as a new class of IL analogues attract much attention due to the advantages such as ease of preparation and easy access to inexpensive raw materials.^[22] Meanwhile, the DESs are usually composed of non-toxic and low environmental impact products.^[23–26] Due to their low vapor pressures, most DESs produce autogenous pressure when heated. Besides, as opposed to only 600 molecules used in traditional

solvothermal synthesis, millions of eutectic mixtures may be available, which greatly increases the possibility of the creation of new porous frameworks.^[27] For example, Wu et al. synthesized the LiMnPO_4 with special nanorods morphology with choline chloride and ethylene glycol as DES.^[28]

In this article, we aim to investigate the synthesis of NVPFO_y with DESs while inspecting the resulted special morphology. Their impact on the electrochemical performance is also studied in details.

2. Experimental Section

2.1 Materials preparation

The NVPFO_y compounds was prepared via “ionothermal” synthesis with DES as solvent. Firstly, $\alpha\text{-VOPO}_4 \cdot 2\text{H}_2\text{O}$ precursor was synthesized through the refluxing of vanadium (V) oxide (Sigma-Aldrich; $\geq 98\%$) and phosphoric acid (VWR; 85%) in 120 mL water for 24h. The final green yellow product was then filtered and washed by acetone. Then the 792 mg $\alpha\text{-VOPO}_4 \cdot 2\text{H}_2\text{O}$ is mixed with 252 mg NaF with a molar ratio of 2/3 in the DES, which is composed of 1.396 g choline chloride and 1.2 g urea with molar ratio of 1/2. The mixture was introduced in to 100 mL Teflon Parr autoclave and stirred for 30 min at 60°C. Then, the mixture was heated in an oven at 200°C during 20h. The powder was retrieved through centrifugation cleaning with water and overnight drying in vacuum at 60°C. Then, the final product was obtained through calcination at 600°C under Argon atmosphere for 2h30.

Although, the DES of choline chloride and urea might suffer partial decomposition at 200°C according to research of Delgao-Mellado et al., this temperature do not prevent the formation of NVPFO_y .^[29] Meanwhile, lowering the reaction temperature (for example, 120°C) results in unsuccessful synthesis of the final desired sample according to the XRD results (**Figure 1**). The materials are composed of unwanted impurities.

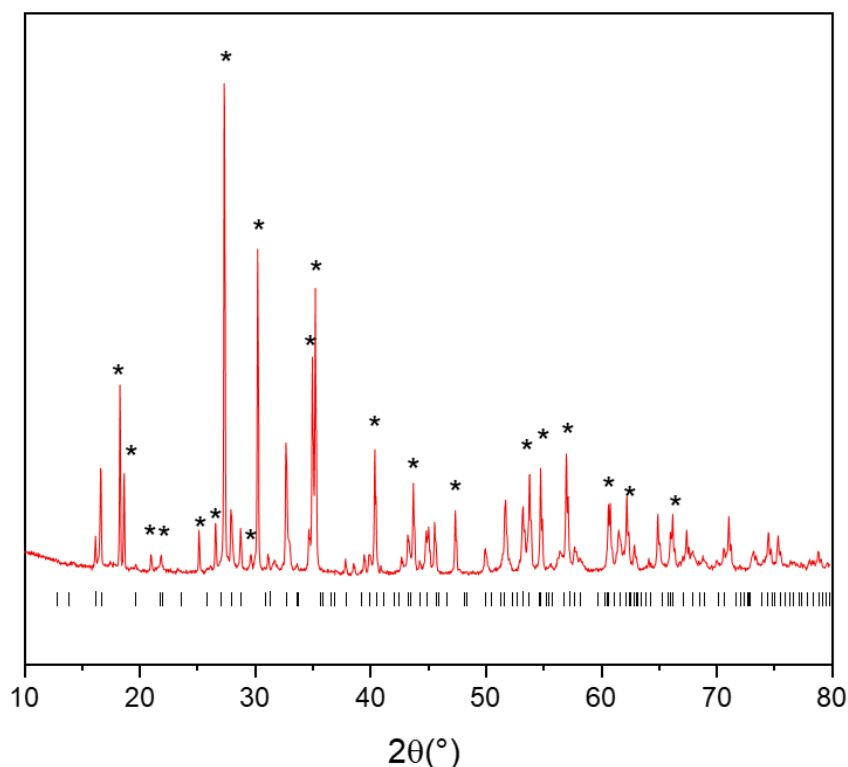


Figure 1: The XRD pattern of the compounds obtained at 150 °C for 20 h and after calcination at 600 °C. The black ticks correspond to theoretical positions of NVPF as reported in ICDD 00-066-0322 and the star marks the impurity peak.

2.2 Characterization techniques

X-ray diffraction (XRD) measurements were carried out by using a BRUKER D8 ADVANCE diffractometer in θ - θ configuration, equipped with a Cu $K_{\alpha 1,2}$ X-ray source. The acquisition was performed in the 2θ angular range of $10^\circ - 80^\circ$ with a step size of 0.0197° . The Rietveld refinements were performed using the FullProf Suite.^[30]

Scanning electron microscopy (SEM) images were taken without any conductive deposition by a Hitachi Model S-3400N microscope.

Fourier transformed infrared (FT-IR) spectra were recorded by using a PerkinElmer Spectrum 400 FT-IR/FT-NIR spectrometer in the wavenumber range of $400 - 4000 \text{ cm}^{-1}$ (mid-IR). Raman spectra were obtained with a confocal LabRAM HR Evolution micro-spectrometer from Horiba, using a 633 nm laser source. They were collected in the range $100\text{-}1300 \text{ cm}^{-1}$, using a 10.6 mm (NA 0.5) focal length lens and with an acquisition time of 20 s and 40 accumulations.

X-ray photoelectron spectroscopy (XPS) spectra were obtained by using an Omicron Argus X-ray photoelectron spectrometer with a 280 W electron beam power and a monochromated $\text{AlK}\alpha$ radiation source (1486.6 eV). Binding energies were calibrated against the C 1s binding energy

at 284.8 eV for all the non-carbon coated materials and at 284.5 eV for the compound after calcination with carbon.

The electrochemical performances of the materials were tested in CR2032-type coin cells. The positive electrodes were prepared as a mixture containing the active material, carbon black, and polyvinylidene fluoride (PVDF) in NMP (N-Methyl-2-pyrrolidone) with the ratio of 88/7/5 (by wt.%). After an hour of thorough mixing, the black ink was casted as a flat film by doctor blade on an aluminum foil and dried in an oven at 60°C. Disks were cut, then pressed under 5 tons and finally dried overnight at 80°C under vacuum. A homemade electrolyte containing a 1 mol/L solution of NaPF₆ (Strem Chemical; 99%) in ethylene carbonate and dimethyl carbonate (EC/DMC = 1/1) with 2 wt.% of fluoroethylene carbonate (FEC) was used for all the electrochemical tests. The assembled cells were cycled in galvanostatic mode, from C/20 to 2C cycling rates between 2.5 and 4.3 V vs. Na⁺/Na. The theoretical capacity being 130 mAh/g (corresponding to 2 Na⁺ reversibly extracted from NVPFO₂), the rate C/20 corresponds to the exchange of 2 Na⁺ in 20 hours. The electrodes possess a typical active mass loading around 6 mg/cm².

3. Results and discussions

3.1 Structural and morphological characterization

The XRD patterns obtained for the compounds synthesized in DES confirm the successful syntheses of phases that belong to the family of NVPFO_y (**Figure 2**). The obtained powder named NVPF-DES presents several small peaks of impurities which probably comes from the organic residues of the DES. Although, water wash through centrifugation can partially eliminate these impurities (**Figure 3**), the NVPF-DES powder must endure a rather high-temperature calcination (600°C) to eliminate organic residues. Besides, the calcination also improves the crystallinity as it can be deduced from sharper and more intense diffraction peaks display in **Figure 2**. The lattice parameters of calcined NVPF-DES (NVPF-DES-c) is determined from the Rietveld refinement, with $a = b = 9.01 \text{ \AA}$ and $c = 10.65 \text{ \AA}$ (**Figure 4**) and indexed in the space group of P4₂/mm. Such c parameter indicates that the final high-temperature calcined NVPF-DES exhibits an O²⁻/F⁻ mixed composition, Na₃V₂(PO₄)₂F_{1.5}O_{1.5} i.e. Na₃V³⁺_{2-y}V⁴⁺_y(PO₄)₂F_{3-y}O_y ($y = 1.5$), according to the work published by Long et al. before.^[6] The coherent domains for NVPF-DES are then calculated using Scherrer equation and are ~ 23 nm along the [001] direction and ~ 22 nm when calculated with (220) reflection. After

calcination, they increase to ~ 40 nm and ~ 33 nm respectively, which indicates that the calcination process improves the crystallinity. Besides, the slight shift of (002) reflection also suggests a change in the final vanadium oxidation state (**Figure 2**). This peak shift towards lower 2 theta, which leads to the increase c parameter according to the Bragg law and thus, decrease the ratio of V^{4+}/V^{3+} as it was seen in the previous chapters.

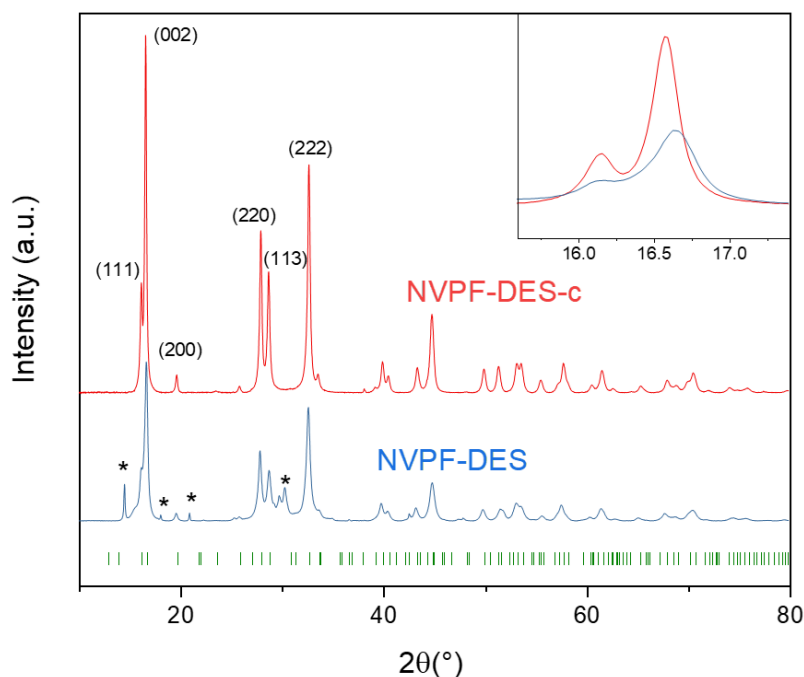


Figure 2: X-ray diffraction patterns of the obtained NVPF-DES and calcined NVPF-DES-c with the inset of zoom of peak (111) and (002). The red ticks correspond to theoretical positions as reported in ICDD 00-066-0322. The stars correspond to impurities probably coming from the DES.

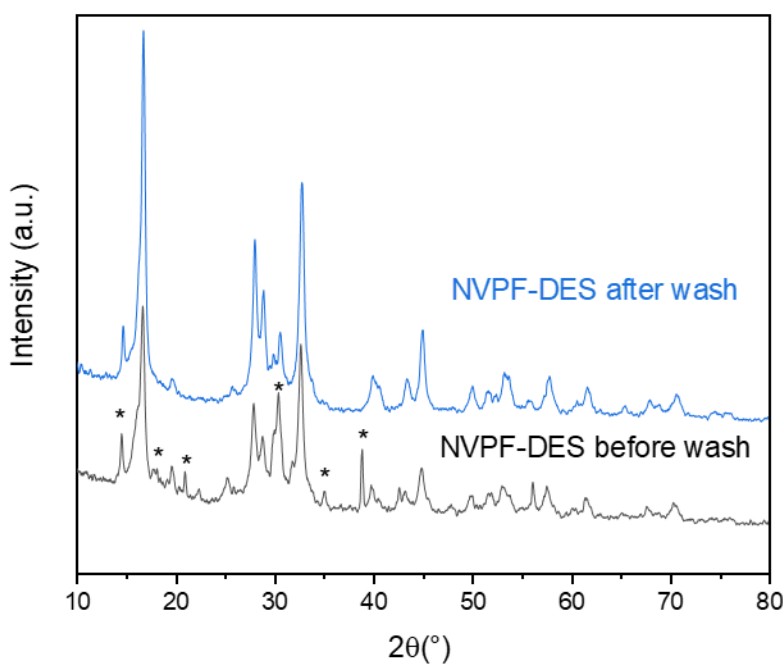


Figure 3: X-ray diffraction pattern for NVPF-DES before and after water wash. The stars correspond to the impurities

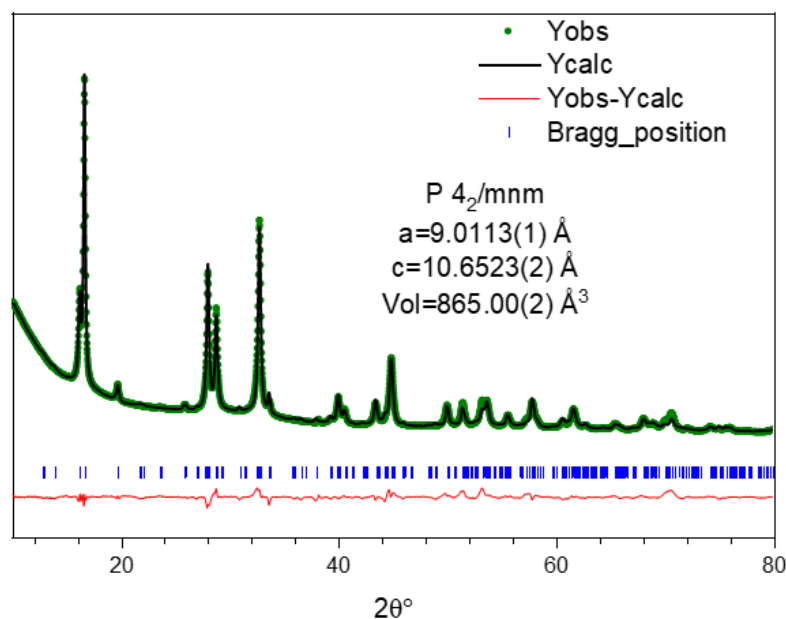


Figure 4: Rietveld refinement of NVPF-DES-c with the cell parameters listed inset.

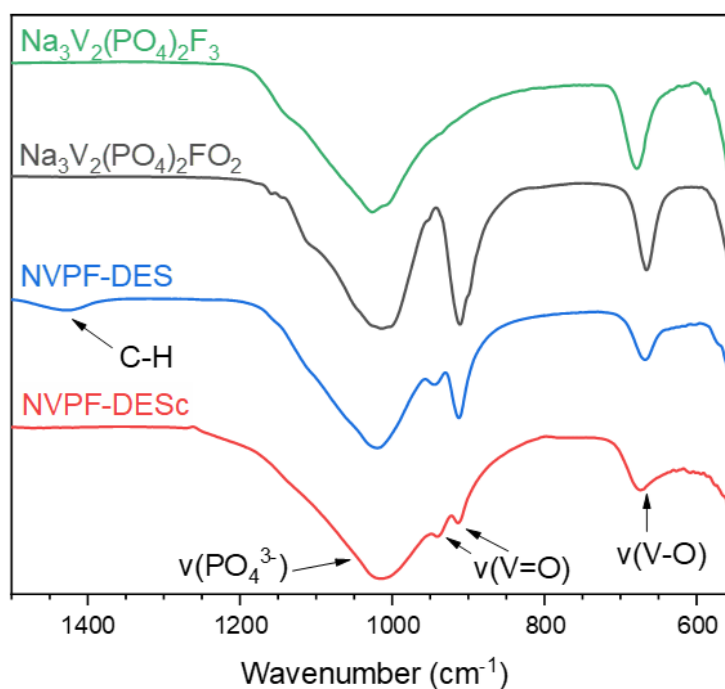


Figure 5: FTIR spectra of NVPF-DES and NVPF-DES-c compared with those of $\text{Na}_3\text{V}_2(\text{PO}_4)_2\text{F}_3$ and $\text{Na}_3\text{V}_2(\text{PO}_4)_2\text{FO}_2$ reference synthesized through solid-state method. The intensities of all the spectra were normalized to the signal corresponding to the vibration of phosphate groups at $\sim 1050 \text{ cm}^{-1}$ to emphasize the V=O bond vibrations.

For all samples, IR analyses demonstrates the appearance of signals at around 675 cm^{-1} corresponding to V-O bonds (**Figure 5**). The two peaks at around 910 and 940 cm^{-1} are characteristic of vibration of covalent V=O bonds. These peaks are very intense for NVPFO₂ and absent for NVPF. While Phosphate groups in NVPF-DES incite one intense and large peak. It can be clearly seen, NVPF-DES possesses one small impurity signals at around 1400 cm^{-1}

corresponding to the organic C-H bonds present in DES. This peak disappears after high temperature calcination. Meanwhile, we can notice that for NVPF-DES, the relative intensity of the V=O peak at 910 cm^{-1} decreases after calcination, which indicates the occurrence of reduction process.^[6]

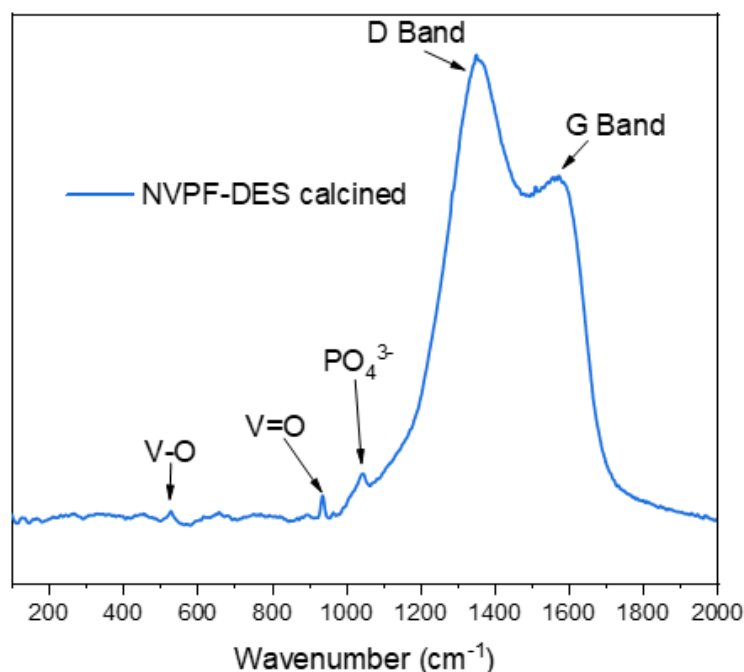


Figure 6: Raman spectrum of NVPF-DES-c calcined at $600\text{ }^{\circ}\text{C}$ and collected from $100\text{-}2000\text{ cm}^{-1}$.

The NVPF-DES and NVPF-DES-c were then characterized by Raman spectroscopy, an efficient and complementary to IR technique to provide information on local environment within the NVPF materials as shown in the previous chapter III. On the **Figure 6**, the peak around 940 cm^{-1} corresponds to V=O vibration while the band at $\sim 530\text{ cm}^{-1}$ and $\sim 1050\text{ cm}^{-1}$ is the signal of bond V-O and phosphate vibration.^[31,32] The very large and intense peaks marked with D Band and G Band correspond to signal of amorphous carbon formed after the calcination of organic DES.^[33] However, the Raman spectra of NVPF-DES is rather different (**Figure 7**). Most of the signals are covered under the noise probably from impurities issued from the decomposition of the DES. According to the study of Delgado-Mellado et al., DES suffer around 10 % mass lose when heated to $200\text{ }^{\circ}\text{C}$ during the thermogravimetric analysis.^[29] However, the synthesis at lower reaction temperature cannot lead to the final NVPF as described before (**Figure 1**). Given that the decomposition at $200\text{ }^{\circ}\text{C}$ has no effect on the final compound, the imperfection is acceptable.

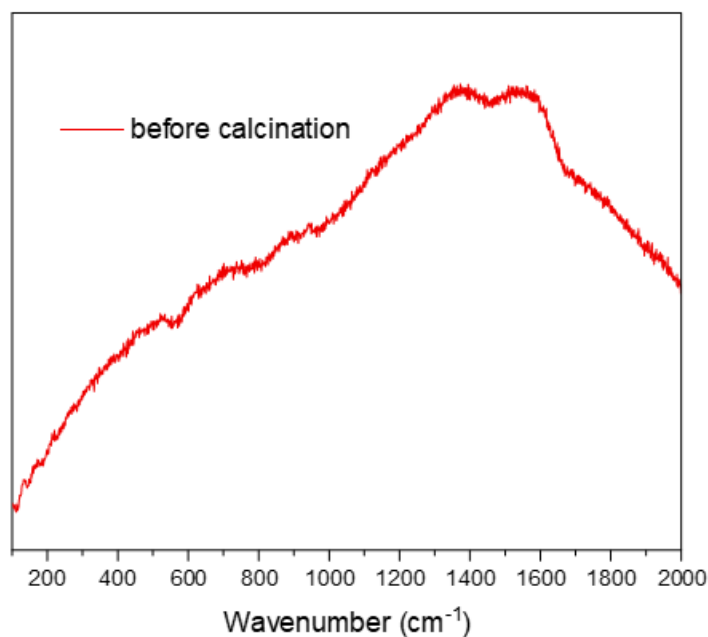


Figure 7: Raman spectrum of NVPF-DES before calcination collected from 100-2000 cm^{-1} .

The vanadium oxidation state has also been estimated by XPS analyses (**Figure 8**). The V2p spectrum of NVPFO₂ reference exhibits two peaks at 517.2 eV and 524.7 eV which are respectively from V2p_{3/2} and V2p_{1/2} transitions, and are consistent with results expected for V⁴⁺ in such polyanionic materials.^[34] On the other hand, NVPF exhibits that the binding energies of V2p_{3/2} and V2p_{1/2} are located at 516.6 eV and 523.7 eV, corresponding to the trivalent vanadium.^[34] The NVPF-DES obtained through the synthesis with “ionothermal” reaction have the same V2p_{3/2} value and slightly lower V2p_{1/2} with 524.5 eV, confirming a composition really close to NVPFO₂. But after calcination, the binding energy of V2p_{3/2} decreased to 517.0 eV and that of V2p_{1/2} decline to 524.2 eV, suggesting that at least the surface vanadyl is likely to get reduced by the carbon created in the process during the high temperature calcination. This is also consistent with the previous IR and XRD findings.

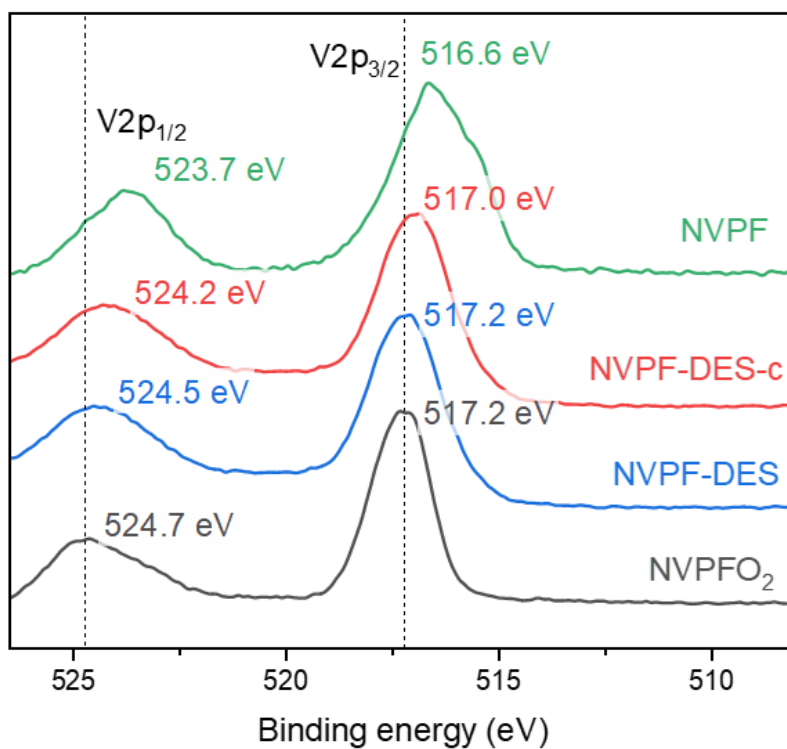


Figure 8: XPS spectra of V 2p orbital for NVPF-DES and NVPF-DES-c materials compared to the reference NVPF and NVPFO₂ reference^[35]

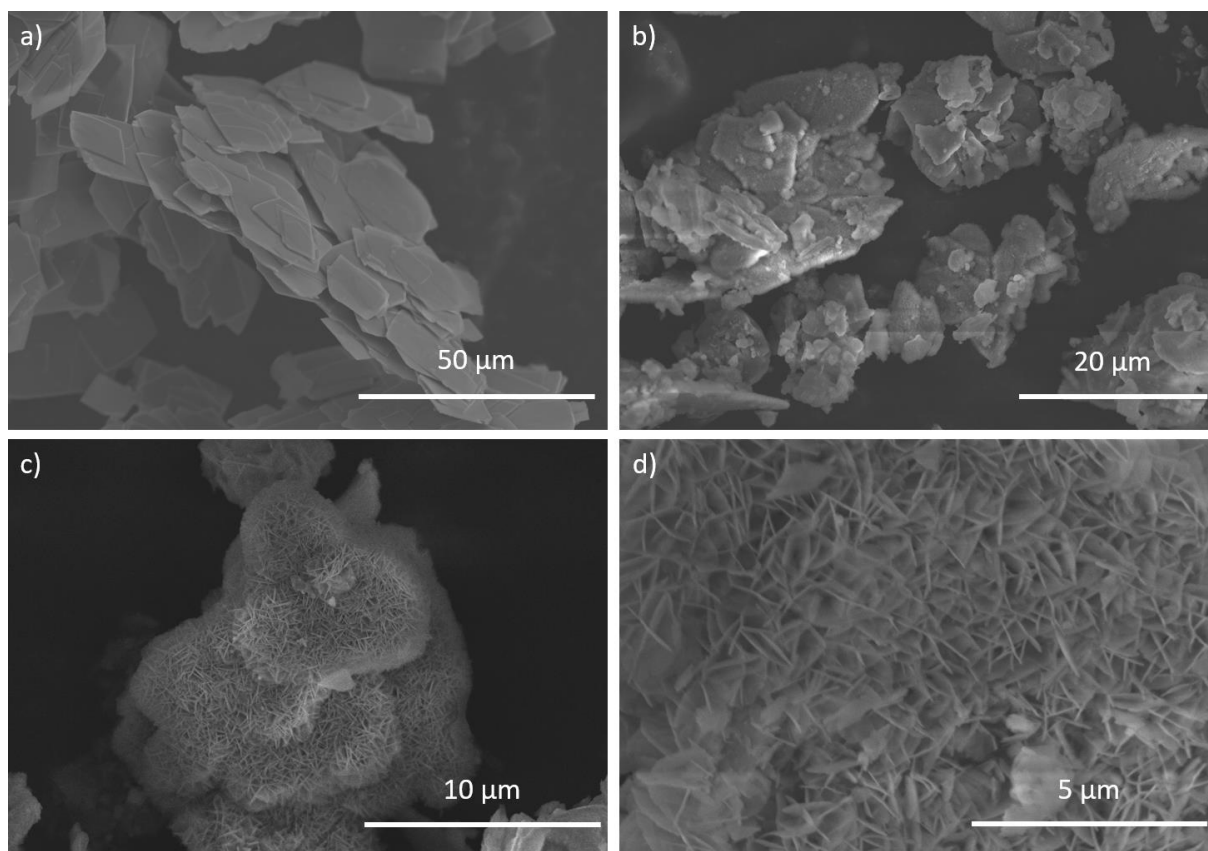


Figure 9: SEM images of a) VOPO₄·2H₂O, b) c) NVPF-DES, d) NVPF-DES-c

Then, the samples were characterized by SEM (**Figure 9**). The NVPF-DES and NVPF-DES-c are obtained through the synthesis reaction from $\text{VOPO}_4 \cdot 2\text{H}_2\text{O}$. $\text{VOPO}_4 \cdot 2\text{H}_2\text{O}$ presents the morphology of tens micrometric large flakes. With these as the basis, NVPF-DES demonstrates generally a morphology of big sheets. However, at a higher level of magnification, we can find some fine details. These slightly thicker sheets are actually interconnected with smaller sheets in the scales of nanometers. In addition, we note that there is no visible change in the external morphology of NVPF-DES after two and a half hours of high-temperature calcination at 600°C . These special morphologies surely increase the contact with electrolyte and thus favorable for the diffusion of sodium ions. At the same time, it can be seen with another sample obtained after five hours of reaction time instead of the normal twenty hours that this particular reticular structure is gradually appearing on the surface of the flakes (**Figure 10**).

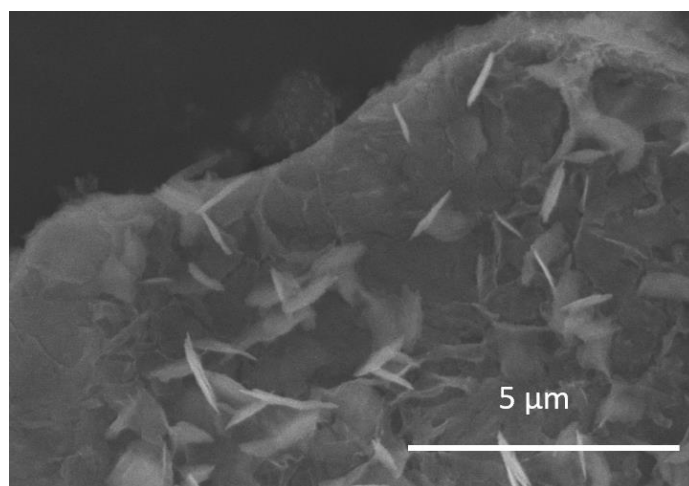


Figure 10: SEM images of NVPF-DES after 5 hours of reaction

The NVPF-DES-c material was further probed by the high resolution TEM. **Figure 11a** confirms the morphology found by the SEM. These flakes are covered by some amorphous parts which might be the carbon-coating formed from the calcination of organic residue. However, as for the lattice fringes, the thickness of these lamellar structures exceeds the distance that the beams of the TEM can traverse. Therefore, we can only look for some small fragments that disintegrate from the big sheets after 30 min sonication. Among these small fragments, some present (200) lattice fringes.

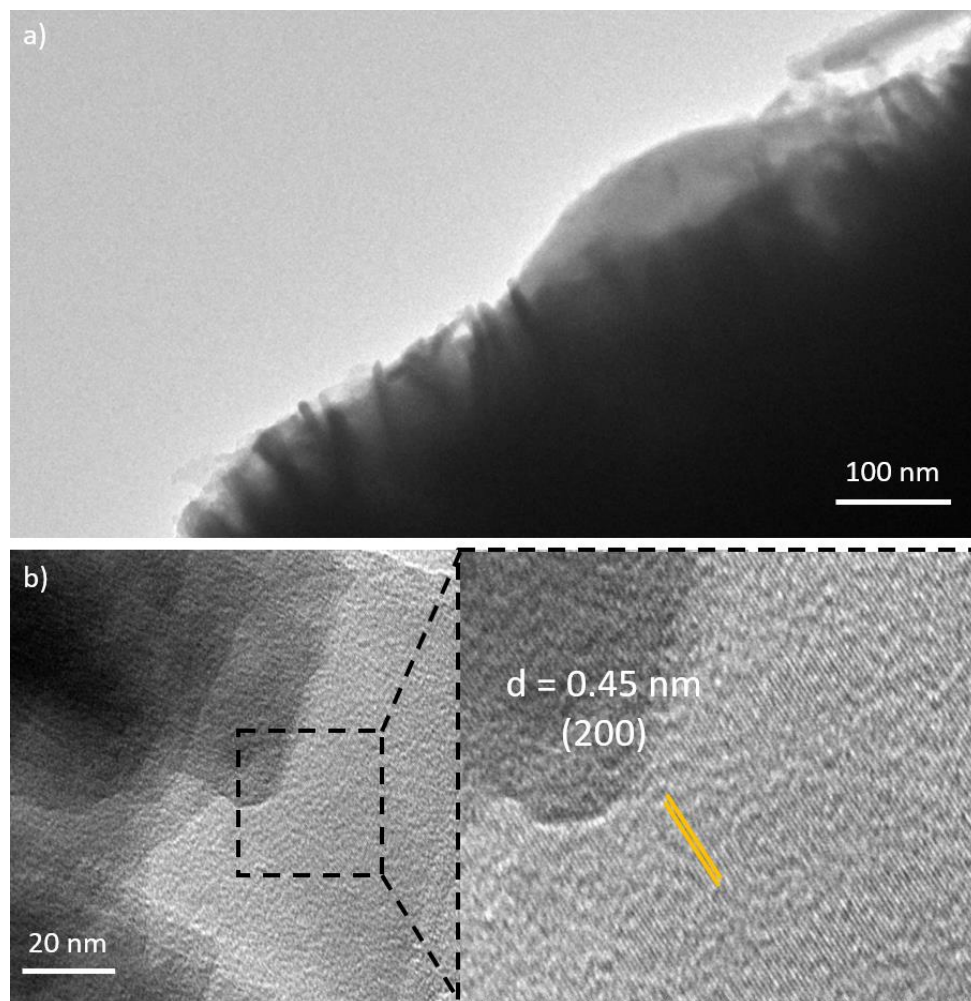


Figure 11: HRTEM for NVPF-DES-c

3.2 Transport kinetics and energy storage performance

The electrochemical performance of the NVPF-DES-c and NVPF-DES was then depicted by galvanostatic measurements in half-cell versus sodium metal. The electrode was undergoing electrode formulation of 88 wt% active material / 7 wt% carbon black / 5 wt% PVDF with high mass loading of $\sim 6 \text{ mg/cm}^2$ (Another formulation of 80% active material / 15 % carbon black / 5% PVDF is still under cycling to see the formulation impact and the data will be integrated to the publication afterwards). The low carbon black content facilitates a perspective close to the practical application of the material's electrochemical performance. **Figure 12a and 12b** demonstrate the galvanostatic charge and discharge curves of the 1st, 2nd and 5th cycles collected within the potential window of 2.5 – 4.3 V versus Na^+/Na at C/20 current. The NVPF-DES presents quite poor electrochemical capacity with $\sim 8 \text{ mAh/g}$ at C/10 current, probably due to the cover of organic DES which prohibits the Na^+ diffusion. The NVPF-DES-c presents two reversible incline sloping plateaus indicating two solid-solution composition domains with the

Na^+ extraction and insertion, as expected from the mixed composition of V^{4+} and V^{3+} . These processes can also be observed through the first derivative curves of the second galvanostatic cycle (**Figure 12d**). The broad peaks at around 3.61 V and 4.07 V at C/20 approve the solid-solution type reaction. The average potential at discharging is 3.57 V and 4.04 V, which are quite similar to the charging potential and signifying the small polarization between these two processes. On the other hand, the pure NVPF and NVPFO₂ show two horizontal plateaus as the figures exhibited from the previous chapter II. To get more information, the materials were charged/discharged at different current densities. As the charge/discharge current increases, the charging/discharging plateau of NVPF-DES-c gradually becomes shorter until it becomes a slightly inclined straight line from an S-shaped curve at 2C (**Figure 12c**).

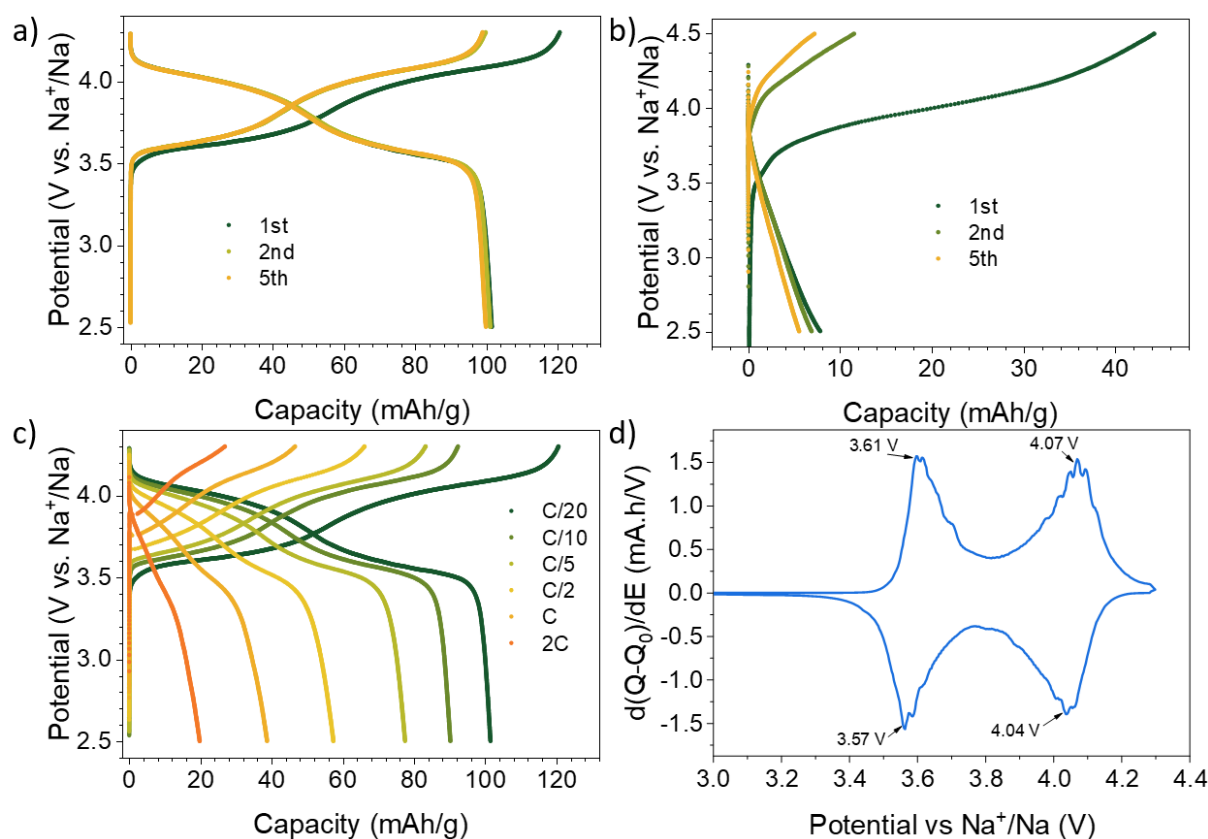


Figure 12: a) and b) galvanostatic charge and discharge curves obtained for NVPF-DES-c and NVPF-DES materials at the cycling rate of C/20. c) charge and discharge curves of NVPF-DES-c from C/20 to 2C. d) Associated derivative curves of the 2th cycles for NVPF-DES-c.

As indicated in **Figure 13a**, at C/20, the NVPF-DES-c exhibits reversible capacities of around 102 mAh/g, close to the theoretic one. But it plunged to 20 mAh/g at 2C. Meanwhile, when the charging/discharging current increases to 2C and drops back to C/20, the battery fully recovers its initial capacity, which indicates that the capacity loss at high currents is due to kinetics limitations and the material keeps a good structural stability. This compound also shows a

capacity retention higher than 82% after around 140 cycles at C/5 with the stable coulombic efficiency of 100%. However, it seems the carbon formed during the calcination process does not provide a very significant effect on the electrochemical performance at high current density.

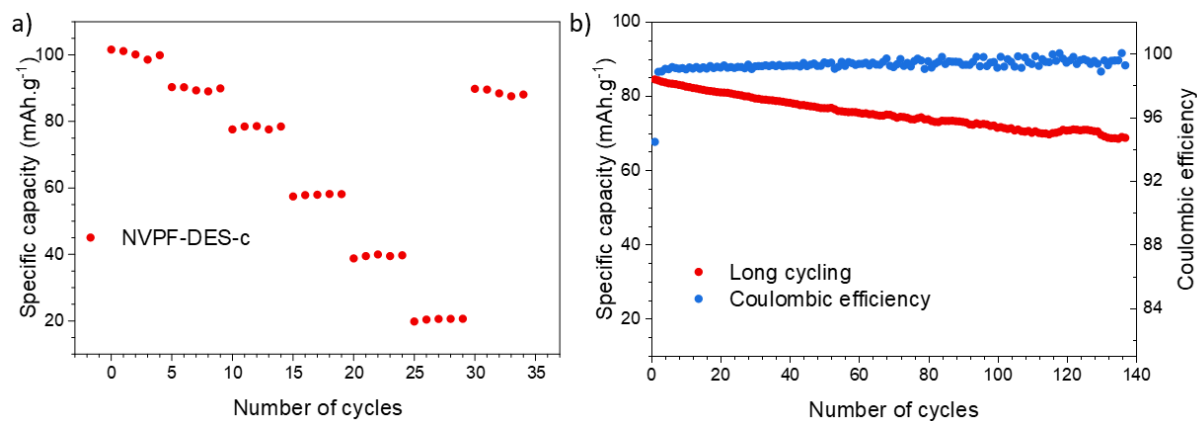


Figure 13: a) specific capacities collected for NVPF-DES-c at various C-rates from C/20 to 2C. b) Long-term cycling performance of NVPF-DES-c at C/5.

4. Conclusion

In summary, this work successfully demonstrates that $\text{Na}_3\text{V}_2(\text{PO}_4)_2\text{F}_{3-y}\text{O}_y$ with special morphology can be synthesized by cheap and environmentally friendly DES, a novel class of IL. Although the final synthesis compound was partially reduced during high-temperature calcination, we also coated a layer of carbon with this synthesis method. And the final synthesis product showed good electrochemical properties. Of course, there is still much room for improvement of this material and its carbon coating to improve the final electrochemical performance at high rates charge/discharge.

Reference

- [1] J. M. Tarascon, *Joule* **2020**, 4, 1616–1620.
- [2] T. Broux, F. Fauth, N. Hall, Y. Chatillon, M. Bianchini, T. Bamine, J. B. Leriche, E. Suard, D. Carlier, Y. Reynier, L. Simonin, C. Masquelier, L. Croguennec, *Small Methods* **2019**, 3, 1–12.
- [3] M. Bianchini, N. Brisset, F. Fauth, F. Weill, E. Elkaim, E. Suard, C. Masquelier, L. Croguennec, *Chem. Mater.* **2014**, 26, 4238–4247.
- [4] M. Bianchini, P. Xiao, Y. Wang, G. Ceder, *Adv. Energy Mater.* **2017**, 7, 1700514.
- [5] Y. U. Park, D. H. Seo, H. Kim, J. Kim, S. Lee, B. Kim, K. Kang, *Adv. Funct. Mater.* **2014**, 24, 4603–4614.
- [6] L. H. B. Nguyen, T. Broux, P. S. Camacho, D. Denux, L. Bourgeois, S. Belin, A. Iadecola, F. Fauth, D. Carlier, J. Olchowka, C. Masquelier, L. Croguennec, *Energy Storage Mater.* **2019**, 20, 324–334.
- [7] T. Broux, T. Bamine, F. Fauth, L. Simonelli, W. Olszewski, C. Marini, M. Ménétrier, D. Carlier, C. Masquelier, L. Croguennec, *Chem. Mater.* **2016**, 28, 7683–7692.
- [8] J. Olchowka, L. H. B. Nguyen, T. Broux, P. Sanz Camacho, E. Petit, F. Fauth, D. Carlier, C. Masquelier, L. Croguennec, *Chem. Commun.* **2019**, 55, 11719–11722.
- [9] Q. Liu, X. Meng, Z. Wei, D. Wang, Y. Gao, Y. Wei, F. Du, G. Chen, *ACS Appl. Mater. Interfaces* **2016**, 8, 31709–31715.
- [10] Q. Liu, D. Wang, X. Yang, N. Chen, C. Wang, X. Bie, Y. Wei, G. Chen, F. Du, *J. Mater. Chem. A* **2015**, 3, 21478–21485.
- [11] X. Shen, J. Zhao, Y. Li, X. Sun, C. Yang, H. Liu, Y. S. Hu, *ACS Appl. Energy Mater.* **2019**, 2, 7474–7482.
- [12] Y. Qi, L. Mu, J. Zhao, Y. S. Hu, H. Liu, S. Dai, *J. Mater. Chem. A* **2016**, 4, 7178–7184.
- [13] Y. Qi, L. Mu, J. Zhao, Y. S. Hu, H. Liu, S. Dai, *Angew. Chemie - Int. Ed.* **2015**, 54, 9911–9916.

- [14] Y. Qi, J. Zhao, C. Yang, H. Liu, Y.-S. Hu, *Small Methods* **2018**, 3, 1800111.
- [15] A. Mukherjee, T. Sharabani, I. Perelshtein, M. Noked, *Batter. Supercaps* **2020**, 3, 52–55.
- [16] N. Eshraghi, S. Caes, A. Mahmoud, R. Cloots, B. Vertruyen, F. Boschini, *Electrochim. Acta* **2017**, 228, 319–324.
- [17] Y. Cao, Y. Liu, D. Zhao, X. Xia, L. Zhang, J. Zhang, H. Yang, Y. Xia, *ACS Sustain. Chem. Eng.* **2020**, 8, 1380–1387.
- [18] C. Shen, H. Long, G. Wang, W. Lu, L. Shao, K. Xie, *J. Mater. Chem. A* **2018**, 6, 6007–6014.
- [19] J. Olchowka, L. H. B. Nguyen, E. Petit, P. S. Camacho, C. Masquelier, D. Carlier, L. Croguennec, *Inorg. Chem.* **2020**, 59, 17282–17290.
- [20] J. Olchowka, T. Tailliez, L. Bourgeois, M. A. Dourges, L. Guerlou-Demourgues, *Nanoscale Adv.* **2019**, 1, 2240–2249.
- [21] J. Olchowka, R. Invernizzi, A. Lemoine, J. Allouche, I. Baraille, D. Flahaut, L. Guerlou-Demourgues, *J. Electrochem. Soc.* **2020**, 167, 100527.
- [22] E. L. Smith, A. P. Abbott, K. S. Ryder, *Chem. Rev.* **2014**, 114, 11060–11082.
- [23] I. Juneidi, M. Hayyan, O. Mohd Ali, *Environ. Sci. Pollut. Res. 2016 238* **2016**, 23, 7648–7659.
- [24] A. K. Halder, M. N. D. S. Cordeiro, *ACS Sustain. Chem. Eng.* **2019**, 7, 10649–10660.
- [25] K. Radošević, M. Cvjetko Bubalo, V. Gaurina Srček, D. Grgas, T. Landeka Dragičević, R. I. Redovniković, *Ecotoxicol. Environ. Saf.* **2015**, 112, 46–53.
- [26] C. Ruß, B. König, *Green Chem.* **2012**, 14, 2969–2982.
- [27] E. R. Cooper, C. D. Andrews, P. S. Wheatley, P. B. Webb, P. Wormald, R. E. Morris, *Nat. 2004 4307003* **2004**, 430, 1012–1016.
- [28] Z. Wu, R. R. Huang, H. Yu, Y. C. Xie, X. Y. Lv, J. Su, Y. F. Long, Y. X. Wen, *Mater. 2017, Vol. 10, Page 134* **2017**, 10, 134.

- [29] N. Delgado-Mellado, M. Larriba, P. Navarro, V. Rigual, M. Ayuso, J. García, F. Rodríguez, *J. Mol. Liq.* **2018**, 260, 37–43.
- [30] J. Rodríguez-Carvajal, *Phys. B Phys. Condens. Matter* **1993**, 192, 55–69.
- [31] F. D. Hardcastle, I. E. Wachs, *J. Phys. Chem.* **1991**, 95, 5031–5041.
- [32] C. J. Antony, A. Aatiq, C. Y. Panicker, M. J. Bushiri, H. T. Varghese, T. K. Manojkumar, *Spectrochim. Acta - Part A Mol. Biomol. Spectrosc.* **2011**, 78, 415–419.
- [33] J. Schwan, S. Ulrich, V. Batori, *J. Appl. Phys.* **1996**, 80, 440.
- [34] Z. Tong, Y. Qi, J. Zhao, L. Liu, X. Shen, H. Liu, *Waste and Biomass Valorization* **2018**, 11, 2201–2209.
- [35] R. Fang, J. Olchowka, C. Pablos, P. S. Camacho, D. Carlier, L. Croguennec, S. Cassaignon, *Batter. Supercaps* **2021**, DOI 10.1002/batt.202100179.

Conclusion

In this PhD work, many compounds of the $\text{Na}_3\text{V}^{3+}_{2-y}\text{V}^{4+}_y(\text{PO}_4)_2\text{F}_{3-y}\text{O}_y$ ($0 \leq y \leq 2$) (NVPFO_y) family were obtained with different morphologies and compositions through various synthesis methods, such as the solvothermal reaction with tuned condition, ionothermal synthesis and high temperature solid-state reaction. The influence of their shape/size and composition on their transport properties and final electrochemical performance were carefully investigated to try to determine the optimal.

Firstly, a series of NVPFO_y with nanospheres, cylindrical aggregates, flakes and sand roses without any carbon coating was synthesized through solvothermal method by playing on different synthesis parameters like water/ethanol ratio, heating rate, stoichiometry of precursors and the adding or not of a surfactant. Through a thorough characterization, the oxygen and fluorine composition were determined for these samples, which were in the range of $0.35 \leq y \leq 0.8$. Under the similar composition, the nanospherical NVPFO_y exhibited the best electrochemical performance, confirming the strong impact of particles' morphology on the energy storage capacity.

Next, four compounds belonging to the NVPFO_y family with different oxygen / fluorine ratio were synthesized by the solvothermal method used in the previous study. These samples with the same nanospherical size and morphology but different compositions provide a good perspective to inspect the effect of O²⁻ substitution on the final electrochemical property. In this part, the Raman spectroscopy was firstly reported for characterizing the oxygen content in the NVPFO_y family and electrochemical impedance spectroscopy permit to evaluate the impact of V⁴⁺/V³⁺ initial ratio on the transport properties. Meanwhile, it also proves that a large amount of mixed V³⁺ and V⁴⁺ is more favorable for the electronic mobility, i.e. the NVPFO_{1.35} in this case.

For a more rigorous comparison of the effect of morphologies on the electrochemical properties, three NVPFO₂ with different morphologies were synthesized via the various routes, such as solvothermal method, ionothermal method and solid-state method. The NVPFO₂ composition were thoroughly confirmed by XRD, NMR, XPS and Raman. The electrochemical impedance spectroscopy demonstrates the nanosizing of NVPFO₂ material and the ionic liquid coating can enhance significantly the electronic and ionic conductivity respectively. Finally, nanosizing is found to be one key parameter for the high rate cycling capacity of the battery and full cell versus hard carbon have been assembled with the best NVPFO₂ material.

In a more perspective chapter, a new synthesis method inspired from ionothermal method was successfully applied to obtain the NVPFO_y material with deep eutectic solvent. The compound presents very special 3D morphology with the carbon coating, showing a good energy storage capacity. There is still potential for continued optimization and improvement.

From the state of art and the results shown in this work, it was demonstrated the possibility to improve the performance of this positive electrode material by optimizing the morphology and composition of NVPFO_y itself. However, the optimization is limited and the poor electronic conductivity due to the structure of the polyanionic material hinders good high rate performance. One alternative is to increase the carbon content in the electrode from the 7% commonly used in this thesis to 15% - 20%, accompanied by integrating NVPFO_y with various carbon sources, such as reduced graphene oxide during or after the synthesis reaction. However, for a given mass, an increase in the carbon source must lead to a decrease in the active material and, subsequently, in the total energy. The other and most promising possibility to overcome the low electronic conductivity is to apply an efficient and homogenous carbon coating on NVPFO_y, similarly to what was done for LiFePO₄. Therefore, achieving the right balance between the two will be the focus of the next research.

Although NVPFO_y materials have not shown advantage on energy density against the NMC (Lithium-Nickel-Manganese-Cobalt-Oxide) or LFP (lithium ferrophosphate), it is still one of the most important positive electrode materials of sodium ion batteries today, which are the viable alternative technology to lithium ion batteries. Sodium ion batteries are still in the early stages of research and development, and only a few companies have put them into production. However, since the pursuit of renewable energy and the protection of the environment in recent years, sodium ion batteries have shown promising results in a relatively short period of time. At the same time, due to the similarity between sodium-ion batteries and lithium-ion batteries, a large number of production facilities can be shared, and existing lithium battery plants can be converted to produce sodium-ion batteries if needed. This also helps alleviate supply chain risk issues in special periods.

Effect of composition and morphology on the electrochemical performance of $\text{Na}_3\text{V}_2(\text{PO}_4)_2\text{F}_{3-y}\text{O}_y/\text{Na}_3\text{V}_2(\text{PO}_4)_2\text{FO}_2$

This PhD thesis is consistent of well controlling all the varieties and comparing the morphology and composition impact of $\text{Na}_3\text{V}_2(\text{PO}_4)_2\text{F}_{3-y}\text{O}_y$ without any carbon coating in order to improve its final electrochemical performance through a more fundamental perspective. Firstly, a series of slightly tuned synthesis with the same precursors were carried out to obtain the $\text{Na}_3\text{V}_2(\text{PO}_4)_2\text{F}_{3-y}\text{O}_y$ particles with different morphologies and similar composition and then to investigate the effect of morphologies on energy storage performance. Next, from one most performant morphology found in the last part, the effect of the oxygen content on transport properties and electrochemical performance within $\text{Na}_3\text{V}_2(\text{PO}_4)_2\text{F}_{3-y}\text{O}_y$ (different O^{2-} substitution percent) were inspected, while keeping the morphologies unchanged. The nanospherical $\text{Na}_3\text{V}_2(\text{PO}_4)_2\text{FO}_2$ found in last part were compared with those synthesized through different methods with the same particle composition but totally different morphologies and surface functionalization to further understand the morphology and surface coating impact on the energy storage capacity. At last, deep eutectic solvent, one kind of ionic liquid, was used as a new synthesis medium to reach a totally new and special morphology not reported before and a new approach to make a carbon coating. In general, the different morphologies and compositions of $\text{Na}_3\text{V}_2(\text{PO}_4)_2\text{F}_{3-y}\text{O}_y$ are obtained separately by controlling and refining a series of synthesis methods. Their influences on the final electrochemistry of the material have also been investigated separately. These studies contribute to the understanding of this material from a fundamental point of view, thus facilitating further optimization.

Cette thèse consiste à bien contrôler toutes les variétés et à comparer l'impact de la morphologie et de la composition de $\text{Na}_3\text{V}_2(\text{PO}_4)_2\text{F}_{3-y}\text{O}_y$ sans aucun revêtement de carbone afin d'améliorer ses performances électrochimiques finales dans une perspective plus fondamentale. Tout d'abord, une série de synthèses légèrement ajustées avec les mêmes précurseurs a été réalisée pour obtenir des particules de $\text{Na}_3\text{V}_2(\text{PO}_4)_2\text{F}_{3-y}\text{O}_y$ de différentes morphologies et de composition similaire pour étudier l'effet des morphologies sur les performances de stockage d'énergie. Ensuite, à partir de la morphologie la plus performante trouvée dans la dernière partie, l'effet de la teneur en oxygène sur les propriétés de transport et les performances électrochimiques dans le $\text{Na}_3\text{V}_2(\text{PO}_4)_2\text{F}_{3-y}\text{O}_y$ (différents pourcentages de substitution de O^{2-}) a été inspecté, tout en gardant les morphologies inchangées. Les $\text{Na}_3\text{V}_2(\text{PO}_4)_2\text{FO}_2$ nanosphériques trouvés dans la dernière partie ont été comparés à ceux synthétisés par différentes méthodes avec la même composition de particules mais des morphologies et une fonctionnalisation de surface totalement différentes pour mieux comprendre l'impact de la morphologie et du revêtement de surface sur la capacité de stockage d'énergie. Enfin, le solvant eutectique profond, un type de liquide ionique, a été utilisé comme nouveau moyen de synthèse pour obtenir une morphologie totalement nouvelle et spéciale, qui n'avait pas été signalée auparavant, et une nouvelle approche pour fabriquer un revêtement de carbone. En général, les différentes morphologies et compositions de $\text{Na}_3\text{V}_2(\text{PO}_4)_2\text{F}_{3-y}\text{O}_y$ sont obtenues séparément en contrôlant et en affinant une série de méthodes de synthèse. Leurs influences sur l'électrochimie finale du matériau ont également été étudiées séparément. Ces études contribuent à la compréhension de ce matériau d'un point de vue fondamental, facilitant ainsi son optimisation ultérieure.